UNIVERSITY OF SOUTHAMPTON

FACULTY OF ENGINEERING, SCIENCE AND MATHEMATICS

School of Ocean and Earth Science

Causes of the Interannual Variability of Deep Convection

by

Laure Grignon

Thesis for the degree of Doctor of Philosophy

August 8, 2009

Graduate School of National Oceanography Centre, Southampton

This PhD dissertation by

Laure Grignon

has been produced under the supervision of the following persons

Supervisors:

Dr. David Smeed

Prof. Harry Bryden

Mr. Peter Challenor

Prof. Gwyn Griffiths

Chair of Advisory Panel:

Prof. Ian Robinson

UNIVERSITY OF SOUTHAMPTON

ABSTRACT

FACULTY OF ENGINEERING, SCIENCE AND MATHEMATICS
SCHOOL OF OCEAN AND EARTH SCIENCES

Doctor of Philosophy

Causes of the Interannual Variability of Deep Convection
by Laure Grignon

Deep water formation in the Labrador Sea and the Gulf of Lion, for example, results from convection. A cyclonic circulation leads to a doming of the isopycnals at its centre, where stratification is then completely eroded by high surface winter buoyancy loss. This thesis assesses the causes of the interannual variability of deep convection.

We first aim to quantify the relative importance of preconditioning, defined as the temperature and salinity structures and contents of the water column before the onset of convection, and of the buoyancy forcing (averaged over one winter) on the final convective mixed layer depth and on the temperature and salinity of the water mass formed. This study focuses on the Mediterranean and uses data from the Medar/Medatlas and Dyfamed data sets. The heat fluxes are studied and characterised. It is shown the the preconditioning is as important as the winter buoyancy fluxes in setting the final depth of convection. At the Dyfamed site (Corsica Strait), the seasonal cycle shows that the stratification frequency reaches a maximum in the intermediate layer in winter. This winter maximum is thought to be of critical importance.

The second (and main) part focuses on the effect of the short-term (O(day)) variability of the surface forcing on convection, using an idealised model. The MIT model is integrated over a square box of size 64km x 64 km x 2km initialised with homogeneous salinity and a linear vertical temperature gradient. The configuration of the model is described and validated. A time-periodic cooling is then applied over a disc of radius 20km at the centre of the surface of the box. It is shown that the final mixed layer depth depends little on this short-term time variability because the lateral buoyancy fluxes are very responsive to the surface ones. Our results are compared with traditional parameterisation of the lateral buoyancy fluxes. General characteristics of the patch are also looked at, such as the rim current, the location of the angular momentum surfaces, the potential vorticity and the residual stratification in the mixed layer. The characteristics of the final water mass in each experiment are studied, showing that the short-term time variability of the forcing has an impact on the characteristics of the water mass formed.

The last part compares the modelling study to gliders data for the Labrador Sea obtained by Peter Rhines and Charlie Eriksen of the University of Washington, WA, USA, in winter 2004-05. In that part of the real ocean, the variability of the boundary current seems more important than the variability in the surface forcing.

Contents

List of Figures

List of Tables

DECLARATION OF AUTHORSHIP

I, Laure Grignon, declare that the thesis entitled 'Causes of the Interannual Variability of Deep Convection' and the work presented in it are my own, and have been generated by me as the result of my own original research. I confirm that:

- this work was done wholly or mainly while in candidature for a research degree at this University;
- where any part of this thesis has been previously submitted for a degree or any other qualification at this University of any other institution, this has been clearly stated;
- where I have quoted from the work of others, the source is always given. With the exception of such quotations, this thesis is entirely my own work;
- I have acknowledged all main sources of help;
- where the thesis is based on work done by myself jointly with others, I have made clear what was done by others and what I have contributed myself;
- none of this work has been published before submission.

Signed: .....

Date: .....

ACKNOWLEDGEMENTS

First, I would like to thank my main supervisor David Smeed, who always reviewed my work with rigour and provided encouragement at the same time as constructive criticism. I am very much indebted to him.

I would also like to acknowledge Harry Bryden for his help on the data analysis and his guidance in the management of my PhD, particularly for encouraging me to apply for a grant to spend some time and work in Seattle.

Then my thanks go to my other supervisors, Peter Challenor, who helped me to understand statistics, and Gwyn Griffiths. They both showed interest for my work despite the fact that it was not in their main area of research, and advised me on more general aspects of my PhD.

Many other people helped me during my time at NOC. I owe much to Lucas Merckelbach, who taught me how to use the MIT model and initiated me to the python language. He always took the time to look into computing issues, and his help saved me a considerable amount of time.

I would like to thank Simon Josey, George Nurser, and Joel Hirschi for their help, both technical and scientific, at various stages of my PhD, as well as Achim Wirth, Julien Le Sommer and Bernard Barnier for helpful discussion after my talk in Grenoble. I would also like to thank Katrin Schroeder for discussions about the circulation in the Mediterranean Sea.

I had the opportunity to spend 3 months working at the University of Washington. I really enjoyed working there, first for the discussions with Peter Rhines about Geophysical Fluid Dynamics, but also for the experiments in the laboratory with Eric Lindahl and Bob Koon. I would also like to acknowledge Eleanor Williams and Charlie Eriksen for their help dealing with gliders data.

My time at NOC was made truly enjoyable by all the people I had the chance to interact with while there. This includes the other postgraduate students, the staff members I went on cruises with, the volleyball and basketball players, as well as many others.

My last thanks go to Frederic Massias, who was my lecturer in Physics when I was studying in Paris. He is the one who showed me that I could enjoy Physics, despite a bad start.

Funding was provided by the National Oceanography Centre, Southampton (NOCS, 50%), the NERC Strategic Research Division (NSRD, 25%) and the National Marine Facilities Division (NMFD, 25 %). The exchange with the University of Washington was funded by the Research Mobility Program (RMP) of the Worldwide University Network (WUN).

Chapter 1

Introduction

Deep convection forms deep water in locations where a high buoyancy loss from a weakly stratified ocean to the atmosphere leads to the formation of a very deep mixed layer (O(1km)). A very dense water mass is, among other locations, formed in the Northern Atlantic and is traditionally thought to drive the thermohaline circulation in the world ocean (Marshall and Schott, 1999b), hence its importance in climate prediction.

The interannual variability of convection could be critical in setting the strength of the overturning circulation. It has been suggested that an increase in the rate of freshwater release in the Arctic could shut down the thermohaline circulation (Rahmstorf, 1995), because it would inhibit convection completely. However, more recent studies suggest that the dependance of the thermohaline circulation on the convection might not be that important (Pickart and Spall, 2007) because the main driving factor would be the upward heat transfer happening closer to the equator.

Winter mixing is also an important process in oxygenating the oceans and has an impact on the biology as mixing brings nutrients close to the surface where light is available.

1.1 Deep convection: processes

1.1.1 Open Ocean Convection

The MEDOC-Group (1970)'s program was the first international collaboration to study deep convection. The site chosen was the Gulf of Lion, in the Mediterranean Sea, because it is relatively accessible even in winter.

They identified three phases of convection, involving a variety of length scales

(see figure 1.1), which makes the process of deep convection particularly challenging and interesting to study:

- The preconditioning: the stratification becomes weaker. This is thought to be created by a cyclonic circulation (MEDOC-Group, 1970; Legg et al., 1998) and/or by topographic features (Hogg, 1973; Madec et al., 1996; Alverson, 1997). Typically, in the Gulf of Lion, the cyclonic circulation is due to the gyre system, with a horizontal scale of O(50-100km).

- The violent mixing phase: convection is observed in the centre of the convective patch, leading to intense mixing and to a deepening of the mixed layer. Sinking occurs in plumes of horizontal scale O(1km) in which the dense water sinks at vertical speeds up to $10cm/s$ (Voorhis and Webb, 1970; Schott and Leaman, 1991). These plumes are mixing agents (Send and Marshall, 1995) associated with a small-scale circulation sometimes modeled as paired, discrete point vortices called hetons (Hogg and Stommel, 1985; Legg and Marshall, 1993) which propel themselves out of the convective patch, leading to horizontal mixing.

- The sinking and spreading phase: the mixed water sinks and spreads horizontally. The spreading of dense water happens through the action of eddies of horizontal scale O(5-10km), thought to be generated at the edge of the convective patch by the baroclinic instability of the rim current (Gascard, 1978; Testor and Gascard, 2006).

1.1.2 Shelf Convection

Shelf convection is due to high buoyancy loss at the surface above a continental shelf. The dense water formed then sinks further from the shelf (cascading). Killworth (1983) identified five ingredients for shelf convection: a reservoir to form deep water, a source of dense water in the reservoir, a reason for deep water to go down the slope away from the reservoir, and the presence of more than one water mass - although, as Manalotte-Rizzoli (1991) points out, the Northern Adriatic Sea is an example of shelf convection involving only one water mass - and a strategic combination of the four previous ingredients to allow the dense water to sink.

In the Gulf of Lion, there is a shelf convective site adjacent to the open ocean convective site, as shown on figure 1.1.2. The shelf acts as a reservoir cooled

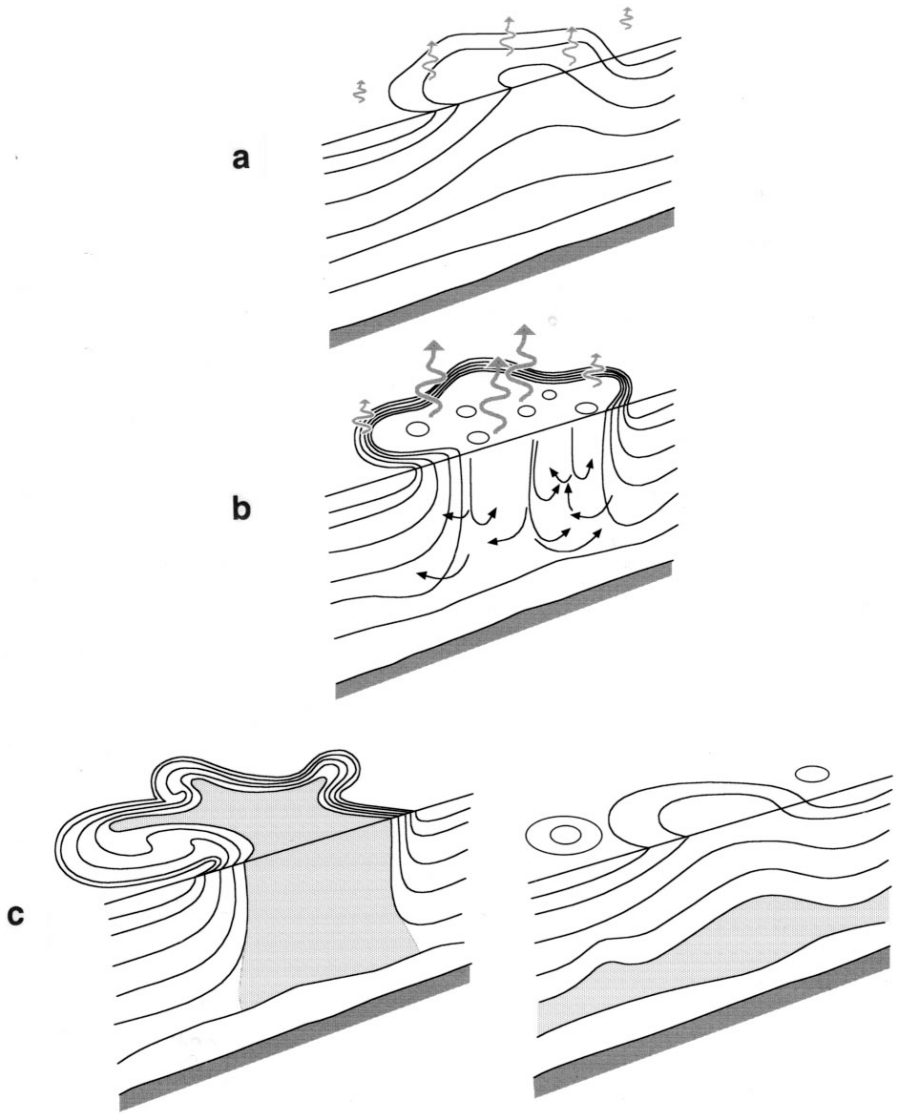

Figure 1.1: Schematic diagram of the three phases of ocean deep convection: (a) preconditioning, (b) deep mixing and, (c) lateral exchange leading to spreading and restratification. Buoyancy flux through the sea surface is represented by curly arrows, and the underlying stratification/outcrops is shown by continuous lines. The volume of fluid mixed by convection is shaded. From Marshall and Schott (1999a).

in winter, hence forming cold and dense water. The boundary current flowing along the coast provides a different water mass, saltier and warmer. When the shelf water is dense enough, it can flow along the canyons of the continental slope (Font et al., 2006; Canals et al., 2006).

1.2 The Mediterranean Sea

1.2.1 General

The Mediterranean is a semi-enclosed sea acting as an evaporation basin. Relatively fresh Atlantic Water enters through the strait of Gibraltar at the surface, and salty water leaves the Mediterranean Sea at the bottom of the strait. Figures 1.3 and 1.4 show a satellite view of the Mediterranean and a schematic of the general circulation according to Millot and Taupier-Letage (2004) for the top (mainly Atlantic Water - AW), the intermediate (mainly Levantine Intermediate Water - LIW) and the deep layers (AdDW: Adriatic Deep Water; AeDW: Aegean Deep Water; TDW: Tyrrhenian Dense water; WMDW: Western Mediterranean Deep Water). In particular, they show that LIW formed in the Eastern Mediterranean and AW are advected towards the Gulf of Lion where WMDW is formed before slumping southward.

We notice the inflow of AW and outflows of LIW and Deep Waters at the Strait of Gibraltar. The Mediterranean Sea acts as an evaporation basin that makes the water saltier. Deep convection occurs in the Atlantic, but not in the Pacific, which is fresher. The salt input from the Mediterranean may be a critical element for the strength of the thermohaline circulation in the Atlantic (Broecker, 1991).

The straits are an important factor in controlling the general circulation of the Mediterranean. The strait of Gibraltar constrains the exchanges between the Mediterranean and the Atlantic. Exchanges between the Eastern and Western Mediterranean Seas are limited by the straits formed by the islands of Corsica, Sardinia and Sicilia.

1.2.2 Eastern basin

During the 1980's and 1990's, observations have shown that the major site of Eastern Mediterranean Deep-Water (EMDW) formation moved from the Adriatic to the Aegean Sea (Lascaratos et al., 1999). This was called the Eastern Mediterranean Transient (EMT) (Roether et al., 1996). This shift may be due to the pecu-

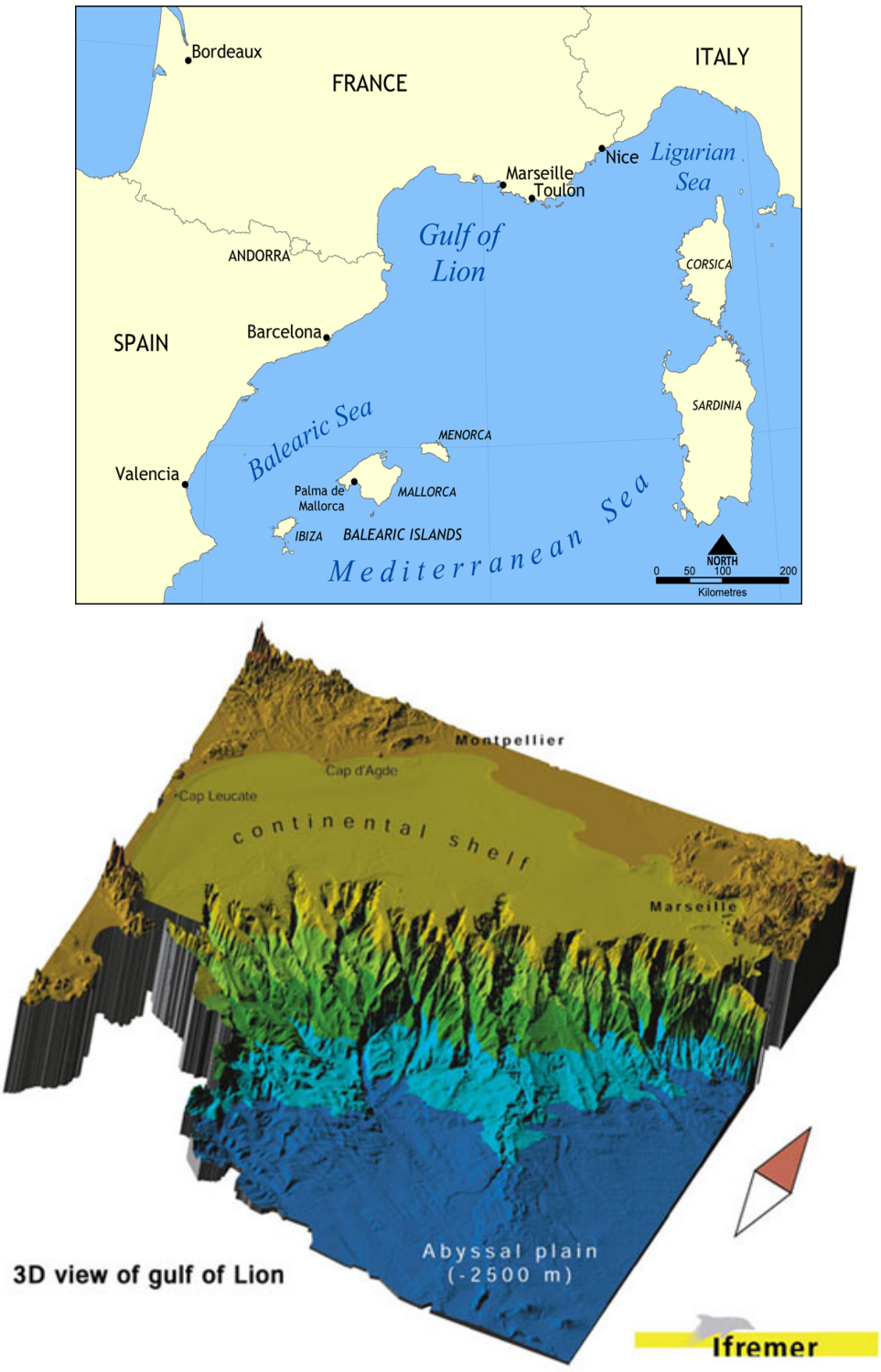

Figure 1.2: Map (top, from www.wikipedia.co.uk) and bathymetry (bottom, from www.ifremer.fr) of the Gulf of Lion.

Figure 1.3: Satellite view of the Mediterranean Sea. Modified from maps.google.com.

liar atmospheric forcing of this period. The dry period 1988-1993 was preceded and succeeded by the very cold winters of 1987 and 1992-93, which potentially led to better conditions in the Aegean for deep-water formation. Another explanation for this transition is the increased net evaporation due to river diversion projects in Russia and Egypt reducing the freshwater inflow (Boscolo and Bryden, 2001). Wu et al. (2000) showed, using a high-resolution model, that the salt added to deeper layers could have come from the top 1000m by a salinity redistribution process triggered by intensive cooling over the Aegean, and that this process was capable of switching the main convection site to the Aegean sea. Stratford and Haines (2002), using a more sophisticated model, showed that the three cold winters of 1987, 1992 and 1993 were enough to generate new Aegean deep water. A more recent assessment of the state of the EMT has been made by Theocharis et al. (2002). He concluded that the EMT was a major climatic event for the Mediterranean Sea, whose signal was fading at the end of the 1990's. However signs of the EMT were present in the western basin in spring 2005 (Schroeder et al., 2006).

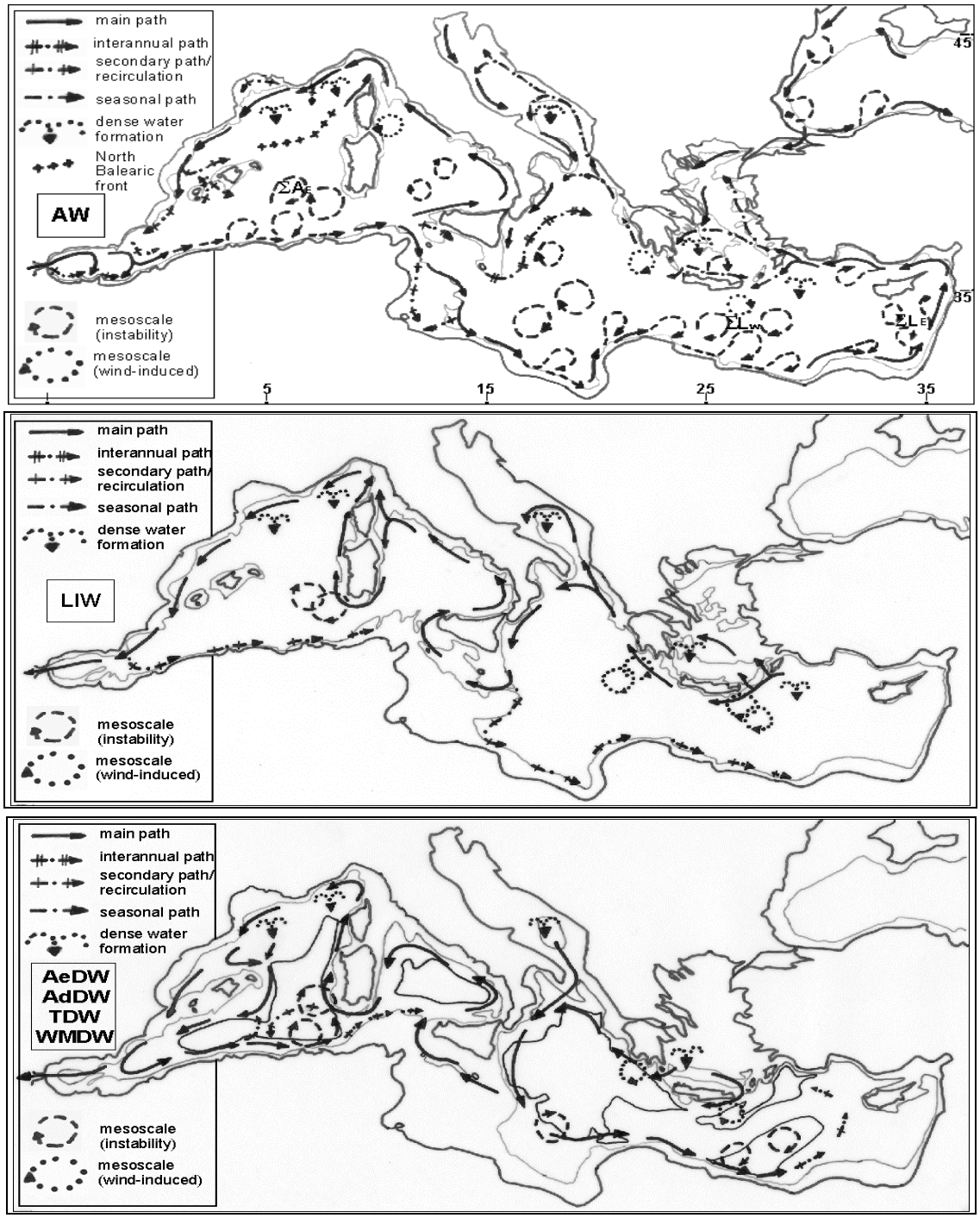

Figure 1.4: Schematic of the circulation in the Mediterranean for the top, intermediate and deep layers. From Millot and Taupier-Letage (2004).

1.3 Convection in the Gulf of Lion

1.3.1 General

The Gulf of Lion has all the elements necessary for deep convection to occur. There is a cyclonic circulation around the area, whose northern part is forced by the Liguro-Provencal current. In winter, the Mistral blowing southwards from Provence and, to a lesser extent, the Tramontana blowing Eastwards from the Pyrenees provide high heat losses that make the water so dense that the convection can reach the bottom of the basin (MEDOC-Group, 1970; Schott and Leaman, 1991; Schott et al., 1996). The convective area is traditionally defined as centered on the Medoc point, at $42^oN, 5^oE$.

1.3.2 Decadal trend

A warming and freshening trend in the water mass situated at the bottom of the Western Mediterranean basin has been identified between 1959 and 1997 (Béthoux et al., 1990, 1998): see figure 1.5. The WMDW appeared to be getting warmer at a rate of $3.47 \cdot 10^{-3o}C/yr$ and saltier at a rate of $1.07 \cdot 10^{-3}/yr$. These changes seem to be density compensated (the ratio of the two trends is close to the ratio between the thermal and haline expansion coefficients), except over winter 2004-05 (Lopez-Jurado et al., 2005). Figure 1.6, shows the trends for the temperature, salinity and density below the 600dbar level in the Balearic Sea, as well as the disruption in the trend for winter 2004-05. Because the depth levels chosen to define the deep water in Lopez-Jurado et al. (2005) (below 600dbar) and Béthoux et al. (1998) (below 2000m) are different, the temperatures, salinities of Lopez-Jurado et al. (2005) are higher than those of Béthoux et al. (1998).

1.3.3 Winter 2004-2005

The WMDW produced by deep convection in the Winter 2004-05 showed a disruption in the warming and saltying trend. The water appeared colder than measured in the last 10 years in the Balearic Sea. The salinity was also lower than measured in the previous 2 years, but still in the range of what had been measured since 1996 (Lopez-Jurado et al., 2005): see figure 1.6. The most notable feature is that this water was denser than observed over the previous ten years. Figure 1.7 shows the locations of the stations at which measurements have been taken, and their corresponding TS diagram. The TS diagram clearly shows the

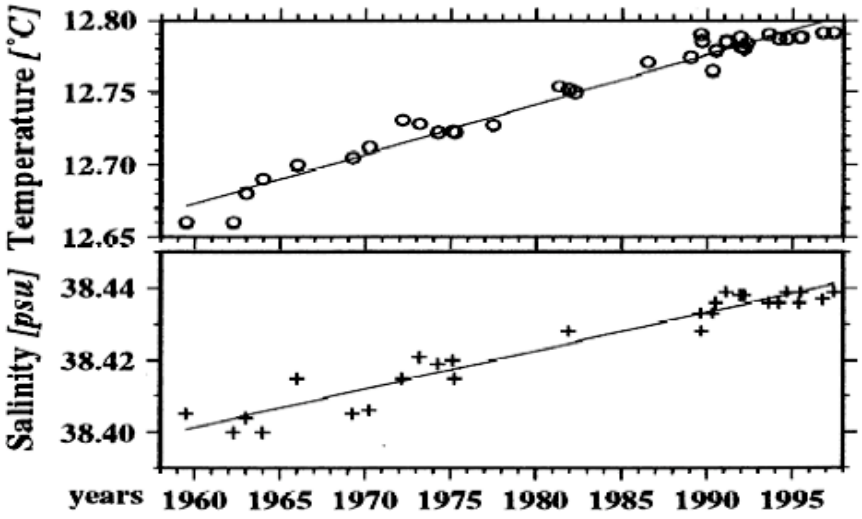

Figure 1.5: Temperature and Salinity trends observed in the deep water of the Algero-Provencal basin over the 1959-1997 period. From Béthoux et al. (1998)

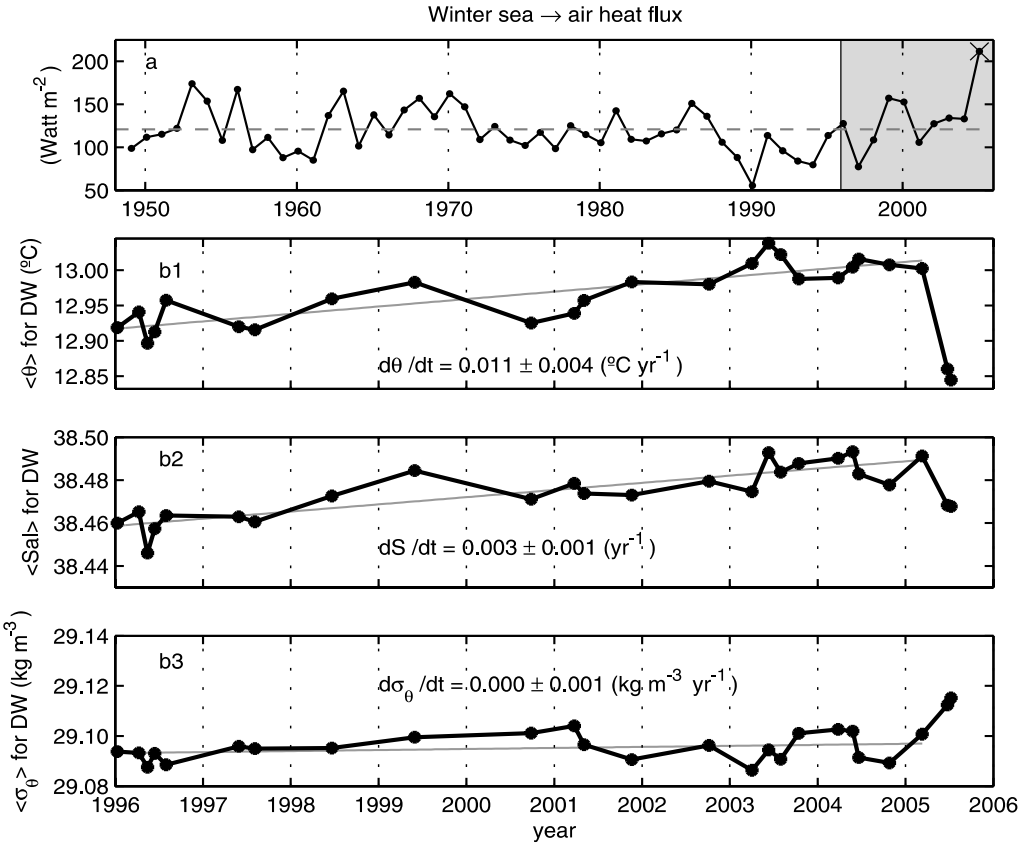

Figure 1.6: (a) Times series of heat flux loss from NCEP/NCAR reanalysis, averaged from December to March in the MEDOC area. (b) Time series of seawater properties in the Balearic Sea averaged from 600dbar to the bottom. The trends have been computed with data until March 2005. From Lopez-Jurado et al. (2005)

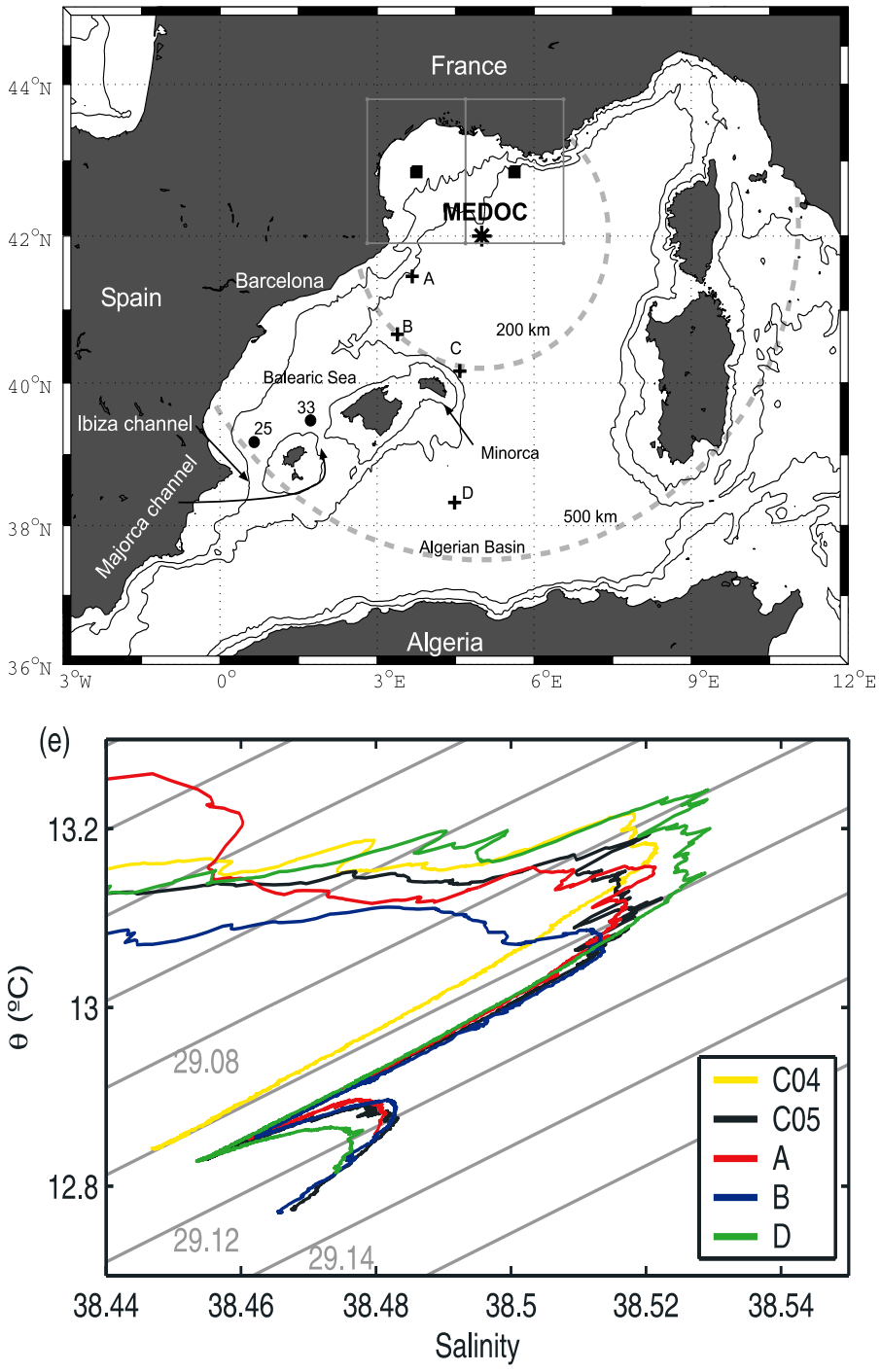

Figure 1.7: TS diagram (bottom) from profiles carried out during summer 2005, and including station C in 2004 at the stations A, B, C and D shown on the map (top). From Lopez-Jurado et al., 1995.

new deep-water, observed in 2005 at station A, B, C (C05) and D, but not at station C (C04) in 2004. It is noticeable by peculiar salinity local maximum and minimum in the densest part of the profiles.

1.3.4 Variability in Mixed Layer Depth

Measurements of the mixed layer depth are not very numerous because they are very hard to get. To obtain them, one has to go to sea when the convective process is active, which usually is a period of high winds. Consequently, its variability is mainly studied using models of different complexity, from simple 1D mixed layer depth model to 3D realistic models (Madec et al., 1991; Mertens and Schott, 1998; Somot et al., 2006): see figure 1.8.

The mixed layer depth is very sensitive to the surface forcing (Mertens and Schott, 1998), primarily due to the heat loss to the atmosphere because of Mistral events. The formula derived by Turner (1973) in an ideal case shows that the buoyancy frequency profile in the convective area should affect the mixed layer depth.

It is not very clear yet what the relationship between the mixed layer depth and the WMDW composition is. Even if convection does not reach full depth during one particular year, it is likely that what has been produced during that year will affect, through the temperatures and salinity structures, convection on subsequent year(s).

1.3.5 Possibles Causes of the Observed Variability

The variability in atmospheric forcing is one of the primary causes for the variability of deep-water formation (Lopez-Jurado et al., 2005; Krahmann and Schott, 1998; Mertens and Schott, 1998). The buoyancy loss at the surface is dominated by the heat loss (Mertens and Schott, 1998), which is correlated to the North Atlantic Oscillation (Rixen et al., 2005). The intensity of buoyancy loss clearly affects the mixed layer depth. However, it is still unclear if the repartition of this buoyancy loss in haline and thermal buoyancy components has an effect on the deep water temperature and salinity. Another remaining question concerns the effect of the shape (day to day variability) of the buoyancy forcing on convection: is its variability very important or is the integrated buoyancy loss the main information that matters?

A second explanation for the variability in deep water properties is what

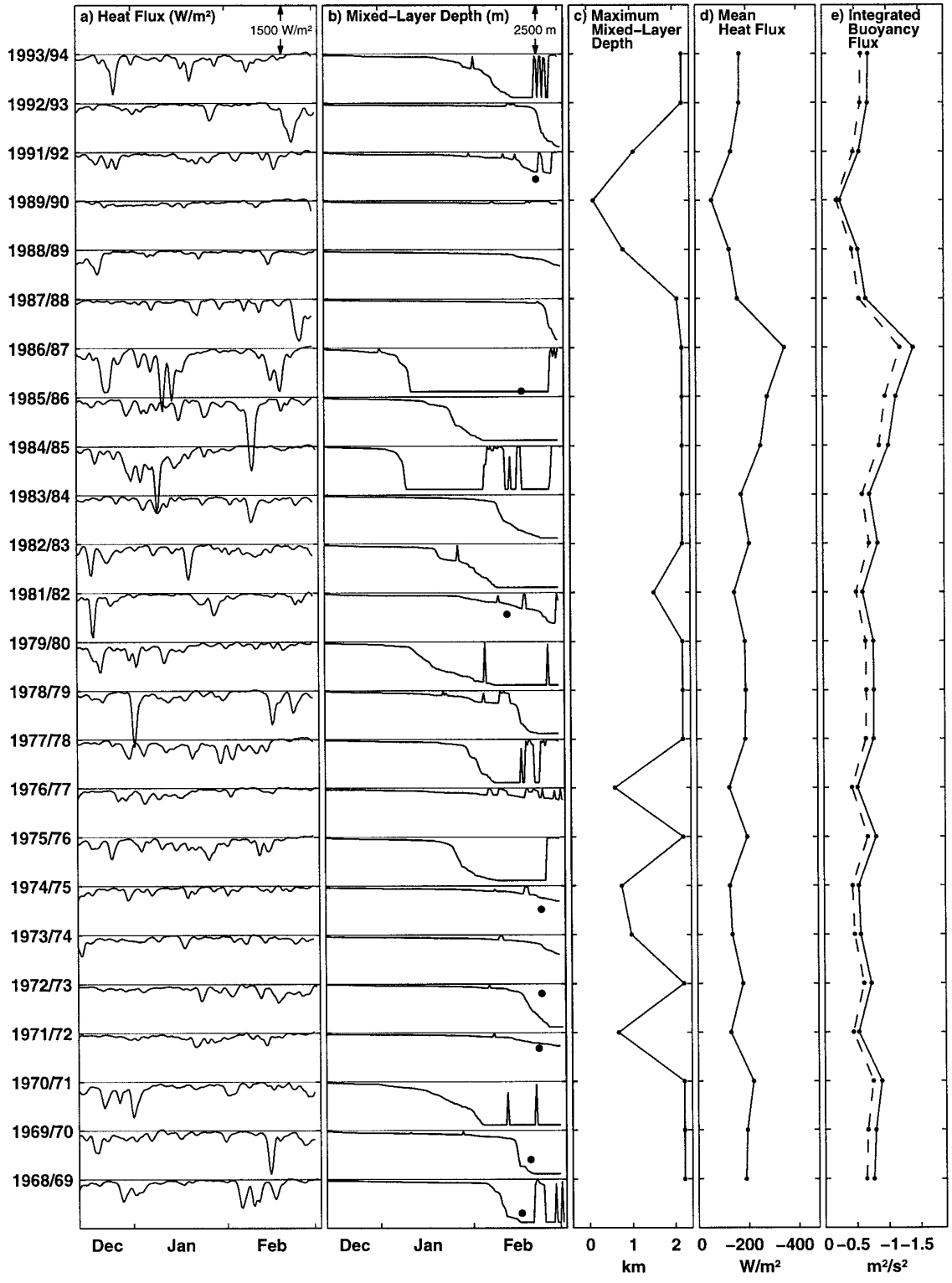

Figure 1.8: (a) Heat flux from coastal weather station data; (b) development of mixed layer depth in the model and observed maximum mixed layer depths (dots); (c) maximum mixed layer depth from the model; (d) mean net heat flux of the winter season; (e) integrated total buoyancy flux (solid) and its dominant thermal component (dashed); for the individual winters from 1968/69 to 1993/94. The winters of 1980/81 and 1990/91 are missing because of the lack of sufficient coastal station observations. From Mertens and Schott (1998).

we call hydrographic preconditioning, that is the temperature and salinity (and hence the density) structure of the water column at the onset of convection. This is related to larger scale changes in the Western Mediterranean:

- Increase in salinity
  - Man-induced (Rohling and Bryden, 1992; Krahmann and Schott, 1998) through river diversion projects.
  - Eastern Mediterranean Transient (Schroeder et al., 2006): this is a change in convective sites in the eastern Mediterranean leading to an import of salt into the western Mediterranean in the 1990s.
- Increase in temperature
  - Greenhouse effect (Béthoux et al., 1998)

One hypothesis is that the new WMDW found in 2005 is a direct product of the shelf convection that would have cascaded from the continental shelf of the Gulf of Lion (Font et al., 2006; Canals et al., 2006). However, one of the water masses formed in winter 2004-05 shows a salinity maximum which cannot be due to shelf water as the latter is to the contrary very fresh. Hence the cascading, although possibly related to the bottom layer characteristics, cannot fully explain the structure of the water column observed. A more likely hypothesis would be that the depth at which the cascading water sinks has an effect on the open-ocean convection, happening further off-shore. It could create a threshold effect - the fact that the water cascades on top or under the Levantine water may be critical.

1.4 Other Sites of Open Ocean Deep Convection in the World Ocean

Deep convection has also been observed in the Labrador and Greenland Seas. The Labrador Sea will be studied in more detail and is the object of chapter 6. In the Greenland Sea, the sequence of events is similar to the Labrador and the Mediterranean Seas, the main difference being the importance of ice through brine rejection in the Greenland Sea. The convective activity in that area was observed to be weak over the last decade (Schott et al., 1993; Marshall and Schott, 1999b). Convection has been also observed in the Irminger Sea, thought to be forced by the Greenland tip jet (Pickart et al., 2003).

1.5 Objectives and methods

We aim to assess the relative importance of different processes on the variability of deep convection. We characterise the variability of deep convection focusing on the maximum mixed layer depth and the temperature and salinity of the WMDW formed. The questions to be answered are:

- What are the relative effects of buoyancy loss compared to preconditioning?
- What are the relative effects of the integrated buoyancy loss compared to the shape (short-term time variability) of the buoyancy loss?

To answer these questions, we will use both model results and observations.

Chapter 2 characterises the heat and buoyancy fluxes in the Gulf of Lion. Chapter 3 focuses on the first question, based on hydrographic data from the Gulf of Lion. Chapters 4 and 5 describe numerical experiments aiming to answer the second question. Chapter 4 describes the configuration and validation of the model used, while Chapter 5 describes the results from experiments performed to answer that question. Chapter 6 confronts the results obtained from the numerical model with gliders' data obtained in the Labrador Sea. The last chapter summarises the main results and concludes the thesis.

Chapter 2

Analysis of the Winter Heat Fluxes in the Gulf of Lion

2.1 Introduction

This chapter is dedicated to the study of the winter heat fluxes in the Gulf of Lion, based on the National Center for Environmental Prediction (NCEP) reanalysis data set. We focus on the contribution of the different components in the heat fluxes and study the short-term (timescale of a few days) variability of the heat/buoyancy fluxes to extract timescales that will then be used to design our numerical experiments. In the Mediterranean, deep convection is associated with Mistral events, which can act intensively during short periods of time. One of the questions of this thesis is whether strong short wind bursts are more efficient than a mild constant wind forcing in deepening the mixed layer. Before answering this question, it is useful to characterise the buoyancy fluxes, and this will be the focus of this chapter.

We first present an overview of the data sets used in the analysis. In the second section, we study the composition of the surface heat fluxes. We then focus on characterising its temporal variability, before concluding.

2.2 Data set

2.2.1 NCEP data

We are using data available online from the NOAA (US National Oceanic and Atmospheric Administration) NCEP/NCAR reanalysis, which is a joint project be-

tween the National Center for Environmental Prediction (NCEP, formerly "NMC") and the National Center for Atmospheric Research (NCAR). The goal of this joint effort is to produce new atmospheric analyses using historical data (1957 onwards) and to produce analyses of the current atmospheric state (Climate Data Assimilation System, CDAS). The data are estimated using both observations and models, so we expect them to perform better in regions where observations are more frequent.

2.2.2 Choice of location

We are interested in convection, and therefore in regions of strong heat loss, in winter (defined as the period between the 1^{st} of December and the 31^{st} of March). The grid point we are going to choose is the one where the heat loss was the most important in February 2005. We choose this period because February is often the month when the violent mixing phase starts, due to strong heat loss. Moreover, the Bulletin commenté n$^o10$ (available on *www.mercator-ocean.fr*) provides an early estimate of the heat fluxes in the Gulf of Lion for February 2005, allowing a rough check of the NCEP data.

The NCEP grid has a horizontal resolution of 1.875^o for the longitude and about 1.9^o for the latitude. The grid point with strongest heat loss in the Gulf of Lion in February 2005 is $3.75^oE; 42.86^oN$. This grid point is very close to the Medoc point at $5^oE; 42^oN$, traditionally considered as the centre of convection. We choose the grid point of highest heat loss rather than the closest one because we expect the NCEP data to slightly underestimate the heat loss in that area due to under-sampling of high winds. Indeed, there are less measurements when the heat loss and wind are important due to the difficulty to take measurements under rough conditions. The point of highest heat loss is actually closer to land because that is where the Mistral wind originates. Therefore, all the time series considered in this document concern this grid point. See figure 2.1 for the heat fluxes of the area considered, quite wide compared to the zone we are actually interested in, and table 2.1 for the corresponding numerical values.

2.2.3 Processing

The NCEP data set contains the latent heat flux Q_L, the sensible heat flux Q_S, the radiative short waves flux Q_{SW}, and the radiative long waves flux Q_{LW}. The total radiative flux is $Q_R = Q_{SW} + Q_{LW}$, and the total heat flux: $Q_{TOT} = Q_L +$

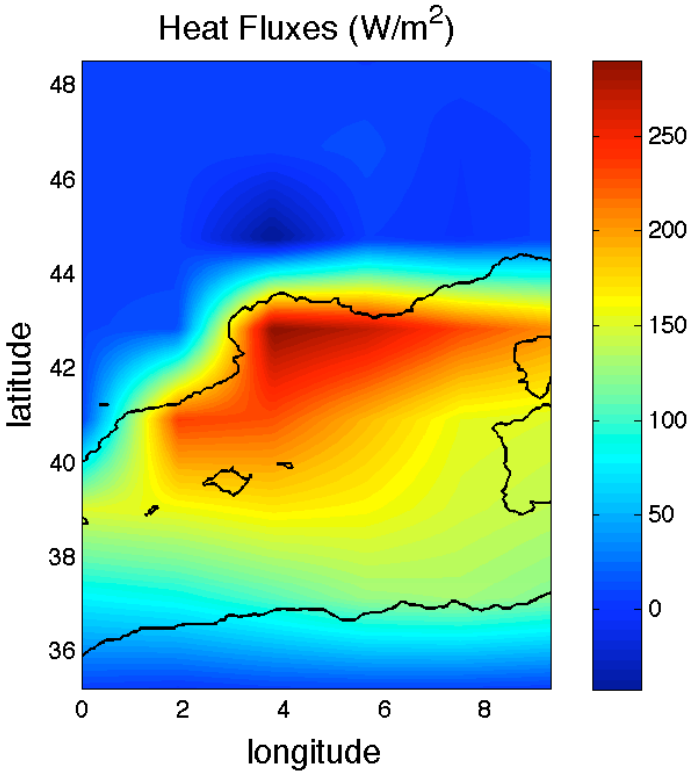

Figure 2.1: NCEP monthly heat fluxes on the Western Mediterranean for February 2005. The black contour line represents the coastline.

Position	0^oE	1.87^oE	3.75^oE	5.62^oE	7.50^oE	9.37^oE
35.24^oN	6.36	2.89	7.64	8.57	8.00	5.71
37.14^oN	78.64	87.43	105.46	126.32	130.32	119.50
39.05^oN	151.50	158.25	168.50	162.54	147.32	138.64
40.95^oN	10.39	234.75	227.39	189.25	154.96	149.75
42.86^oN	9.04	12.86	291.07	271.50	232.93	205.89
44.76^oN	8.68	6.43	-45.29	5.1071	-1.64	7.18
46.67^oN	7.50	8.82	7.36	12.75	-0.25	6.57
48.57^oN	9.96	8.68	8.00	4.14	8.68	10.71

Table 2.1: NCEP monthly heat losses over a wide area around the Gulf of Lion in W/m^2 in February 2005. Land areas are characterised by a lower heat loss. The grid point of strongest heat loss is in gray.

$Q_S + Q_R$. Daily values are readily available for all components apart from the radiative fluxes. The only NCEP radiative fluxes available for the last fifty years are the monthly values, while we need to study daily variations in the total heat loss. Therefore, we will try to get a better estimate using the values we have and interpolation schemes. Daily data are available for the NCEP radiative fluxes over the last three years, which will allow us to assess the different methods.

Four methods tested

The first method consists in keeping the monthly values without doing any interpolation. It is the simplest one, but generates error due to the fact that there is an annual trend in the radiative fluxes, which is perceptible when we observe the evolution of the daily radiative fluxes over a month.

The second method is a linear interpolation. We consider each monthly mean as the daily value at mid-month, and join each mid-month value with a straight line. The trouble with this method is that the monthly means are not conserved. In our case, the integrated heat fluxes are going to be important as they have a direct influence on the rate of deepening of the convective mixed-layer. If we do not keep the monthly means, we lose a useful offset in the integrated heat fluxes.

The third method allows a correction for the annual cycle in the radiative fluxes. Indeed, the radiative fluxes describe a sinusoid of a period of one year. In this method, we fit a sinusoid with a one-year period to the monthly means. This sinusoid is actually due to the short wave fluxes and appears because the length of the day varies over the year, as does the distance from the sun to the point considered. The outgoing long wave fluxes have less important variations.

The last method is described in Killworth (1996). Its advantage is that it conserves the actual monthly means. It is based on the same linear interpolation as the second method, but done from pseudo-data (pseudo monthly means in our case). These pseudo monthly means are chosen so that a linear interpolation that uses them would give the actual monthly means we have in our NCEP data.

Comparison of the methods' results

We assess the methods using the daily data available for the winters 2002-03 to 2004-05. We do not assess the simple linear interpolation because it is comparable to Killworth's method, except that the monthly means are not conserved, which will be a problem when using the heat fluxes in the analysis or to force a model. We use two elements to assess the three other methods: the root-mean-square (RMS) error, and the maximum (MAX) error. Figure 2.2 compares the daily interpolated fluxes with the actual NCEP daily fluxes for the last three winters. Table 2.2 compares the three methods for the three years.

Killworth's method and the sinusoidal interpolation are the best methods in terms of RMS error, and are comparable in their performances in terms of both RMS and MAX errors. We choose the Killworth's method because it conserves

the monthly means, and performs slightly better.

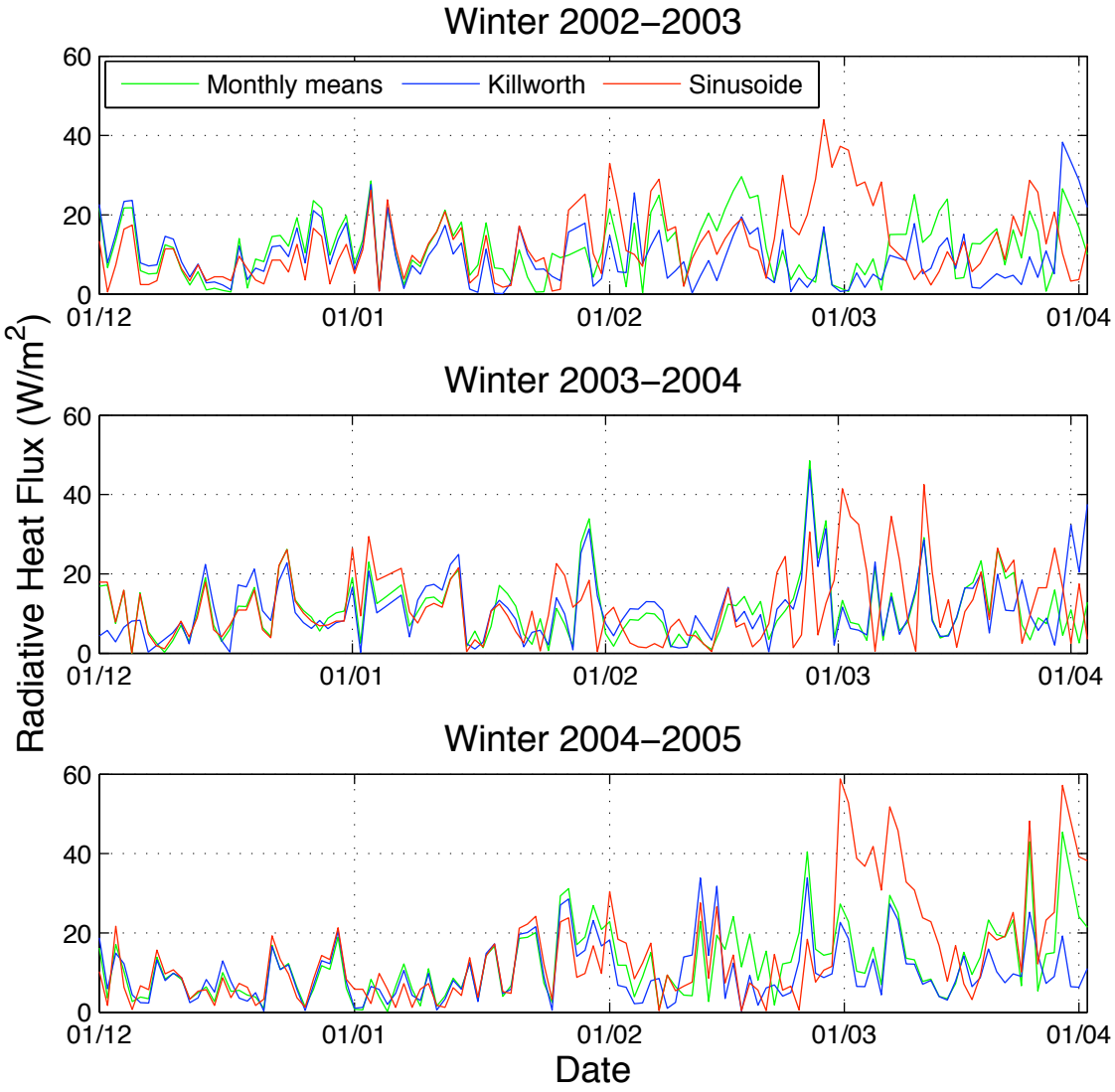

Figure 2.2: Magnitude of the difference between the NCEP daily radiative fluxes and the daily fluxes interpolated from the NCEP monthly radiative fluxes for the three methods: using the monthly means (red), Killworth's method (blue) and the sinusoidal interpolation (green).

	RMS error (W/m^2)			**MAX error** (W/m^2)		
Winter	02-03	03-04	04-05	02-03	03-04	04-05
Monthly means	15.6	15.1	19.8	44.0	42.5	58.8
Killworth's method	12.2	13.9	12.5	38.3	46.3	33.9
Sinusoidal interpolation	13.9	13.7	15.4	29.6	48.5	45.4

Table 2.2: Assessment of each method. The error values have not been normalised, as we only need to compare the values between each other.

2.3 Composition

2.3.1 Heat Flux

Now that we can obtain a satisfactory estimate for the radiative fluxes, we can calculate the total heat fluxes for all the years available in the NCEP data set (about 50 years).

The heat flux for each winter is shown in appendix A. We observe that the radiative fluxes are not very important for the short-term variability (on a timescale of a few days) - the short and strong bursts are due to sharp variations in the latent and sensible heat fluxes, which seem to follow the same pattern. However, the radiative fluxes are responsible for the seasonal variations, due to the short wave incoming radiation (linked to variations in the inclination of the Earth and in the length of the day).

Figure 2.3 shows the contribution of each component of the heat fluxes for typical (i.e. averaged over the period 1949-2005) winter months. The same diagram for each year is displayed in appendix A. The tendency of the mean total heat loss is to decrease from December to March. Hence the maximum value occurs in December while the violent mixing generally occurs in February. The latent heat flux predominates, and the radiative flux is only a negligible part of the total heat flux.

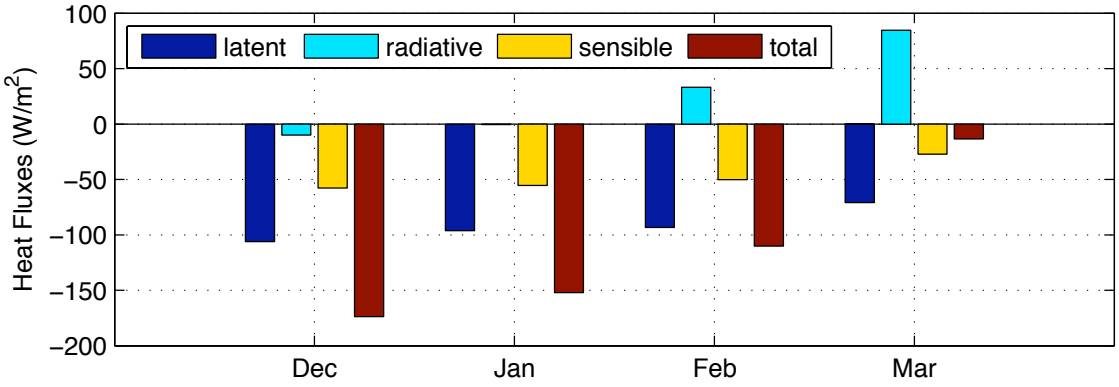

Figure 2.3: Average composition of the heat fluxes from the winter 1949-1950 to the winter 2004-2005. It shows the radiative (light blue), the latent (dark blue), and the sensible (yellow) contributions. The total heat flux is in red.

2.3.2 Heat Flux variability

The periods of strong heat loss are associated with Mistral events. These can be very variable on short timescales. To illustrate this, figure 2.4 shows the total

heat fluxes for winter 2004-05. Periods of high heat losses are very intense and short-lived.

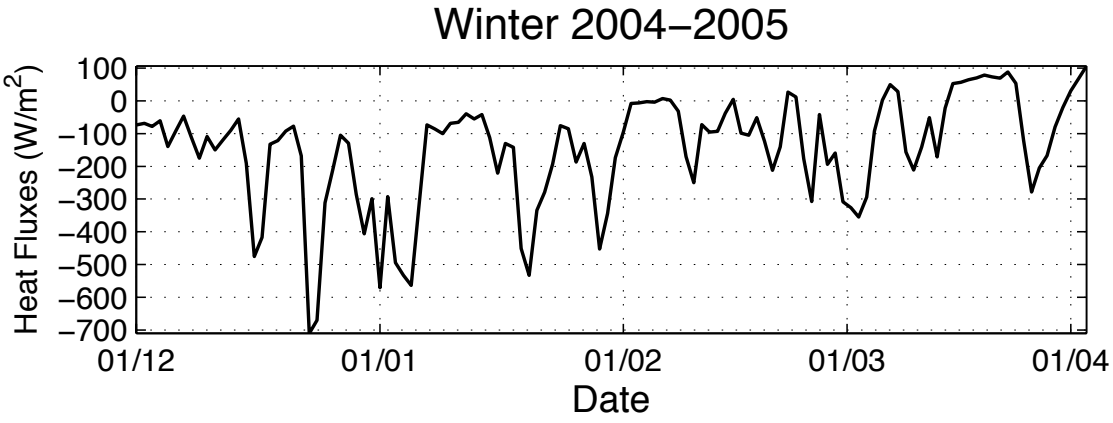

Figure 2.4: Total heat fluxes (W/m^2) for winter 2004-05.

In this section we study in more detail the short-term variability of the heat fluxes. We calculate, for each component and each year, a discrete derivative. If we have a variable v, its discrete derivative is dv defined as: $\forall i$, $dv(i) = (v(i) - v(i + di))/di$. In our case, $di = 1day$ and the units of this derivative will be $W/m^2/day$. We calculate this discrete derivative for each component of the total heat flux and plot them on figure 2.5. This derivative is useful to observe short-term variability (day to day), but does not give much information on the long term variability. Therefore, we do not see the annual variation in the radiative flux. We notice that the main contribution to this variability is due to the latent and sensible fluxes variability. To quantify this pattern, we calculate the mean ratio (in $\%$) of the derivative of the sensible fluxes to the derivative of the total fluxes. We do the same for the latent and the radiative fluxes. Results are shown in table 2.3, and give a good measurement of the contribution of each component to the variability of the total heat flux. They show that the latent heat flux is the major contributor in the day to day heat fluxes variability, accounting for more than half of it. The sensible component account for about 1/3 of the variability, and the radiative component is not important in the short-term variability.

Latent Heat Flux	61.90%
Sensible Heat Flux	36.40%
Radiative Heat Flux	1.60%

Table 2.3: Mean ratio between the discrete derivative of each component of the total heat fluxes and the discrete derivative of the total heat flux.

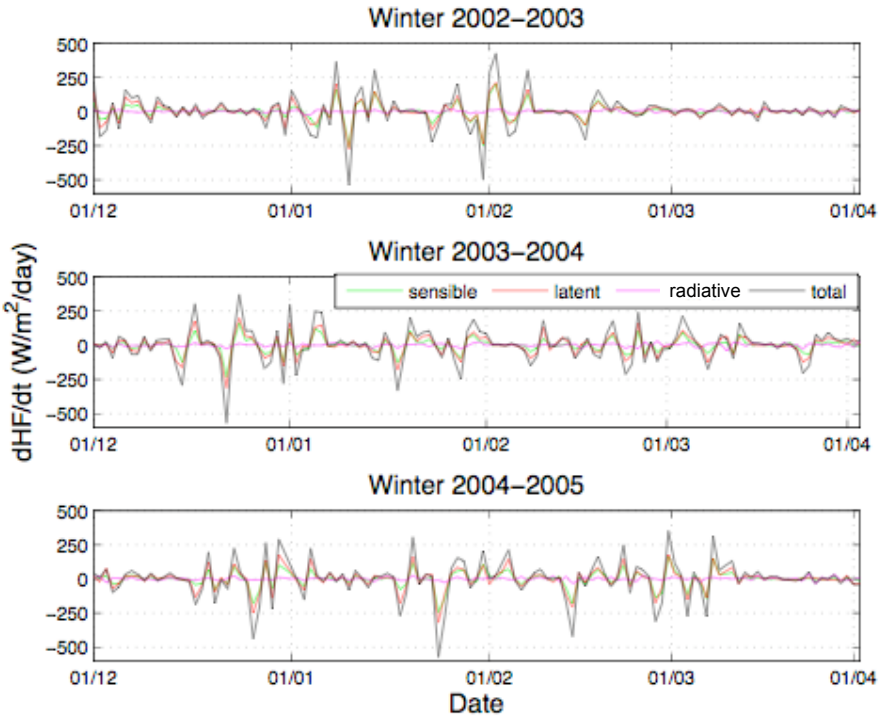

Figure 2.5: Discrete derivative for each heat flux for the last three winters, in $W/m^2/day$.

2.3.3 Correlation between the latent and sensible components

The heat fluxes time series show a possible correlation between the sensible and the latent heat fluxes. We here investigate this correlation to find out if it is significant. Figure 2.6 is a scatter plot of the winter latent heat loss against the winter sensible heat loss. The correlation coefficient has a value of 0.9454 for a negligible significance (i.e. the probability of getting a correlation as large as the observed value by random chance is less than 10^{-15}), so we do have a correlation. This correlation is in agreement with a heat loss mainly due to the dry and cold southward Mistral (or even to the dry and cold eastward Tramontana). If we neglect the radiative flux, and we have seen it was a reasonable assumption, this means that we can express the heat flux as a function of the evaporation only.

The correlation between the latent and sensible heat fluxes allow us to have an estimate of the total heat flux while knowing only the value of the evaporation term. According to the best linear fit, we have $Q_S = 0.73 \cdot Q_L - 19 W/m^2$. We write: $Q_S = p_1 \cdot Q_L + p_2$. Actually, the plot seems to show that a linear fit is not what corresponds most: fitting $log(Q_S)$ to $log(Q_L)$ yields $log(Q_S) = 1.3 \cdot log(Q_L) - 2.3$. However, finding a polynomial of higher order P such that $Q_S = P(Q_L)$ makes little sense if we cannot explain physically that dependance. We consider a P of

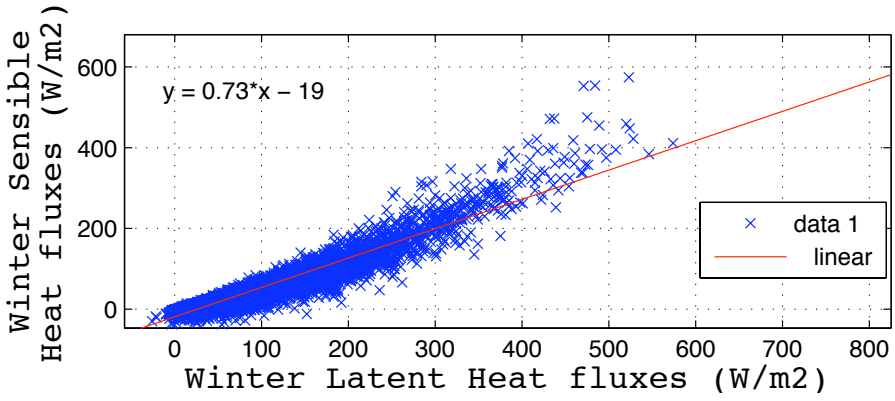

Figure 2.6: Scatter plot of the winter sensible heat loss over the winter latent heat loss. The red line shows the best linear fit, whose equation is given in the top left corner of the plot.

order 1 for our simple analysis.

We now explore a bit further the implication of the correlation between the heat flux and the evaporation on the temperature and salinity of the deep water. Let us consider a volume V of water, which extends from the surface to the bottom, and with a horizontal area of $1m^2$, and a total depth of H. We consider that it has a mean temperature T. We could use a stronger assumption, considering a homogenous temperature, but we can express the sensible heat loss as a function of evaporation only, so we do not actually need the surface temperature. The heat content of this volume is: $\rho H \times c \times T$, where ρ is the density of the seawater in the control volume and c is the heat capacity of seawater. We do not consider any lateral heat exchange in this simple calculation, so the variation of heat content in only due to the surface heat flux. We do not consider any heat dissipation, which acts on much longer timescales than convection. Therefore, we have: $\rho H \cdot c \cdot \frac{dT}{dt} = Q_S + Q_L + Q_R$. The radiative flux can be neglected, so, we have: $\rho H \cdot c \cdot \frac{dT}{dt} = (p_1{+}1){\cdot}Q_L{+}p_2$. Introducing the evaporation $E(m/s)$: $\rho H{\cdot}c{\cdot}\frac{dT}{dt} = (p_1{+}1){\cdot}\rho{\cdot}L{\cdot}E{+}p_2$, where L is the latent heat. We will use it under this form: $\rho \cdot H \cdot c \cdot \Delta T = ((p_1 + 1) \cdot \rho \cdot L \cdot E + p_2) \cdot \Delta t$.

We now consider the salt content: $\rho V S$, which is constant because of salt conservation. In a more realistic case, it is actually as if we considered that the water evaporated through the surface was replaced by water of the same salinity as the volume of water considered. For the salinity S, we need to consider a homogenous water column, because the exchange depends on the salinity at the surface. As the salt content is constant, we have $\Delta V \cdot S + V \cdot \Delta S = 0$. Therefore $\Delta S = -\frac{S}{V}\Delta V = -\frac{S{\cdot}E{\cdot}\Delta t}{H}$.

We can now work out the ratio $\frac{\Delta T}{\Delta S} = -\frac{(p_1{+}1){\cdot}\rho{\cdot}L{\cdot}E{+}p_2}{\rho{\cdot}c{\cdot}S{\cdot}E}$. If $p_2 = 0$ (which can be

justified for periods of very strong heat loss), we can simplify: $\frac{\Delta T}{\Delta S} = -\frac{(p_1+1)\cdot L}{c\cdot S}$. Using $L = 2.5 \times 10^6 J/kg$, $c = 3900 J/kg/K$, and the typical value for the Mediterranean Sea given in Marshall and Schott (1999a): $S = 38.5$, we obtain $\frac{\Delta T}{\Delta S} = -29K/psu$. Considering a heat loss only due to the latent heat loss would lead to: $\frac{\Delta T}{\Delta S} = -17K/psu$. This gives a new framework to study the evolution of the composition of deep water.

As a comparison, the surface thermal expansion coefficient α and the haline contraction coefficient β are in the ratio $\frac{\beta}{\alpha} = \frac{7.6\times10^{-4}psu^{-1}}{2.0\times10^{-4}K^{-1}}$, according to the surface values given in Marshall and Schott (1999a) for the Mediterranean Sea, which corresponds to $\frac{\beta}{\alpha} = 3.8K/psu$. This tells us that an increase in salinity of $1psu$ would be density compensated by an increase in temperature of $3.8K$, or, inversely, a increase in temperature of $1K$ would be density compensated by an increase of the salinity of $0.26psu$. The previous calculation indicates that, in the idealised case considered, if the temperature decreases by 1K, the salinity will increase by $0.0345psu$, considering a sensible heat loss proportional to the latent heat loss, and by $0.0589psu$ with a total heat loss only due to latent heat loss. Therefore, if the composition of the deep water varies as was just described, its density will change as well.

Evaporation leads to a decrease of temperature and an increase of salinity, hence both thermal and haline components act to increase the density. From the two ratios calculated above, we can estimate if the density is mainly changed due to the change in temperature or due to the change in salinity. The change in density due to a change in temperature is $\alpha\Delta T$ while the change in density due to a change in salinity is $\beta\Delta S$. The ratio of these two is $\frac{\alpha\Delta T}{\beta\Delta S} = \frac{-17}{3.8} = 4.5$. Hence, for a given evaporation rate, the resulting change in temperature is going to affect the resulting density 4.5 times more than the resulting change in salinity.

2.3.4 Correlation with the North Atlantic Oscillation (NAO)

We use James Hurrel's NAO index data (Hurrell, 1995), updated by Todd Mitchell, which can be accessed on the University of Washington's website.
($http://tao.atmos.washington.edu/data\_sets/nao/$)

These data are the Lisbon (Portugal) minus Stykkisholmur (Iceland) normalized December to March average sea level pressure anomalies. To compare with the heat fluxes, we use December to March average heat fluxes for each year. Figure 2.7 compares the winter average heat fluxes with the winter average NAO for 1950-2000.

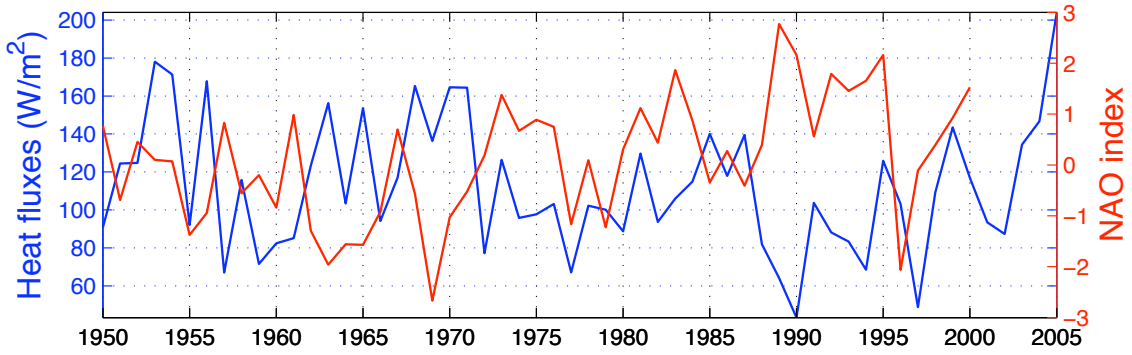

Figure 2.7: Winter Heat Fluxes and NAO index.

When we consider the period from about 1983 to 1995, there seems to be a quite clear anti-correlation between the NAO and the heat loss. However, what happens just next, in 1995/1996, seems to show the opposite. Physically, it is not clear how the two can interact. Let us assume that the strong heat loss at the grid point considered is mainly due to Mistral events, the Mistral being a Southward wind. A very high NAO index both corresponds to an enhancement of the sea level pressure gradient between the South and the North of Europe, and so to more iso-latitude winds, which can inhibit the formation of the Mistral. Therefore, the very high NAO index of the period 1983-1995 can physically be correlated to the very low heat loss we observe.

The correlation coefficient between the heat fluxes and the NAO index for the period 1950-2000 is -0.356, and the probability P of getting a correlation as large as the observed value by random chance, when the true correlation is zero, is $P = 0.010 < 0.05$, therefore the correlation is significant. This indeed shows an anti-correlation between the NAO and the heat loss.

However, Rixen et al. (2005) found a correlation coefficient of 0.48 between the heat flux anomalies and the NAO index, using the same NAO index that we have used, and the NCEP-NCAR winter reanalysis (January to March, while we have used them from December to March). The difference between our calculation and theirs is that they studied the period from 1960 while we have started the study from 1950. This should not lead, though, to such a different correlation coefficient. Particularly, we would expect it to be of the same sign in both case. It shows that the relationship between the NAO and the Mistral is complex, as the NAO is a large scale pattern while the Mistral wind is formed locally.

2.4 Statistical Analysis

The aim here is to know if the temporal variability of the heat fluxes follows any pattern, for example if there is a preferred duration for the periods of high/low heat loss. If so, we can then compare that time with restratification timescales. If not, it will give us indications that we can later use to design numerical experiments.

2.4.1 Methods

To define the time period, we use a cut-off parameter that will be a heat flux taking the values of $100W/m^2$, $200W/m^2$, $300W/m^2$, $400W/m^2$, and $500W/m^2$. We study the duration of the periods where the heat loss is lower/higher than this cut-off value. Figure 2.8 shows an example for year 2005-06 for a cut-off value of $400W/m^2$. For this winter, the data kept would be $[5, 9, 5, 2, 1, 1]$ (duration in number of days) for the high heat loss, $[24, 11, 1, 6, 6]$ for a low heat loss. N will be, in this section, the number of samples.

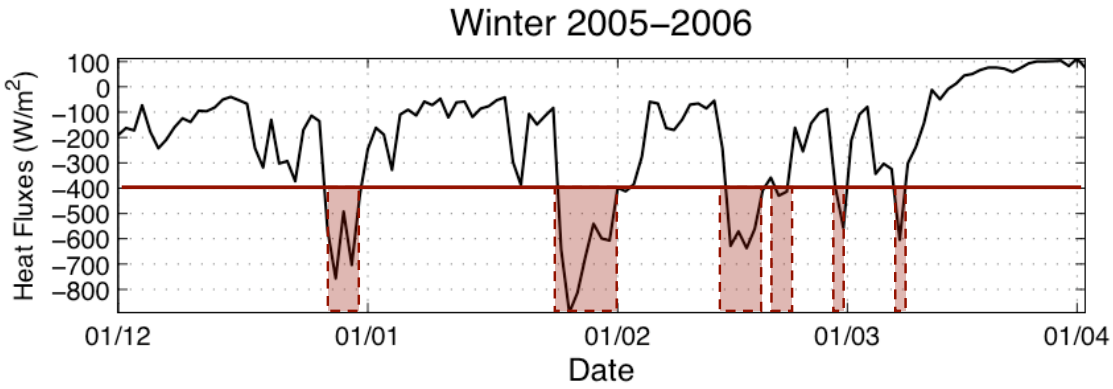

Figure 2.8: Example of definition of the periods of high heat loss (red shaded area) for a cut-off value of $400W/m^2$ for winter 2005-06. Similarly, the low heat loss periods would be the periods of time between the red shaded area.

2.4.2 Results for low heat loss

Figure 2.9 shows the histograms of the distribution of the number of periods of low heat loss over their duration, for the five cut-off values. The plots resemble the exponential distribution, which is one type of normal distribution (distribution of random phenomena), hence we show the corresponding exponential distributions as well, calculated using the method of the maximum likelihood. Table 2.4 shows the means, standard deviation and the results of the goodness of

fit test for these distributions. We performed a chi squared goodness of fit test between the histograms and the exponential fits, with all the bins containing more than 5 elements.

The good fits obtained with the goodness of fit tests show that the distribution obtained could be the result of a random process. For the experiment with a cut-off value of $100W/m^2$, the confidence level is lower than the 5%, but it is not very far behind (3%). More details about the tests performed here are given in appendix B.

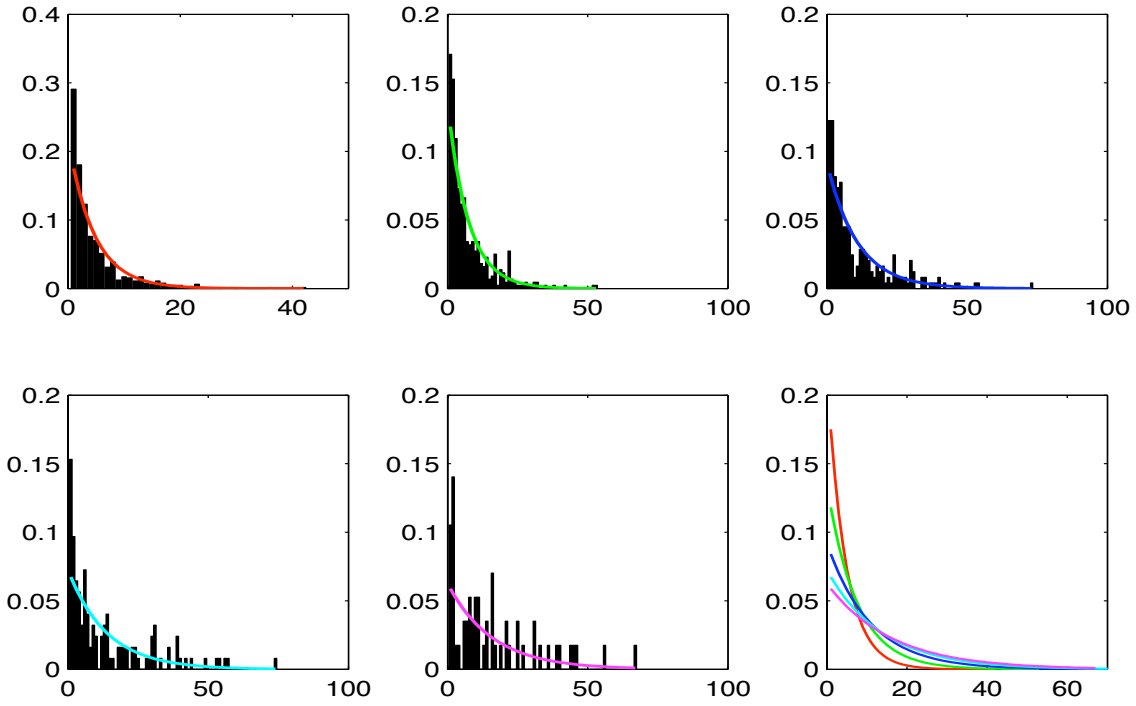

Figure 2.9: Density distributions of the periods of relatively low heat loss. The vertical axis shows the normalised number of low heat loss periods, and the horizontal ones the duration of these periods. The figures, from top left to bottom right correspond respectively to the cut-off value of $100W/m^2$, $200W/m^2$, $300W/m^2$, $400W/m^2$, and $500W/m^2$. The last graph shows the five fitted distributions, to check their evolution when we increase the cut-off value.

Cut-off value (W/m^2)	**Mean** (days)	**Variance** (days)	**N**	χ^2	ν	α
100	4.59565	26.2101	643	12.2	5	0.032
200	7.38952	62.1972	439	6.4	5	0.274
300	10.8327	137.9268	245	9.3	4	0.053
400	13.8065	229.198	154	3.3	4	0.501
500	15.9649	239.8559	57	0.72	2	0.695

Table 2.4: Statistics on the low heat loss periods. N is the number of samples in the data set, χ^2 the statistic chosen to assess the goodness of fit, ν the degree of freedom and α the confidence level.

2.4.3 Results for high heat loss

What we call high heat loss here means higher than one of the cut-off values chosen. Figure 2.10 shows the histograms of the duration of periods of high heat loss for the five cut-off values. The corresponding exponential distributions are shown, calculated using the method of maximum likelihood. Table 2.5 shows the means, standard deviation and the results of the goodness of fit test for these distributions. We performed the same goodness of fit tests as in the previous section.

For the periods of high heat loss, the tests show that the exponential distribution is not such a good fit. We can see that our actual distribution is shifted towards lower values compared to the results obtained for the periods of low heat loss, and there is less spread in the values taken by the durations of the periods. This could explain the fact that even though it 'looks good' on the graph, the test does not yield a very good fit. We also tried to fit the distributions with other classical distributions, without much result. We cannot conclude that the durations of the periods of strong heat loss are random, but we can say that the periods of strong heat loss typically last 2 days.

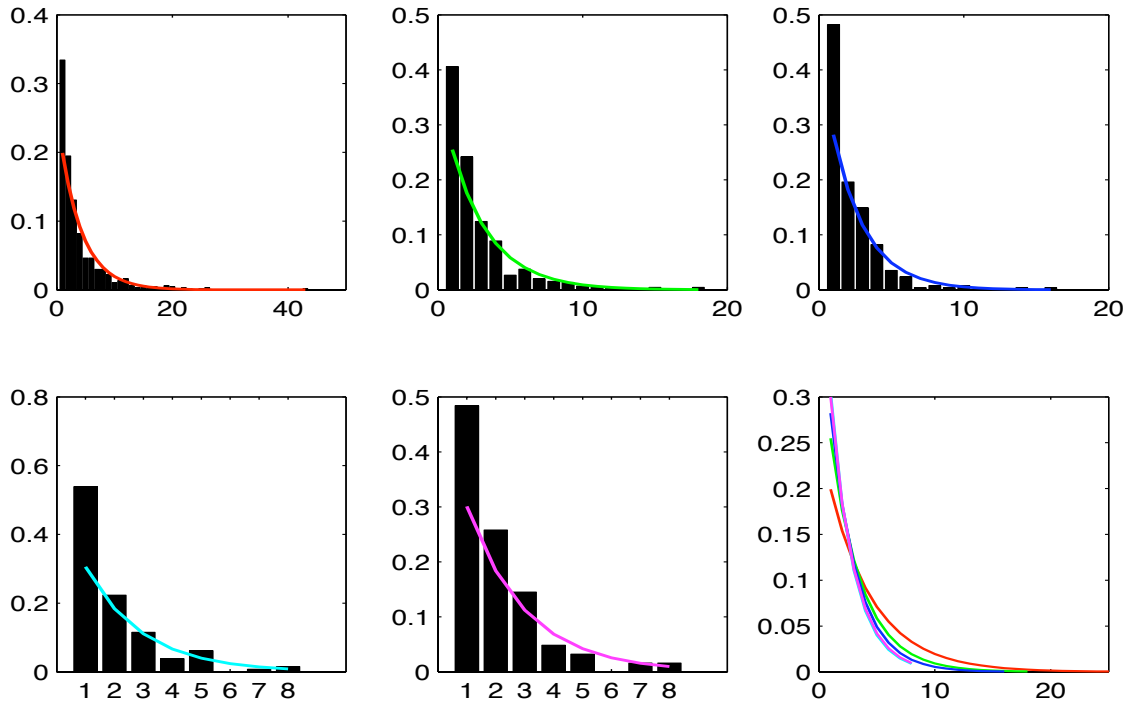

Figure 2.10: Density distributions of the periods of relatively high heat loss. The vertical axis shows the normalised number of high heat loss periods, and the horizontal ones the duration of these periods. The figures, from top left to bottom right correspond respectively to the cut-off value of $100W/m^2$, $200W/m^2$, $300W/m^2$, $400W/m^2$, and $500W/m^2$. The last graph shows the five fitted distributions, to check their evolution when we increase the cut-off value.

Cut-off value (W/m^2)	**Mean** (days)	**Variance** (days)	**N**	χ^2	ν	α
100	3.87816	18.7619	673	11.4	4	0.022
200	2.71397	6.5869	451	16.1	5	0.006
300	2.2902	3.9942	255	12.9	3	0.005
400	1.96923	2.1231	130	1.7	0	-
500	2.03226	2.1301	62	0.8	0	-

Table 2.5: Statistics on the high heat loss periods. N is the number of samples in the data set, χ^2 the statistic chosen to assess the goodness of fit, ν the degree of freedom and α the confidence level.

2.5 Conclusion

In this chapter we have calculated winter heat and buoyancy flux time series for the Gulf of Lion from the NCEP reanalysis data. We have established that the buoyancy fluxes are dominated by the heat fluxes, hence by the latent and sensible components. This is true of the day to day variability too. We showed that the sensible and latent components of the heat flux were correlated. We found a correlation between the heat flux and the NAO that contradict previously published results, and conclude that further work would be needed to confirm and explain a possible correlation.

We performed a statistical analysis on the short-term ($O(days)$) variability of the heat fluxes. It allowed us to extract typical timescales and to show that the occurrence of strong heat loss events could result from a random process, but that the periods of strong heat loss lasted typically 2 days. We will use the timescales to design idealised experiments.

Chapter 3

Importance of the Preconditioning on the Interannual Variability of Deep Convection

3.1 Introduction

What we mean by 'preconditioning' here relates to the heat and salt contents and distributions in the water column before the onset of convection. In that sense, we deal with hydrographic preconditioning rather than with dynamic preconditioning, which would be related to the doming of the isopycnals due to the cyclonic circulation. Figure 3.1 shows climatological profiles of potential temperature and salinity for the Gulf of Lion. The LIW creates a subsurface temperature and salinity maximum around 300m - the LIW typically lies between 200m and 600m depth (Emelianov et al., 2006) - and the buoyancy frequency N decreases significantly below this level. The composition of the different water masses presents an interannual variability that should affect convection. Their stratification, defined as the vertical buoyancy gradient:

$$N^2 = -\frac{g}{\rho_0}\frac{d\rho}{dz} \tag{3.1}$$

where g is the acceleration due to gravity, ρ refers to the potential density and ρ_0 is a constant reference density, is expected to affect the intensity of convection while temperature and salinity characteristics are expected to affect the resulting deep water formed.

We want to define and assess the relative importance of the precondition-

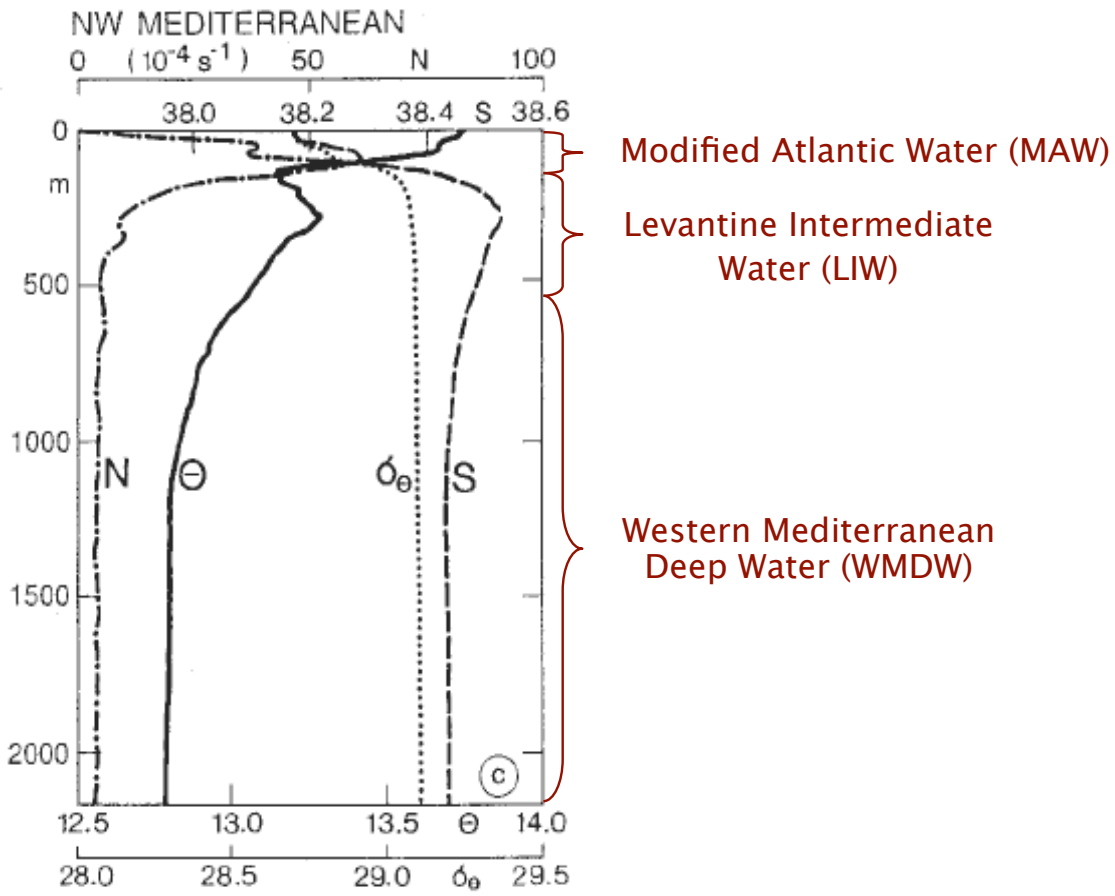

Figure 3.1: Climatological profiles of potential temperature Θ, salinity S, potential density σ_Θ and buoyancy frequency N for the North Western Mediterranean. From Marshall and Schott (1999a).

ing on the deep water composition (T and S) and on the convective mixed layer depth, compared to the surface buoyancy forcing. Sections 3.2 and 3.3 study the seasonal and interannual variabilities of this preconditioning using in-situ data. Section 3.4 studies possible correlations between the surface forcing and the composition of the deep water formed. Sections 3.5 and 3.6 focus on the deepening of the mixed layer.

3.2 Seasonal Variability of the Preconditioning

3.2.1 At the Medoc Point

Medar data

The overall objective of the MEDAR/MEDATLAS II project is to make available a comprehensive data product of multi-disciplinary in-situ data and information for the Mediterranean and Black Seas, through a wide cooperation of Mediterranean countries. It is the result of the compilation of different inventories. Data

were quality checked and interpolated on a regular spatial grid. The processing is described on the website (*http://modb.oce.ulg.ac.be/backup/medar/medar.html*). It provides data from before 1991 up to 2002, as well as a climatology, which we use here. Climatological data can be downloaded for the whole Mediterranean, with a vertical resolution varying from 5m near the surface to 500m at the bottom. We use data corresponding to the Gulf of Lion, which covers the area between 3^oE and 12^oE of longitude, and between 42^oN and 45^oN of latitude. We focus in this section on profiles at (42^oN, 5^oE), traditionally considered as the centre of the convective area (Medoc point).

Results

Figure 3.2 shows MEDAR climatological profiles of temperature, salinity and mean buoyancy frequency N^2 for three layers. The top layer goes from the surface down to 100m, what we will call the intermediate layer in the rest of the chapter is the layer between 100m and 400m depth, and the deep layer ranges from 400m down to 2000m. To try to separate the effects of temperature and salinity on N^2, we also plotted N^2_{temp}, that is the buoyancy frequency of a water column with the same temperature profile but a constant salinity of 36, and N^2_{sal}, the buoyancy frequency of a water column with the same salinity profile but a constant temperature of 12°C. Note that we have $N^2_{tot} \neq N^2_{temp} + N^2_{sal}$ in general, because of the non linearity of the equation of state, but it is quite close to being equal for the values chosen for the constant temperature and salinity (it is valid as long as a linearisation of the equation of state is appropriate around the values chosen for T and S).

The top layer (0-100m) exhibits a clear seasonal cycle. It gets warmer and fresher between April and July, building a stratification which is then eroded between July and December. N^2_{tot} reaches very low values between January and March, because of convection that makes the water colder and saltier. The buoyancy frequency shows a peak in July, which is mainly a temperature effect, due to the seasonal increase of the surface heat fluxes. In that layer, N^2 has an order of magnitude of $10^{-4}s^{-2}$.

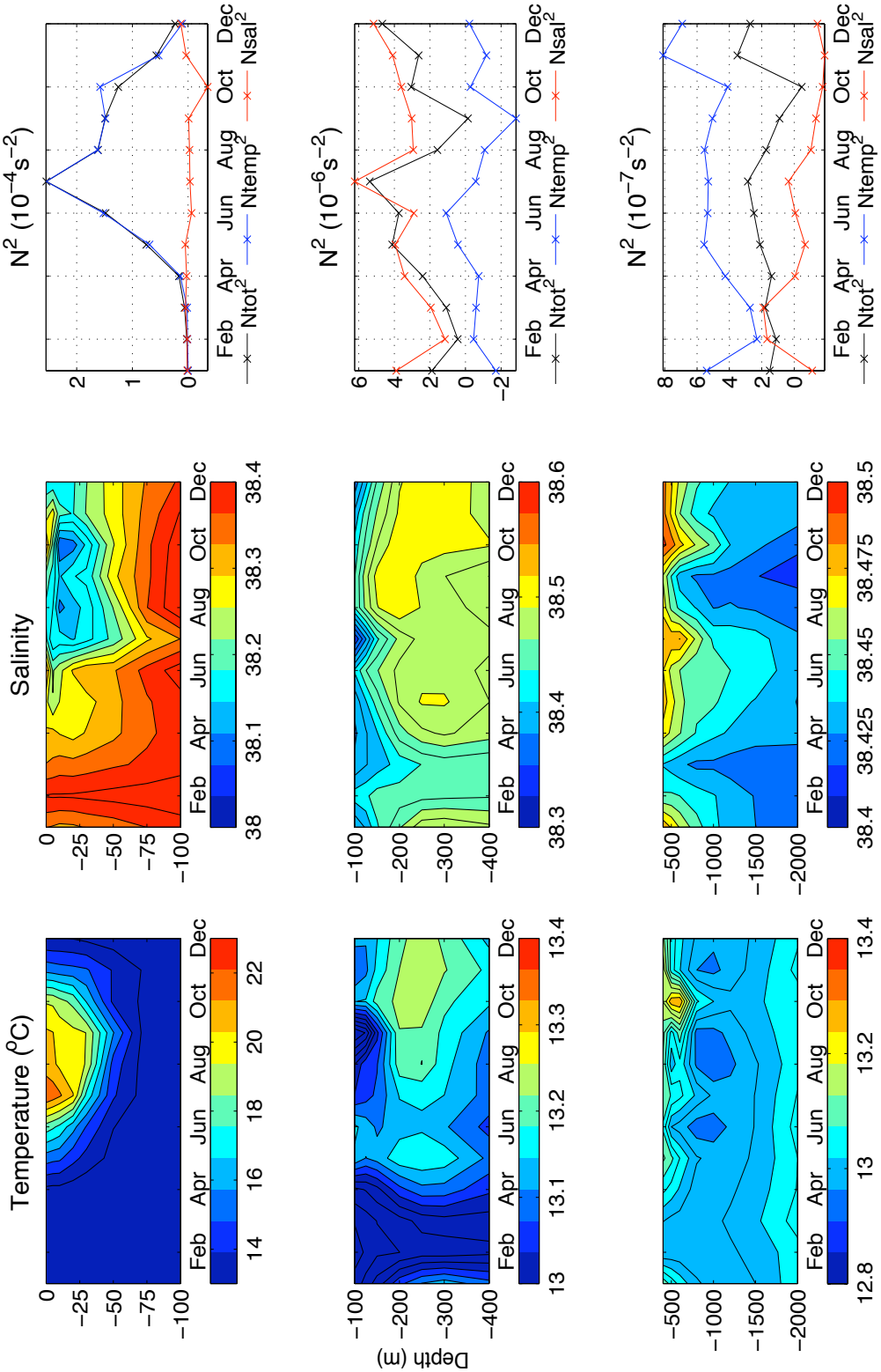

Figure 3.2: Temperature (left), salinity (centre) and mean vertical buoyancy gradient (right - see text for definition of N^2_{tot}, N^2_{temp} and N^2_{sal}) for the top (0-100m), intermediate (100-400m) and deep (below 400m) layers, over time (months) on the horizontal and depth (m) on the vertical, for the Medar data at the Medoc site.

In the intermediate layer (100-400m), taken as representative of the LIW, N^2 has an order of magnitude of $10^{-6}s^{-1}$, in which the salinity signal predominates with a stratifying effect while the temperature has a destabilising effect for most of the year (i.e. except in May and June). These tendencies are linked to the choice of our layers compared to the T and S maxima of the LIW. Above the T maxima, N^2_{temp} is negative while it is positive below. For S, it is the opposite. Note that the two maxima are not exactly at the same depth. The mean tendency we observe in the layer chosen simply means that the layer is not symmetrical relative to the maxima, but is shifted towards shallower depths, i.e. we sample more water above the maxima than below in this layer. The temperature and salinity profiles show the erosion of the stratification in February and March, due to convection. The layer then gets saltier and warmer over the rest of the year, with a maximum temperature and salinity in December. The buoyancy frequency shows two maxima, one in July, likely associated with summer stratification, and another in December, probably of advective origin. In this chapter, we will show the importance of this winter maximum layer which, to our knowledge, has not been reported before. However, Vignudelli et al. (1999) observed, with a mooring, that the transport through the Corsica Channel was usually stronger in winter than in any other season. Figure 3.3 shows the total water transport through the Corsica Channel (see figure 1.3 for location) as calculated by Vignudelli et al. (1999), which is winter intensified for most of the years (winters 1985-86 until 1987-88 and 1996-97), but not all of them (e.g. winters of the early 1990's).

In the deep layer (below 400m), the stratification is weaker, of order $10^{-7}s^{-1}$. the temperature in that layer has a stabilising effect while the salinity a destabilising one. The non linearities there are such that $N^2_{tot} \neq N^2_{temp} + N^2_{sal}$. Temperature and salinity are much more homogeneous in depth there than in the rest of the water column, and are more constant over time. The temperature plot shows a warming in October, at depths of around 1000m. The salinity seems to vary over a period of 6 months, with a freshening above 1000m depth in March and another one in September. The March freshening is associated to a cooling, hence can be related to convection. As the mixed layer deepens, its salinity is mainly set by the salt content because the surface buoyancy flux is dominated by its thermal component. Hence the salinity of the mixed layer is the mean salinity of the initial profile between the surface and the mixed layer depth. When the mixed layer reaches deeper than the salinity maximum of the LIW, we observe a freshening due to entrainment of fresher water from below. The September freshening hap-

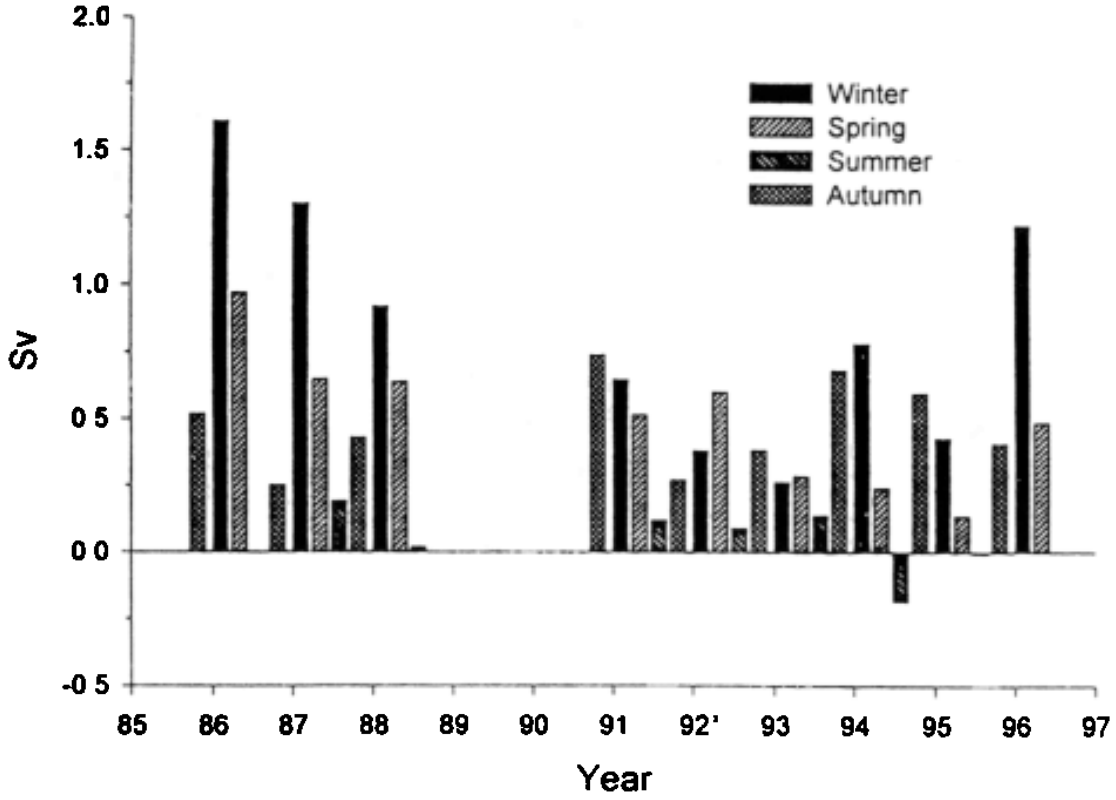

Figure 3.3: Seasonal total water transport in the Corsica Channel during 1985-96 in Sverdrup ($10^6 m^3/s$). From Vignudelli et al. (1999).

pens just before the October warming which is also associated with an increase of the salinity around 800m. At these depths and in the absence of convection in September, the freshening seems to be due to advection. There are at that time traces of LIW above, around 200m, so the freshening is not related to something happening at the surface. Its cause remains unclear. The increase in temperature and salinity in October could be associated to restratification due to an increased inflow of LIW. Variations of both salinity and temperature do not have a big impact on the buoyancy frequency because stratification remains weak ($10^{-7} s^{-2}$) in the deep layer.

3.2.2 In the Corsica Channel

Dyfamed Data

Since 1991, the Laboratoire d'Océanographie de Villefranche has conducted almost monthly cruises in the Corsica strait in the framework of the Dyfamed (Dynamics of Atmospheric Fluxes in the Mediterranean Sea) investigation, to complement time-series of biogeochemical parameters obtained at the same site with

a mooring from 1988. The data are available online (www.obs-vlfr.fr/sodyf/).

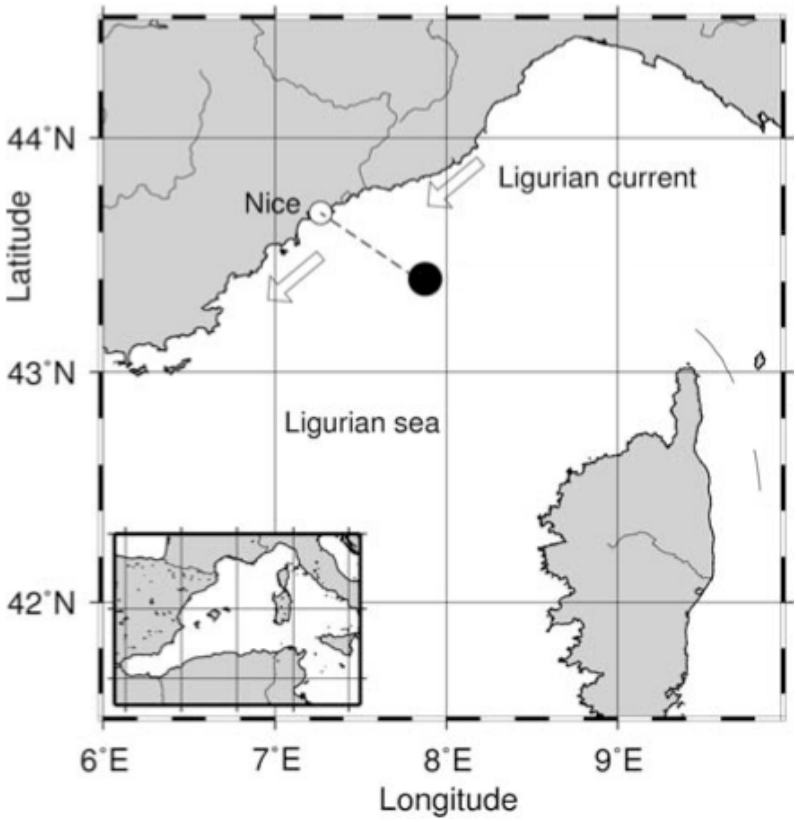

Figure 3.4: Location of the Dyfamed site (black dot).

Figure 3.4 shows the location of the Dyfamed site - it is at the edge of the convective area, so we expect to see some signs of shallow convection in the seasonal cycle (Smith et al., 2008). They provide a better time series than can be obtained at the Medoc site, because the CTD casts have been carried out on a quasi-monthly basis over about 10 years, and with a consistent methodology. The Dyfamed site is just south of the Liguro-Provencal, or Northern, Current, which advects the water towards the convective area, so we consider that the data observed there are representative of hydrographic preconditioning. In fact, we should expect it to be a bit more stratified (i.e. more resistant to convection). The underlying assumption in our approach is that we can separate hydrographic and dynamic preconditioning. The dynamic preconditioning, i.e. the uplifting of the isopycnal due to the cyclonic circulation, occurs at the Medoc site but not at the Dyfamed one, further weakening the stratification. This assumption, however coarse and unrealistic, leads to a much simpler problem in which we consider that the observed interannual variability at the Dyfamed site is then representative of the one at the Medoc site if we neglect the interannual variability due to changes in the strength of the cyclonic circulation.

Results from Dyfamed data at the Dyfamed site

In the top (0-100m) layer, we observe a similar pattern as for the Medar data concerning the late winter restratification, except that it seems to restratify deeper at the Medar site than at the Dyfamed site, and the temperatures are lower in winter at the Medar site than at the Dyfamed site. This is consistent with the known location of convection, which should be more intense at the Medoc point than at the Dyfamed site. The salinity in the top layer shows that winter convection is less strong at the Dyfamed site, as expected. The top layer is generally fresher at the Dyfamed site than at the Medar one. At the Dyfamed site, the surface freshening seems to be interrupted in August, and starts again in fall. This could be either due to surface freshwater forcing or to advection, and has little effect on the stratification. The surface freshwater fluxes do not show a similar seasonal cycle, hence it is more likely to be caused by advection.

The intermediate (100-400m) layer shows signs of convection, mainly in the temperature data. The LIW's subsurface salinity and temperature maxima are again more apparent at the Dyfamed site than at the Medoc one. The LIW layer seems to lie slightly deeper in the water column at the Dyfamed site than in the convective area. This could be attributed to the cyclonic circulation around the convective area that causes a doming of the isopycnals. This circulation is less intense in summer, but is still present. The stratification at the Dyfamed site in that layer shows signs of erosion by convection, particularly in March. However, the buoyancy frequency reaches a maximum in winter, presumably resulting from advected LIW. This very salty water mass, formed in the Levantine Basin and the southern Aegean Sea in February and March under the influence of dry and cold continental air masses, is then advected towards the western Mediterranean, mainly through the Corsica strait as part of the Liguro-Provencal current. Its salty signature can make it very stratified and could create the winter maximum observed in the stratification of the intermediate layer, and found in both the Medar and Dyfamed data sets.

To study the seasonal cycle, we define an average Dyfamed year. We first interpolate the profiles in time for the period 1995-2004 included, and then calculate an average profile for each month. The result is shown on figure 3.5 for temperature, salinity and buoyancy frequency. The color scale is the same as used for figure 3.2, to allow comparison. The data are available with a vertical resolution of 2db, but we use a 10db average in the present analysis.

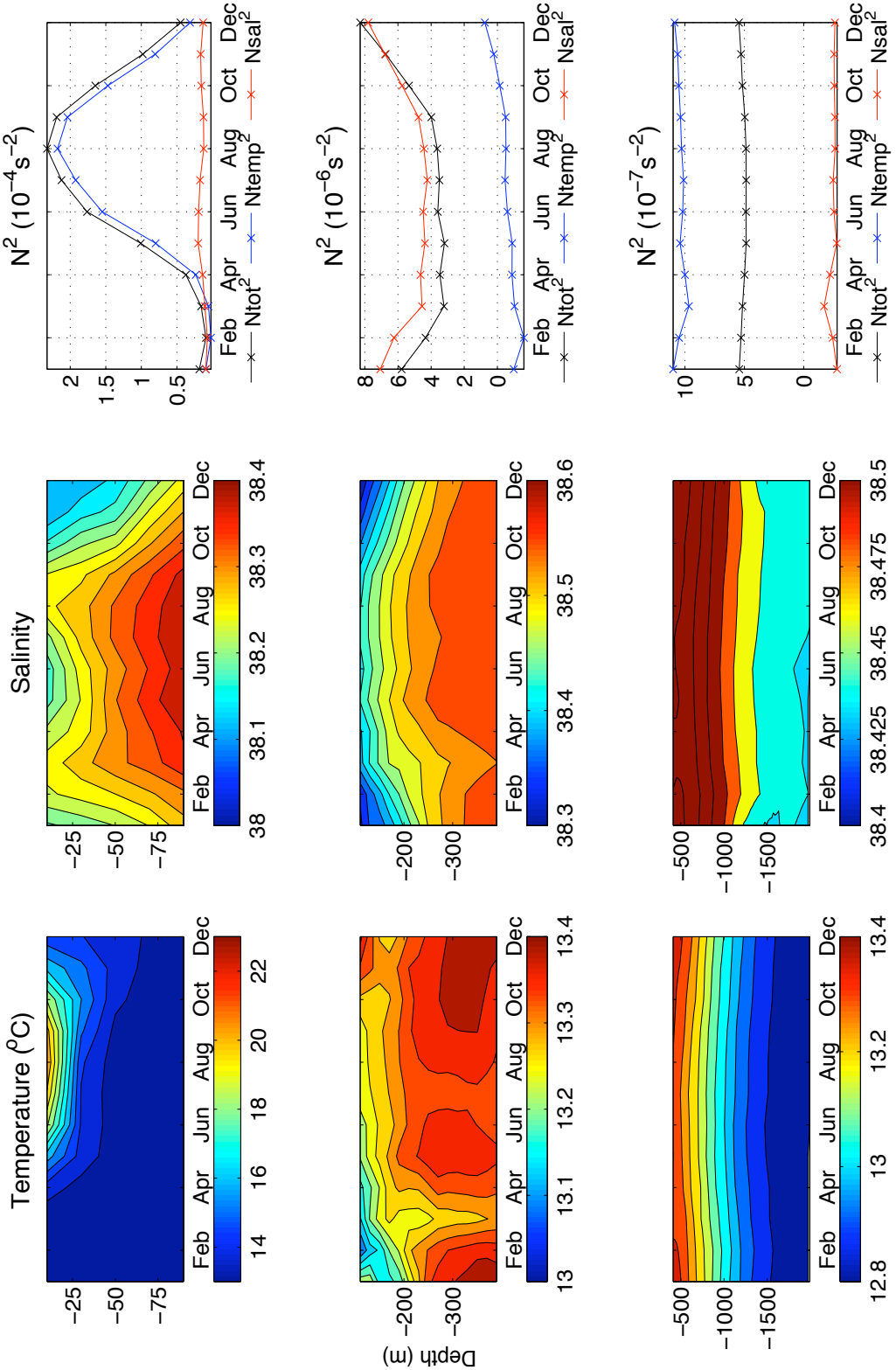

Figure 3.5: Temperature (left), salinity (centre) and mean vertical buoyancy gradient (right - see text for definition of N^2_{tot}, N^2_{temp} and N^2_{sal}) for the top (0-100m), intermediate (100-400m) and deep (below 400m) layers, over time (months) on the horizontal and depth (m) on the vertical, for the Dyfamed data.

In the deeper layers, the stratification is more pronounced at the Dyfamed site than in the convective area, because the Dyfamed site is less affected by convection. The deep water seems to be denser at the Dyfamed point, but we should remember that none of these profiles are full depth ones, so what we observe as being deep water is not necessarily the bottom water.

Results from Medar data at the Dyfamed site

To compare the two data sets Medar and Dyfamed at a same location, we also display a similar figure as 3.2 and 3.5, which shows the data from the Medar climatology at the Dyfamed location (43.25^oN, 7.50^oE): see figure 3.6.

The Medar and Dyfamed data sets at that location show very good qualitative agreement in the seasonal cycle of the buoyancy frequency N^2. The surface warming happening in summer is more pronounced in the Medar data set than in the Dyfamed one, leading to a higher maximum in the stratification in the Medar data set in July and August.

In the intermediate layer, the Medar data set shows a stronger convective signature, leading to a weaker March stratification than in the Dyfamed data set. The December maximum of stratification in the intermediate layer is present in both data sets. Its value is $5 \cdot 10^{-6} s^{-2}$ at the Medoc point if we use the Medar data. It is $8 \cdot 10^{-6} s^{-2}$ at the Dyfamed point if we use the Medar data, and $10 \cdot 10^{-6} s^{-2}$ if we use the Dyfamed data. Hence this maximum appears to be higher at the Dyfamed point than at the Medoc one, which is consistent with the fact that it originates from the eastern side of the Corsica strait.

The record obtained for the deeper layer is much steadier in the Dyfamed data set than in the Medar one, although the resulting stratification is not changed much and remains around $5 \cdot 10^{-7} s^{-2}$ during the year for both data sets.

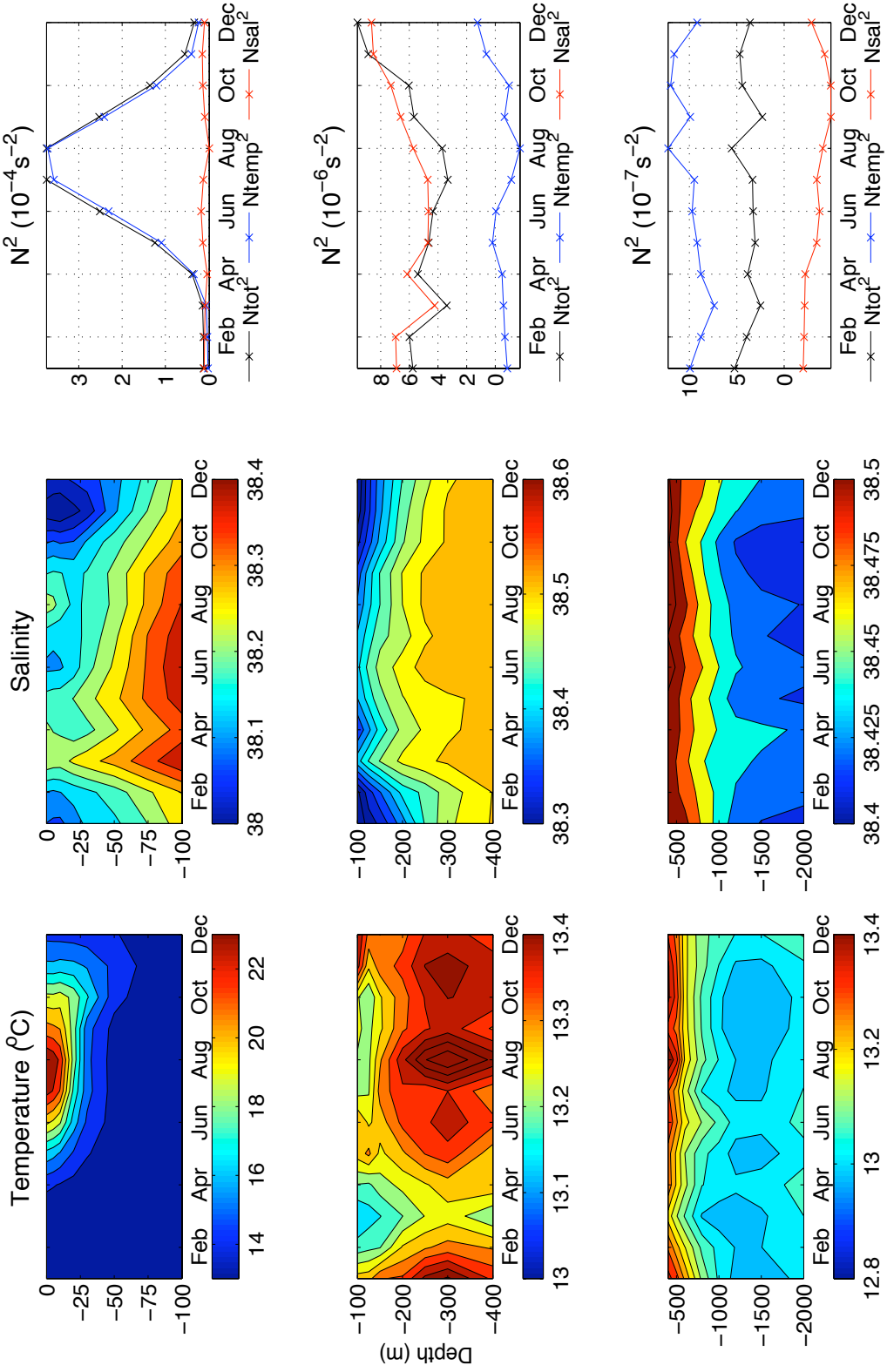

Figure 3.6: Temperature (left), salinity (centre) and mean vertical buoyancy gradient (right - see text for definition of N^2_{tot}, N^2_{temp} and N^2_{sal}) for the top (0-100m), intermediate (100-400m) and deep (below 400m) layers, over time (months) on the horizontal and depth (m) on the vertical, for the Medar data at the Dyfamed location.

3.3 Interannual Variability of the Preconditioning at the Dyfamed site

3.3.1 Temperature

We study the evolution of the temperature using the Dyfamed data set for the three layers defined previously, and for the whole water column. Figure 3.7 displays the values of the mean temperature interpolated at the 1^{st} of December for each year between 1995 and 2004 with thick lines for all layers to emphasise the interannual variability of the signal. This date is taken as representative of the pre-convection state. Table 3.1 contains the values of the means, standard deviations and trends for all thick lines.

	0-100m	**100-400m**	**400-2000m**	**0-2000m**
mean (^oC)	14.34	13.37	13.03	13.14
std (^oC)	0.47	0.07	0.04	0.06
trend ($^oC/year$)	0.056	0.009	0.012	0.013

Table 3.1: Mean, standard deviation (std) and trend for the thick plots of figure 3.7, which represent the averaged temperature for each layer on the 1^{st} of December of each year between 1995 and 2004.

The seasonal cycle is clearly apparent in the top layer. It is also visible in the intermediate layers where we see clearer signs of convection, for example at the beginning of years 1997, 1999, 2000, 2003 and 2005. The seasonal signal is much weaker in the bottom layer, where observations are also less dense.

Trends show a slow warming in the top and intermediate layers, but the associated change in temperature for a year is ten times smaller than the standard deviation (std), and the trends are not clearly visible on figure 3.7. For the bottom layer, however, the warming is visible on the graph, at a rate of $0.012^oC/year$, so the associated change in temperature during a year is of the same order of magnitude as the std. This results in a warming trend for the mean temperature of the whole column above 2000m of $0.013^oC/year$. This is comparable to the trend of $0.011^oC/year$ obtained by Lopez-Jurado et al. (2005) for the water below 600m in the Balearic Sea. Like they did in the deep water, we also notice that the water between 400m and 200m was colder in December 2004 than in the previous years, leading to a similar disruption of the warming trend as observed in the deep water of the Balearic Sea.

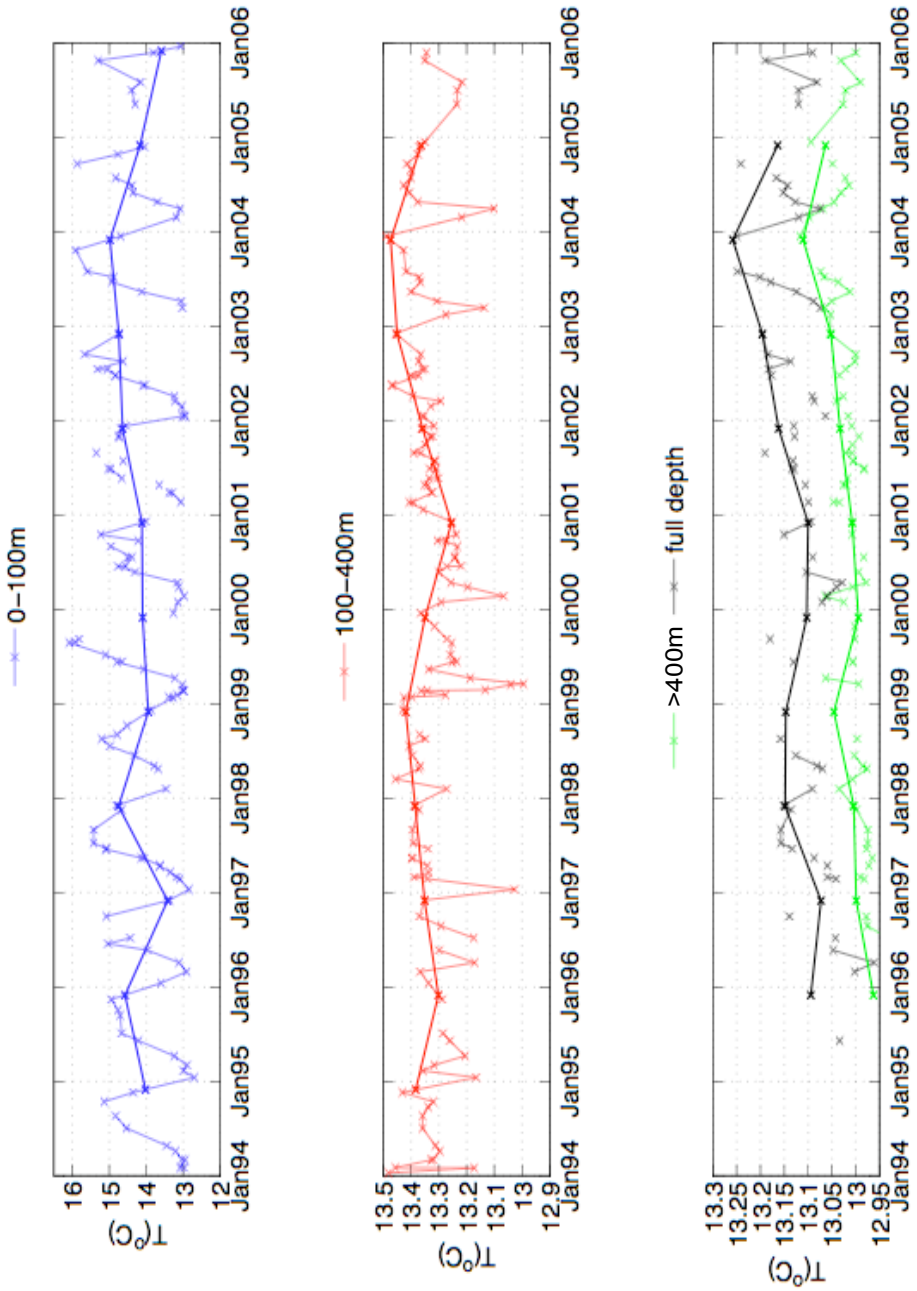

Figure 3.7: Temperature (^oC) from the Dyfamed data set averaged for the 0-100m (top, blue), the 100-400m (middle, red), the 400-2000m (bottom, green) and the 0-2000m (bottom, black) layers. For each plot, the corresponding thick line joins the interpolated values for the 1^{st} of December of each year between 1995 and 2004.

3.3.2 Salinity

We now study the evolution of the salinity with the Dyfamed data set. The approach taken is the same as for the temperature. Results are shown on figure 3.8. Table 3.2 contains the values of the means, standard deviations and trends for all thick lines of figure 3.8.

	0-100m	**100-400m**	**400-2000m**	**0-2000m**
mean (psu**)**	38.176	38.485	38.494	38.477
std (psu**)**	0.076	0.027	0.015	0.014
trend ($psu/year$**)**	0.0037	0.0030	0.0043	0.0041

Table 3.2: Mean, standard deviation (std) and trend for the thick plots of figure 3.7, which represent the averaged temperature for each layer on the 1^{st} of December of each year.

As for the temperature data, the seasonal cycle for salinity can be observed in the top and intermediate layers, although the interannual variability has a larger amplitude compare to that of the seasonal cycle. We see signs of convection in the intermediate layer, for example at the beginning of year 1997, but it is much less obvious than it was for temperature. At the beginning of year 1998, the signal in the intermediate layer looks like it could be caused by convection, but there is only a slight drop in the temperature in the intermediate layer at that time, ruling out this explanation.

The salinity in the top layer shows an important interannual variability compared to the variability of the seasonal cycle, and no trend is visible on figure 3.8, although table 3.2 indicate a slow salinification. However, the change associated to that trend for 10 years, which is the length of the records on which it is calculated, is smaller than the std, while it would need to be bigger for the trend to be significant.

The variability of the salinity in the intermediate layer is less than that of the top layer (smaller std). A trend is measured although, once again, it is not either visible on the graph nor significant compared to the std.

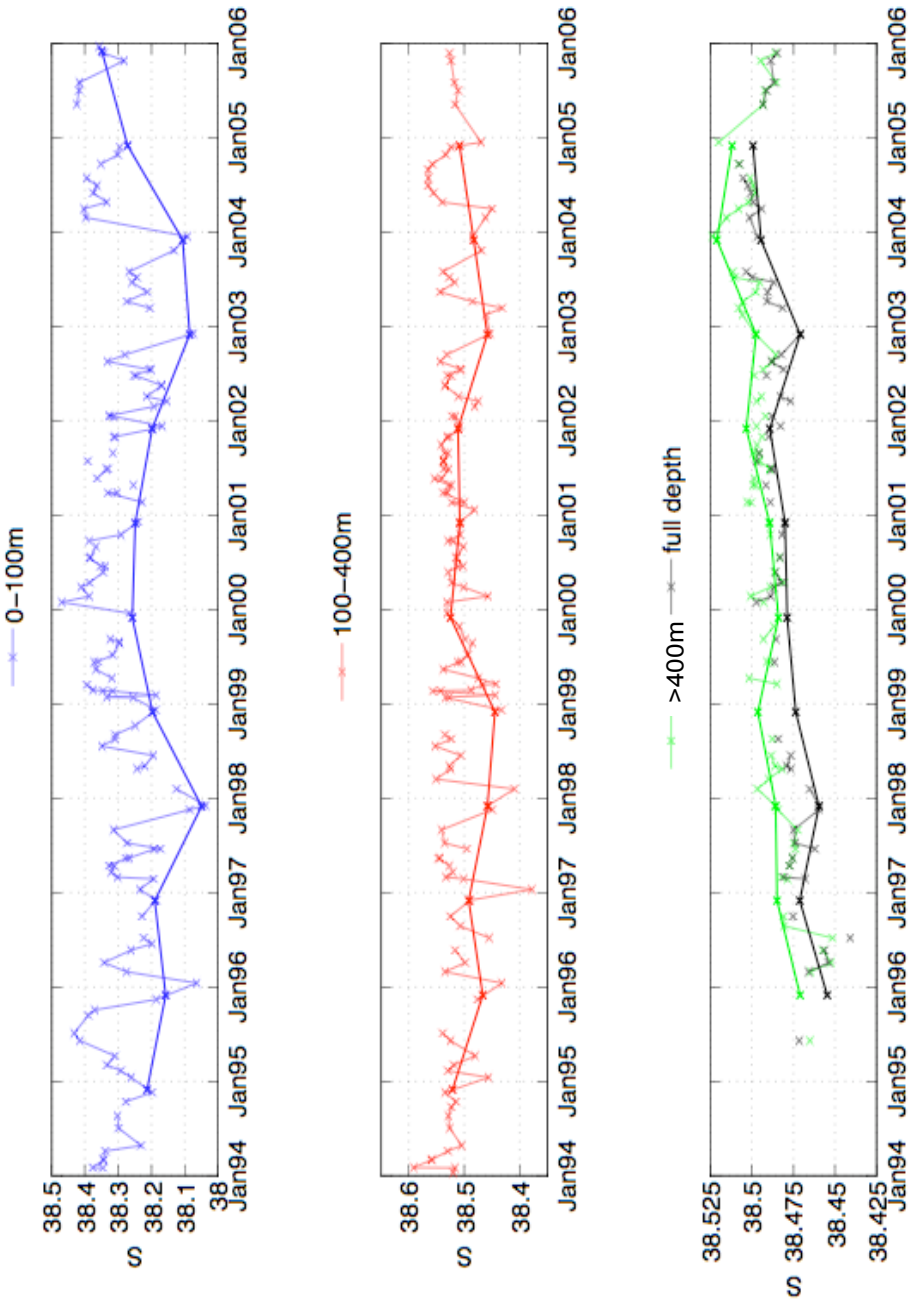

Figure 3.8: Salinity from the Dyfamed data set averaged for the 0-100m (top, blue), the 100-400m (middle, red), the 400-2000m (bottom, green) and the 0-2000m (bottom, black) layers. For each plot, the corresponding thick line joins the interpolated values for the 1^{st} of December of each year between 1995 and 2004.

We observe a different situation in the bottom layer. The change due to the salinification trend for 10 years is larger than the std, and the trend is apparent on figure 3.8. The bottom water appears to be getting saltier at a rate of $0.0043 psu/year$, close to the trend of $0.003 psu/year$ observed by Lopez-Jurado et al. (2005) for the water below 600m in the Balearic Sea. They also observed a small decrease of the salinity in summer 2005 while the record at the Dyfamed site does not show this disruption in the trend. The trend in deep water salinity results in a salinification trend of $0.0041 psu/year$ in average for the whole water column between the surface and 2000m depth.

3.3.3 Density

We now study the evolution of the potential density using the Dyfamed data set for the three layers defined previously, and for the whole water column, as shown on figure 3.9. The method is the same as used for the temperature and salinity. Table 3.1 contains the values of the means, standard deviations and trends for all thick lines.

	0-100m	**100-400m**	**400-2000m**	**0-2000m**
mean (kg/m^3)	28.56	29.02	29.10	29.06
std (kg/m^3)	0.148	0.030	0.004	0.011
trend ($kg/m^3/year$)	-0.0094	0.0005	0.0009	0.0003

Table 3.3: Mean, standard deviation (std) and trend for the thick plots of figure 3.9, which represent the averaged temperature for each layer on the 1^{st} of December of each year.

The potential density of the top layer exhibits a seasonal cycle with maxima in density occurring in January/February, when convection is expected to be the strongest, and minima in late summer/early fall, due to surface heating. In the intermediate layer, for most years, the density minimum occurs in December or January. This is consistent with the December maximum in the stratification observed in the Dyfamed and Medar records. If we consider a constant density at a given depth, an increase in density at the surface will lead to a smaller gradient, hence a weaker stratification, and a lower surface density will lead to a stronger stratification.

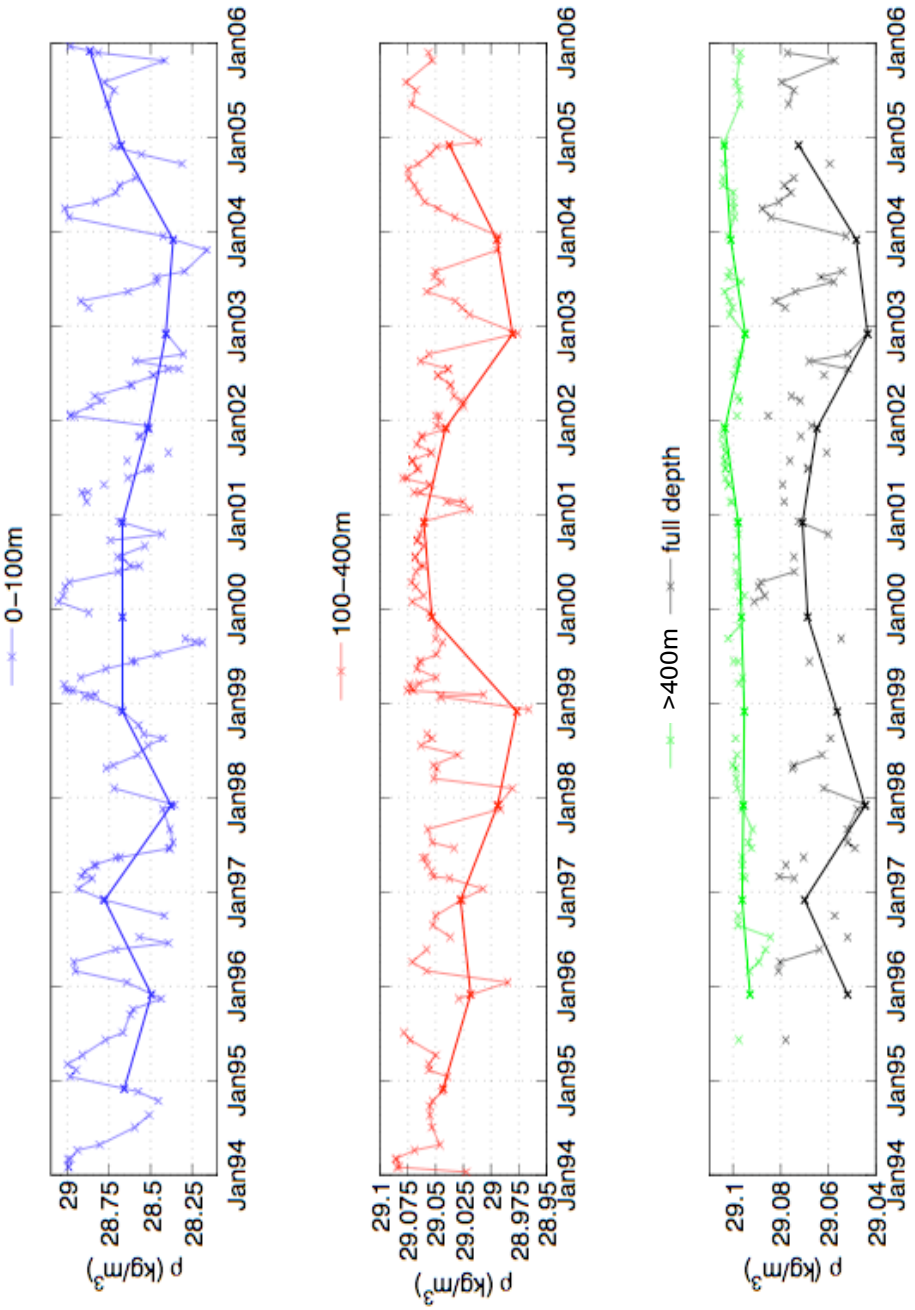

Figure 3.9: Potential density from the Dyfamed data set averaged for the 0-100m (top, blue), the 100-400m (middle, red), the 400-2000m (bottom, green) and the 0-2000m (bottom, black) layers. For each plot, the corresponding thick line joins the interpolated values for the 1^{st} of December of each year between 1995 and 2004.

The potential density in the top and intermediate layers do not show significant trends over the 1995-2004 period, as shown by the fact that the change associated to the trends of table 3.3 over 10 years are much smaller than the std. However, the 400-2000m layer appears to be getting denser at a rate of $9 \cdot 10^{-4} kg/m^3/year$, trend which is significant when compared to the std. This does not result in a trend for the whole 0-2000m layer, whose variability is dominated by that of the top and intermediate layers. The std for the potential density of the 400-2000m layer is indeed very small.

We notice on figure 3.9 that the potential density at the beginning of December increased of about $0.04 kg/m^3$ in the top layer over the period 2004-2006, and of about $0.05 kg/m^3$ in the intermediate layer over the period 2003-2006. Lopez-Jurado et al. (2005) observed an increase of the density of the water below 600m in the Balearic Sea between fall 2004 and summer 2005 of $0.03 kg/m^3$. A possible scenario would be that the intense convection of winter 2004-05 in the Gulf of Lion transferred the increased density to the deep water, while it did not during previous years because of milder winters. Hence the increase of the density of the deep water would be due to that of the top and intermediate waters before convection rather than to the high buoyancy fluxes that only increased the rate of transfer of properties to the deep water. The increase of potential density in the top and intermediate layers is due to both an increase of the salinity and a decrease of the temperature.

3.3.4 Stratification

For each layer, we calculate the vertical buoyancy gradient N^2_{tot} for all Dyfamed profiles between 1994 and 2006. This is shown on figure 3.10 (black). As described in section 3.2, we can decompose N^2_{tot} into a vertical buoyancy gradient due to the temperature gradient N^2_{temp} (blue) and one due to the salinity gradient N^2_{sal} (red). The pink line links the summer maxima of stratification for the top layer and the winter maxima for the intermediate layer.

As for the Medar data, we observe that the stratification and its variations are mainly set by the temperature, which is responsible for the seasonal cycle in the top layer, while the salinity dominates the seasonal signal in the intermediate layer. Temperature has a stabilising effect in the top layer, but a destabilising one in the intermediate layer. Salinity has a stabilising effect in both the top and intermediate layers.

The annual maximum of N^2 varies from year to year, as does the date at which

it is reached (although we are limited here in our analysis by the frequency at which the profiles have been obtained). This is shown by a thick pink line which connects the maximum between them. In the top layer, the maximum value of N^2 is reached in late summer while it is reached in winter by the intermediate layer. The data for the bottom layer are too sparse to yield clear conclusions.

We use the pink line to characterise the interannual variability of the stratification. In the intermediate layer, it presents striking similarities with the interannual variability of the potential density between 2000 and 2005. The stratification in the intermediate layer increases over the 2000-2003 period. Simultaneously, the potential density in that layer decreases. Between December 2002 and December 2004, the density increase coincides with a decrease of the stratification. To explain this, we remember that the stratification is proportional to the vertical density gradient. As the density of the intermediate layer increases, it gets closer to the density of the water just below, hence decreasing the vertical gradient and leading to a water column that can be eroded more easily.

Convection in winter 2004-05 was very intense not only because of very high fluxes but also because the stratification was quite weak, hence the water column was easier to erode. Summer heating did not lead to a stratification in the top layer as high as it was in the previous years, and the winter maximum in the intermediate layer was lower than in the two previous years. The origin of that winter maximum appears to be a critical element in setting the maximum convective mixed layer depth that can be seen as a proxy for the rate of transfer of the surface properties to the deep water. The transport in the Corsica Channel as measured by Vignudelli et al. (1999) can be compared to the stratification we observe at the Dyfamed site for the overlapping years 1995-1996 (figure 3.3). The winter transport in 1995 is about $0.4Sv$ and more than doubles to about $1.2Sv$ in 1996. Similarly, the stratification in the intermediate layer more than doubles its value between 1995 and 1996. Unfortunately, there are not many overlapping years, but this is another hint that the winter maximum of stratification in the intermediate layer is due to increased water transport, and probably to an increased inflow of LIW, at the Dyfamed site. The fact that we do not observe a similar feature in the top layer rules out a surface effect.

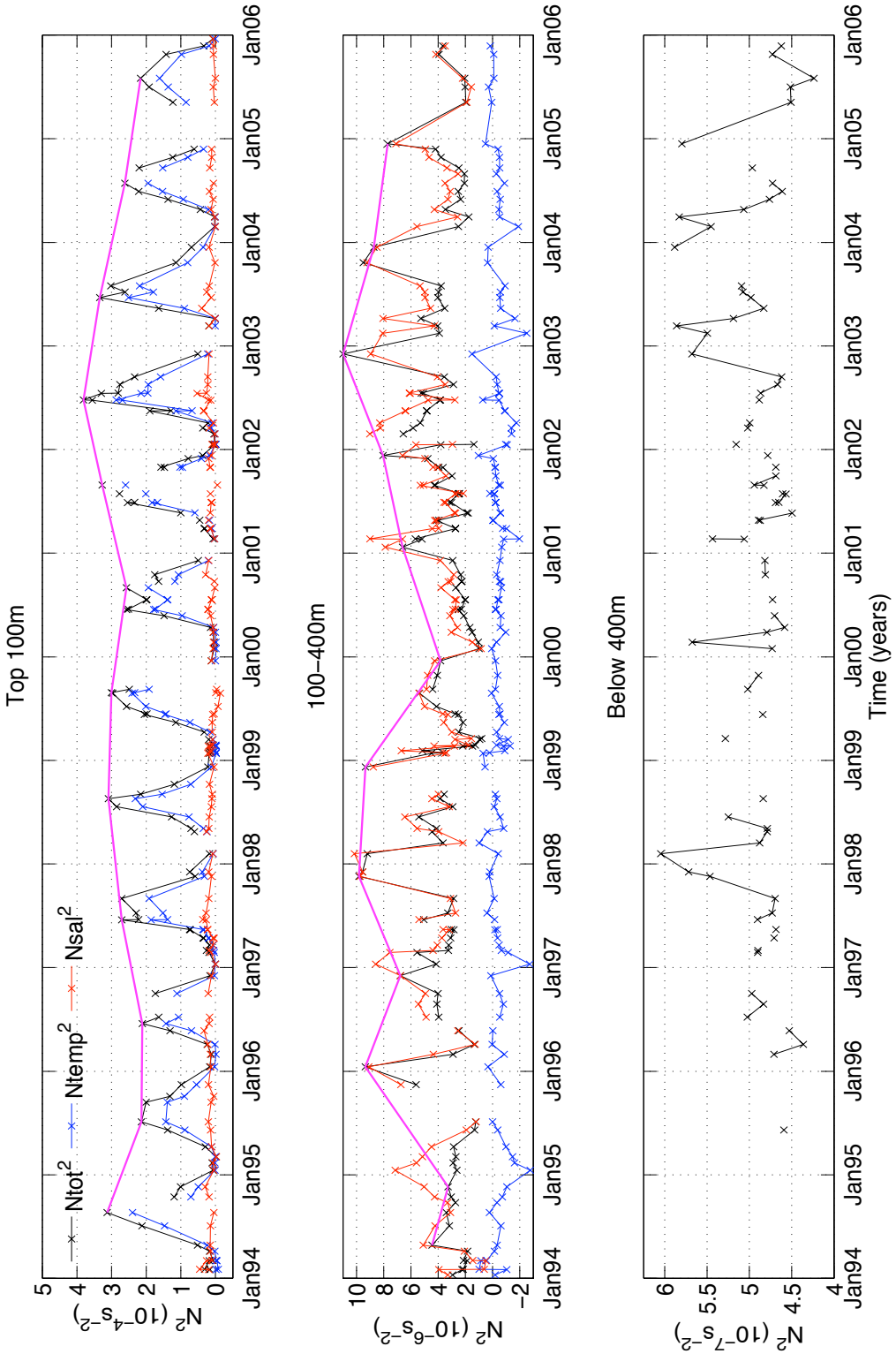

Figure 3.10: Mean vertical buoyancy gradients for the top, intermediate and bottom layers from the Dyfamed data set. See text for a more detailed description.

3.4 Influence of the buoyancy fluxes on the WMDW composition

3.4.1 Data sets

Buoyancy Fluxes

The Buoyancy Fluxes are calculated from the NCEP data. The calculation of the heat fluxes are described in chapter 2. The surface buoyancy flux depends on the heat and freshwater fluxes at the surface, and can be expressed as (Marshall and Schott, 1999a):

$$B = \frac{g}{\rho_0}(\frac{\alpha_\theta}{c_w}H + \rho_0\beta_s S(E-P))) \tag{3.2}$$

where:

- g is the acceleration due to gravity, $g = 9.82m/s^2$;
- ρ_0 is a constant reference density, $\rho_0 = 1000kg/m^3$;
- α_θ is the thermal expansion coefficient, $\alpha_\theta = 2.0 \cdot 10^{-4}K^{-1}$;
- c_w is the heat capacity of water, $c_w = 3900J/kg/K$;
- H is the total heat flux in W/m^2;
- β_s is the haline contraction coefficient, $\beta_s = 7.6 \cdot 10^{-4}K^{-1}$;
- S is the surface salinity. In our calculations, we take it as a constant: $S = S_0 = 38.35$;
- E is the evaporation in m/s, P is the precipitation in m/s; so $E - P$ is the net freshwater flux out of the ocean.

All these values are typical of the surface Mediterranean Sea (Marshall and Schott, 1999a). We use precipitation data from NCEP but calculate the evaporation using the latent heat flux. We choose data corresponding to the Medoc area, at the same location as studied in the previous chapter.

We can decompose the buoyancy flux: $B = Bt + Bs$. Bt is the thermal part of the buoyancy flux:

$$Bt = \frac{g}{\rho_0}\frac{\alpha_\theta}{c_w}H \tag{3.3}$$

and Bs its haline part:

$$Bs = g\beta_s S(E - P)) \tag{3.4}$$

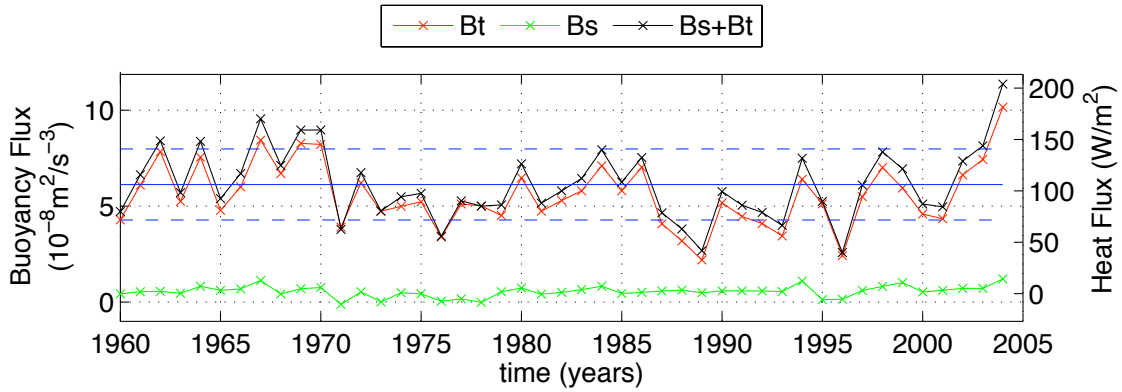

Figure 3.11: NCEP mean winter buoyancy fluxes (black) over the years (years indicated are the ones in which the winter starts), and its thermal (red) and haline (green) components Bt and Bs for the grid point chosen as representative of the Medoc area in chapter 2. The blue plain line shows the mean value of the mean winter buoyancy fluxes over the years. The dashed blue lines show the mean plus or minus a standard deviation.

We have calculated the mean buoyancy forcing for the winter period, between the 1^{st} of December and the 31^{st} of March of the next year, as shown on figure 3.11. The daily time series of buoyancy fluxes for each winter of these 50 years are shown in appendix A. We notice that the thermal component Bt, linked to the heat fluxes, is dominant. We consider a constant surface salinity to calculate the haline part of the buoyancy fluxes, which leads to a small error when calculating Bs. Since the haline part of the buoyancy flux is only a small contribution to the total buoyancy flux, this error can be neglected.

We notice that the periods of strong buoyancy loss coincide both with strong heat loss and net evaporation, because both heat and freshwater fluxes are strongly linked to the evaporation.

Figure 3.11 also shows the mean value of the mean winter buoyancy fluxes over the years (blue plain line). The dashed blue lines show the mean plus or minus a standard deviation. The mean corresponds to a heat flux of $108.9W/m^2$, and the standard deviation to one of $32.8W/m^2$. We notice that there are no trends in the winter surface buoyancy fluxes, so the warming trend observed in the deep water (figure 1.5) either results from a change in summer surface buoyancy fluxes, or from a larger-scale hydrographic change in the Mediterranean. There were a few intense winters in the 1960's - winters 1962-63, 1964-65, 1967-68 and 1969-70 during which convection has been observed by MEDOC-Group (1970). Winter

1970-71 was the last of a series of intense winters after which the mean winter buoyancy flux is not larger than the mean plus a standard deviation, until winter 2004-05. In fact, we see that the winter buoyancy flux increases between 2000-01 and 2004-05, reaching a peak higher than observed in the previous 50 years. It is likely that this increase was also present in other parts in the Mediterranean, including at the formation sites of other water masses, like the Aegean Sea and Levantine basin where the LIW is formed. As it was happening over 3 years it could be responsible for the decrease in temperature and increase in salinity and density observed at the Dyfamed site in the top 0-400m.

Data for the WMDW composition

For the present analysis, we use the data forming the base of Béthoux et al. (1990, 1998) for the T and S of the WMDW formed in the Gulf of Lion and then spread in the Algero-Provencal basin where it has been sampled between $2000m$ and $2700m$ depth over the period 1959-1997 (courtesy of Béthoux, see figure 1.5). Hydrological station from 1959 to 1994 are referenced in Béthoux and Gentili (1996); 1995-97 data were acquired aboard CNRS/Insu ships. Béthoux et al. (1998) mentioned that the trends observed concern the entire deep water below about $800m$.

3.4.2 Correlation Tests

We performed correlation tests between the NCEP surface buoyancy fluxes at the Medoc site and the composition (temperature and salinity) of the deep water as measured by Béthoux et al. (1998) in the Algero-Provencal basin. The purpose of these tests is to study if the variability in buoyancy fluxes can affect the composition of the deep water formed.

For each year, we consider the winter averaged (December to March inclusive) buoyancy fluxes $B(year)$, that we separate into its haline (only due to evaporation and rainfall effects) and thermal (due to heat fluxes) components, Bs and Bt. Then we write $Bt(year) = \overline{Bt} + \Delta Bt(year)$ and $Bs(year) = \overline{Bs} + \Delta Bs(year)$ where the overbar denotes the average over winters from 1960-61 to 1998-99.

For the deep water data, we interpolate the data from Béthoux et al. (1998) to have the temperature and salinity of the deep water in the Algero-Provencal basin in September of the next year. We can decompose the value for each year as $T(year) = \overline{T} + \Delta T(year)$ and $S(year) = \overline{S} + \Delta S(year)$. We calculate correlation coefficients between ΔT, ΔS, ΔBt and ΔBs, shown in table 3.4.

We notice the important correlation between the variations in temperature and salinity, corresponding to density compensation. The correlation between the two components of the buoyancy fluxes is due to the evaporation term that appears in both the latent heat flux and the haline buoyancy flux.

We see a correlation between $\alpha\Delta T$ and ΔBt, but none between $\beta\Delta S$ and ΔBs. This is due to the predominance of the thermal part in the surface buoyancy flux, and confirms that the salinity variations only follow the temperature ones (density compensation), which set up the dynamics. The good correlation between $\beta\Delta S$ and ΔBt also emphasises this point.

The poor correlation between $\beta\Delta S$ and ΔBs explains the poor correlation between the ratios $\frac{\alpha\Delta T}{\beta\Delta S}$ and $\frac{\Delta Bt}{\Delta Bs}$ (0.018), and leads us to conclude that there is no correlation between the composition of the buoyancy flux and the characteristic of the deep water. Rather, the temperature and density of the WMDW are set by the thermal buoyancy loss, which as a consequence of the equation of state also sets the salinity. This density compensation is thought to be related to the dynamics of convection, although it is not fully understood. The variability of preconditioning must be responsible for the variability of the deep water composition, unless the exchanges with the surrounding waters (cascading, lateral fluxes through baroclinic eddies) are important.

	$\alpha\Delta T$	$\beta\Delta S$	ΔBt	ΔBs
$\alpha\Delta T$				
$\beta\Delta S$	0.97 (0.00)			
ΔBt	0.36 (0.02)	0.38 (0.01)		
ΔBs	-0.03 (0.82)	- 0.04 (0.83)	0.56 (0.00)	

Table 3.4: Correlation tests between NCEP buoyancy fluxes and deep water characteristics. The number in brackets is the probability of getting a correlation as large as the observed value by random chance. A very low probability means that the correlation is significant.

3.5 Preconditioning vs. buoyancy forcing: Impact on the mixed layer depth

3.5.1 The one-dimensional (1D) model

We have implemented a 1D model based on Turner's formula (Turner, 1973). It only uses buoyancy conservation and yields, for the rate of deepening:

$$h(t) = \sqrt{\frac{2 \cdot \int B_0 dt}{N^2}} \tag{3.5}$$

where $h(t)$ is the depth of the mixed layer at time t, B_0 is the buoyancy flux and N is the buoyancy frequency, assumed constant here. This formula assumes that:

- $h(t=0) = 0$,
- the mixed layer is fully mixed,
- there is no lateral buoyancy gradient.

Formula 3.5 is derived in appendix C.

However, we want to study a more general case, with a time-dependant surface buoyancy flux and a depth-dependant stratification, so we integrate Turner's formula by pieces. Details and validation of the model are given in appendix C. This model still assumes a fully mixed layer and no lateral buoyancy gradient.

3.5.2 An example: the Doconug CTD data

Doconug 1, 2 and 3 were 5-day cruises carried out in the Gulf of Lion at the end of January, February and March 2007, carried out on the Thetys II (INSU-CNRS) and led by Pierre Testor as part as a glider deployment program. Figure 3.13 shows the location of the CTD casts made during the first cruise. Convection was not very intense that winter - at the end of March 2007, the maximum mixed layer depth measured was about $400m$.

The 1D model can be used to assess how close a T/S profile is to deep convection. We used the uncalibrated CTD profiles to initialise the 1D model and plot the mixed layer depth as a function of the integrated heat flux: see figure 3.13. (At the time at which this work was done, calibration of the data had not been done yet and is not necessary for the point we are making here.)

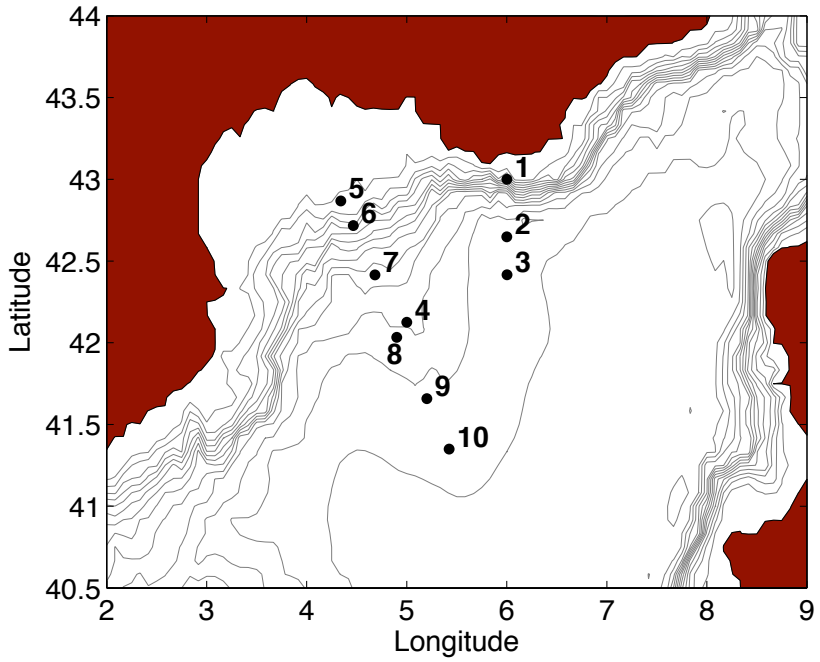

Figure 3.12: Location of the CTD casts for the Cruise Doconug 1.

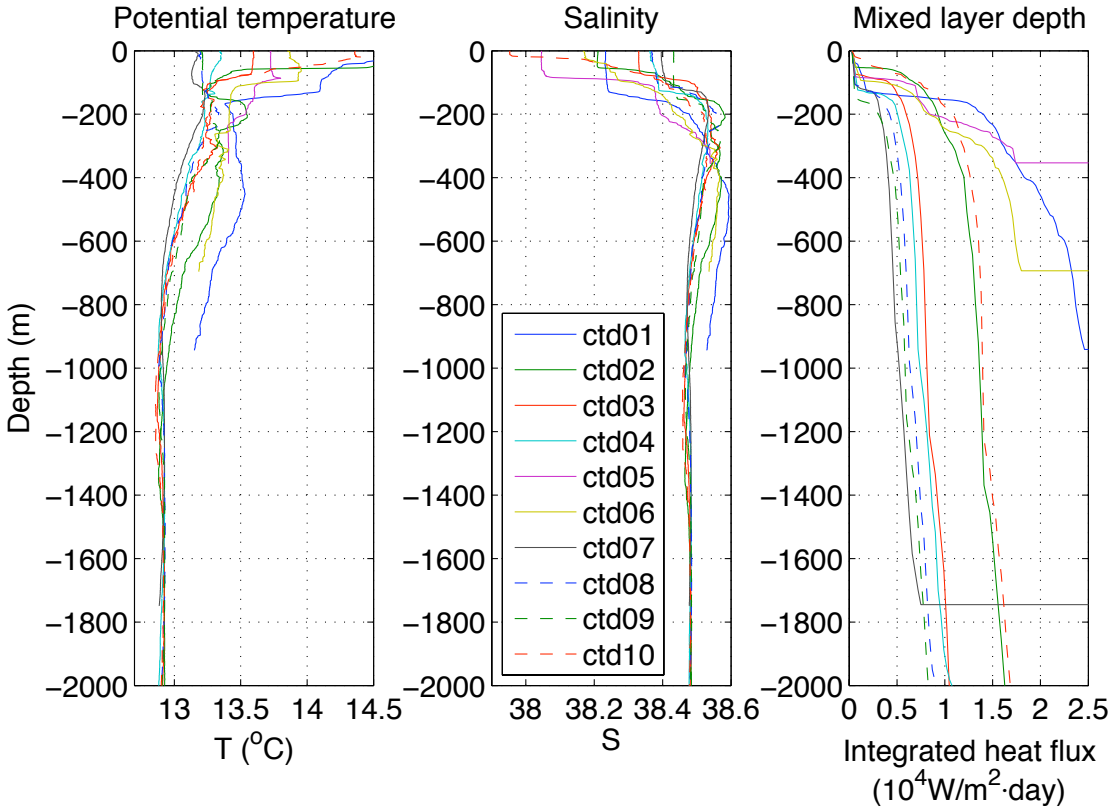

Figure 3.13: Temperature and Salinity profiles from the cruise Doconug 1, and mixed layer depth as a function of the integrated flux applied in the model when initialised with the Doconug profiles.

We first notice that the shallow profiles, taken on the continental shelf, are further from convection than the ones taken in the open-ocean area. However, what would happen if, while convection is occurring in the open-ocean, some water from the shelf was advected towards the convective patch? The water from the shelf has different T/S characteristics than the water from the open ocean - is this going to have an effect on the dynamics? What we see here is that the water on the shelf is actually more buoyant than further offshore, so this does not support the cascading hypothesis, at least not for the winter 2006-07, which was mild.

Secondly, for all profiles, the surface layer is very easy to deepen, indicating that convection has already started. There is below the mixed layer a jump in the buoyancy frequency that slows the deepening very significantly. The deepening then goes faster as the mixed layer depth increases, reflecting the fact that the deepening does not require so much buoyancy loss once the LIW layer has been eroded. We observe the same pattern when running the 1D model initialised with the MEDAR climatological profiles and forced by a constant buoyancy loss (not shown here) - the LIW acts as a barrier against convection.

3.5.3 Stratification and surface buoyancy fluxes

In terms of heat fluxes

To quantify the relative importance of the preconditioning compared to the buoyancy fluxes, we compare the heat flux necessary to reach one particular depth for one particular profile (from the Dyfamed data set) with the NCEP integrated heat flux for winters 1995-96 to 2004-05. The point is to compare the change in mixed layer temperature due to the deepening of the mixed layer (change in the heat content due to entrainment of colder/warmer water from below) with the change due to surface heat loss. We calculate:

$$\Delta BC_h^T = g\alpha \int_h^0 (T(h) - T(z))dz \tag{3.6}$$

where $\alpha = 2.3 \cdot 10^{-4} K^{-1}$ is the coefficient of thermal expansion and T the potential temperature. ΔBC^T refers to a change in buoyancy content associated with the change in heat content, under the assumption of a linear equation of state.

The corresponding plots are shown on figure 3.14. We can analyse them in terms of change in heat content. Each line corresponding to ΔBC_h^T for different

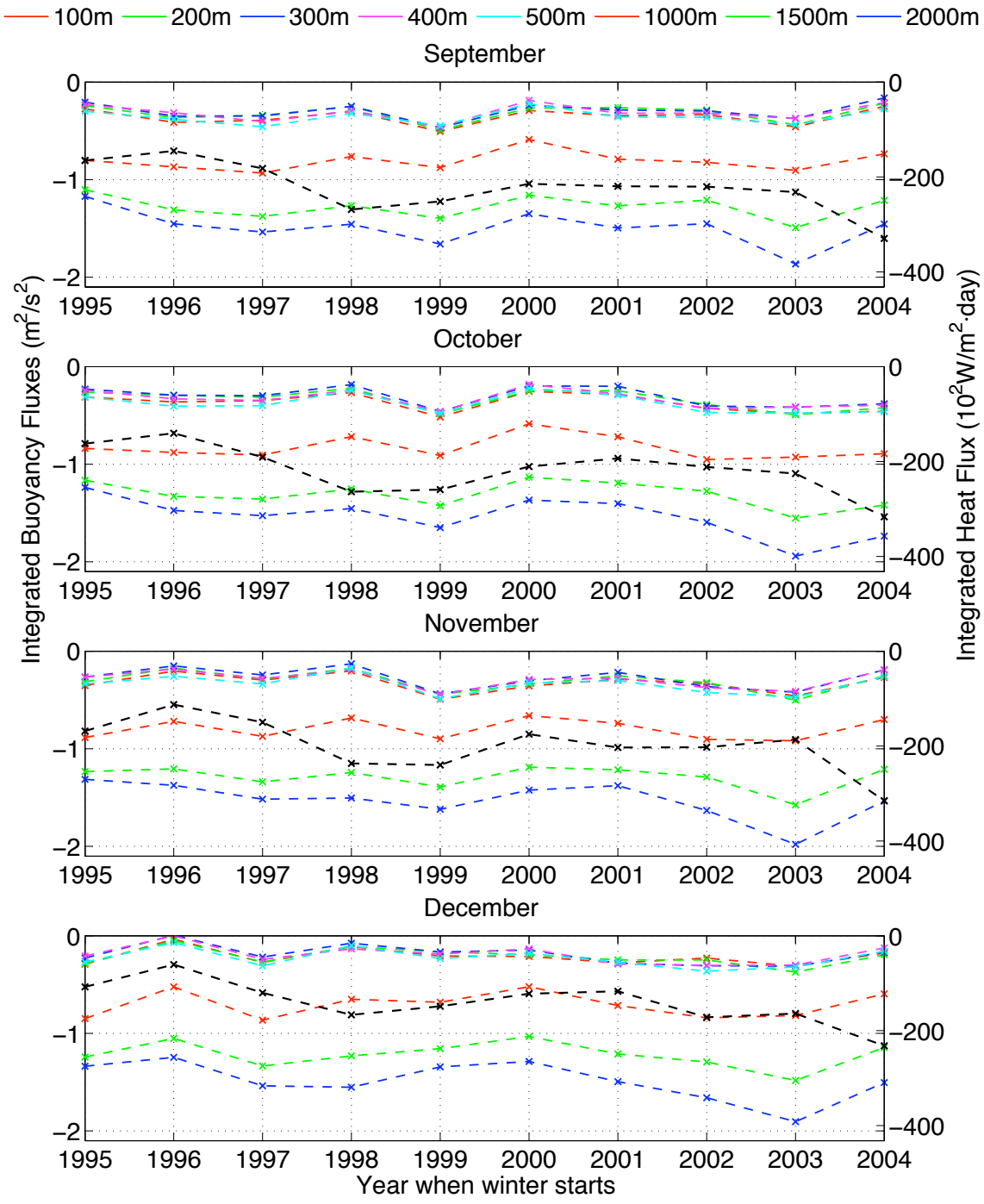

Figure 3.14: Heat fluxes that would be necessary to have a convective mixed layer of depth of h, calculated from the Dyfamed profiles, and actual integrated buoyancy fluxes (thick black line) from NCEP, for each winter from the 1^{st} of the month until the end of March of the next year, if the salinity in the water column was homogeneous.

values of h shows the difference in heat content of the water column between the initial Dyfamed profile and the final (when the mixed layer has a depth h) profile. To help our analysis, we have also plotted the evolution of the temperature and salinity of a mixed layer depth eroded by a pure surface heat flux as a function of the mixed layer depth for an average December month at the Dyfamed site, as well as the actual profiles - see figure 3.15. It shows that the temperature of the mixed layer decreases until the mixed layer depth reaches about 250m depth. Below that, the entrainment of warmer LIW water from below is not offset by the surface cooling and the temperature increases as the mixed layer deepens. The cooling there is mainly used to erode the stratification due to salinity. Below about 1000m, the temperature and salinity both slowly decrease with depth. For that particular profile, the value of ΔBC_h^T is linked to the area below the temperature curve.

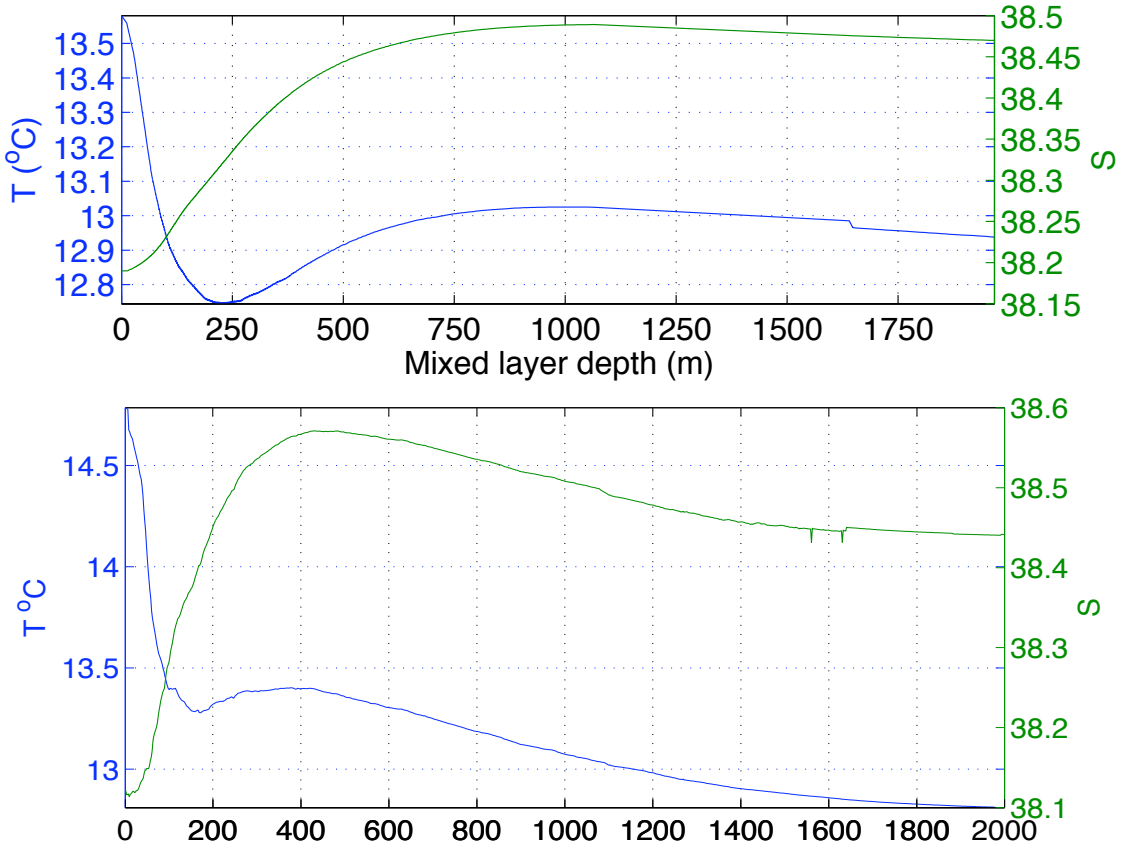

Figure 3.15: Top: Evolution of the temperature and salinity of the mixed layer eroded by a pure heat flux as a function of the mixed layer depth for a typical December profile from the Dyfamed data set (the profile is the same as used for the seasonal cycle analysis), shown in the bottom panel.

In the top layer, we have seen that the stratification was mainly set by the temperature. In that layer, it is not a bad approximation to consider a roughly

homogeneous salinity because the vertical temperature gradient is responsible for the stratification. The heat loss is mainly used to deepen the temperature gradient in that layer, so we expect a situation in which the temperature of the mixed layer is close to that of its base. We can observe the seasonal weakening of the stratification in the top layer due to cooling at the surface. Deepening the mixed layer down to 100m results in a smaller change in heat content for a December profile than for a September one, because the surface water has already been cooled. Comparing different years, we notice that the difference between the December and September months changes from year to year. For example, for winter 1995-96, the seasonal weakening of the stratification in the top layer is not noticeable, while it is significant for the next winter. If we compare winters 1999-2000 and 2000-01, we see that the top of the water column had a higher heat content in September in 1999-2000 than in 2000-01. In December, they both had about the same surface heat content. Winter 2004-05 is peculiar because the heat content in the top 100m seems to have increased in October and decreased in November and December, so it is roughly the same for September and December. We can associate this to a relatively warm September month that did not cool the top layer, as confirmed by the similarities between the values of the NCEP integrated heat flux for integration period starting on the 1^{st} of September (black line on top panel of figure 3.14) and on the 1^{st} of December (black line on second panel of figure 3.14).

Between 100m and 500m, however, the water column is mainly stratified by salinity. This is reflected in the fact that the plots corresponding to results for $h = 100, 200, 300, 400$ and $500m$ are so close together. In that layer, the surface heat loss is used to erode the stratification due to salt, and the deepening of the mixed layer entrains warmer LIW from below. Hence the difference in heat content between the time at which $h = 100m$ and the time at which $h = 500m$ is very small. The warming due to entrainment of water from below is more or less offset by the heat loss at the surface. Using figure 3.15, this corresponds to the minimum in mixed layer temperature reached when the mixed layer depth is about 250m, the depth at which the surface cooling exactly offsets the warming from below. Above that level, the surface cooling is more important, resulting in a cooling of the mixed layer, while below the entrainment of warmer water is more important, hence the increase in temperature.

Below 500m, the situation is again that of a stratification mainly due to the vertical gradient of temperature. So the deepening of the mixed layer below that

level, even if it was only due to the haline part of the buoyancy forcing, would lead to a cooling of the mixed layer. When the mixed layer deepens below 500m, the change in its temperature is both due to the surface heat loss and to entrainment of cold water from below.

We can compare the results for the $2000m$ level, which we use as the bottom depth in the following analysis, with the surface heat loss, to get information about the temperature of the deep-water formed, still in a 1D framework. We assume here full depth convection, hence deep water formation. Under that assumption, we compare the results for $h = 2000m$ with the integrated surface heat flux starting in December. The result for $h = 2000m$ represents the change in heat content due purely to a deepening of the mixed layer while the integrated surface heat flux represents the change in heat content purely due to the forcing. Theoretically, we can write that part of the surface heat flux SHF goes into the change in heat content between the initial time and the time at which convection reaches the bottom ΔHC_{2000m} and that the rest of the surface heat loss goes into a pure cooling of what will become deep water ΔHC_{DW}: $SHF = \Delta HC_{2000m} + \Delta HC_{DW}$ or equivalently $\Delta T_{SHF} = \Delta T_{2000m} + \Delta T_{DW}$, where SHF is the surface heat flux, and the subscript $2000m$ refers to the change in heat content/temperature necessary to reach $2000m$ depth while DW refers the the change in heat content/temperature corresponding to a pure cooling of the water mass after the 'bottom' ($2000m$) has been reached. In reality, figure 3.14 shows that $SHF < \Delta HC_{2000m}$, due to the limitation of our analysis. The assumption that is not valid is that the salinity is roughly homogeneous, which would lead to having the temperature of the mixed layer depth being that of its base, which is not the case in general - it is only true of buoyancy/density. Hence using the temperature at the base of the mixed layer for the temperature of the mixed layer is not the right choice and provides a reference state with an offset for each depth considered. As it is an offset, our previous analysis on the variability of the signal still holds if the temperature jump at the base of the mixed layer remains the same for one particular depth every year. [1]

However, we can look at the difference between SHF and ΔHC_{2000m}. We expect the water formed to be colder when this difference is smaller. For example,

[1]Note that we could calculate $\Delta BC_h^T = g\alpha \int_{h(t)}^0 (T_{MLD} - T(z, t = 0))dz$. The calculation of T_{MLD} could be done by using the heat flux necessary to reach h when considering the density profile. We would have $T_{MLD} = \frac{1}{h}\int_h^0 T(z, t = 0) - \Delta T_{surf}$ where ΔT_{surf} is the equivalent change in temperature for the purely thermal buoyancy flux necessary to erode the density gradient down to that depth. We would then obtain $\Delta BC_h^T \propto \Delta T_{surf}$, and this would give the same information as studied in the next paragraph.

we notice that winter 2004-05 coincides with the minimum difference between SHF and ΔHC_{2000m} over our record, and this corresponds to a year when the deep water formed was much colder than previously observed. Figure 3.14 confirms that this is both due to a water column with a lower heat content than in the previous years (less heat loss necessary to reach $2000m$ depth), and to a high heat loss at the surface. We can show that the anomaly in buoyancy forcing was stronger that the anomaly in heat content. ΔBC^T_{2000m} for winter 2004-05 is within 0.47 standard deviation of the mean over our 10 year record while the surface buoyancy fluxes for that year is within 1.99 standard deviations of the mean over the same period. We now consider $\tau = \Delta BC^T_{2000m} - \int SBF$ where $\int SBF$ is the winter integrated surface buoyancy flux. Over our record, we always have $\tau - \overline{\tau} < 0.7std(\tau)$ except for winter 2004-05 for which $\tau = 1.99std(\tau)$. For most of the 10 year record, the heat content of the water column varies similarly as the surface flux while we have the opposite situation for winter 2004-05. The reasons for this similarity and its disruption for winter 2004-05 are not clear. Is it merely a coincidence, or is it related to a larger scale change? Could colder fluxes over the Gulf of Lion be related to a warming in the eastern part of the basin, maybe both being an effect of a large-scale atmospheric circulation pattern like the NAO? This is beyond the scope of the present study.

In terms of buoyancy fluxes

Considering only the temperature in the previous analysis was equivalent to assuming a vertically homogeneous salinity. We have seen that this was too strong an assumption, particularly in the intermediate layer, to lead to a realistic analysis. We now perform a similar analysis for the buoyancy profiles, considering both temperature and salinity effects on the stratification. The buoyancy fluxes necessary to reach a depth h is defined, following the 1D approach, by:

$$\Delta BC = \frac{g}{\rho_0} \int_{h(t)}^{0} (\rho(h,t) - \rho(z, t=0)) dz \tag{3.7}$$

where $g = 9.82m/s^2$ is the acceleration due to gravity, ρ the potential density, $\rho_0 = 1000kg/m^3$ a reference density and h the mixed layer depth. ΔBC refers to a change in buoyancy content, with the same units as a buoyancy flux integrated over time. The choice of initial time to define $\rho(z, t = 0)$ might be critical, hence we perform the calculation for four different initial times: the 1^{st} of September, October, November and December. For example, for the month of December, we

interpolate the Dyfamed data to have daily profiles and extract a profile that is the mean one between the 15^{th} of November and the 15^{th} of December. We do this for each year from winter 1995-96 to winter 2004-05. We can then compare the value obtained with the actual surface buoyancy fluxes (from NCEP) between the first day of the month considered and the 31^{st} of March of the next year. Figure 3.16 shows the results for the four months chosen as initial times. The colored lines show the amount of buoyancy that has to be removed for the mixed layer depth to reach different depths as indicated in the legend while the black lines give the NCEP winter integrated buoyancy flux from the initial time chosen until the end of March of the next year. The scale on the right shows the equivalent winter integrated heat flux in $10^2 W/m^2 \cdot day$. For example, an integrated heat flux of $-100 \cdot 10^2 W/m^2 \cdot day$ corresponds to 100 days at a heat flux of $100 W/m^2$ or 10 days at $1000 W/m^2$.

Comparing the black line on figure 3.16 with the colored lines can allow us to estimate the expected final mixed layer depth for one particular winter, in a 1D framework - it is given by the relative position of the black line to the coloured ones. For instance, if we consider the bottom plot corresponding to an initialisation at the beginning of December, we expect shallow convection in winters 1995-96, 1996-97 and 1997-98 to about 200m, while the next winters were probably more intense, with an expected final mixed layer depth of 1500m for winter 1998-99, and an intense convection reaching deeper than 2000m in winters 1999-2000 and 2000-01. Convection in the next three winters seems to have been rather weak, with mixed layer depths shallower than 400m. Figure 3.16 shows that convection in winter 2004-05 should have been intense not only because of very high surface buoyancy loss, but also because of relatively low stratification within the LIW layer. We notice that, once the 500m level has been reached, the column does not require much more buoyancy loss to be fully mixed. Once again the LIW appears as a critical barrier to convection.

Deep convection requires more buoyancy flux to deepen in December than in fall, which goes against the concept of preconditioning. This is due to the winter maximum of buoyancy frequency in the intermediate layer. We expected the buoyancy loss occurring between September and December to weaken the stratification, which is what we observe if we look at the buoyancy loss necessary to get a mixed layer depth of 100m. The amplitude of this surface (0-100m) weakening presents an interannual variability. For example, for winter 1995-96, about the same amount of buoyancy is required for the mixed layer to reach the 100m

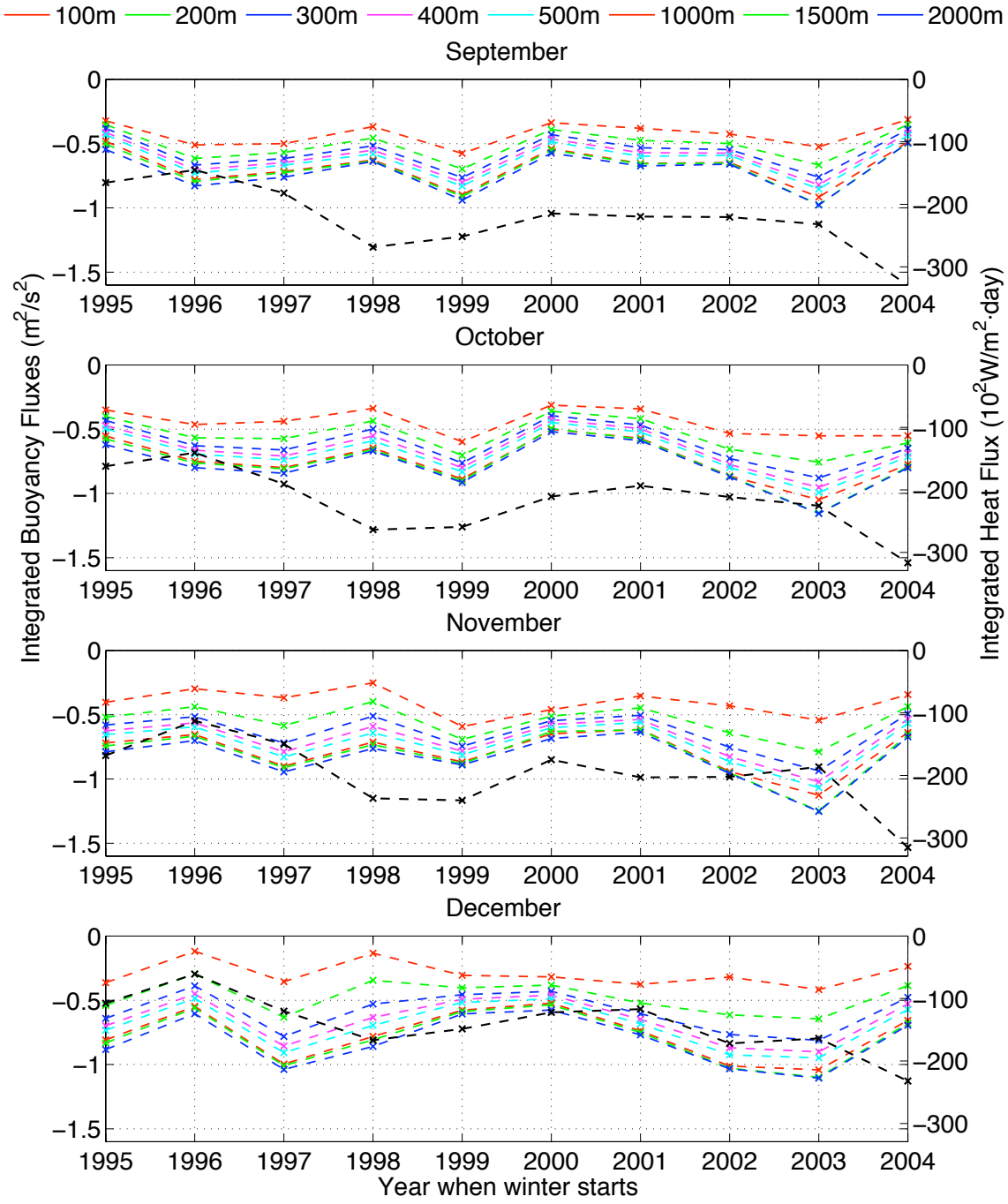

Figure 3.16: Buoyancy fluxes that would be necessary to have a convective mixed layer of depth of h, calculated from the Dyfamed profiles, and actual integrated buoyancy fluxes (thick black line) from NCEP, for each winter from the 1^{st} of the month until the end of March of the next year.

level in December as in September. However, for some years, the weakening quite significant - winter 1999-2000 is a good example of an efficient weakening of the surface stratification between September and December. However, if we consider the integrated buoyancy loss necessary for the mixed layer to reach the 500m level, we see that it often requires more buoyancy in December than in September. There are significant similarities between that curve in December and the interannual variability of the stratification in the intermediate layer shown on figure 3.10, because the calculation performed here is equivalent to running a 1D model on the chosen Dyfamed profile. There are two processes acting in opposite ways. The fall surface buoyancy loss acts to reduce the stratification in the top layer, to an extent that depends on the magnitude of the surface buoyancy loss, hence facilitating convection. On the other hand, the advection of LIW leads to a maximum in the stratification of the intermediate layer that has a tendency to inhibit convection.

Table 3.5 shows the means and standard deviations for the winter integrated buoyancy fluxes and for the buoyancy flux necessary to reach some of the depth levels, for calculations in which the winter starts on the 1^{st} of December, both in terms of buoyancy and equivalent heat fluxes. Each of the means and standard deviations is calculated on a 10-sample data set, each sample representing one winter. We see that the standard deviation (std) for the actual winter integrated buoyancy fluxes and for the flux necessary to reach the (near) bottom are very similar. We use the std as a proxy for the variability. The winter integrated surface buoyancy loss has a variability similar to, although slightly larger than, the variability of the amount of buoyancy necessary for the mixed layer depth to reach 2000m. Hence we can conclude that, under the assumption that the interannual variability at the Dyfamed site is representative of that at the Medoc site, the interannual variability of the surface buoyancy loss and that of the preconditioning have an effect of similar magnitude on the final convective depth. As seen previously, most of the buoyancy loss required to get convection at 2000m is actually used to deepen the mixed layer down to 500m.

Table 3.5 also shows that, even in a 1D framework for which all the potential energy gained by surface buoyancy loss is used to deepen the mixed layer, an average winter does not lead to a convective mixed layer deeper than 500m at the Dyfamed site. If we consider that the difference between the winter integrated buoyancy flux X_{BF} and the buoyancy necessary for the mixed layer to reach a

	BF	**100m**	**500m**	**2000m**
mean (m^2/s^2)	-0.686	-0.294	-0.696	-0.817
std (m^2/s^2)	0.225	0.101	0.182	0.197
mean ($10^2 W/m^2 \cdot day$)	-141	-60	-143	-168
std ($10^2 W/m^2 \cdot day$)	46	21	37	41

Table 3.5: Mean and standard deviation (std) for the winter (from the 1^{st} of December until the 31^{st} of March of the next year) integrated buoyancy fluxes (BF) from NCEP, and for the buoyancy flux necessary to reach depths of 100, 500 and 2000m in terms of buoyancy and equivalent heat fluxes, calculated using the Dyfamed data.

depth h, which we call X_h is a random quantity that follows a normal distribution, we can estimate the probability that the mixed layer reaches that depth. The time series $X_{BF} - X_h$ has a mean of $0.01 m^2/s^2$ and a standard deviation (std) of $0.242 m^2/s^2$ for $h = 500m$. It has a mean of $0.130 m^2/s^2$ and a std of $0.266 m^2/s^2$ for $h = 2000m$. Assuming a normal cumulative distribution function for $X_{BF} - X_h$, we find that the probability that the depth h is reached is 48% for $h = 500m$ and 31% for for $h = 2000m$. Hence, only 31% of winters are expected to lead to deep water formation. This figure should be higher at the Medoc site, where dynamic preconditioning due to the cyclonic circulation further erodes the stratification. Carrying out a similar analysis at the Medoc site would be more indicative of the convective process, although we would need a better time series at the Medoc site than we have at the moment using the Medar-Medatlas data, particularly for the winter months.

3.6 Temperature and Salinity contributions to the deepening

Turner's formula does not distinguish between temperature and salinity effects on density. However, considering a linear equation of state - which is acceptable in the case of the Mediterranean because we are not close to the freezing point - and linear temperature and salinity profiles with corresponding stratification frequency N_t^2 and N_s^2 - which is always true if considered locally - we can write:

$$h^2(t + dt) - h^2(t) = \frac{2 \cdot \int (B_t(t) + B_s(t)) dt}{N_s^2 + N_t^2} \tag{3.8}$$

We can write that as the sum of a deepening due to salt plus a deepening due

to temperature minus a coupled term:

$$h^2(t+dt) - h^2(t) = \frac{2\int B_t(t)dt}{N_t^2} + \frac{2\int B_s(t)dt}{N_s^2} - 2\frac{N_s^4 \cdot \int B_t(t)dt + N_t^4 \cdot \int B_s(t)dt}{N_s^2 \cdot N_t^2 \cdot (N_s^2 + N_t^2)} \tag{3.9}$$

We could compare these different terms using values typical of the Mediterranean, but they have such a variability with both depth and time that it does not provide a clear picture. Instead, we can write $B_s = k_B \cdot B_t$ where k_B is a non dimensional factor. This is not a big approximation as we have seen that B_s and B_t are well correlated. Similarly, we can write $N_s^2 = k_N \cdot N_t^2$ as N_s^2 and N_t^2 have both been assumed linear.

We now have:

$$h^2(t+dt) - h^2(t) = \frac{1+k_B}{1+k_N} \cdot \frac{2\int B_t(t)dt}{N_t^2} \tag{3.10}$$

We can now conclude that:

- if $k_B > k_N$, the coupling will lead to a deeper mixed layer;
- if $k_B < k_N$, the coupling will lead to a shallower mixed layer;
- if $k_B = k_N$, the coupling has no effect.

In the real ocean, however, it is not that simple. k_B is usually of order 10^{-1} for the Gulf of Lion, but k_N changes with depth. Using the Dyfamed data plotted on figure 3.5, we see that we usually have $0 < k_N < 1$ in the top layer, $k_N < 0$ in the intermediate layer and $k_N \sim -0.2$ in the deep layer. The value of k_N varies significantly depending on the season in the top and intermediate layers, but is quite stable in the deep layer. Hence, the coupling between temperature and salinity would act towards a further deepening. However, it is difficult to estimate what happens within the mixed layer - is it really homogeneous and if not, what does the residual stratification look like? Moreover, the assumption of a linear equation of state does not hold well in the deeper layer.

3.7 Conclusion

Some elements of the preconditioning have not been considered here, like the strength of the cyclonic gyre. Rather, we took an approach based on the circu-

lation of water masses. We focused on what we called a hydrographic preconditioning rather than a dynamic one. Our analysis of the convective event was made in a 1D framework, neglecting any lateral advective fluxes that could affect the patch during convection.

We saw that the three layers of the water column are in different regimes. The top layer has a stratification mainly due to the temperature vertical gradient, and undergoes a seasonal cycle with a summer increase of temperature and stratification. The intermediate layer, above the Levantine Intermediate Water subsurface maximum, is stratified by the vertical salinity gradient and its stratification presents a maximum in December whose timing and magnitude are of critical importance for convection. This maximum was observed both in the Dyfamed and Medar data sets, and both at the Dyfamed and Medoc locations. There might be a correlation with the transport through the Corsica strait, although the cause of that winter maximum is yet to be investigated.

We studied the interannual variability at the Dyfamed site and showed that the deep water there presented warming and salinification trends similar to that observed in the deep water of the Balearic Sea by Lopez-Jurado et al. (2005). The deep water at the Dyfamed site also presents a high density in December 2004 as observed in the deep water of the Balearic Sea in the following summer. This was combined to a relatively low winter maximum in the stratification of the intermediate layer.

We compared the variability of surface buoyancy flux and preconditioning at the Dyfamed site and showed that they had similar orders of magnitude, although the surface buoyancy flux has a slightly larger variability. We showed that, in a 1D framework and using the Dyfamed data as initial profiles for convection, less than 1/3 of winters were expected to lead to deep water formation. We then looked at the heat content of the water column before winter at the Dyfamed site and showed that it varies in a similar way as the surface fluxes, except for winter 2004-05 which led to the formation of very cold deep water. The reason for this similarity and its disruption is thought to be related to larger scale atmospheric circulation of the NAO type, and is a question that remains open for now.

The picture emerging from this analysis is that convection transfers the properties of the pre-convection water column to the bottom layer. The rate of transfer - for which the mixed layer depth is a proxy - is set by the surface heat loss and by preconditioning. For a given mixed layer depth, the surface fluxes have no

or very little impact on the resulting salinity of the water formed, while the temperature of the bottom water will be affected by both the initial heat content of the water column and the surface heat flux. This is a result of the dominating influence of the heat flux on the surface buoyancy flux.

Chapter 4

Deep Convection with the MIT model: Control Run

4.1 Introduction

This chapter describes how we simulate deep convection with the MIT model. We briefly present in the introduction some background about modeling deep convection, to explain the choices we have made. The next section focuses on the MIT model and the configuration used in our experiments. We then present results from a control run, in which the surface forcing is kept constant, checking that the evolution of the convective patch agrees with our expectation. Before concluding, we show results from experiments in which we have varied some of the parameters (intensity of the forcing and area on which it is applied), to validate our configuration.

Modeling Deep Convection

Modeling deep convection is first modeling an oceanic mixed layer. Nurser (1996) reviewed the different models and observations of the mixed layer, and enumerated the different forcings applied on the mixed layer:

- Surface (wind) stress, which is applied on the momentum, and generates an input of turbulent kinetic energy leading to mixing,
- Buoyancy forcing:
  - Heat fluxes: surface heat fluxes (sensible, latent and net outward radiation), and inward solar radiation, which penetrates deeper in the water column and depends on the albedo.

– Freshwater forcing: evaporation, precipitation, river run-off.

Kraus and Turner (1967), using a one-dimensional model of the seasonal thermocline, showed that "during the winter, convection due to surface cooling dominates the processes which deepen the layer". That is, the surface wind stress is not going to matter so much. This is consistent with the fact that we have a deep mixed layer in winter - mixing due to wind might affect convection at the beginning, when the mixed layer is shallow, but it is not going to drive the deepening of a deep mixed layer. Using a 2-level model, Killworth (1985) showed that the Ekman pumping only had an influence on the extent of the area occupied by convection, which is something Kraus and Turner (1967) could not observe with their 1D model. Considering buoyancy conservation of a non-rotating fluid stratified by salt and forced by heat fluxes, Turner (1973) derived a formula for the convective mixed layer depth (derived in appendix C).

Killworth (1989) concluded on the parameterisation of deep convection that:

- deep convective mixing is non-penetrative,
- there is no need to mix dynamical quantities when tracers are mixed by convection,
- vertical resolution has to be adequate, particularly near the surface,
- timesteps have to be identical for temperature and momentum during the process.

More recently, Paluszkiewicz and Romea (1997) suggested a one-dimensional parameterisation for deep convection in ocean models. They used a parcel model, with equations based on the physics of entraining buoyant plumes. Their main addition to a simple convective adjustment is that the exchange of properties between the plume and its surroundings is also parameterised.

Sander et al. (1995) identified thermobaric effects when comparing different forms for the equation of state. Although, as Garwood (1991) highlighted, these are important only near the freezing point, therefore not significant in the Mediterranean Sea.

In global simulations, it is also necessary to parameterise lateral advection and mixing by mesoscale eddies generated by baroclinic instability. There is a widely used example of a parameterisation for isopycnal mixing in Gent and McWilliams

(1990). Here, we want to resolve the baroclinic eddies, so our simulations must have a sufficient resolution and we will not need such a parameterisation.

4.2 Presentation of the model

4.2.1 The MIT Model

General

The model used here is a Global Circulation Model (GCM) developed at the Massachusetts Institute of Technology (MIT). It integrates the Navier-Stokes equations, has non-hydrostatic capabilities (Marshall et al., 1997b, 1998b), and can be run on parallel computers (Marshall et al., 1997a). It exploits the fluid isomorphism between air and water, and as such can be used to model the atmosphere (Marshall et al., 2004). It uses an Arakawa C-grid (Arakawa and Lamb, 1977). Horizontal coordinates can be either cartesian, polar or spherical (Adcroft et al., 2004). On the vertical, either z- or p-coordinates can be used. The topography is represented as piecewise constant slopes, i.e. it uses the partial-step method (Adcroft et al., 1997).

Deep Convection in the MIT model

There are different ways of modeling convection with the MIT model. It is possible to either resolve non-hydrostatic convection, which requires very fine resolution and small time steps. We want here to study the restratification process, which requires modelling the whole convective patch. It would be very expensive in time and computer power, so we choose to parameterize convection. There are different methods of parameterisation:

- Simple convective adjustment scheme: instantaneous mixing by rearrangement of density pairs. The convective adjustment algorithm is called at a frequency chosen in input. This method is the most widely used in ocean models.
- Increasing the diffusivity when instability is found (Yin and Sarachik, 1994).
- Using the K-Profile Parameterisation (KPP), which mixes away unstable density profiles with a 3D parameterisation scheme for turbulence (Large et al., 1994; Klinger et al., 1996).

Marotzke (1991) compared three convective schemes commonly used in GCMs and investigated their influence on the stability of the thermohaline circulation. Each algorithm aimed at removing static gravitational instability even when the ocean is modelled as hydrostatic. Static stability was checked at the end of each time step. Among these schemes were the first two methods presented above. Marotzke (1991) showed that they guarantee static stability and are insensitive to the time step. Moreover, they allow the global model to avoid a spontaneous collapse of the thermohaline circulation.

We want to integrate the model over an area large enough to be able to simulate the whole convective patch, therefore we cannot afford the resolution necessary to resolve the plumes. We choose a hydrostatic version of the model, with a convective adjustment scheme called at every integration time step. As recommended by Killworth (1989), we will use the same timestep for tracers and momentum, and the convective adjustment only mixes tracers. The model is run in parallel mode, on four processors.

4.2.2 Configuration

Grid description and Boundary conditions

We use an ocean box of $128 \times 128 \times 40$ grid points. The horizontal resolution is $500m$, which is much smaller than the Rossby radius ($5 - 10km$) as the Coriolis parameter is $f = 10^{-4}s^{-1}$. We use a variable vertical resolution of $10m$ in the top $100m$ of the water column, of $40m$ in the $100 - 500m$ layer, and $75m$ below. Hence, the box has a size of $64km \times 64km \times 2km$. The model is run over periods of 80 to 130 days, corresponding to the duration of a winter. We use a timestep of $60s$, although the outputs we will present are snapshots taken every $24h$.

Our set-up employs either periodic or relaxation boundary conditions at the sides, a no slip boundary condition at the bottom, and has an implicit free surface. In the case of relaxation boundary conditions, we prescribe the temperature and salinity at the sides of the box to the initial profiles and set all velocities to $0m/s$.

Viscosities and Diffusivities

In their experiments, Legg et al. (1998) used a diffusivity of $K_h = K_v = 0.7m^2 \cdot s^{-1}$ for a grid scale of $\Delta x = \Delta y = 195.3m$ and $\Delta z = 125m$, and a Prandtl number $Pr = 1$ (i.e. a viscosity equal to the diffusivity) to study how a pre-existing mesoscale

eddy preconditioned the convective patch. Jones and Marshall (1993) used $K_h = 5m^2 \cdot s^{-1}$ and $K_v = 0.2m^2 \cdot s^{-1}$ with a similar grid $\Delta x = \Delta y = 250m$ and $\Delta z = 100m$ to simulate the whole patch and study its restratification. These two studies both used non-hydrostatic models, hence needed higher viscosity and diffusivity coefficient to dissipate the energy of the plumes.

The deepening of the mixed layer is sensitive to the values of diffusivities. We have run the MIT model for 4 sets of diffusivities, for initial profiles measured at the Dyfamed sites on the 1^{st} of November 2004, and NCEP heat fluxes. Figure 4.1 shows the initial profiles and surface forcing used in this set of simulations. Figure 4.2 shows the profiles at the centre of the patch for these runs after 62 days of simulation, that is just after a period of high buoyancy loss (the scales are different from the one used for the initial profiles). All simulations have a Prandtl number $Pr = 1$.

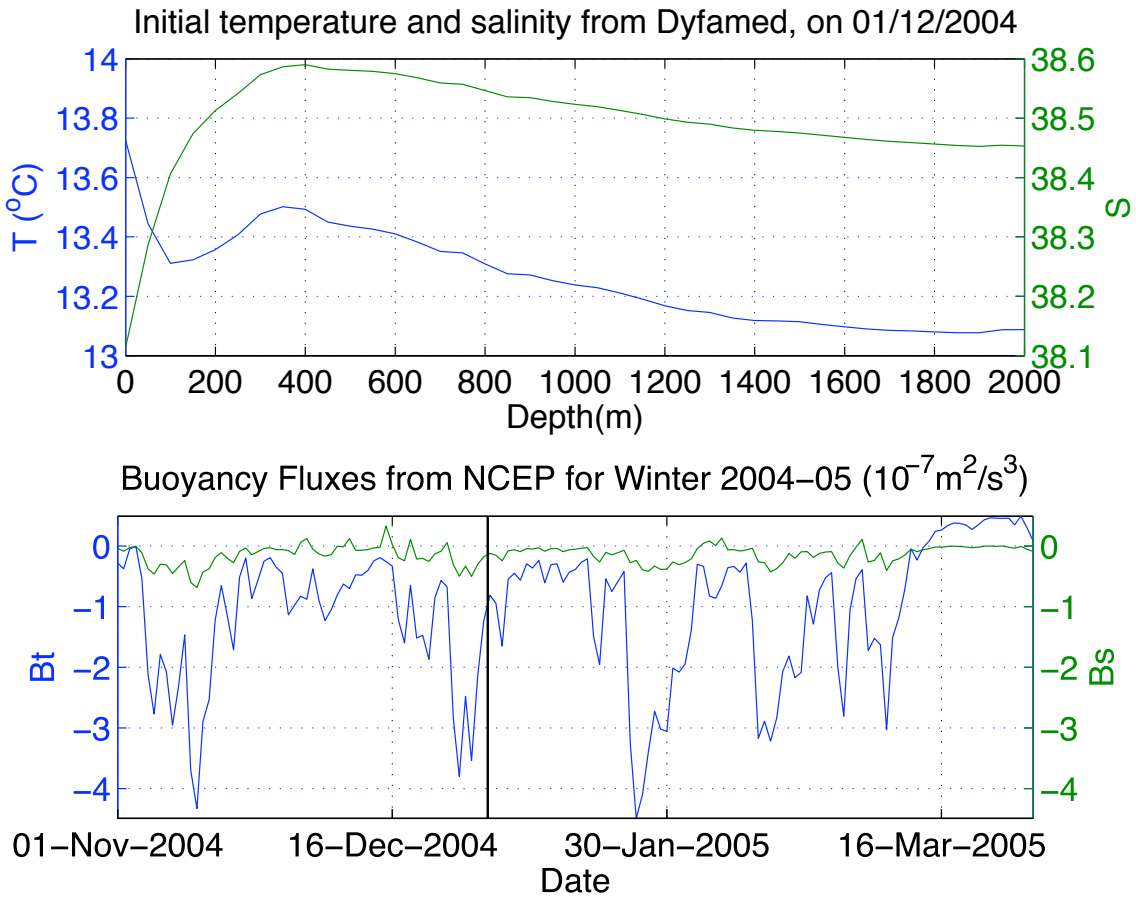

Figure 4.1: Initial profiles and buoyancy forcing used for the 1D and MIT models. The simulation starts on the 1^{st} of November 2004-05. The black vertical line on the bottom panel indicates the time at which the profiles of figure 4.2 have been plotted.

It is clear that only the run with $(K_h, K_v) = (5m^2/s, 0.001m^2/s)$ does not show

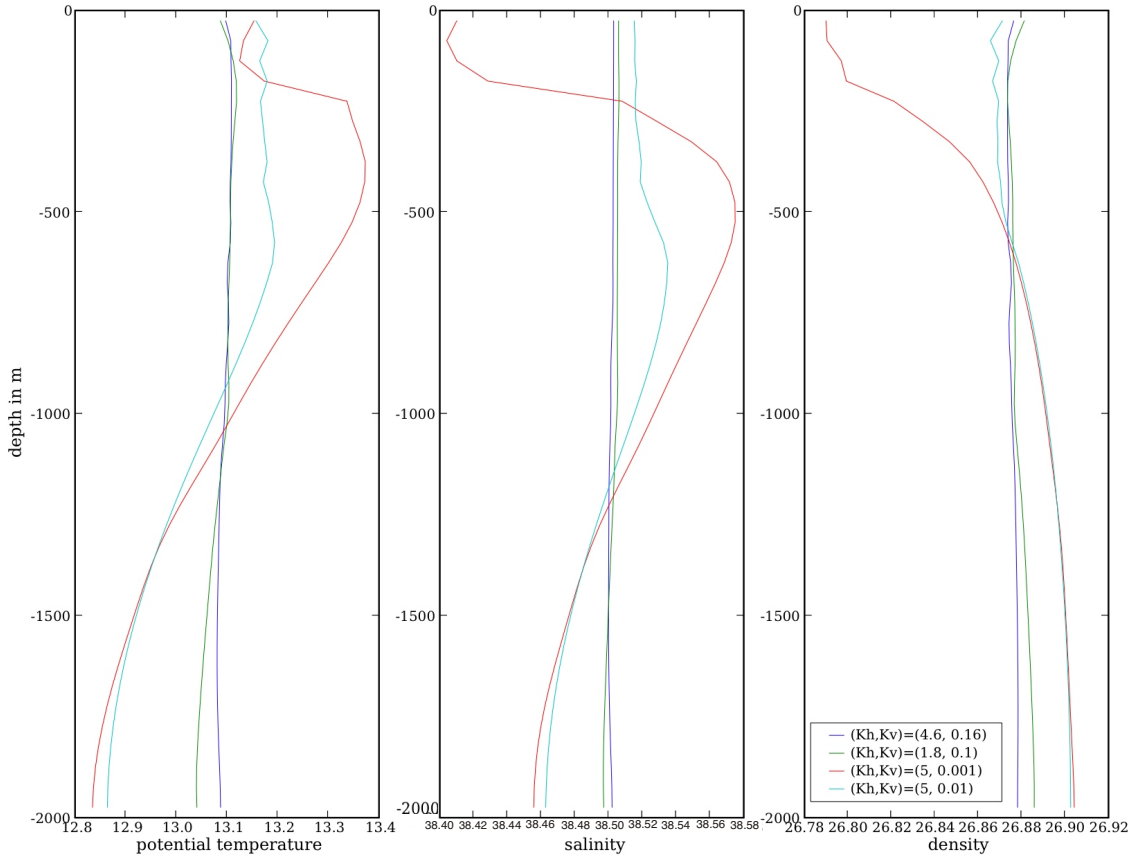

Figure 4.2: Comparison between runs with different diffusivities. Profiles of temperature, salinity and density at the centre of the patch after 62 days of simulation, i.e. on the 1^{st} of January 2005. Diffusivities are given in m^2/s. K_h stands for the horizontal diffusivity and K_v for the vertical one. Note that the scale is different from figure 4.1 as the range of values is also different.

a fully mixed regime. The vertical diffusivity is too important in the other runs, and make the stratification disappear. In Legg et al. (1998), this was compensated by a stabilising bottom heat flux. However, it is best to keep the vertical viscosity as low as possible. Legg et al. (1998) needed this higher diffusivity to dissipate the energy of the plumes and keep the model stable. This is not a constraint we have in our hydrostatic model, which does not resolve the plumes. As a comparison, the same type of calculation using a 1D model leads to a mixed layer of $1500m$ if starting on the 1^{st} of November. However, the 1D model does not contain any physics for restratification, and we can expect the MIT model to restratify significantly between the periods of high buoyancy loss at the beginning of November, and at the end of December. Forcing the 1D model for only the second half of the month of December leads to a final mixed layer of $230m$, close to that observed in the MIT model.

The effect of the horizontal diffusivity Kh is not clear. However, it acts on such a slow time scale that the advection due to baroclinic eddies will dominate

the lateral buoyancy fluxes, so we do not expect the system to be very sensitive to changes in Kh, as long as the baroclinic eddies are generated in a sensible way, and this will be how we validate our choice.

Initial conditions and Forcing

We have two options to localise convection: we can either localise the forcing, or modify the temperature and salinity profiles to create a mesoscale eddy (Legg et al., 1998). We choose to use horizontally homogeneous initial temperature and salinity profiles, zero initial velocities (the mesoscale eddy is then generated by the localised forcing), and the forcing will be applied on a disc of radius R. We only apply a heat loss at the surface, as we have shown in chapter 2 that the buoyancy loss was dominated by the heat flux. We do not apply any wind stress. We use a linear equation of state as we are far from the freezing point (Garwood, 1991).

Chapman (1998) studied the effect of a decay region for the forcing on the horizontal scaling of the baroclinic eddies. He concluded that with an abrupt transition, this scale was internally constrained, and set by the Rossby radius, while with a decay region large enough, the scale of that region set the scales of the eddies. Hence we choose not to introduce a decay region.

Figure 4.3 summarises the configuration of the model used here. Table 4.1 gives the value of the parameters used in the model.

Horizontal Diffusivity κ_H	$2m^2/s$
Vertical Diffusivity κ_V	$10^{-3}m^2/s$
Horizontal Viscosity ν_H	$2m^2/s$
Vertical Viscosity ν_V	$10^{-3}m^2/s$
Reference density ρ_0	$1029kg/m^3$
Thermal Expansion Coefficient α	$2.4 \cdot 10^{-4}K^{-1}$
Haline Expansion Coefficient β	$7.6 \cdot 10^{-4}psu^{-1}$
Heat capacity c_p	$3900J/kg/K$
Coriolis parameter f	$10^{-4}s^{-1}$
Gravity constant g	$9.82m/s^2$

Table 4.1: Parameters used in the model.

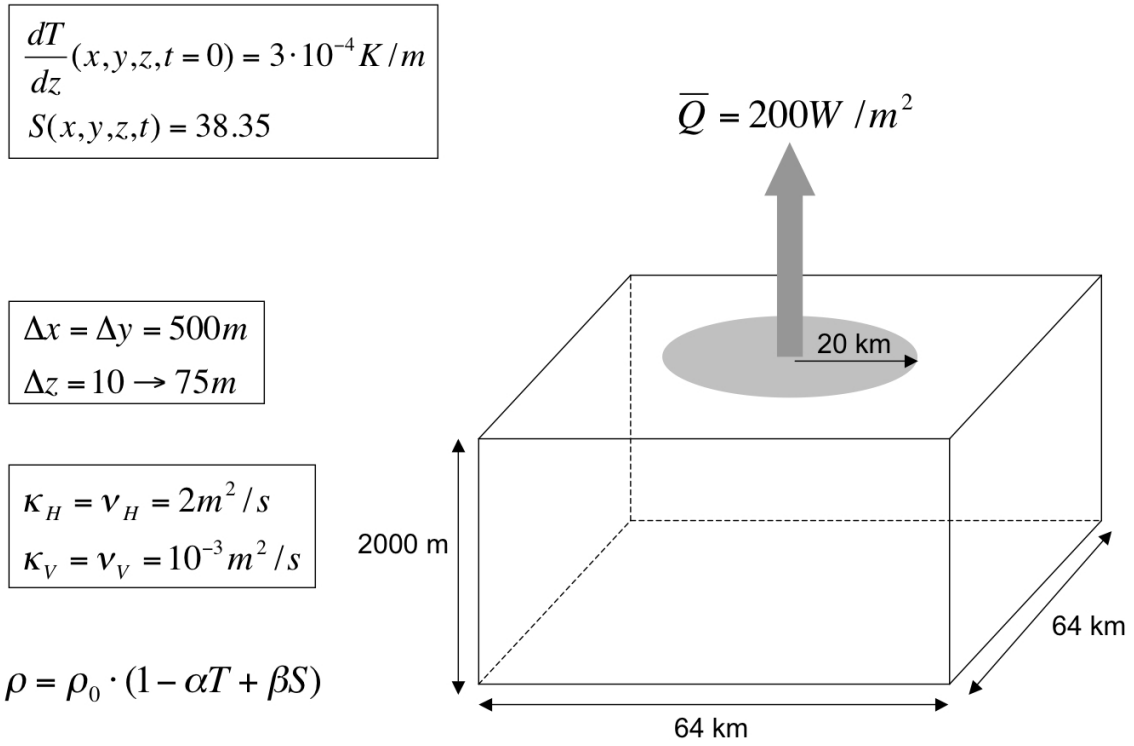

Figure 4.3: Summary of the model configuration for typical runs like the control run.

4.3 Results from the Control Run

4.3.1 Configuration

For the control run, we apply a constant cooling of $Q = 200W/m^2$ (surface buoyancy loss of $B_0 = 1.2 \cdot 10^{-7} m^2/s^3$) over a disc of radius $r = 20km$ on an ocean linearly stratified by a vertical temperature gradient (the salinity is kept homogeneous over the whole domain):

$$\frac{dT}{dz}(x, y, z, t = 0) = 3 \cdot 10^{-4} K/m \tag{4.1}$$

Hence the buoyancy frequency is $N = 7.87 \cdot 10^{-4} s^{-1}$ and $N/f = 7.87$. This is an aspect ratio as N can be related to a vertical scale and f to a horizontal scale. Typical baroclinic eddies scale as the Rossby radius of deformation $R_0 = Nh/f$ so an eddy of vertical scale of $1km$ will scale as $R_0 = 7.87km$ horizontally.

Another common non-dimensional number for deep convection is the natural Rossby number (Marshall and Schott, 1999a). It indicates the parameter regime for which convection is influenced by rotation (linked to plume dynamics):

$$R_0^* = (\frac{B_0}{f^3 h^2})^{1/2} = 0.5 \tag{4.2}$$

for a mixed layer depth $h = 700m$. Marshall and Schott (1999a) note that values between ~ 0.01 to 1 are relevant to oceanic deep convection.

4.3.2 Top View

Figure 4.4 shows the temperature and velocities after 4, 8, 12 and 16 days of cooling, for the top grid cell ($5m$ depth for the temperature and horizontal velocities and $10m$ depth for the vertical velocity). We see eddies forming at the edge of the patch, noticeable both by their horizontal and vertical velocity signatures. The eddies propagate towards and away from the centre of the patch. The centre of the patch is almost affected at day 16. Before that, the temperature at the centre remains homogeneous. This exchange between the surroundings and the centre of the patch is likely to have an effect on the final composition of the deep water formed. The interannual variability of the day-to-day variability of the forcing could then have an effect not only on the mixed layer depth, but also on the composition of the water formed even if the final mixed layer depth is the same.

As Marshall and Schott (1999a) review, the method of perturbation analysis carried out in a quasi-geostrophic framework leads to similar results as for the Eady problem for baroclinic instability (Eady, 1949) in the case of a patch large compared to the Rossby radius of deformation $R_0 = NH/f$, with H the depth of the ocean. In our simulation, $R_0 = 15.7km$. This is smaller although quite close to the radius R of our patch. Eady (1949) predicted that the scale of the disturbance is $l \sim Nh/f$ where h is the depth of the mixed patch - the mixed layer depth matters more than the actual depth. We perform the analysis at the beginning of the simulation, when the mixed layer depth does not reach below $700m$, so we expect this theory to still be valid in our case.

time (days)	**4**	**8**	**12**	**16**
h (m)	350	495	594	706
l (km)	2.7	3.9	4.7	5.6

Table 4.2: Scale of the disturbance l for the mixed patch of depth h calculated from Eady (1949).

Table 4.2 shows the scale of the disturbance, according to Eady (1949)'s theory, for each day shown on figure 4.4. We should notice here that the mixed layer depth increases with time, so the state of the disturbances at one particular time might be a response to the state of the rim current at another previous time. The scales roughly agree with figure 4.4 for days 12 and 16, when we can see eddies

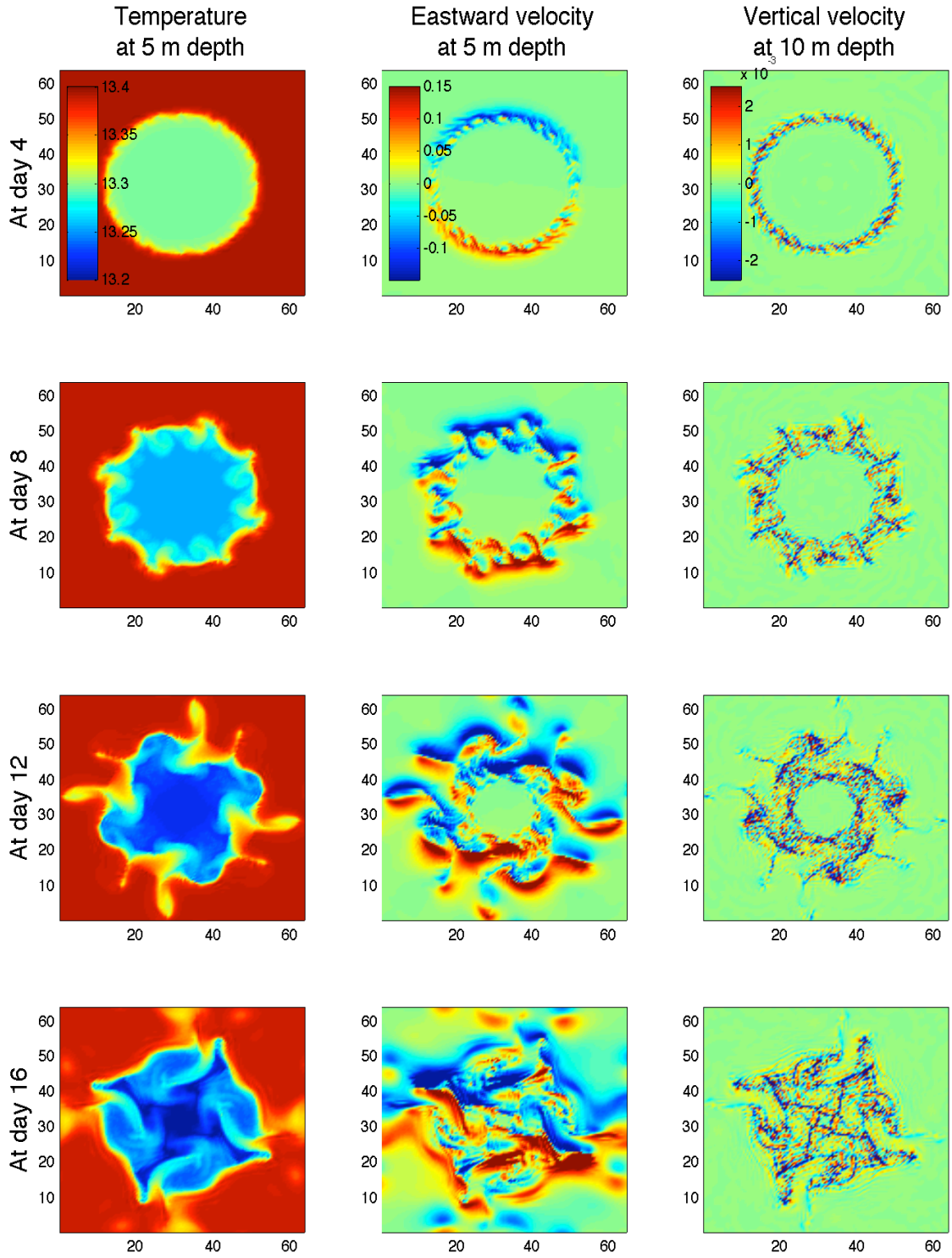

Figure 4.4: Temperature (°C), Eastward and Vertical velocities (m/s) at the grid point the closest to the surface.

pinching off. Before then, the disturbances are wave-like, with the eddies not clearly formed yet, so it is more difficult to estimate their scale precisely.

The growth rate of the fastest growing mode in the Eady problem is $\sigma_{max} = \frac{f}{N} \cdot u_z$. In a convection problem, we consider a rim current in thermal wind balance (which is not necessarily our case yet at the beginning of the simulation), hence $fu_z = -b_y$ where b is the buoyancy. We can write $b_y \sim \Delta b/l$, and the scale of the disturbances seems a reasonable choice to define the length scale used in the gradient calculation: $l = Nh/f$. We have $\Delta b \sim N^2 h$ (convection assuming a fully mixed layer and a non-perturbed ambient fluid) at the surface. This yields: $\sigma_{max} \sim f$, which corresponds to a few (~ 17) hours in our case. The rim current reaches its thermal wind balance on the same timescale, so the onset time of the instability is more likely related to the time it takes the lateral buoyancy gradient to be strong enough for the rim current to develop.

4.3.3 Mixed Layer Depth

To perform calculations of the mixed layer depth, we first select the profiles at the centre of the patch ($r \leq R/10$ where r is the distance from the centre of the patch and R the radius of the patch) and take the horizontal average of all these profiles as representative of what happens at the centre of the patch. We end up with one profile per time step: $\rho(t, z)$. We calculate the mixed layer depth using two different methods, giving complementary information.

The first method detects the shallowest density jump in the profile (we choose a threshold value of $\Delta\rho = 10^{-5} kg/m^3$). This method does not give much information about the mixed layer depth as soon as the patch shows restratification at the surface (capping), so we define another method to calculate the mixed layer depth that will give more information in these cases.

In the second method, the mixed layer depth is defined using the initial density profile by:

$$h(t) = \min\{z \in [0, 2000] : \frac{1}{z} \int_z^0 \rho(t, z) dz - \rho(1, z)\} \tag{4.3}$$

that is, for each depth level, we calculate the mean density of the water above and compare it with the density at that level at the initial time. The mixed layer depth will be the depth level at which the difference between these two values is minimum. This method relates more to the 'density content' of the mixed layer and is less sensitive to restratification than the previous one. It relies on the fact

that the density of the mixed layer, if fully mixed, is the same as the initial density at the mixed layer depth (because we suppose that there is no entrainment).

Figure 4.5 displays the results from the two calculations of the mixed layer depth for the control run. We see that indeed the second method is less sensitive to restratification than the traditional one (density jump). However, the density jump occasionally shows a deeper mixed layer than the other method. This is probably caused by a mixed layer which is not fully mixed, but with density variations within it smaller than the threshold value chosen for the density jump method.

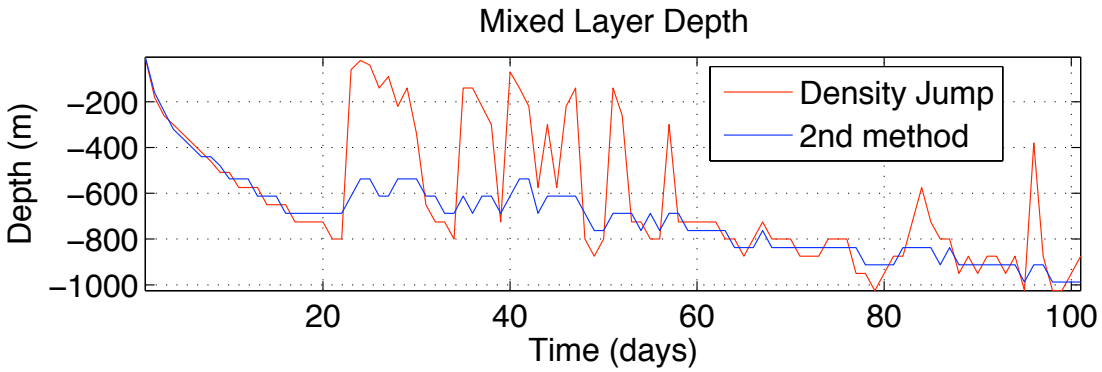

Figure 4.5: Mixed layer depths for the control run, calculated from the density jump method (red) and from the initial density profile comparison (blue).

The mixed layer depth evolves as expected. The deepening is first quadratic, as expected from one-dimensional prediction, until the lateral buoyancy fluxes offset the surface loss (Visbeck et al., 1996). The 1D prediction holds until day 17 or 18, which coincides with the time at which the baroclinic eddies reach the centre (figure 4.4).

4.3.4 Lateral Buoyancy Fluxes

We calculate for each simulation the lateral buoyancy fluxes out of a box of side $2R$, centered at the centre of the patch, with its sides parallel to the sides of the model's box and tangent to the patch. Figure 4.6 sketches the box. The lateral buoyancy fluxes are defined as:

$$latBF = -\frac{g}{\rho_0}(\sum \rho_i u_i S_i - \sum \rho_j u_j S_j + \sum \rho_k v_k S_k - \sum \rho_l v_l S_l) \tag{4.4}$$

where u and v are the eastward and northward velocities, and $S = dydz$ or $S = dxdz$ the area for each grid cell. See figure 4.8 for results concerning the control run (named r20q200). The convention used means that a positive lateral

buoyancy flux corresponds to an inflow of buoyancy and vice-versa.

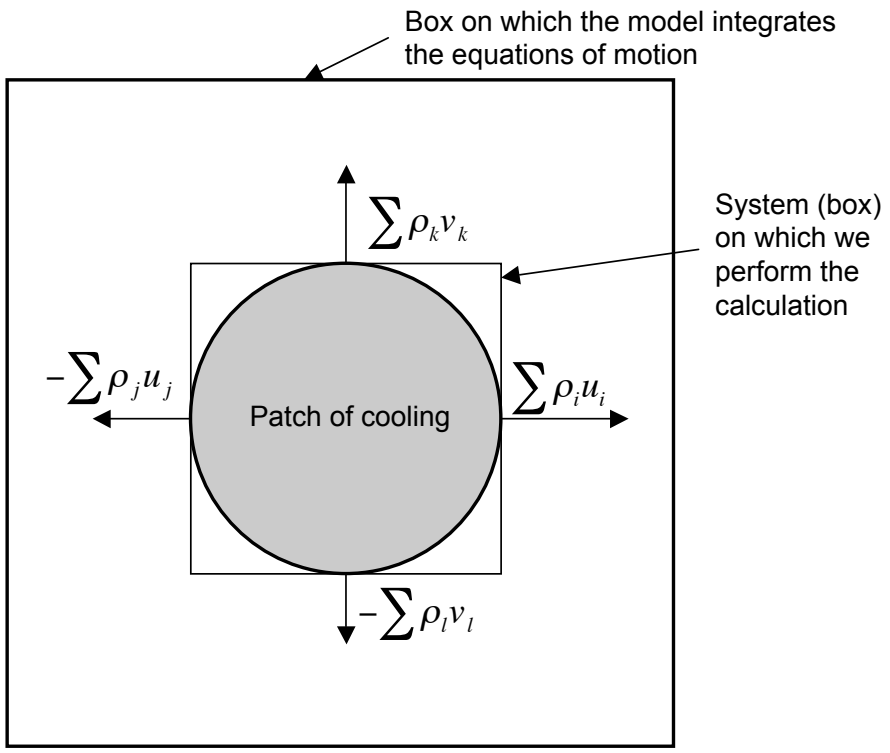

Figure 4.6: Sketch explaining how we calculate the lateral buoyancy fluxes. The i index refers to all the grid points on the right interface of the box. Indices j, k, l are similarly defined for the other vertical sides of the box.

We also, as a check, computed the buoyancy content of this box at each time step. We then analysed the buoyancy budget of the box. If BC is the buoyancy content, $latBF$ the lateral advective buoyancy fluxes and $surfBF$ the surface buoyancy fluxes, we should have, $\Delta BC = latBF - surfBF$. Figure 4.7 shows that this is indeed what we find. It shows the buoyancy budget of the patch and the box in terms of fluxes (top) and of buoyancy content/integrated buoyancy flux (bottom). The change in buoyancy content of the patch ($dBCpatch$) is very close to that of the box tangent to the patch (dBC). Figure 4.7 also confirms that we have $surfBF = \Delta BC - latBF$ so we can conclude that horizontal diffusion does not have a big effect on the buoyancy flux compared to advection, and can be neglected. Therefore, calculating the buoyancy content of the patch itself is a good way of estimating the lateral buoyancy fluxes out of the patch rather than outside a box whose sides are tangent to the patch. Comparison of the estimated fluxes out of the patch and the calculated fluxes out of a box tangent to the patch actually shows little difference, so we will be using the easiest/quickest of the two methods, i.e. the one using the box rather than the patch (faster computation).

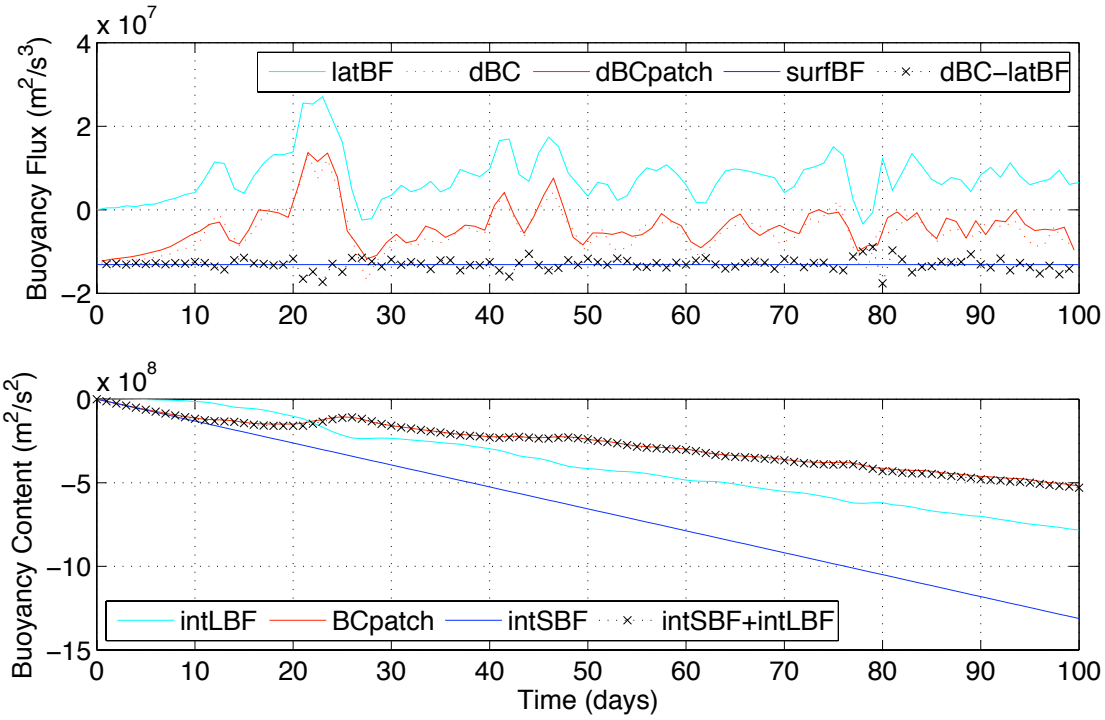

Figure 4.7: Buoyancy budget in term of fluxes (top) and of content/integrated fluxes (bottom). $latBF$ ($intLBF$ in integrated value) are the horizontal fluxes through the sides of the box tangent to the patch. dBC is the change in heat content of the box while $dBCpatch$ ($BCpatch$ in integrated value) is the change in buoyancy content of the box tangent to the patch. $surfBF$ ($intSBF$ in integrated value) is the surface buoyancy forcing.

The lateral buoyancy fluxes for the control run are plotted on figure 4.8 (r20q200 experiment). They increase almost exponentially at the beginning until they overshoot their 'equilibrium' value (particularly for the control run with periodic boundary conditions) and then drop abruptly. After 30 days, they seem to be in a steadier regime, being quite variable around a mean value. This overshooting is common to instability problems and is related to the time it takes for the instability to develop. In our case, the baroclinic instability is that of the rim current, so the lateral buoyancy gradient first needs to be established before the instability can start developing.

4.3.5 Time Evolution

As figure 4.5 shows, the model first deepens quadratically with time according to Turner's law (Turner, 1973) - we will call this the Turner regime. Then lateral buoyancy fluxes offset the surface ones and there is hardly any deepening - we will call this the post-Turner regime. This evolution is in agreement with previously published works (Marshall and Schott, 1999a; Visbeck et al., 1996)

4.3.6 Effect of the Boundary Conditions

We here compare relaxation boundary conditions and periodic ones at the sides of the box. Most of the runs presented in this chapter have periodic boundary conditions, although we will see that it was not the most appropriate choice. Figure 4.8 compares the control run with periodic boundary conditions (r20q200), with the same run with relaxation boundaries in which temperature and salinity have been prescribed at the sides to be the same as the initial ones (OBCSr20q200).

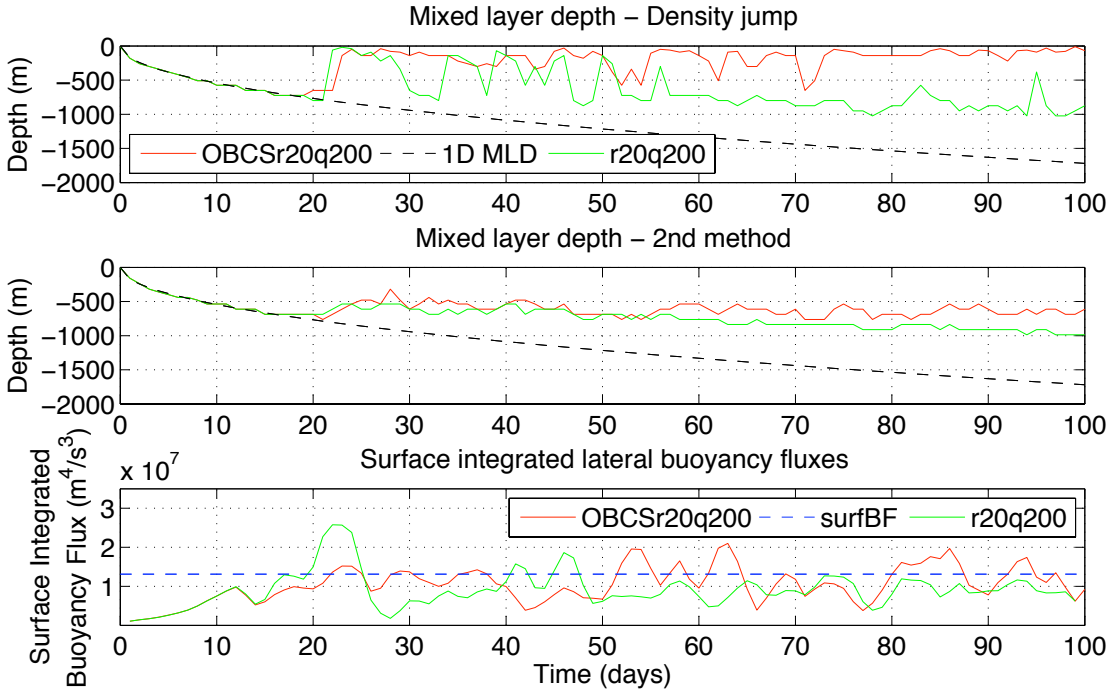

Figure 4.8: Test on boundary conditions. Comparison between two experiments: reference - $r = 20km$ and $f = 1 \cdot 10^{-4}s^{-1}$ (green), with relaxation boundary conditions having prescribed temperature and salinity (red). The two top panels shows mixed layer depths and the bottom panel shows the mean lateral buoyancy fluxes out of a box tangent to the patch. The black dotted line is the 1D prediction in the top panels, and the magnitude of the surface cooling in the bottom one.

The final mixed layer depth for the two experiments is comparable until about the 12th day, when the boundaries start being reached. After that, in the control run that has periodic boundary conditions, the deepening slowly continues because the buoyant water coming into the patch is a mix between convected and ambient waters instead of being only ambient water. We will have to keep this in mind when analysing the results. We also notice that the lateral buoyancy fluxes hardly show any overshooting in the run with relaxation boundary conditions and the reason for that is not clear, as we do not expect the boundary conditions to matter much that early in the simulation.

4.4 Experiments with different radii and cooling rates

4.4.1 Description of Experiments

	10km	**15km**	**20km**	**25km**	**30km**
100W/m^2			#100		
128W/m^2				#128	
200W/m^2	#10	#15	#20	#25	#30
300W/m^2			#300	#r25q300	
400W/m^2			#400	#r25q400	

Table 4.3: List of the experiments and of their names, for different radii of the disc of cooling and different surface heat losses.

Table 4.3 shows the series of experiments carried out to study the effect of the radius of the patch R and of the cooling rate Q. All other parameters have the same value as used in the control run. We will be looking at the mixed layer depths to make a quantitative comparison with Visbeck et al. (1996), who compared a theoretical law predicting the mixed layer depth with laboratory and numerical experiments. We will then look at the lateral buoyancy fluxes and their vertical structure for a more qualitative understanding. We first study the effect of the radius of the patch, then the effect of the cooling rate and eventually compare two (twin) experiments for which the total amount of buoyancy removed from the patch is the same, but with different cooling rates and radii.

4.4.2 Varying the radius

For this series of experiments, we keep a cooling rate of $Q = 200W/m^2$ with a disc of radii $R = 10, 15, 20, 25, 30km$. Figure 4.9 displays the mixed layer depth calculated with the density jump method. The middle panel contains the plot of the mixed layer calculated with the second method. We also plot the mixed layer depth reconstructed from the lateral buoyancy fluxes (dotted lines), which is calculated using the 1D (Turner's) formula in which we replace $\int surfBFdt$ by $\int(surfBF - latBF)dt$. We notice the very good agreement with the mixed layer depth calculated using the second method, due to the fact that they both related to the buoyancy content of the mixed layer. The bottom panel is a plot of the lateral buoyancy fluxes.

There are important discrepancies between the two calculations of the mixed layer depth, due to restratification effect, and the second method seems to be

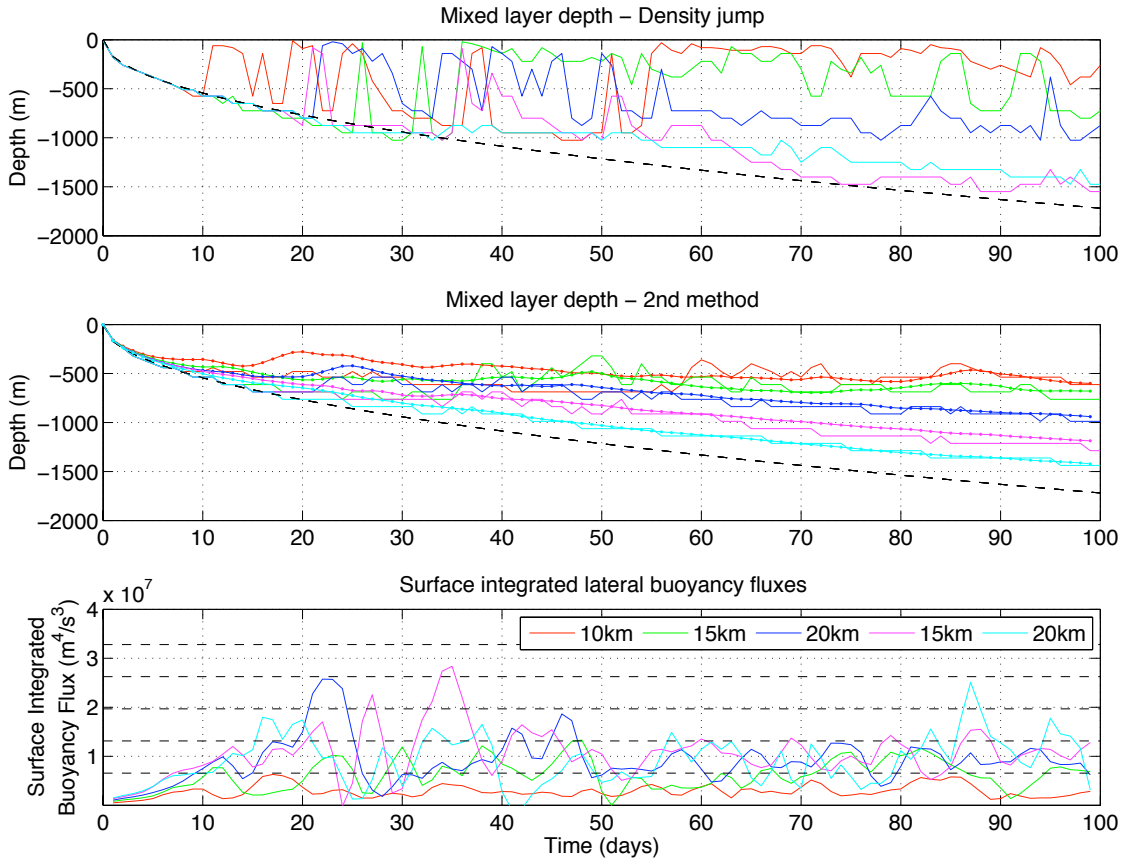

Figure 4.9: Results from 5 runs where $Q = 200W/m^2$ and with different radii $R = 10, 15, 20, 25, 30km$ for the disc of cooling. The two top panels show the mixed layer depths. The black dashed line shows the evolution of the mixed layer according to Turner's formula (Turner, 1973) and the other dotted lines on the 2^{nd} panel are the MLD reconstructed from the lateral buoyancy fluxes. The 3^{rd} panel shows the surface integrated lateral buoyancy fluxes out of a box tangent to the patch, calculated over the whole depth of the box.

more adapted to our purposes. The final mixed layer depth increases with the radius of the patch, which is satisfying - the mean buoyancy loss being the same in all experiments, the total buoyancy loss increases quadratically with the radius of the patch, while the perimeter around which the buoyancy gain occurs only increases linearly with the radius. As expected, the mixed layer depth follows the 1D model at first, until the lateral buoyancy fluxes become strong enough and offset the buoyancy loss to the atmosphere. It then stabilises around that value. For most runs, the deepening slows down when the lateral buoyancy fluxes reach a value close to that of the surface ones, but not for runs with $R = 25, 30km$. In these cases, the boundary conditions can be felt, and the deepening never stops, which correspond to lateral buoyancy fluxes never offsetting the surface buoyancy loss because the lateral exchanges do not bring in warm enough water. The final mixed layer depth and the time at which it is reached vary depending on the radius of the patch, and on the cooling. We will study these at the end of this

chapter.

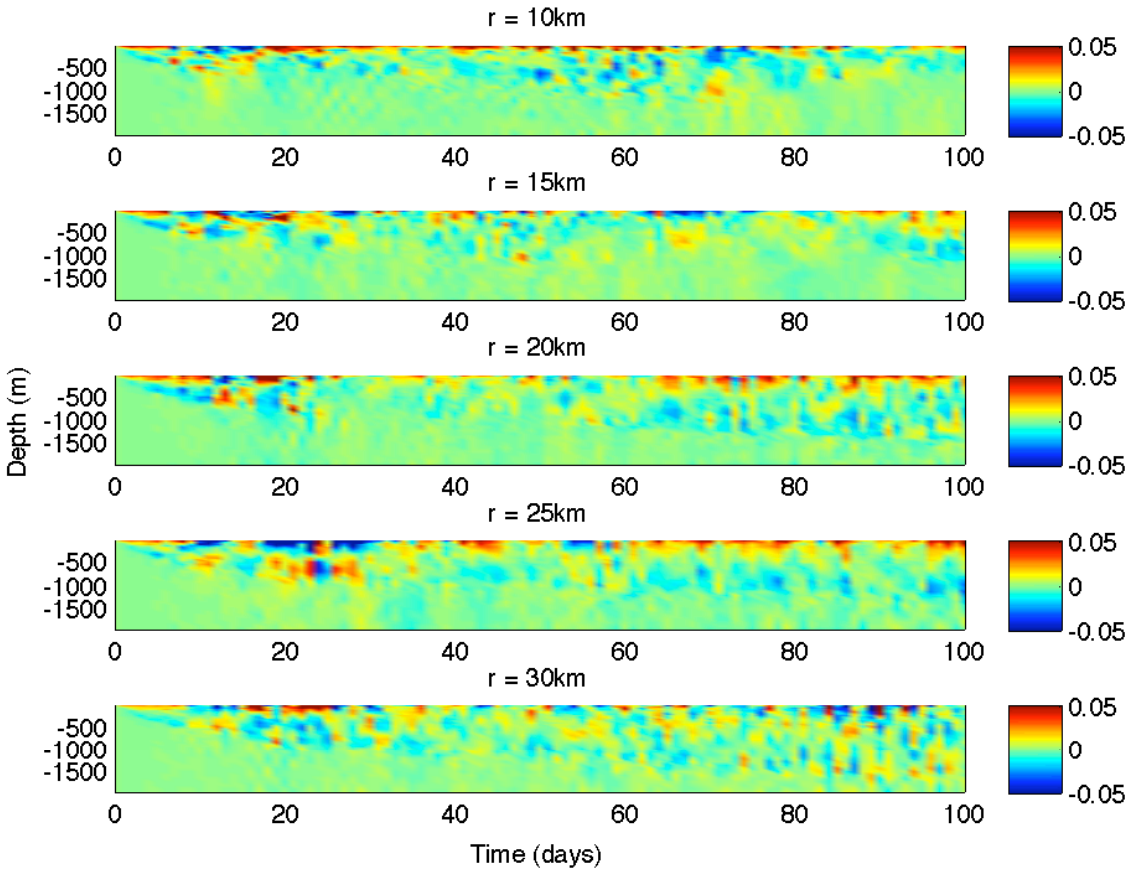

Figure 4.10: Lateral buoyancy fluxes, integrated around the patch, in m^4/s^3 (there is surface factor corresponding to Sxz or Syz) at the edge of the patch as a function of time and depth for different radii.

The vertical structure of the buoyancy fluxes (figure 4.10) shows that it varies along the mixed layer depth, but can be neglected below. At the edge of the patch, they do not vary linearly with depth as could be expected from baroclinic instability (through a response to the horizontal temperature gradient). Rather, there appear to be two regimes, sketched on figure 4.12. At the beginning of each simulation, we are in regime A, with an inflow in the top of the mixed layer and an outflow below.

We should remember here that we are looking at the total lateral buoyancy fluxes and not only at the eddy fluxes. The buoyancy fluxes are proportional to the term $\overline{uT}^\theta$, where $\overline{x}^\theta$ refers to the azimuthal average of x. We have: $\overline{uT}^\theta = \overline{u}^\theta \cdot \overline{T}^\theta + \overline{u'T'}^\theta$. Calculating these two terms, we find that $\overline{u}^\theta \cdot \overline{T}^\theta$ dominates and is two orders of magnitude larger than $\overline{u'T'}^\theta$. However, when we consider that $\overline{u(T - \overline{T}^{z,\theta})}^\theta = \overline{u}^\theta \cdot \overline{(T - \overline{T}^{z,\theta})}^\theta + \overline{u'(T - \overline{T}^{z,\theta})'}^\theta$, we find that the eddy term dominates, with vertical distributions shown in the next chapter. Note that the rela-

tionship between the two averages is: $\overline{u(T-\overline{T}^{z,\theta})}^{\theta} = \overline{uT}^{\theta} - \overline{u}^{\theta} \cdot \overline{T}^{z,\theta}$. We deduce from this that the signal whose vertical structure is shown on figure 4.10 is dominated by the $\overline{u}^{\theta} \cdot \overline{T}^{z,\theta}$, hence mainly reflect the radial velocity structure rather than the eddy one.

A stationary eddy will not result in any signature on the average signal. We can get a sense of this by considering an eddy azimuthal velocity $u_e(r_e)$ where r_e is the distance from the centre of the eddy. When we calculate the azimuthal average around the patch, we use the velocities of the eddy on the perimeter of the patch. For each radius, there are two points of intersection, each contributing in equal magnitude but with opposite sign to the average, hence the cancellation. See for example the cyclonic eddy at the edge of a convective patch on figure 4.11. A stationary eddy will have $U_e = 0m/s$. Now, if we consider a non stationary eddy, the velocities at the intersections will be $(u_e(r) + U_e) \cdot u_r$ and $(u_e(r) - U_e) \cdot u_r$ where u_r is the unit vector radial to the patch, and the symmetry is broken. A non stationary eddy contributes to the average velocity. Hence, the signal we are looking at, although it is an average, can be related to the motion of the eddies around the patch.

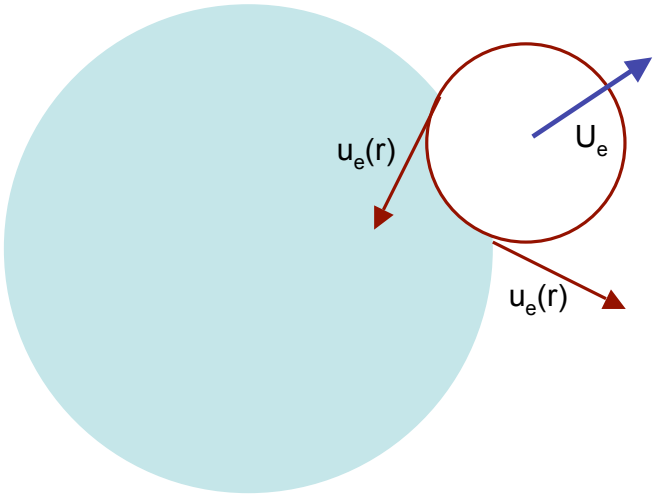

Figure 4.11: Sketch illustrating how an eddy can contribute to the average signal.

Water is initially coming in at the top and leaving near the base of the mixed layer, as sketched on figure 4.12. We call this regime 'regime A'. We can link the lateral transport in this regime to a net effect of baroclinic instability eddies. The instability is stronger near the surface because of a higher lateral buoyancy gradient. Mass conservation imposes that the water leaving the patch has to come back in it somewhere, and this compensation is occurring where the horizontal

temperature gradient is the weakest, i.e. in the lower part of the mixed layer. It also follows what we would expect from a simple adjustment under gravity, with dense water slumping at its neutral level. About 5 to 10 days, the patch is in a different regime (regime B) for which cold water leaves the patch near the top and warm water flows towards the patch near the bottom of the mixed layer. The patch then seems to oscillate between these two regimes. We associate regime B to the relaxation happening after the pinching off of baroclinic eddies: as the eddies carry cold water away, that water has to be replaced by ambient, warmer water. Note that each of the two regimes should result in a circulation around the patch, through the stretching term in the equation of conservation for potential vorticity. Regime A should be associated with a cyclonic (anticyclonic) circulation near the top (base) of the mixed layer, while regime B should be associated with an anticyclonic (cyclonic) circulation near the top (base) of the mixed layer, to account for the conservation of vorticity. In classical studies using idealistic models like ours, the initial quadratic deepening is associated with the rim circulation of regime A, as it is in our case. A more detailed study of the rim circulation is presented in the next chapter.

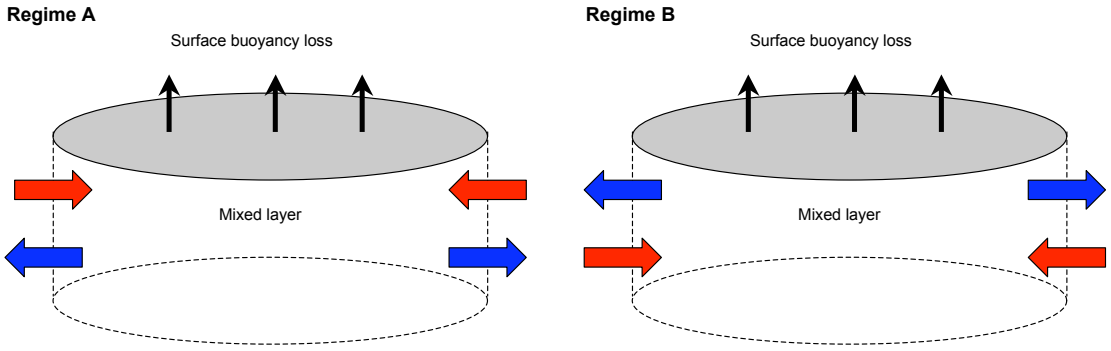

Figure 4.12: Sketch describing the two regimes of buoyancy exchange at the edge of the patch. The convention for colour of the arrows is the same as for figure 4.10.

We can also characterise the onset of instability - at the very beginning of each run, there is a buoyancy flux into the patch in the top half of the mixed layer, and away from it in the lower half of the mixed layer. This is suddenly reversed for a short period, which can be associated to the overshooting of the lateral buoyancy fluxes over their equilibrium value. Then, in most runs, the patch oscillates between the two regimes. We can associate this to the life cycle of an eddy. It first develops, stronger near the surface due to the enhanced horizontal density gradient. It is first a wave-like disturbance and then grows as a stationary eddy until it pinches off then is detached from the convective patch. The pinching off

leads to outward motion of water which is then replaced by an inward flow of ambient fluid as part of the relaxation process. The variability of the lateral buoyancy fluxes is much patchier for $R = 30km$. In that case, our simple explanation does not hold that well because the mixed layer is deeper and boundary effects cannot be neglected.

4.4.3 Varying the cooling rate

The radius is $R = 20km$ for all the experiments of this section, and the cooling rate takes the values $Q = 100, 200, 300, 400, 500W/m^2$. See figures 4.13 and 4.14.

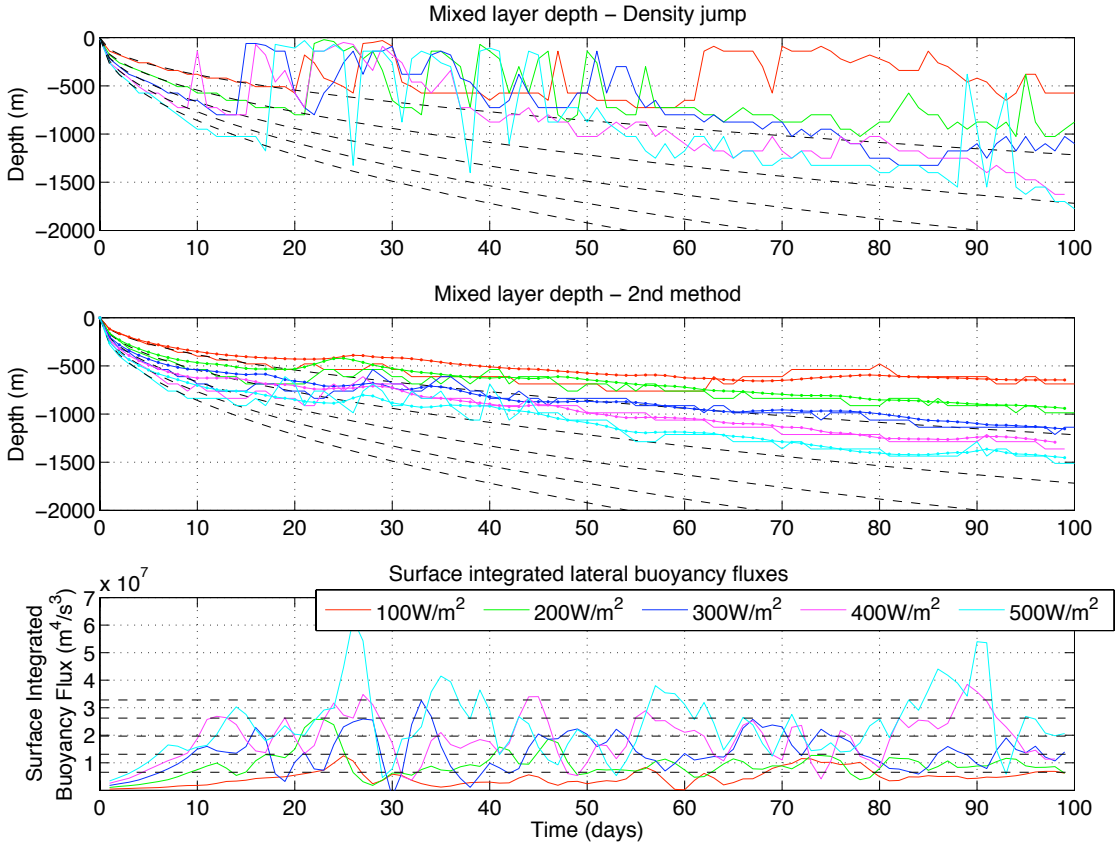

Figure 4.13: Results from 5 runs where $r = 20km$ and with different cooling rates $Q = 100, 200, 300, 400, 500W/m^2$. The two top panels show the mixed layer depths. The black dotted lines show the evolution of the mixed layer according to Turner's formula (Turner, 1973). The bottom panel show the mean (i.e. surface averaged) lateral buoyancy fluxes out of a box tangent to the patch, with the black dashed lines corresponding to the surface forcing.

The results from these experiments are qualitatively similar to the ones in the previous section. The final mixed layer depth and the mean lateral buoyancy loss increase with the rate of cooling, as does the total buoyancy loss over the patch.

The vertical structure of the lateral buoyancy fluxes shows that these are positive near the surface, even for deep mixed layers, which makes sense if we con-

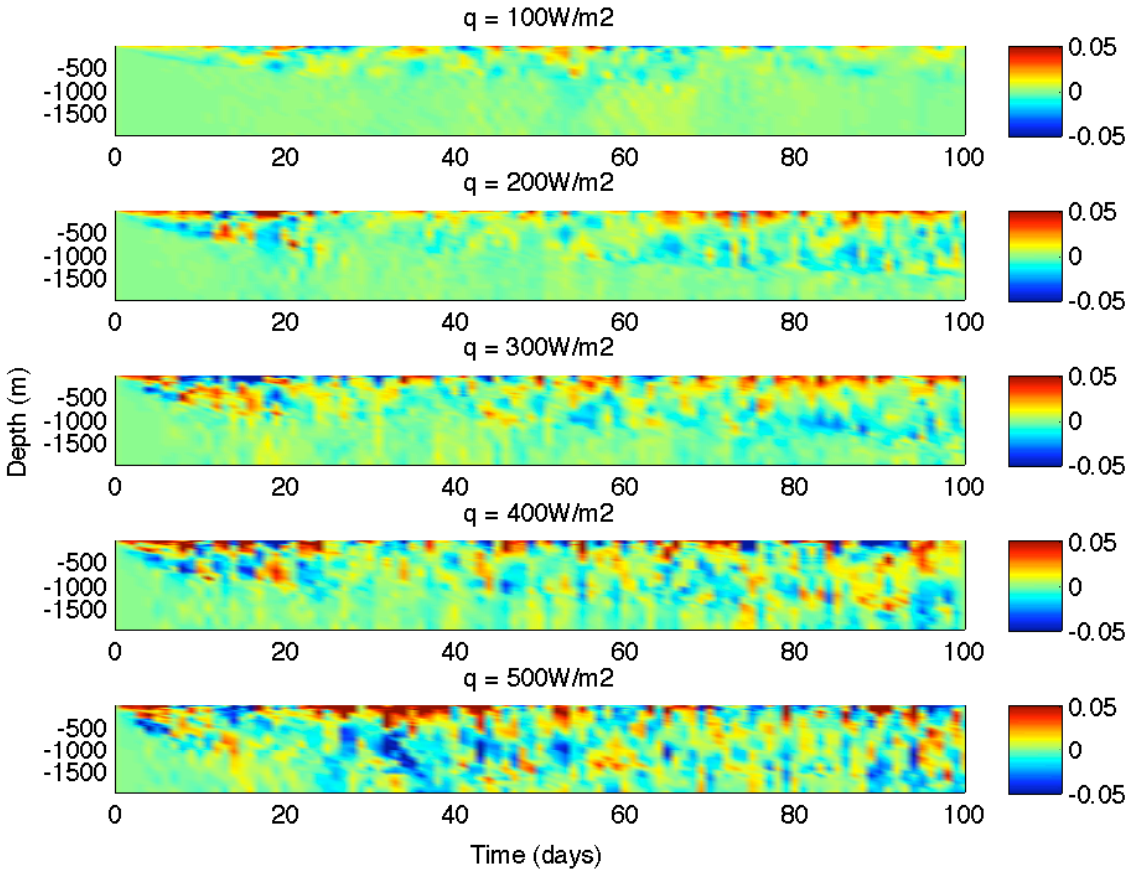

Figure 4.14: Lateral buoyancy fluxes in m^4/s^3 (there is surface factor) at the edge of the patch as a function of time and depth for different surface heat losses.

sider the baroclinic instability of a rim current strongest near the surface.

4.4.4 Twin Experiments

This section focuses on results from two experiments with the same total (surface integrated) heat loss over the patch: $(r, Q) = (25km, 128W/m^2)$ and $(r, Q) = (20km, 200W/m^2)$. We want to know if what is actually important is the cooling rate itself or the total amount of buoyancy lost by the patch. See figures 4.15 and 4.16.

The mixed layer depth varies similarly for these two experiments, which implies that the mixed layer depth is a function of $B_0 \cdot r^2$. However, the time at which this final depth is reached is not the same. Also, the overshooting of the lateral buoyancy fluxes is more important in the case $(r, Q) = (20km, 200W/m^2)$. The vertical structure of the buoyancy fluxes shows more activity in that latter case, because of a stronger surface forcing.

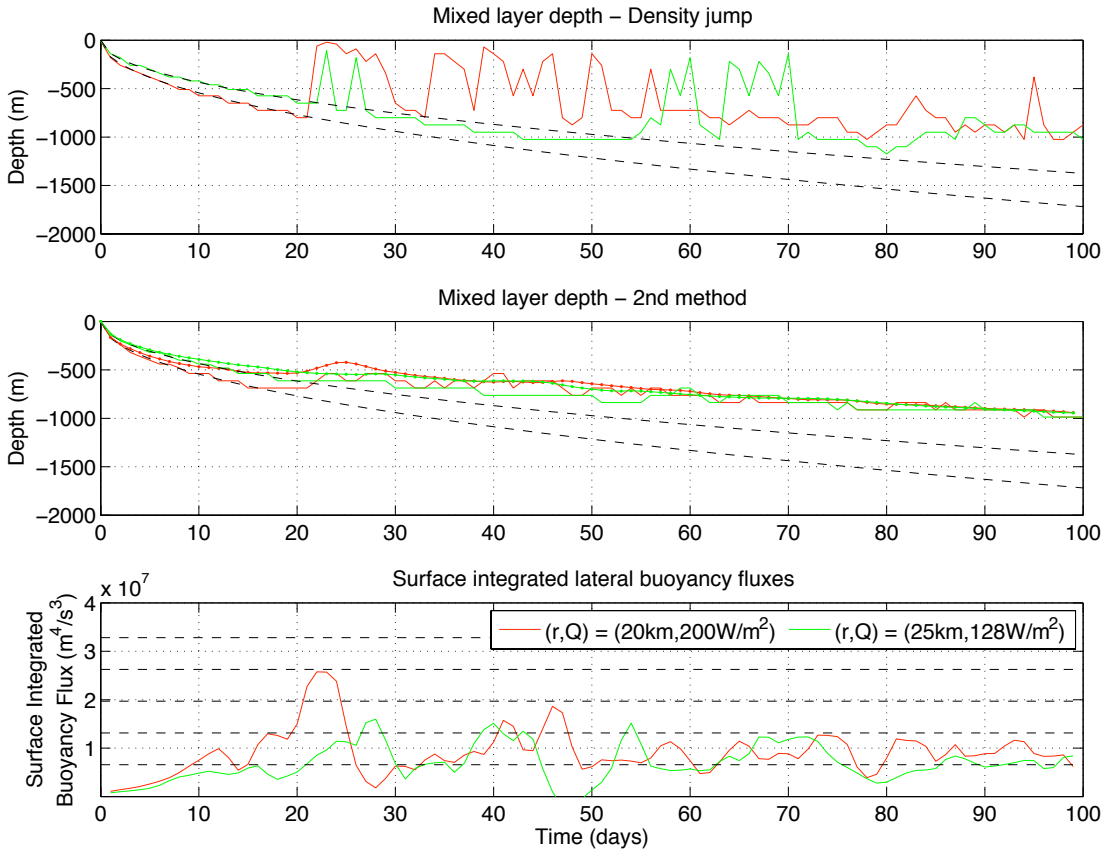

Figure 4.15: Results from 2 runs where the integrated surface buoyancy forcing stays the same: $(r, Q) = (20, 200)$ and $(r, Q) = (25, 128)$. The two top panels show the mixed layer depths. The black dotted lines show the evolution of the mixed layer according to Turner's formula (Turner, 1973). The bottom panel show the mean (i.e. surface averaged) lateral buoyancy fluxes out of a box tangent to the patch.

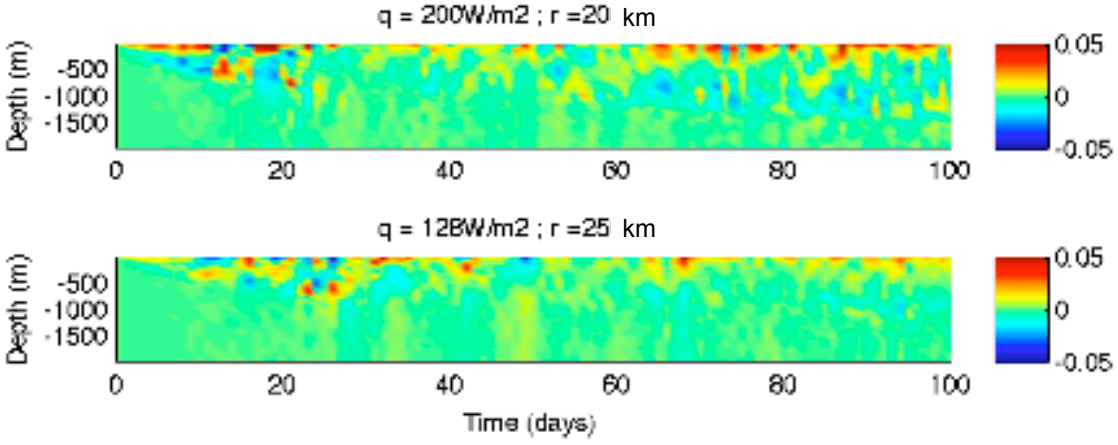

Figure 4.16: Surface integrated lateral buoyancy fluxes in m^4/s^3 at the edge of the patch as a function of time and depth for different surface heat losses.

4.4.5 Comparison with Visbeck et al. (1996)

Theory

Visbeck et al. (1996) considered a patch of radius R undergoing a constant buoy-

ancy loss B_0. They calculate the final mixed layer depth h_f and the time at which it is reached t_f using the fact that, at these depth and time, the lateral buoyancy fluxes out of the patch $\overline{v'b'}$ are equal to the buoyancy loss at the surface:

$$\int\int B_0 dA = \int_h^0 \overline{v'b'} dl dz \tag{4.5}$$

They parameterise the lateral buoyancy flux term as:

$$\overline{v'b'} \propto \frac{\overline{b'^2}}{N} \tag{4.6}$$

This parameterisation relies on the fact that the radial velocity of eddies generated by the baroclinic instability of the rim current is proportional to the azimuthal velocity of the rim current, linked to the lateral buoyancy gradient through thermal wind balance. It yields:

$$h_f = \gamma \frac{(B_0 R)^{1/3}}{N} \tag{4.7}$$

$$t_f = \beta (\frac{R^2}{B_0})^{1/3} \tag{4.8}$$

with $\gamma = 3.9 \pm 0.9$ and $\beta = 12 \pm 3$, determined empirically from numerical and laboratory experiments. Their results agree quite well (see figure 4.17) with previous laboratory and numerical experiments. Although, due to the way $\overline{v'b'}$ is parameterised, the final mixed layer depth does not depend on the Coriolis force, which is counter-intuitive.

We will here show that their theoretical result depends critically on the length scale chosen as representative of the baroclinic zone. First, we can assume that $\overline{v'b'} \propto \overline{ub'}$ where u is the velocity of the rim current, because the eddies are generated by the instability of the rim current. Second, the rim current is in thermal wind balance, hence: $fu_z = -b_y$ and $f\overline{u} = -h\frac{b'}{l_{bz}}$ where l_{bz} is the width of the baroclinic zone. Assuming a fully mixed layer within the part of the patch which is far enough from the edge ($N^2(r < R - l_{bz}/2, t) = 0 s^{-2}$) and a non-affected stratification for the fluid outside of the patch ($N^2(r > R + l_{bz}/2, t) = N^2(r, t = 0) s^{-2}$), we can write $b' = N^2 h$. This leads to:

$$\overline{v'b'} \propto \frac{h}{f} \frac{\overline{b'^2}}{l_{bz}} \propto \frac{h^3 N^4}{f l_{bz}} \tag{4.9}$$

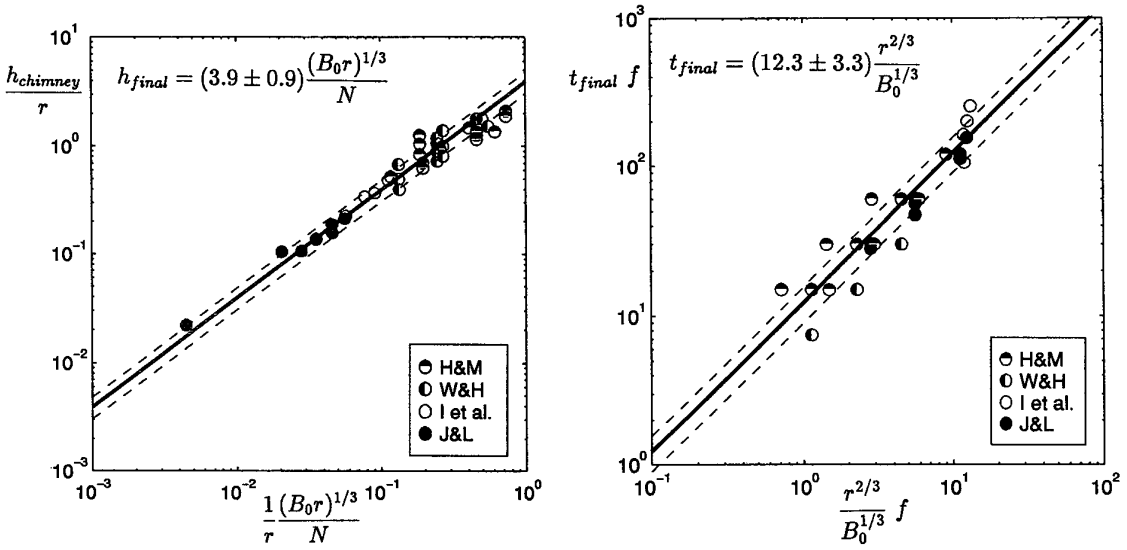

Figure 4.17: Final mixed layer depth and time at which it is reached in numerical (performed by Hufford and Marshall - H&M - and Jones and Lascaratos - J&L) and laboratory (performed by Hufford and Whitehead - W&H and Ivey et al. (1995) - I et al.) experiments. From Visbeck et al. (1996).

Eddies are generated on a scale $R_0 = \frac{Nh}{f}$. If we choose $l_{bz} = R_0$, we find Visbeck et al. (1996)'s result. Figure 4.4 showed that the deepening stops when the baroclinic eddies have reached the centre of the patch. At that time, we can choose $l_{bz} = R$ with R the radius of the patch. This yields:

$$\overline{v'b'} \propto \frac{N^4 h^3}{Rf} \tag{4.10}$$

The final mixed layer depth is then given by:

$$h_f \propto \frac{(B_0 R^2 f)^{1/4}}{N} \tag{4.11}$$

and the time at which the final mixed layer depth is reached is:

$$t_f \propto \frac{N^2 h_f^2}{B_0} \propto \frac{R f^{1/2}}{B_o^{1/2}} \tag{4.12}$$

In this formulation, h_f has a dependance on $B_0 R$, in agreement with what we observed in our twin experiments. Both t_f and h_f depend on f, although weakly in the case of h_f. The dependancy on the other terms is not very different. We already mentioned that Chapman (1998), introducing a decay region for the buoyancy forcing around the patch, found that the scale of that decay region could set l_{bz}. Chapman and Gawarkiewicz (1997) studied a coastal polynya sketched on figure 4.18. They found scalings corresponding to $l_{bz} = \sqrt{Wb}$. Similarly, we could

think of a baroclinic zone that would scale as the geometric mean between the radius of the patch and the Rossby radius of deformation: $l_{bz} = \sqrt{RR_0} = \sqrt{\frac{RNH}{f}}$. This leads to: $h_f \propto \frac{(B_0^2 R^3 f)^{1/7}}{N}$ and $t_f \propto \frac{R^{6/7} f^{2/7}}{B_0^{3/7}}$.

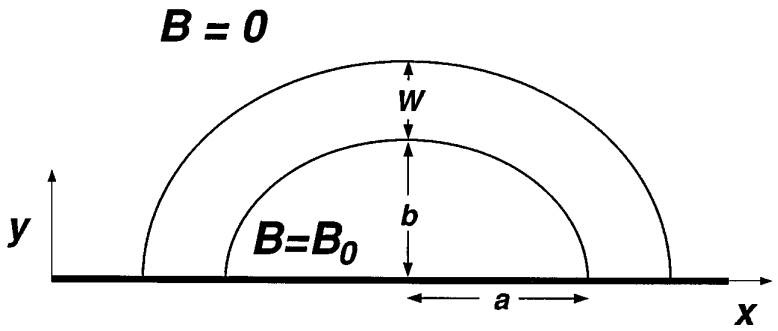

Figure 4.18: Sketch of the polynya studied by Chapman and Gawarkiewicz (1997).

Results

For each experiment, we calculate t_f as the time at which the actual mixed layer depth reached equilibrium, which we define as the time at which the mixed layer depth differs from the 1D prediction by more than $\epsilon = 100m$. The final mixed layer depth h_f is then calculated as the mean depth between $t = t_f$ and $t = 80days$.

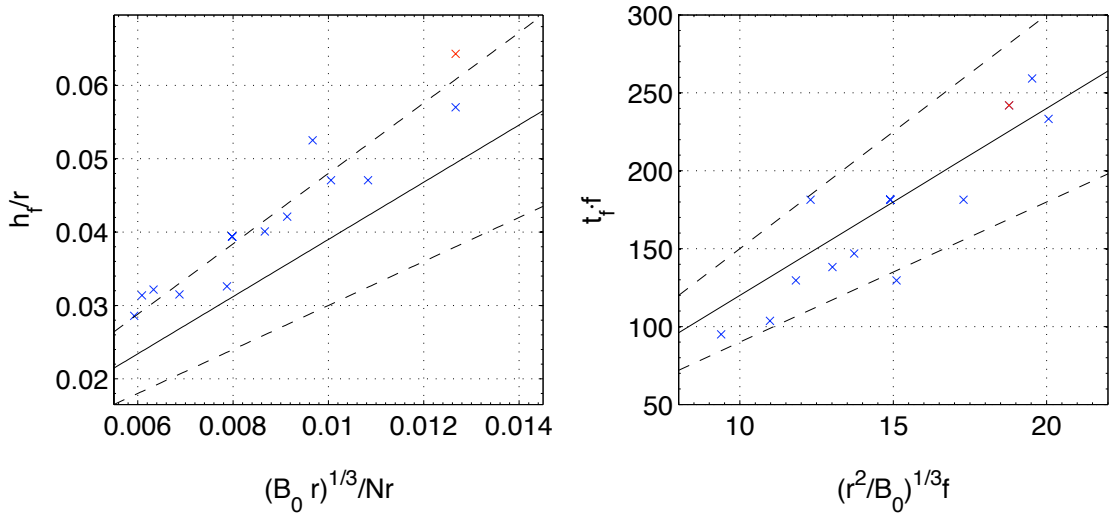

Figure 4.19: Final non dimensional depths h_f/R and times $t_f f$ it takes to reach the final depth in our numerical simulations (blue) and predictions from Visbeck et al. (1996) (in plain black line for their mean prediction, and dashed black lines for the mean prediction plus or minus a standard deviation) . In blue are the experiments with $f = 10^{-4}s^{-1}$ and in red with $f = 2 \cdot 10^{-4}s^{-1}$.

Figure 4.19 shows the agreement between our results and Visbeck et al. (1996)'s predictions in terms of non dimensional final mixed layer depth h_f/R and time

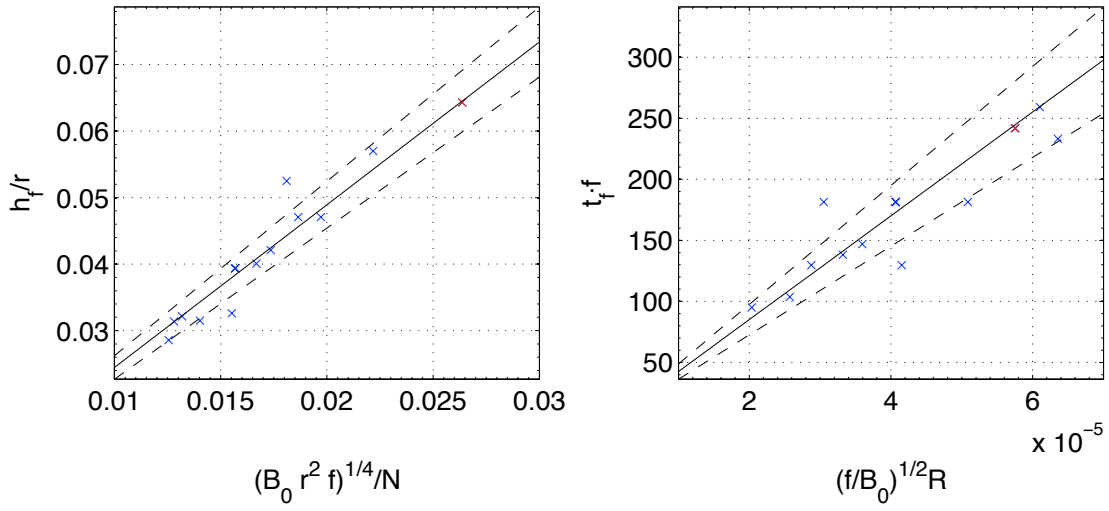

Figure 4.20: Final depths and times it takes to reach the final depth in our numerical simulations (blue) and predictions from the theory modified from Visbeck et al. (1996) in which the width of the baroclinic zone is taken as being the radius of the patch (black). In blue are the experiments with $f = 10^{-4}s^{-1}$ and in red with $f = 2 \cdot 10^{-4}s^{-1}$.

at which it is reached $t_f f$. Note that the data presented here are on a normal scale while figure 4.17 uses a logarithmic one, because we have a much smaller range of values than they do. We notice that the agreement with their theory is very good. We also present results from an experiment with a smaller radius patch of $r = 10km$, a surface forcing of $Q = 200W/m^2$ and a higher Coriolis force of $f = 2 \cdot 10^{-4}s^{-1}$. The final mixed layer depth in that case is very close to that of the control run. This contradicts the idea of a final mixed layer depth independent of the Coriolis force, because a change in the radius of the patch would have led to a change in the final mixed layer depth if the Coriolis force had no impact. Although, the data from this simulation fit with Visbeck et al. (1996)'s theory, according to which the final mixed layer depth does not depend on the Coriolis force. Rather, it hints to a dependance of the final mixed layer depth on $f \cdot r$, i.e. on the ratio between the radius of the patch and a Rossby radius. This contradicts both theories, but we cannot conclude as we only have one experiment. Moreover, the boundary conditions can have different effects in each case as the radius of the patch is different.

Figure 4.20 displays the agreement between the theory taking the radius R as the width of the baroclinic zone: $h_f = \gamma' \frac{(B_0 r^2 f)^{1/4}}{N}$ and $t_f = \beta' R(\frac{f}{B_0})^{1/2}$. We calculate γ' and β' defined as the mean constant of proportionality with errorbars given by the standard deviation, following Visbeck et al. (1996)'s method. We find $\gamma' = 2.45 \pm 0.18$ and $\beta' = 4.25 \cdot 10^6 \pm 6.22 \cdot 10^5$. The theory fits quite well with the final mixed layer depth predictions, but it does not perform very well for t_f.

	10km	**15km**	**20km**	**25km**	**30km**
100W/m^2			15.44 (8.12)		
128W/m^2				18.72 (9.84)	
200W/m^2	18.68 (7.86)	28.89 (12.14)	30.44 (14.27)	28.55 (12.13)	19.71 (10.16)
300W/m^2			45.31 (21.00)	55.82 (17.27)	
400W/m^2			60.98 (24.68)	54.05 (31.62)	
500W/m^2			77.57 (35.24)		

Table 4.4: Mean lateral buoyancy fluxes in the post-Turner regime in $10^{-3}m^2/s^3$ and their standard deviation in brackets.

Table 4.4 shows the mean and standard deviation (in time) of the surface averaged lateral buoyancy fluxes ($Sav(latBF)$) in the post-Turner regime (corresponding to the term $\overline{v'b'}$). We notice that the standard deviation around this mean are relatively important compared to the mean itself. They are calculated so that we have $Sav(latBF) \sim \frac{h}{H}\overline{v'b'}$ where H is the total depth in the model, due to the fact that $Sav(latBF)$ is dominated by the eddy term (this is shown in more detail in the next chapter).

For experiments with the same radius, $\overline{v'b'}$ varies linearly with B_0. A linear fit yields: $\frac{h}{H}\overline{v'b'} = 2.6 \cdot 10^5 B_0 - 5 \cdot 10^{-4} m^2 s^{-3}$ for patches of radius $r = 20km$, with a residual of $1.1 \cdot 10^{-3} m^2 s^{-3}$, so the fit is very good. From the theory, the deepening is arrested when $\overline{v'b'} = \frac{B_0 R}{2h}$ hence $\overline{v'b'} \propto B_0 R$. This good agreement validates the assumption that the lateral buoyancy fluxes arrest the deepening.

For a constant in time B_0, table 4.4 shows that the surface averaged lateral buoyancy flux varies like a parabola as the radius increases, with a maximum at $r = 20km$, while we expect a linear variation according to the theory. We suspect that it is because the theory does not hold when the patch is too small compared to the Rossby radius or when it is too big compared to the size of the box (effect of the boundaries) over which we integrate the model. An example of a patch too small has been realised in the laboratory and is shown in appendix D. If the patch is on a horizontal scale close to that of the Rossby radius of deformation, the patch has a position that varies significantly around the forcing region.

4.5 Conclusion

We have presented here the model and the configuration that will be used for the experiments with time-varying forcing, as well as some of the key variables (mixed layer depth and lateral buoyancy fluxes) we will calculate. The hydrostatic equations are integrated with the MIT model in an eddy-resolving but not plume resolving configuration. Convection is parameterised using a convective adjustment scheme. The model is initialised with a linear stratification caused by temperature variations while the salinity is kept homogeneous. The diffusivities and viscosities are chosen so as to allow convection and baroclinic eddies at the edge of the convective patch.

We validated the control run, and showed it presented the two expected phases. First the convective layer deepens quadratically with time (as with a 1D model). Then the mixed layer depth remains constant as the surface buoyancy loss is offset by the lateral buoyancy fluxes.

Finally, we presented results from simulations in which some of the parameters were changed: the rate of buoyancy loss and the radius of the patch. Our results agree quite well with previously published work, although there are elements the theory does not account for. First, the theory of Visbeck et al. (1996) leads to an expression for the mixed layer depth that does not depend on the Coriolis force. A comparison between different simulations seems to show that the mixed layer depth depends on the product of the radius of the patch and the Coriolis force, that is on the ratio between the radius of the patch and some Rossby radius to be defined. The second point is that, as shown in our twin experiments, a critical element in setting the final mixed layer depth is the total amount of buoyancy removed from the fluid at the surface, that is a term in $B_0 r^2$, rather than the $B_0 r$ of Visbeck et al. (1996). We developed a theory based on the same method as Visbeck et al. (1996), but with the width of the baroclinic zone chosen to be the radius of the patch R rather than the Rossby radius of deformation R_0. This theory leads to a dependance of the mixed layer depth on $f^{1/4}$ and on $(B_0 R^2)^{1/4}$.

Chapter 5

Effect of time varying forcing on deep convection: a modeling study

5.1 Introduction

The comparison of different winters suggested that the short- term (on a time scale of a few days) time variability of the buoyancy loss had an effect on the final depth of convection. Hong et al. (2007) simulated winters 1998-99 and 1999-2000 in the Mediterranean and arrived at the conclusion that time variability on such timescales causes ”large differences in the preconditioning and the mixing stage of convection”. Our study focuses on the mixing stage only.

This is not only a theoretical problem but is highly relevant to convection in the oceans for two reasons. First, we have seen that the heat fluxes in the Mediterranean are highly variable on a timescale of a few days due to outbursts of the Mistral wind. Second, the control run experiment emphasised that baroclinic instability has an onset time of a few days. We already know that baroclinic instability is important after the convective deepening (Jones and Marshall, 1993; Visbeck et al., 1996; Legg et al., 1996; Marshall et al., 2002), but its effect during the deepening is not well known. We have seen in the previous chapter that if the forcing is kept constant, the lateral buoyancy fluxes will offset the surface fluxes after a few days - the duration of the initial transient state depends on the strength of the forcing, the radius of the patch and the initial stratification. If we now consider a time varying forcing on similar timescales, the system might never reach a steady state - this also allows us to test the efficiency of the restratification processes. Previous studies of restratification focused on the time it takes to restratify completely the convective patch, from a fully mixed state to a strat-

ified one. Here, we look at the transition between convective patches of varying depths and residual stratifications. When the surface heat loss is high, we expect the residual stratification to decrease and the depth to increase. When it is low, we expect a slight decrease of the depth and an increase of the residual stratification. How do the magnitudes of the variations of the mixed layer stratification and depth compare depending on the forcing? Does baroclinic instability have time to significantly restratify during the fraction of the period when the heat loss is low?

We will first describe the experiments whose study is the object of this chapter. Then we will the show primary results. We will see that those results bring up new questions that we will try to answer in the following discussion section.

5.2 Description of the experiments

5.2.1 Description

We perform experiments with a time periodic surface cooling, the periods being of 4, 10 and 20 days. Each experiment has exactly the same parameters as in the control run, apart from the surface heat forcing. The forcing is based on an idealised forcing described by figure 5.1 and table 5.1.

$$Q = \begin{cases} Q_{high} & \forall t : nT \leq t < nT + T_{high} \\ Q_{low} & \forall t : nT + T_{high} \leq t < (n+1)T \end{cases}$$

T_{high} refers to the part of the period for which the heat loss is high, noted Q_{high}. Similarly T_{low} refers to the part of the period for which the heat loss is low, noted Q_{low} The periods and amplitudes are chosen to cover the range of periods and amplitudes observed in the Mediterranean. We define the forcing at four regularly spaced (in time) points per period, and there is a linear interpolation between these points, as illustrated on figure 5.1. The red dots represent the four points used in the interpolation and the red line is the actual forcing used. The mean cooling over a period is always $\overline{Q} = 200W/m^2$, as in the control run. As a comparison, we have run a simulation with sharp changes in the forcing (T10q800sharp), whose results will also been shown.

We performed two series of nine experiments - the first one with periodic boundary conditions (BC) on the sides and the second one with open boundary conditions, as we did for the control run. Results were qualitatively similar. We

will be showing results from the open BC runs in most cases, except when stated otherwise.

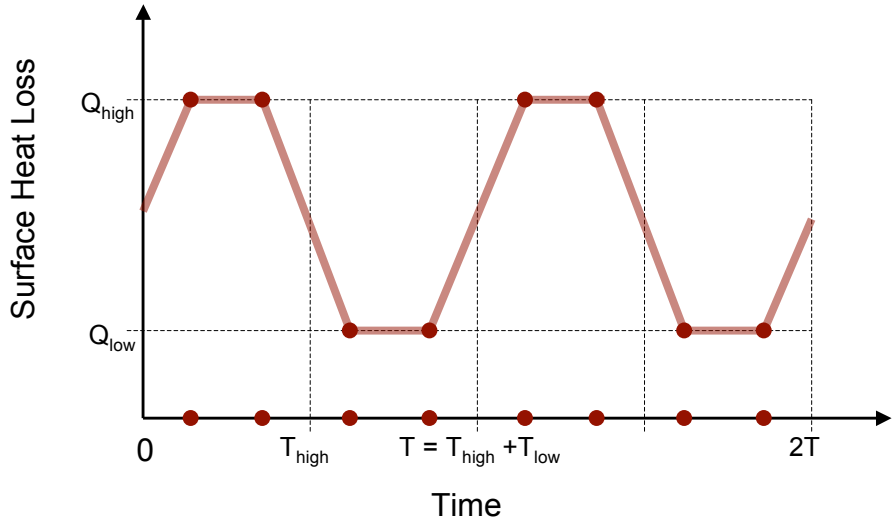

Figure 5.1: Schematic defining the parameters used to form the surface heat flux.

$(\mathbf{Q_{high}}, \mathbf{Q_{low}})(W/m^2)$ $(\mathbf{T_{high}}, \mathbf{T_{low}})$	$(\mathbf{400, 0})$ $(\mathbf{T/2, T/2})$	$(\mathbf{500, 100})$ $(\mathbf{T/4, 3T/4})$	$(\mathbf{800, 0})$ $(\mathbf{T/4, 3T/4})$
$\mathbf{T = 4days}$	T4q400	T4q500	T4q800
$\mathbf{T = 10days}$	T10q400	T10q500	T10q800
$\mathbf{T = 20days}$	T20q400	T20q500	T20q800

Table 5.1: Name and description of the experiments performed and compared in this section.

Keeping the same mean cooling rate for all experiments, it can be shown that:

$$(T_{low} + T_{high})\overline{Q} = T_{high}Q_{high} + T_{low}Q_{low} \tag{5.1}$$

We also have $T = T_{low} + T_{high}$, hence each experiment can be characterised by the choice of three parameters among these (i.e. we considered a fixed $\overline{Q}$). If we use T, $\alpha_T = \frac{T_{high}}{T}$ and $\alpha_Q = \frac{Q_{high}}{\overline{Q}}$ as these three parameters, we can write:

$$T_{high} = \alpha_T T \tag{5.2}$$

$$T_{low} = (1 - \alpha_T)T \tag{5.3}$$

$$Q_{high} = \alpha_Q \overline{Q} \tag{5.4}$$

$$Q_{low} = \frac{1 - \alpha_T \alpha_Q}{1 - \alpha_T}\overline{Q} \tag{5.5}$$

5.2.2 Discussion

We here investigate a few theoretical arguments. First, the value of the ratio $\phi = \frac{T_{high}}{t_f(Q_{high})}$ where $t_f(Q_{high})$ is time at which the final mixed layer depth is reached for a run with constant surface forcing $Q = Q_{high}$ is expected to be of critical importance. If $\phi > 1$, the final mixed layer depth reached at $t = T_{high}$ will be $h_f(Q_{high})$. Values of t_f for the different cooling rates used in our experiments are in table 5.2.

$\mathbf{Q(W/m^2)}$	100	200	400	500	800
$\mathbf{t_f(days)}$	28	21	15	12	9.5 (est)

Table 5.2: t_f for different cooling rates as calculated from numerical experiment (see previous chapter). For $Q = 800W/m^2$, it is an estimated value extrapolated using a dependance to the power of $-1/2$ on the cooling rate.

We notice that in all the experiments, we have $T_{high} < t_f$. The ratio ϕ is then a measure of how close we are to reaching the final mixed layer dept at $t = T_{high}$. The values are displayed in table 5.3.

$\mathbf{Q_{high}}(W/m^2)$	400	500	800
$\mathbf{T = 4days}$	0.13	0.083	0.11
$\mathbf{T = 10days}$	0.33	0.21	0.26
$\mathbf{T = 20days}$	0.67	0.42	0.53

Table 5.3: Ratio $\phi = \frac{T_{high}}{t_f(Q_{high})}$ for all experiments.

The other critical time ratio is $\psi = \frac{T_{low}}{T_{restrat}}$. Jones and Marshall (1997) used the same theoretical arguments as Visbeck et al. (1996) presented in the previous chapter joined to numerical experiments to get an estimate of the restratification timescale. They found:

$$T_{restrat} = 56\frac{R}{NH} \tag{5.6}$$

In our case, the radius of the disc of cooling is $R = 20km$, and the stratification $N = 7.87{\cdot}10^{-4}s^{-1}$ and for a mixed layer depth $H = 800m$, we find a restratification time of $T_{restrat} \sim 20days$. Hence, in all our experiments, we expect to have $T_{low} < T_{restrat}$.

This formulation for the restratification timescale assumes that the width of the baroclinic zone l_{bz} scales like the Rossby radius of deformation $R_0 = \frac{NH}{f}$. We can derive a more general formulation of the restratification timescale using

the same method as Jones and Marshall (1997) apart from this assumption. This yields:

$$T_{restrat} \propto \frac{l_{bz} R f}{N^2 H^2}. \tag{5.7}$$

We have seen in the previous chapter that the cooling stops when the baroclinic eddies have reached the centre of the patch, hence the baroclinic zone could be scaled on the Rossby radius of deformation. Choosing $l_{bz} = R$ leads to:

$$T_{restrat} \propto \frac{R^2 f}{N^2 H^2}. \tag{5.8}$$

In this chapter, we will try to keep the parameterisation as general as possible, hence we will keep the l_{bz} term.

5.3 Results

5.3.1 Mixed Layer Depth

Figure 5.2 displays the mixed layer depth for the runs with periodic boundary conditions at the sides. We notice that the final mixed layer depth in all experiments is very close to the one of the control run - the time variability of the surface forcing does not seem to have any impact on it. Results for different boundary conditions at the sides will be shown. This shows that, if the time variability is on the order of a few days, only the integrated value of the surface buoyancy loss matters.

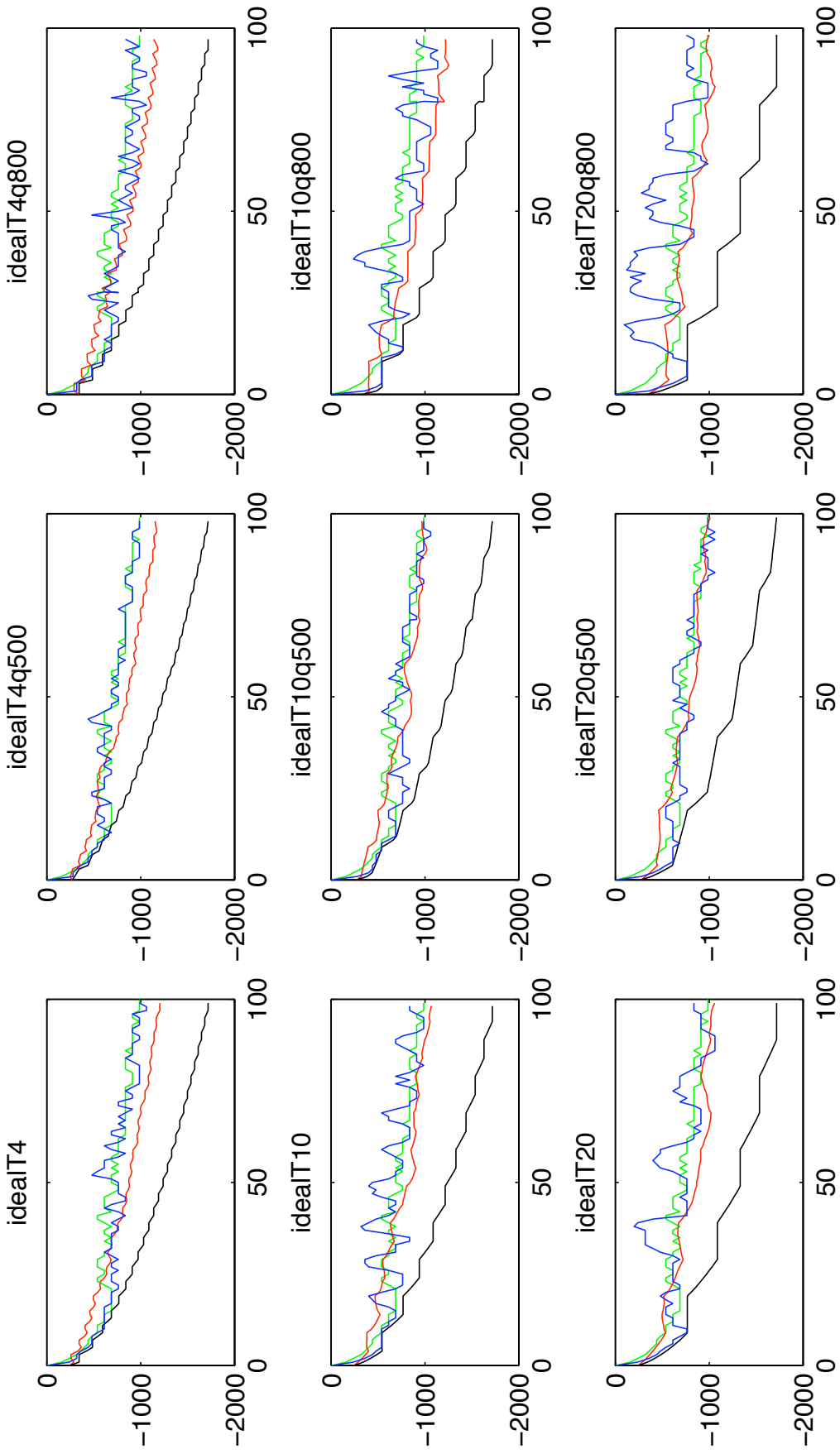

Figure 5.2: MLD calculated using the second method for the time varying forcing runs (blue) and the control run (green), 1D equivalent MLD (black) and reconstructed MLD from the lateral buoyancy fluxes (red) for which we use the 1D formula with a forcing in which the lateral buoyancy fluxes have been substracted to the surface forcing.

5.3.2 Lateral Buoyancy Fluxes

We now look at the lateral buoyancy fluxes for the experiments with open boundary conditions, as well as their vertical structure - figure 5.3. The lateral buoyancy fluxes adapt very quickly to the surface forcing, which explains why there is very little impact of the time variability of the buoyancy loss on the mixed layer depth. This is surprising because we do not expect baroclinic instability to react so quickly to the forcing. Moreover, we do not observe the strong overshooting of the instability that we saw in the control run. We can compare figures 5.3 and 4.13. The speed at which the near-equilibrium value of the lateral buoyancy flux is reached, as well as the magnitude of this value, depends on the cooling rate, as seen in the previous chapter. Using the linear variation between the surface cooling rate and the 'equillibrium' value of the lateral buoyancy flux, table 5.4 gives that value for the different cooling rates applied, in terms of surface integrated values. We notice that for all four cooling rates considered, the lateral heat flux is 75.1% of the surface heat flux, with a standard deviation of 0.7% around the value of the ratio between the two. In the experiments with time varying forcing, the 'equilibrium' value for the lateral buoyancy fluxes is not reached when T_{high} is too short.

$\mathbf{Q(W/m^2)}$	100	400	500	800
$\mathbf{Q\pi R^2(10^{10}W)}$	12.56	50.26	62.83	100.53
Lateral Buoyancy flux $\mathbf{(10^7 m^4/s^2)}$	0.49	1.95	2.48	3.82
Lateral Heat flux $\mathbf{(10^{10}W)}$	9.38	37.34	47.49	76.16

Table 5.4: 'Equilibrium' value for the lateral buoyancy fluxes for the different surface cooling rates applied. To allow comparison between the surface and lateral heat fluxes, we also show the surface integrated surface heat flux $QR^2\pi$ and the surface integrated lateral heat flux.

The lateral BF are not homogeneous with depth, and their structure is complex. During the first few days of each simulation, they indicate an inward flow near the surface and a outward one at the bottom of the mixed layer. Below the mixed layer, the lateral fluxes are negligible. We then see a reversal of that behaviour after a few days, after which it seems to oscillate between these two regimes. In the run T20q800, we see that this behaviour is repeated at each 20 day cycle, with a reversal happening when the cooling rate changes abruptly.

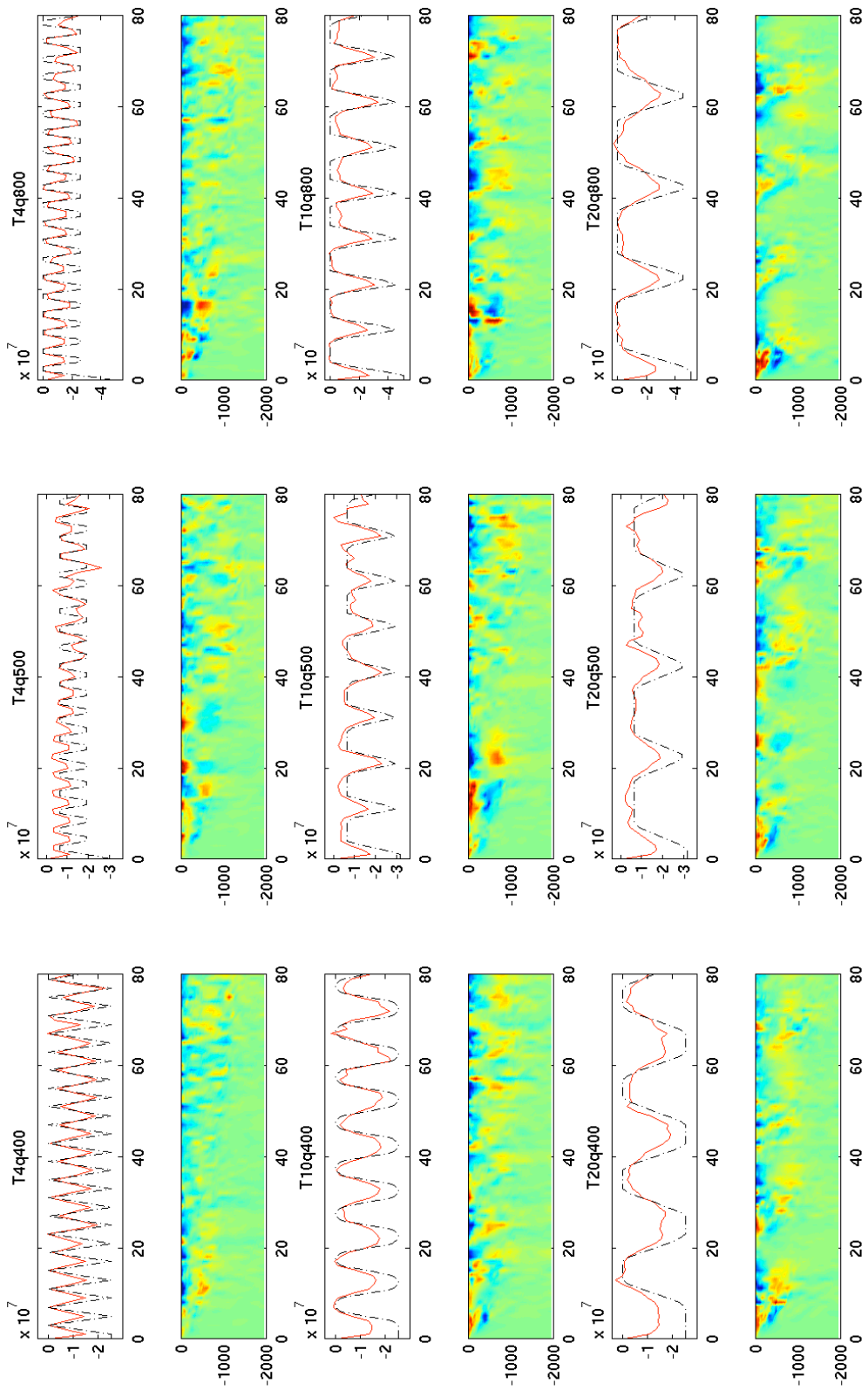

Figure 5.3: Total surface (dashed) and the negative of the total lateral (solid red) buoyancy fluxes (in m^4/s^2) for all the time-varying experiments as well as the vertical structure of the buoyancy fluxes just below (color range is $[-2 \cdot 10^7, 2 \cdot 10^7]$). Horizontal axis is time (days), and vertical is depth (m). Note that the scale for the total lateral buoyancy fluxes depends on the amplitude of the cooling.

We now compare the integrated values of the surface and lateral buoyancy fluxes, plotted on figure 5.4. These are plotted for the runs with open boundary conditions at the sides. We notice that although the change in buoyancy content of the patch follows similar curves for all, there is a slight difference between them. To emphasise this, figure 5.4 also indicates the value of the change in buoyancy content $\Delta BC = \int SBFdt - \int LBFdt$ at day 80. It shows that, although we do not notice much difference on the final mixed layer depths, the time variability of the forcing does induce a small difference in the heat content of the patch between the different experiments. ΔBC decreases as Q_{high} increases, hence the term $\int LBFdt$ increases with Q_{high}. There is no clear trend as we change the period. As a comparison, for the run with constant forcing $Q_0 = 200W/m^2$, $\Delta BC(80days) = -6.73 \cdot 10^{13} m^4/s^2$, which indicates that the lateral buoyancy fluxes have been much less active in that case. The fact that we observed similar mixed layer depths for all our experiments hints to a difference in the repartition of the buoyancy within the mixed layer. The mixed layer should be completely mixed in all cases. However, if we consider that the water within that layer is not fully mixed (i.e. $N^2 > 0$), we would expect it to be more mixed in the case of the control run than in the other cases.

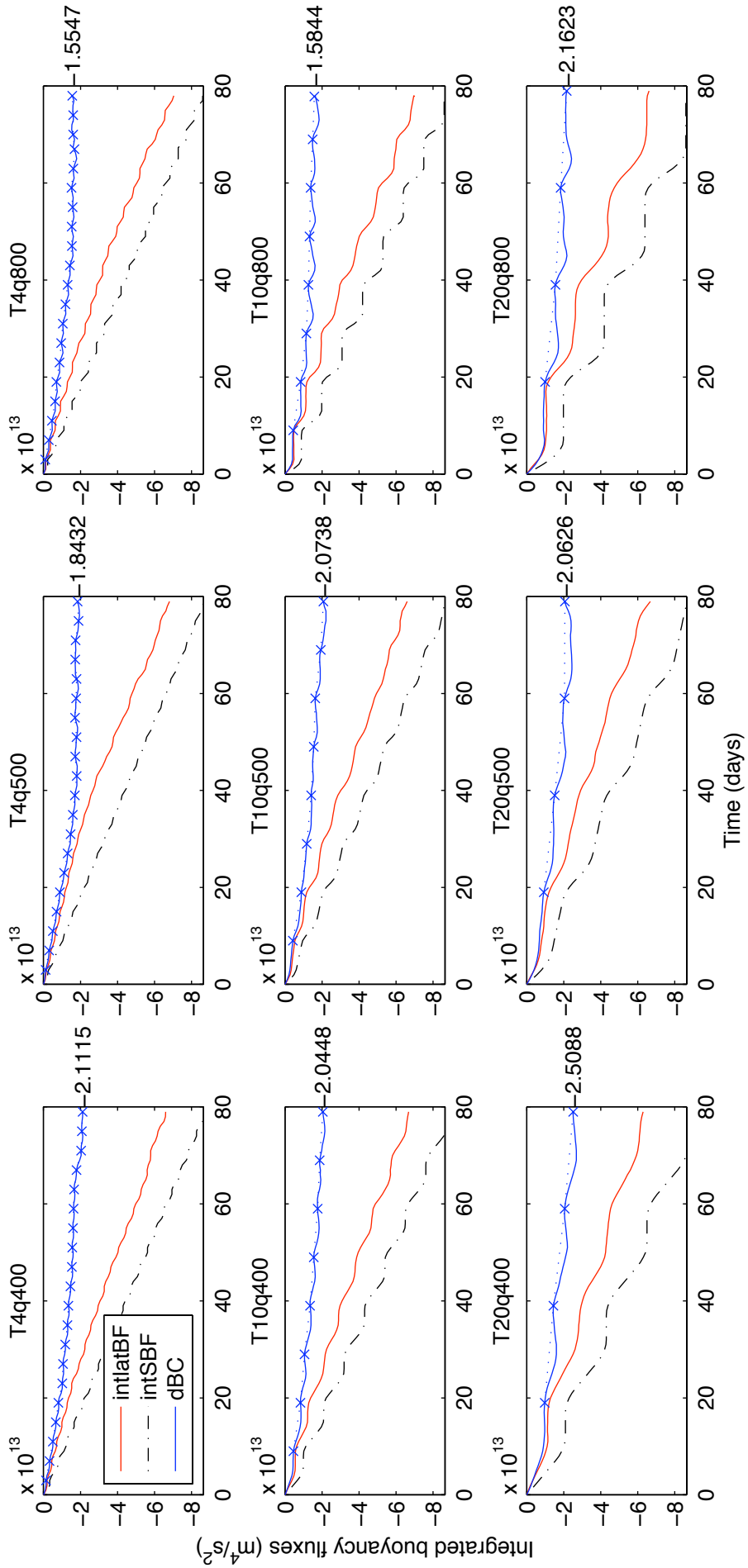

Figure 5.4: Integrated surface (black) and lateral (red) buoyancy fluxes, and the difference between them (blue, dBC). The blue dotted lines links the values of dBC (ΔBC) at the end of each period.

5.3.3 Comparison between periodic and relaxation boundary conditions

We compare here the two types of boundary conditions. Figure 5.5 compares the mixed layer depths and the lateral buoyancy fluxes for some of the experiments.

We notice the same discrepancies for the mixed layer depth as we had for the control run. For periodic BC, the deepening slows down drastically in the post-Turner regime but does not stop as it does in the simulations using prescribed T/S at the sides. Over the first 20 days of each simulation, the agreement between the mixed layer depths for runs with different BC is very good. The lateral buoyancy fluxes respond very quickly to the forcing for both types of boundary conditions, although there are some differences in the magnitude of this response. They are very similar in the Turner regime, and show important differences only after the time it takes for the patch to 'feel' the boundaries. We notice that for the runs with $T = 4days$, between days 20 and 70, the lateral buoyancy fluxes oscillate over a larger magnitude for the run with open BC than for the run with prescribed T/S at the sides. This is related to differences between the mixed layers. The one for the periodic BC run is deeper than the one for prescribed T/S at the sides. This can be explained by the fact that in the periodic BC case, the lateral buoyancy fluxes become negligible, while they do not in the run with prescribed T/S at the sides. This provides the extra buoyancy for the mixed layer to be shallower in the latter case. On the first hand, we would expect the lateral density gradient at the edge of the patch to be sharper in the runs with prescribed T/S at the sides because the ambient water should be less affected by the spreading of cold water from the convective patch, hence warmer. On the other hand, a deeper mixed layer should lead to a colder convective patch, which would tend to sharpen the lateral density gradient across the edge of the patch. It illustrates the close connection between mixer layer depth, horizontal density gradient and lateral buoyancy fluxes that feed on this gradient and reduce it.

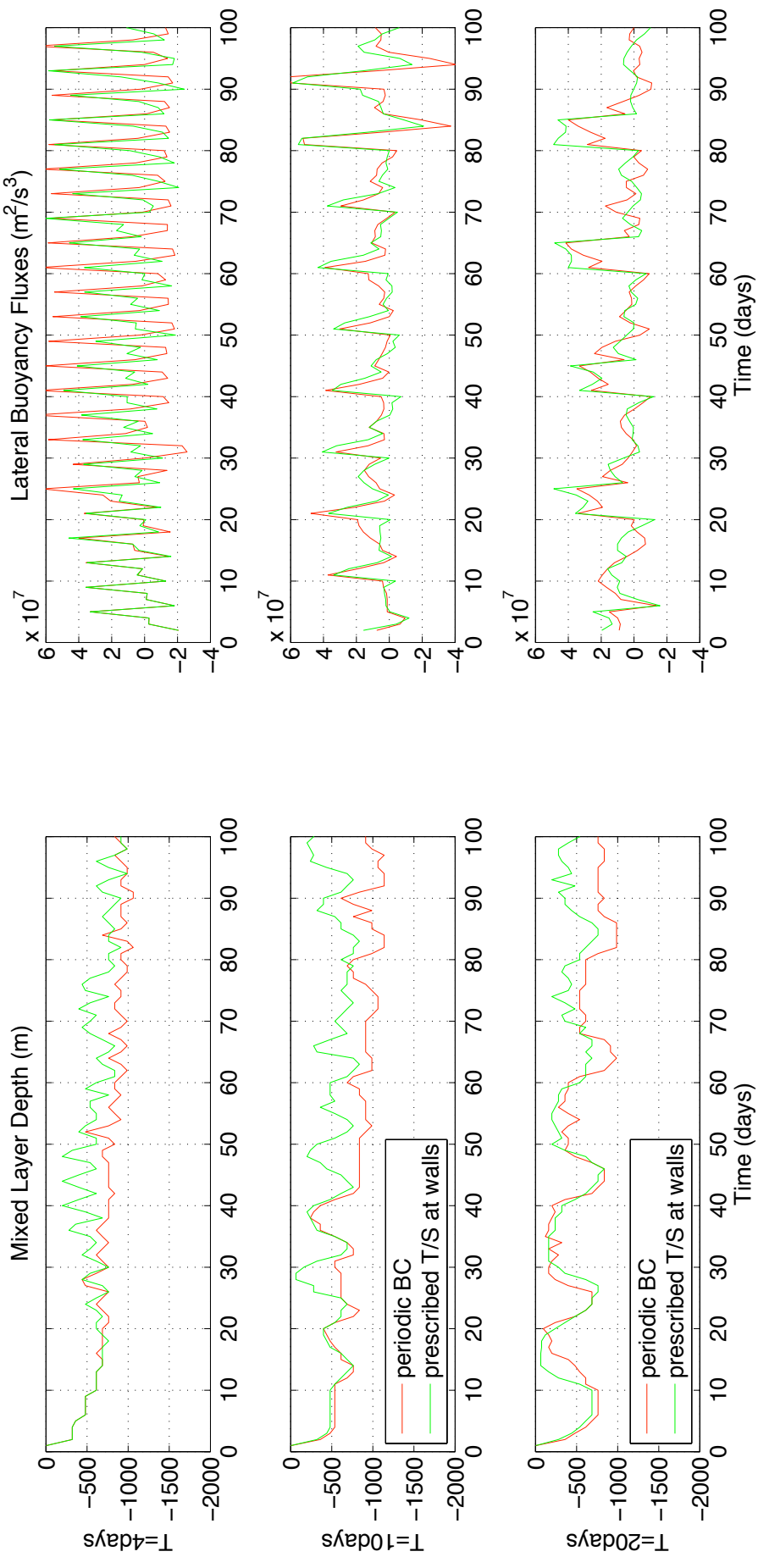

Figure 5.5: Mixed layer depths calculated using the second method (left) and total lateral buoyancy fluxes (right, in m^4/s^3) for runs with $T_{high} = T/4$, $Q_{high} = 800W/m^2$ and different boundary conditions. The top panel displays results for patch undergoing a forcing of period 4 days, the middle panel of period 10 days, and the bottom panel of period 20 days.

5.3.4 Zonal averages

Calculation

To perform the calculation of the zonal average of a variable $f(r, \theta, z, t)$ (in circular polar coordinates - see figure 5.6 for a sketch) we first interpolate its value along a circle of radius r, with $r \in Rpos = [1, 2, ..., 29]km$ at locations (r, θ, z, t). θ is chosen so that we calculate $n = \frac{2\pi r}{dr}$ values along that circle, where $dr = 500m$. Therefore dr represents the spatial resolution for that calculation, and corresponds to a resolution in θ of $d\theta = \frac{dr}{r}$. We then calculate the average value of the variable over these n positions, so we end up with $\overline{f}^{\theta}(r, z, t)$.

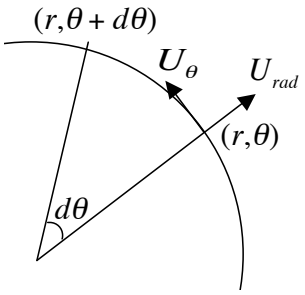

Figure 5.6: Sketch to describe the zonal average calculation and defining the zonal and azimuthal velocities.

To have something meaningful concerning the horizontal velocities, we need to calculate (U_{rad}, U_{θ}) as defined on figure 5.6 before averaging.

Top view

The top view of the zonal averages of temperature and velocity components for the runs with prescribed T/S at the sides is shown on figure 5.7. The surface temperature shows a strong periodicity. We notice incursions of warm water as far as the centre of the patch during periods of weak/no cooling which is a sign of quick recapping of the mixed layer by restratification processes and happens in an uneven way. On top of the periodic signal for the temperature, there is a cooling trend due to the effect of the convected water advected away from the patch towards the ambient water.

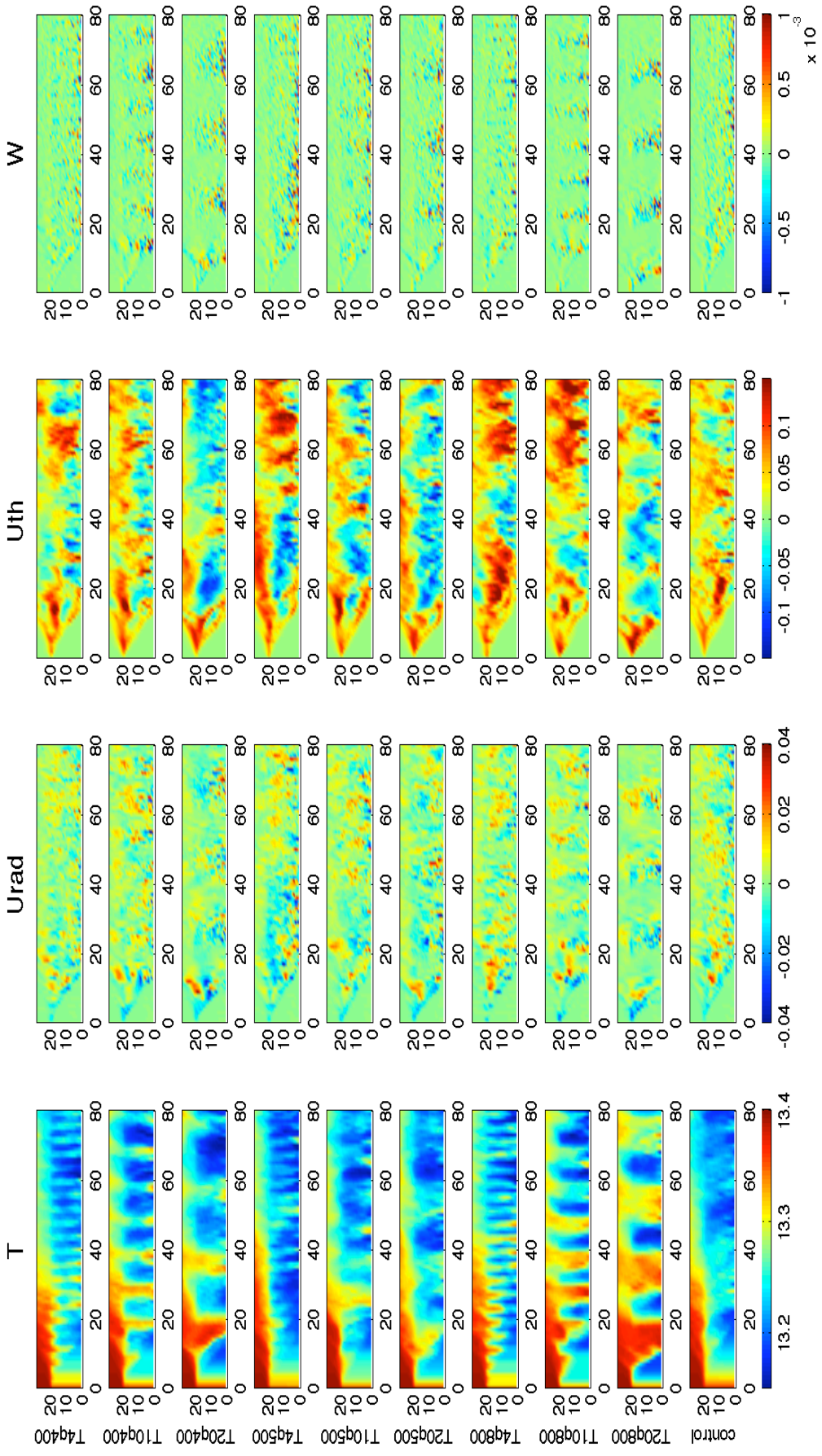

Figure 5.7: Top views of the zonal averages of the temperature T (°C), radial, azimuthal (at $z = -5m$) and vertical (at $z = -10m$) velocities $Urad$, Uth and W (m/s) for the nine experiments and the control run. Horizontal axis is time (days), and vertical is radius from the centre of the patch/box (km).

The velocities all show the development of the baroclinic zone during the first 20 days of the simulations. The top views of the radial and vertical velocities $Urad$ and W show the initial widening of the baroclinic zone, which is not stopped during the period of low cooling. It reaches the centre of the patch at a time which depends on the time variability of the forcing, and which is shorter for the runs with variable forcing. Table 5.5 shows the time at which the eddies start reaching the centre for the nine runs with periodic forcing. The longer the period, the faster the centre of the patch is reached by eddies. This can be explained by the fact that a longer total period also means a longer T_{high}.

	q400	q500	q800
T4	14	16	17
T10	13	16	15
T20	12	12	11

Table 5.5: Time at which the azimuthal velocity near the centre has a magnitude bigger than $0.01m/s$ in days for the nine experiments with periodic forcing. The first row gives the value of the high forcing Q_{high} and the first column the value of the period T.

Note that the widening of the baroclinic zone does not happen at the same rate towards and away from the centre of the patch. This asymmetry can be seen on the azimuthal velocity top view, which shows the development of the rim current.

We also notice the surprising fact that the azimuthal velocity tends to become anticyclonic in the post-Turner regime for some simulations, but not all of them, and particularly not for the control run. However, the control run using periodic BC also shows this anticyclonicity (not shown here), which seems to concern mainly the center of the patch. It looks like there is a anticyclonic tendency inside the patch and a cyclonic one around it, and that what we observe is a result of a compromise between the two, which differs depending on the experiment. Figure 5.8 explain how the formation of eddies can generate an anticyclonic circulation. The cyclonic eddies are in red while the anti-cyclonic one is in blue. The black dotted line delimitates the approximate location of the disc of cooling. Cyclonic eddies form around the patch, and the branch of their circulation closer to the centre of the disc generates an anticyclone contained within the disc of cooling. The periods during which the anticyclonicity gets stronger seem to coincide with a strong restratifying inflow of warm water, as visible on the temperature plots. This can be explained by the fact that eddies that develop led to more exchange between the patch and the ambient water, and tend to spin faster, hence

generating more anti-cyclonicity within the patch.

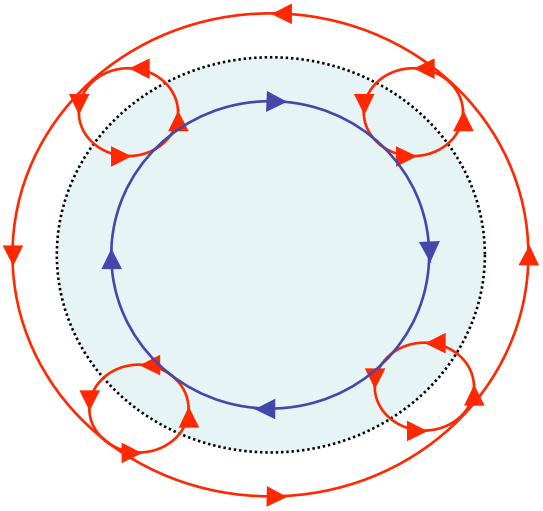

Figure 5.8: Sketch of the top view explaining the relationship between eddies and anticyclonic circulation.

Note that here the vertical velocities are not plume-like structures but result from along isopycnal flow because the convective adjustment takes care of what would otherwise be a diapycnal mixing. They are linked to eddy dynamics, as can be noticed on figure 5.7. Indeed, vertical velocities are significant only within the baroclinic zone. They are intensified by surface cooling, which hints at the intensification of the eddy activity when the surface heat loss is strong.

Side view at r=20km

Figure 5.9 displays the zonal averages of the temperature T and of the horizontal components (U_{rad}, U_θ) of the velocity at the edge of the patch (r=20km). We see the periodic signal in T and U_{rad}, but it is less obvious for U_θ. The deepening and restratification cycle is visible in the temperature structure. For longer periods T and stronger cooling Q_{high}, the restratification signal is particularly strong.

There is no clear correlation between U_{rad} and U_θ, although it seems that, in the Turner regime, the surface inflow is associated with a cyclonic behaviour and the outflow near the bottom of the mixed layer with an anticyclone. This is consistent with the conservation of vorticity (vortex stretching term). The azimuthal velocity also shows that the rim current appear to reach deeper than the mixed layer. We can compare U_{rad} with the lateral BF. Note that a positive U_{rad} corresponds to negative lateral BF.

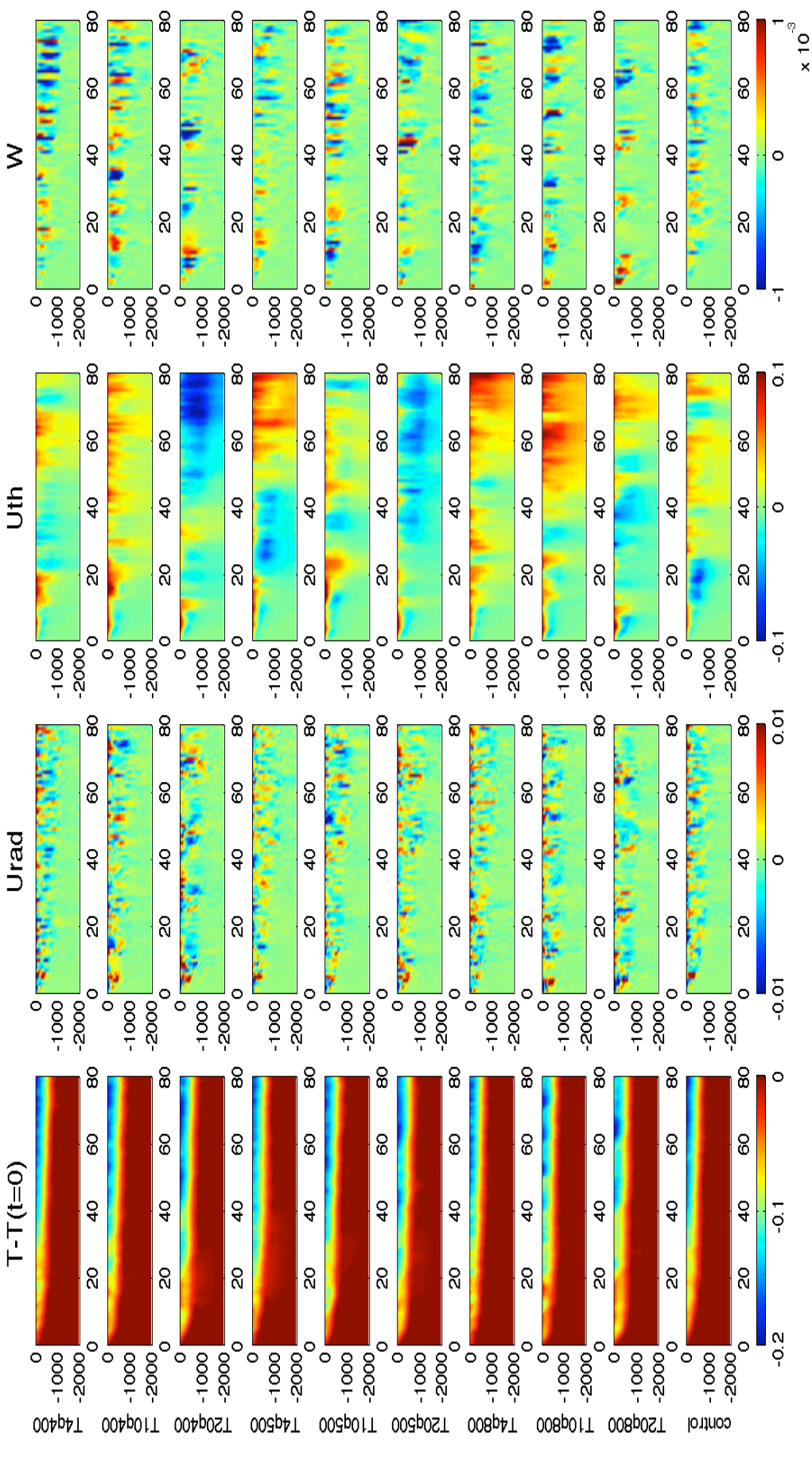

Figure 5.9: Side views at 20km of the zonal averages of the temperature (°C), radial, azimuthal and vertical velocities (m/s) for the nine experiments and the control run. Horizontal axis is time (days), and vertical is depth (m).

The periodic signal in the vertical velocity is less marked in the vertical than it is in the top view, although it is clearly visible for runs with a period of $20days$. The sign of the vertical velocity seems random and probably does not bear much physical significance here, because the places of downwelling/upwelling are very localised, so the results are very sensitive to the location (here radius) at which we observe the vertical velocity.

5.3.5 Additional runs

Run with $T_{high} > t_f$

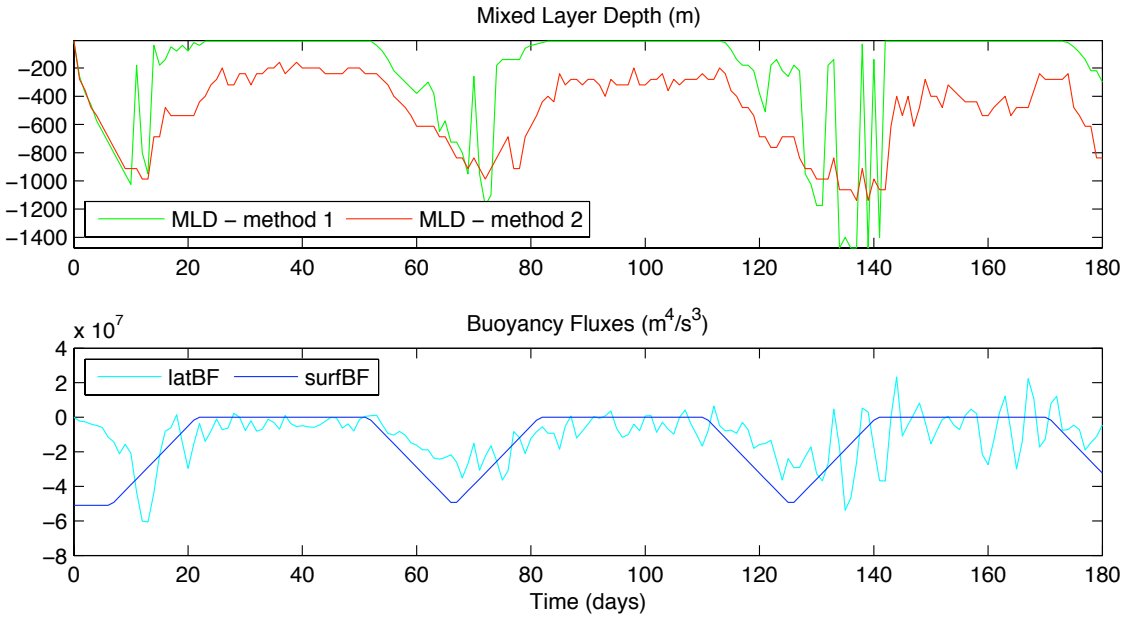

Figure 5.10: Mixed layer depth (top) and buoyancy fluxes (bottom) for the run T60q800.

In all our previous experiments, we had $T_{high} < t_f$. We here perform an experiment with $T = 60days$ and $Q_{high} = 800W/m^2$, hence $T_{high} = 15days > t_f = 9.5days$. We use open boundary conditions at the sides. Figure 5.10 shows the evolution of the mixed layer depth and the lateral buoyancy fluxes. The mixed layer depth calculated using the density jump method shows that the deepening carries on even at the third period. However, the second method, which is more linked to the buoyancy content of the mixed layer, is roughly the same at each of the high forcing periods, i.e. at t such that $nT < t < nT + T_{high}$. The discrepancies between the two methods show that we cannot assume a fully mixed convective layer here, except for $t < t_f$. The deepening is confirmed by the fact that the lateral buoyancy fluxes, although they get as high as the surface fluxes around day 15, do not reach such a high value during the next two cycles.

Run with abrupt changes in the forcing

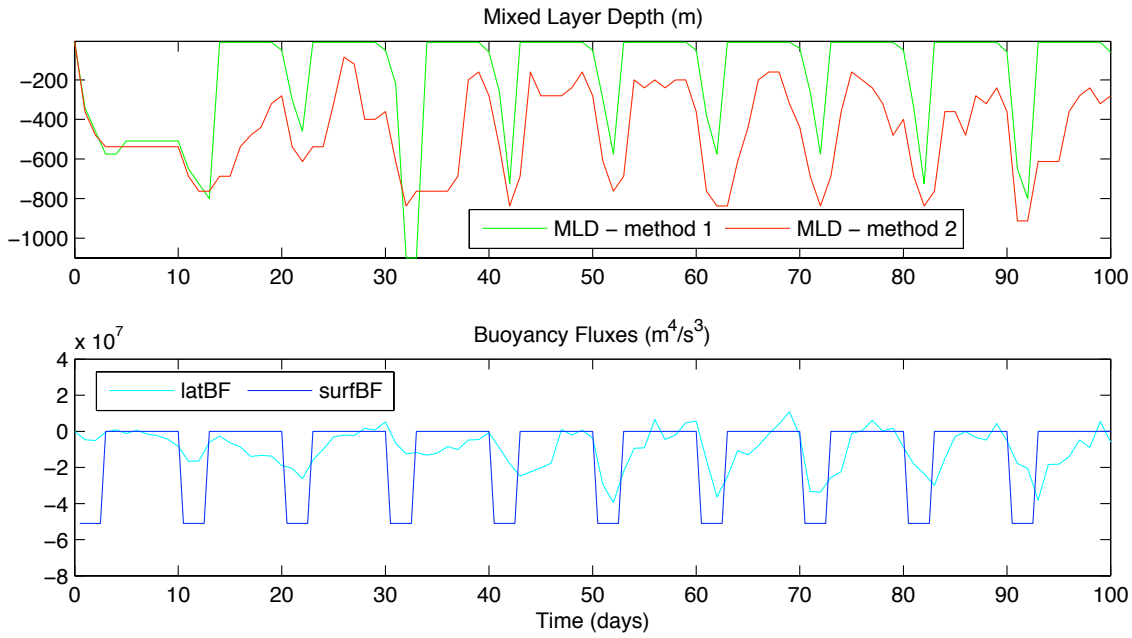

Figure 5.11: Mixed layer depth (top) and buoyancy fluxes (bottom) for the run T10q800sharp.

This experiment has a forcing similar to the T10q800 experiment, except that the forcing has not been smoothed: we call it T10q800sharp. The mixed layer depth and lateral buoyancy fluxes are shown on figure 5.11. The final mixed layer depth in that run is unchanged compared to the run using a smooth forcing. We notice that it takes some time for the lateral buoyancy forcing to develop at the beginning of each period. It shows that there is a limit in responsiveness. It also takes some time for the lateral buoyancy fluxes to stop acting after the forcing has stopped, hence the quick re-capping of the mixed patch by more buoyant water.

Run with a constant cooling for 20 days and no cooling thereafter

Figure 5.12 shows the mixed layer depth and lateral buoyancy fluxes for a run called 'short' for which a constant cooling of $Q = 200W/m^2$ was applied for 20 days, and then no cooling at all for the rest of the simulation. The evolution during the first 20 days is the same as for the control run as expected. When the cooling stops, we observe a very quick recapping (see MLD method 1 - density jump) while the increase in stratification below the recapping layer increases steadily and takes much longer to recover. In fact, it has not completely restratified by the end of the simulation, after 100 days, as shown by the MLD calculated using the second method. After the end of the cooling, the lateral buoyancy fluxes oscil-

lates around a value close to $0m^4/s^3$ with an amplitude that decreases with time, becoming negligible after the 50th day of the simulation.

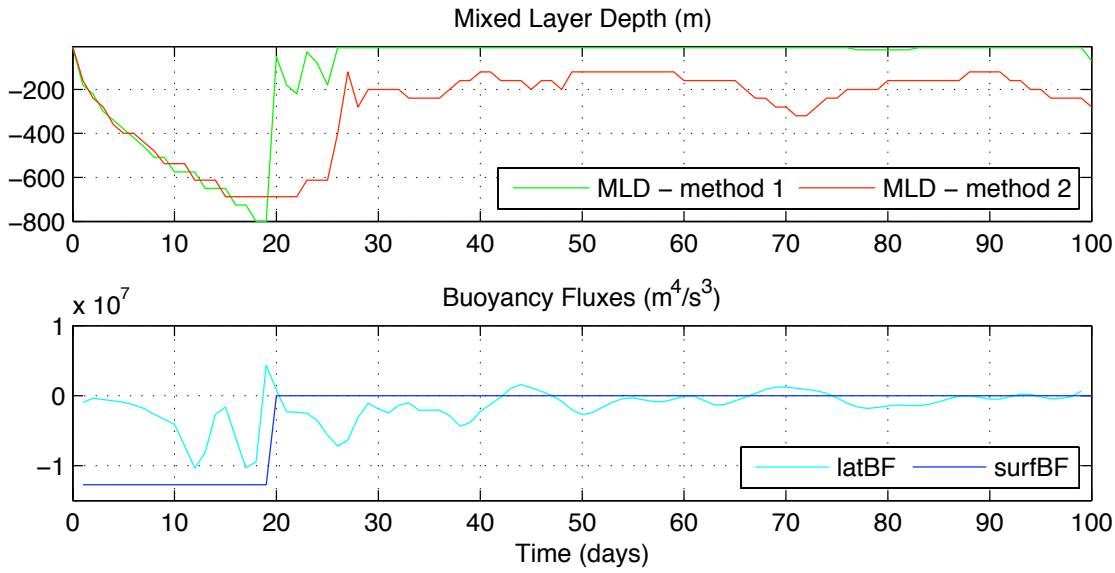

Figure 5.12: Mixed layer depth (top) and buoyancy fluxes (bottom) for the run short.

5.3.6 Summary and new questions

We showed that the time variability of the surface forcing does not have a large impact on the mixed layer depth in our simulations. This is due to the lateral buoyancy fluxes responding very quickly to that surface forcing. We also showed that the rim current around the patch tended, in some cases, to be anticyclonic, which is unexpected too.

The next sections aim at answering these questions:

- Why do the lateral buoyancy fluxes respond so quickly to the surface forcing? We will study baroclinic instability more closely.
- Why does the rim current exhibit an anticyclonic behaviour? We will look at the structure of the convective patch and the circulation linked to convection.
- Does the time variability of the forcing affect the properties of the deep water formed?

5.4 Geostrophic adjustment and inertial oscillations

5.4.1 Background

The fluid under the disc where the forcing is applied gets cooler and denser than the ambient fluid, and will tend to reduce its potential energy by slumping towards its level of neutral density. This horizontal circulation is limited by the Coriolis force because the water flowing away from the patch has a horizontal velocity which is deflected, resulting in the formation of a rim current in (geostrophic) thermal wind balance around the patch. This is a Rossby adjustment problem (Rossby, 1938). The initial potential energy is split into geostrophic kinetic and potential energies during the adjustment (Ou, 1986; Blumen and Wu, 1995).

Some of the energy during the geostrophic adjustment is also radiated away in inertia-gravity waves. Reznik et al. (2001), Zeitlin et al. (2003) and Plougonven and Zeitlin (2005) considered the nonlinear geostrophic adjustment problem and found that the adjustment was taking place on two timescales. The fast component of the adjustment, on a timescale $(fR_0)^{-1}$ where f is the Coriolis parameter and R_0 the Rossby number, corresponds to the emission of linear inertia gravity waves rapidly propagating (unbalanced motions), while the slow component, on a timescale f^{-1}, remains close to geostrophic balance (balanced motion). In our case, the geostrophic adjustment is not the only process that can lead lead to the emission of inertia-gravity waves. Unstable flows in geostrophic balance can emit inertial waves during the instability process, as seen in the laboratory (Afanasyev et al., 2008) and numerically (Viudez and Dritschel, 2006). Viudez and Dritschel (2006) noticed that the wave packet emission is very localised, both in space and time. These processes are likely to take place in our model, although we do not think they are responsible for any net lateral transport of buoyancy. At a first order, waves radiate energy, but not material. Figure 5.20 shows the decomposition of the fluxes. We are only interested in the middle column here, representing the part of the flux due to $\overline{\overline{u_r}^{\theta}\overline{T} - \overline{T}^{z,\theta}}^{\theta}$, i.e. the product of the radial velocity averaged around the patch with the zonally averaged temperature anomaly. We associate this part of the component with the geostrophic adjustment. (The figure will be described in more detail later in this chapter.) The fluxes due to the geostrophic adjustment are not visible anymore once the patch has reached its final depth, so we conclude that the adjustment has reached its equilibrium state.

There is another aspect of the geostrophic adjustment which is thought, not

to be responsible for the lateral buoyancy fluxes themselves, but for the fact that they respond so quickly to the forcing, and this is frontogenesis. Ou (1984) found that geostrophic adjustment could sharpen the horizontal density gradient by producing convergence regions. These results have been confirmed by the more realistic model of Blumen and Wu (1995). This process could imply an increased growth rate for baroclinic instability due to the sharpening of the horizontal density gradient. However, we are dealing here with growth rates so fast that it is difficult to observe which phenomenon leads which using only daily snapshots.

5.4.2 Rim current

We saw that the rim current could be anticyclonic, and here investigate why. Figure 5.13 compares the rim current to the lateral density gradient at the edge of the patch, defined as:

$$grad = mean(\frac{\partial \overline{\rho}^{\theta}}{\partial r} | r \in [19.5, 20.5]km) \tag{5.9}$$

The two are very similar. This correlation can be explained by the thermal wind balance $f\frac{\partial U_\theta}{\partial z} = -\frac{\partial b}{\partial r}$, as expected from the theory. However, we did not expect to have a density gradient in that direction (negative), i.e. water colder outside the patch than inside for a given depth. This seems to happen mainly during low surface forcing periods, and could be associated with the quick recapping. During periods of high surface forcing, the density gradient tends to be positive, at least near the surface. In general, it is more positive near the surface than at depth. Figure 5.14 confirms this in a more quantitative way by plotting the corresponding values near the surface. Indeed, the rim current is always in thermal wind balance, or very close to it. These plots are built using daily snapshots, hence we can conclude that the geostrophic adjustment occurs on a timescale shorter than a day (indeed, $\frac{1}{f} \sim 17h$). Moreover, the top layer shows the same periodicity as the lateral buoyancy forcing, except in the $q500$ series in which the surface cooling is never completely switched off. Also, we see than in all runs, both the rim current and the lateral buoyancy gradients tend to decrease over the 50 days of the simulation while it is not the case for the lateral buoyancy fluxes. We can relate the decrease in the lateral buoyancy gradient to the fact that the system starts to feel the domain boundaries after some time - the ambient water slowly cools down due to horizontal mixing with cold convective water. Figure 5.14 also shows occasional reversal of the lateral buoyancy gradient leading to an anticyclonic rim

current. Note that this has no effect on the lateral buoyancy fluxes. The short reversal in the direction of the horizontal buoyancy gradient can be explained by the life cycle of baroclinic eddies. When they pinch off to carry cold water away, there is a temporary replacement of that cold water by warmer ambient water. If all the eddies are pinching off at different times, this does not have an effect on the resulting mean rim current. But as we apply a periodic forcing, we constrain in time the development of the eddies, hence leading them to develop and pinch off more or less simultaneously. This affects the zonally averaged lateral buoyancy gradient.

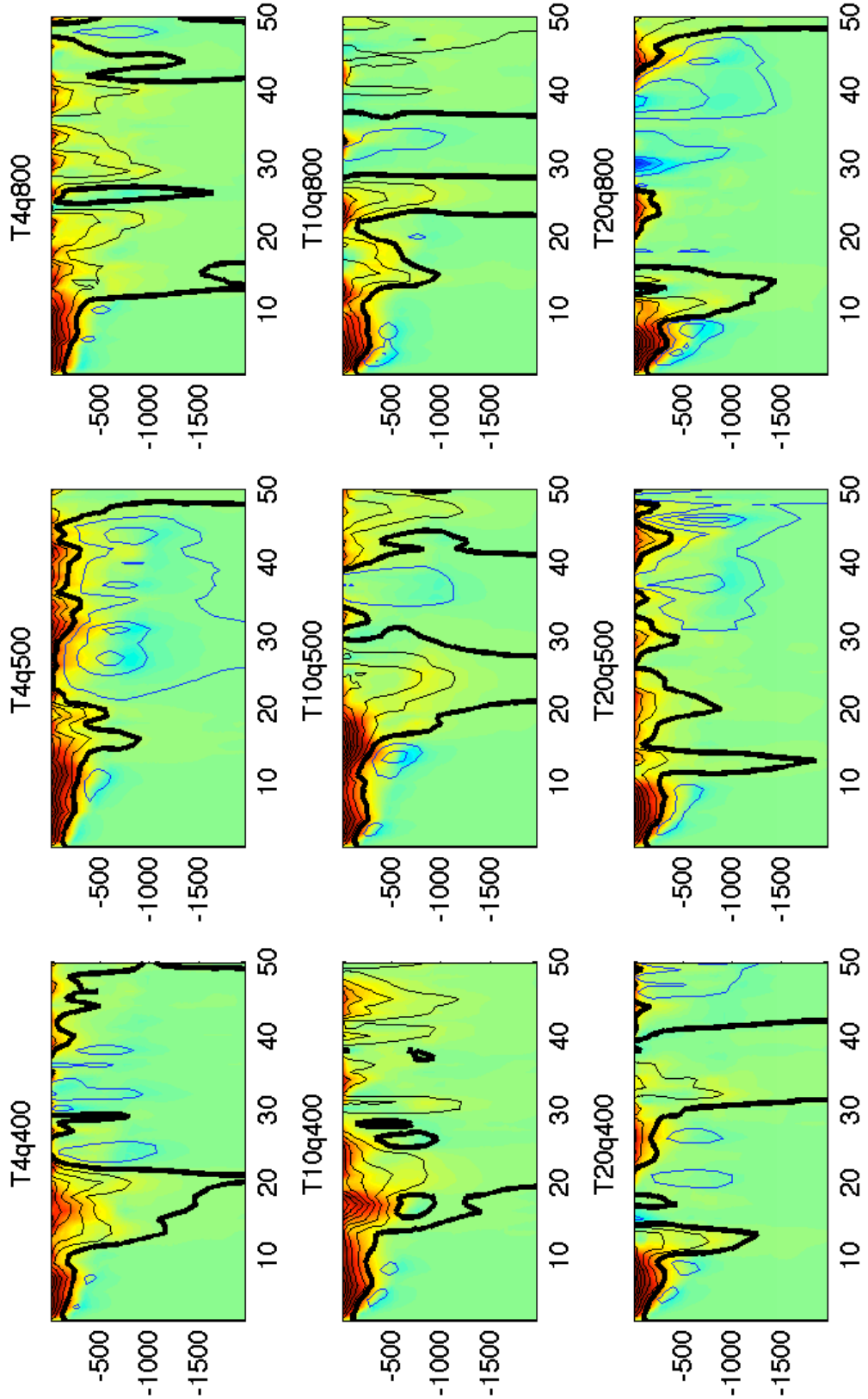

Figure 5.13: Lateral density gradient at the edge of the patch - the color range is $[-5 \cdot 10^{-4}, 5 \cdot 10^{-4}] kg/m^4$ - and zonal average of the azimuthal velocity at the same location (contours). The thick black contour line indicates $U_\theta = 0m/s$. Contour lines are spaced every $0.2m/s$, with black (blue) lines for positive (negative) values. Horizontal axis is time (days), and vertical is depth (m).

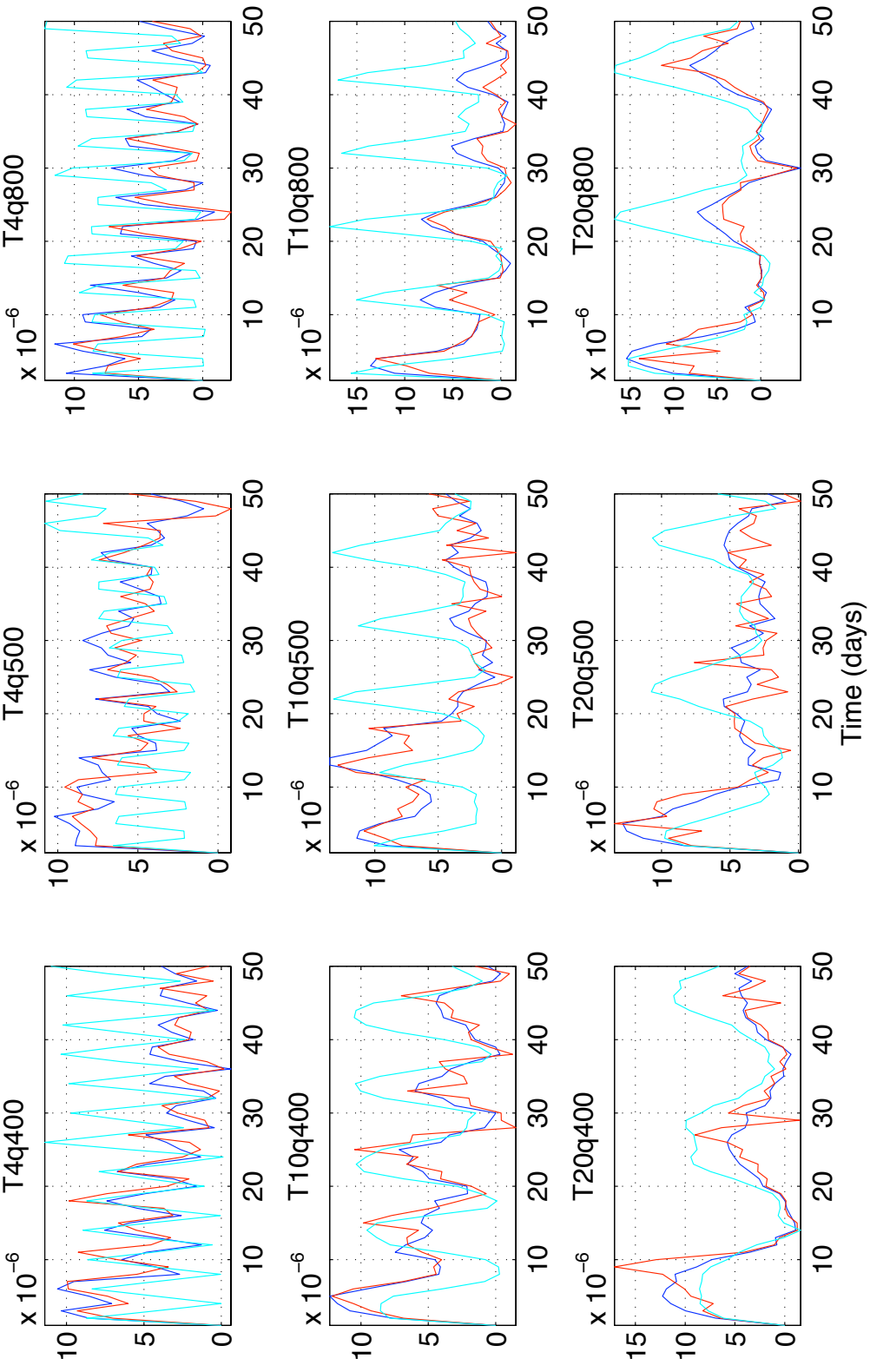

Figure 5.14: Zonal velocity shear times the Coriolis force (red) and zonally averaged radial buoyancy gradient (blue) in the top layer at $r = 20km$. The cyan line represents unscaled lateral buoyancy fluxes.

5.5 Symmetric instability and slantwise convection

Haine and Marshall (1998) enumerated the different types of instabilities an oceanic mixed layer can be exposed to. Among these is the symmetric instability, which is a mixed gravitational-centrifugal instability. The lateral buoyancy gradient leads to the formation of a rim current in thermal wind balance. This current tilts the angular momentum surfaces (m-surfaces). The gravitationally unstable parcels then move along slanted rather than vertical paths, hence the name of slantwise convection. This phenomenon was first identified in the atmosphere (Emanuel, 1994).

Straneo et al. (2002) transposed the parcel theory from the atmosphere to the ocean. We can write an analog to the angular momentum, called the zonal absolute momentum ZAM: $m = u - fy$. Let $M = U - fy$ be the mean ZAM. Then the Lagrangian equations of motion for the gravitationally unstable parcel are:

$$\frac{\partial m}{\partial t} = 0 \tag{5.10}$$

$$\frac{\partial u}{\partial t} = f(M - m_0) = f\Delta m \tag{5.11}$$

$$\frac{\partial w}{\partial t} = -(B - b_0) = -\Delta b \tag{5.12}$$

where b_0 and m_0 are the initial buoyancy and ZAM of the parcel. They resolve these equations for a horizontally and linearly stratified mean flow: $B(y, z) = \alpha y + N^2 z$. For $\sqrt{\alpha} = 10^{-4} s^{-1}$, the parcel trajectory is plotted on figure 5.15.

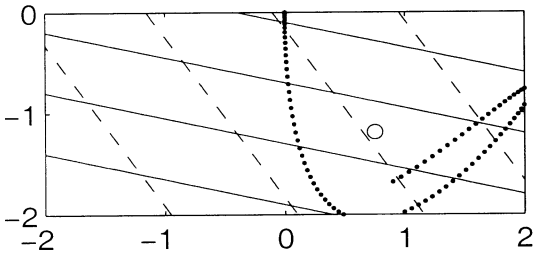

Figure 5.15: Parcel trajectories (dotted line) plotted in the y-z plane (axes units are in kilometers). The equilibrium point is an open circle. ZAM surfaces are dashed (contour interval is $0.1 m/s$) and isopycnals are solid (contour interval is $5 \cdot 10^6 m/s^2$). From Straneo et al. (2002).

Note that the parcel goes further than its equilibrium position not only in the vertical, but also in the horizontal direction.

Parcel theory yields that the flow becomes unstable to symmetric instability when:

$$R_i < \frac{f}{\eta} \tag{5.13}$$

where η is the vertical component of the absolute vorticity, $R_i = N^2_{mix}/\frac{\partial u}{\partial z}^2$ is the Richardson number (Emanuel, 1994; Haine and Marshall, 1998), and N^2_{mix} the stratification in the mixed layer.

Straneo et al. (2002) noted that, because convecting parcels will tend to follow ZAM surfaces, there will be a weak stratification left within the mixed layer. Figure 5.23 displays the temperature difference between $z = -200m$ and $z = -762.5m$ at the centre of the patch ($r <= 2km$) for the different simulations. During the first 20 days or so, the temperature difference decreases, corresponding to the deepening of the mixed layer. Once the mixed layer is deeper than $-762.5m$, the stratification increases again, in a variable way depending on the simulations. There is a residual stratification in the mixed layer which is completely eroded only when the cooling lasts long enough. The run called 'short' shows that the mixed layer recovers a restratification very quickly although it is not as strong as the initial stratification.

The zonal absolute momentum surfaces and the isopycnals are plotted for run T10q800 (figure 5.16) and for the control run (figure 5.17). They confirm that there are times for which, at the same z-level, the water is lighter at the centre than around the edge of the patch (day 21 for example, for run T10q800), as seen on figure 5.13. The instability at the surface is also apparent, for example at day 12 for the control run (figure 5.17). We recall here that we are looking at snapshots rather than daily averages. These represent evidence of internal waves at the base of the mixed layer - the isopycnals are not flat below the mixed layer in several occurrences in both runs. Both runs show a different structure in the isopycnals depending on the regime. When the mixed layer deepens, i.e. in the Turner regime, the isopycnals are almost vertical at the edge of the patch. After that, and this is very clear in the control run, they remain mostly horizontal. Run T10q800 also shows clear signs of recapping, at day 24, for example. The stratification near the surface increases rapidly. We also see that the dense water tends to slump horizontally.

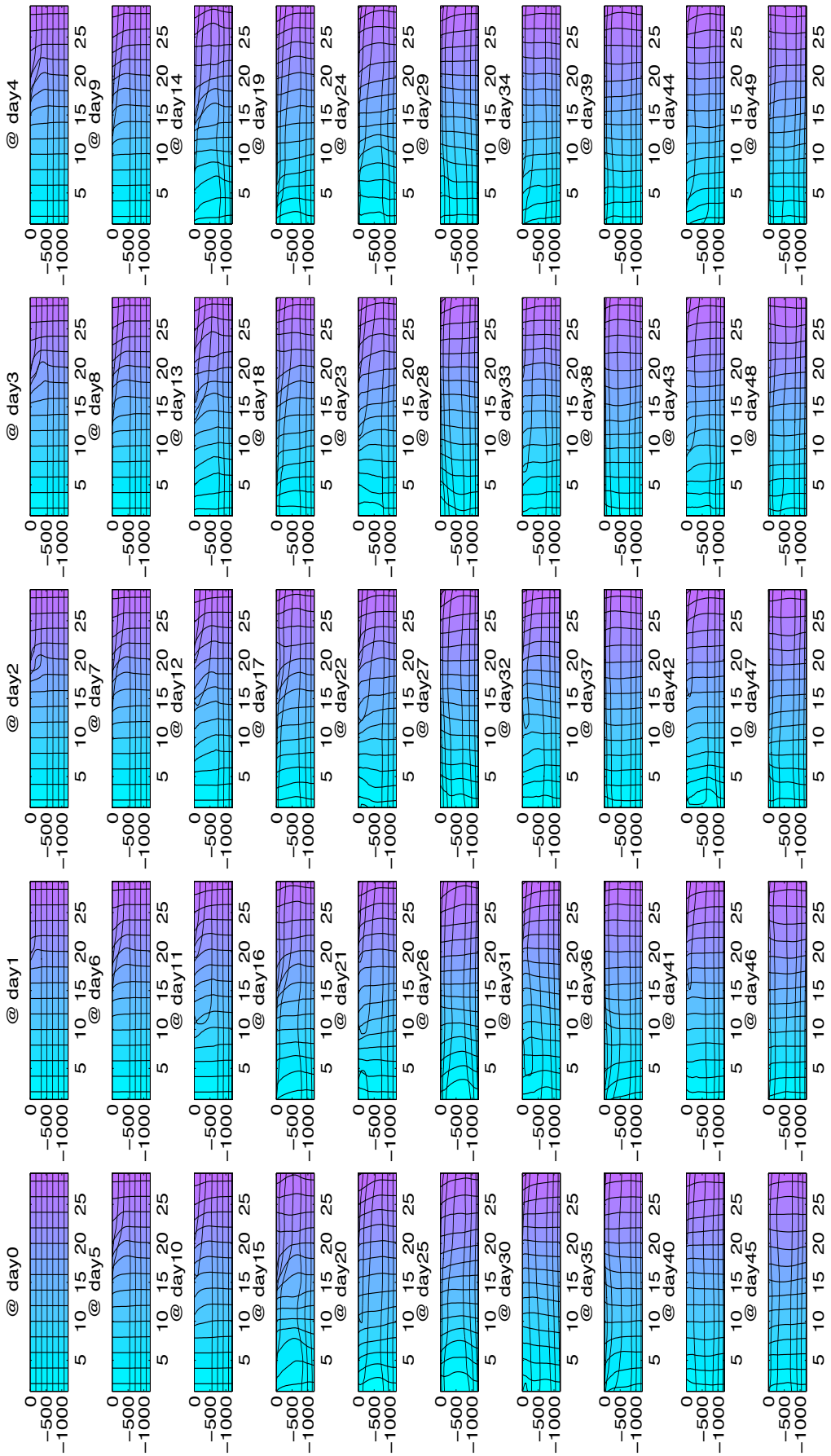

Figure 5.16: Snaphots with the angular momentum surfaces (filled contours, every $0.1m/s$) and the isopycnals (contours) for the 50 first days of the experiments T10q800 with open boundary conditions. Horizontal axis is distance from the centre of the patch (km), and vertical is depth (m).

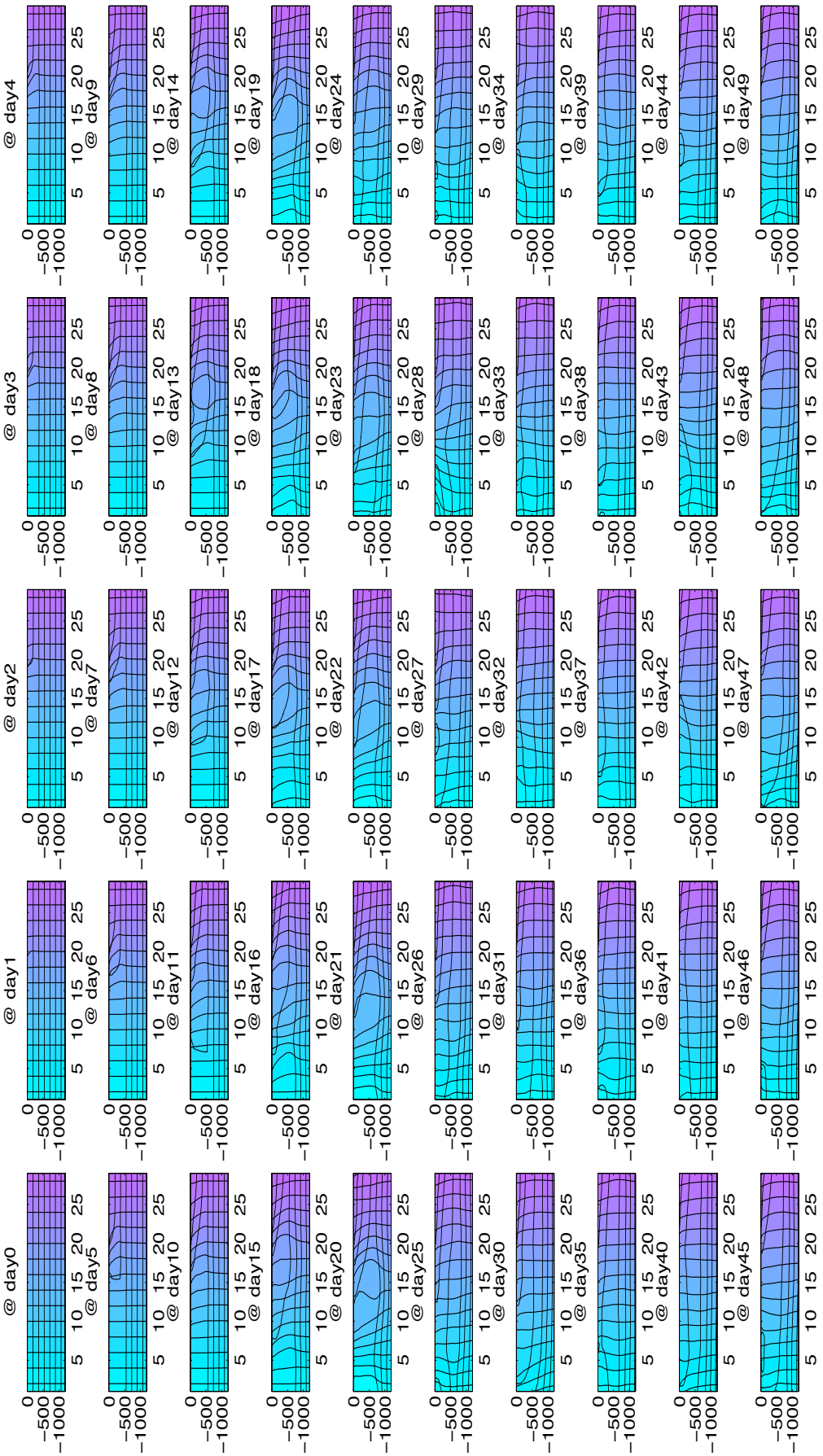

Figure 5.17: Snaphots with the angular momentum surfaces (filled contours, every $0.1m/s$) and the isopycnals (contours) for the 50 first days of the experiments r20q200 (control run) with open boundary conditions. Horizontal axis is distance from the centre of the patch (km), and vertical is depth (m).

What appears to be important for slantwise convection is the relative angle between the isopycnals and the angular momentum surfaces. Each reflects the tendency for growth of the instability they are associated with - the angle of the isopycnals with the horizontal gives information about gravitational instability while a tilt of the m-surfaces compared to the vertical axis indicates that centrifugal instability may play a role. As the relative angle between the isopycnals and the angular momentum surfaces becomes smaller, we are more likely to observe slantwise convection, that is an interaction between the two types of instabilities. This angle is very reduced mainly when the forcing applied at the surface is significant, because it tilts the isopycnals, leading to the tilting of the m-surfaces through thermal wind balance. However, we do not think that slantwise convection is responsible for the lateral buoyancy fluxes in our model. Indeed, the plumes are not resolved in the present configuration because the model is hydrostatic. Hence, when gravitational instability occurs in the model, it is dealt with using the convective adjustment, which suppresses any possibility of mixing along slanted paths. However, we do expect slantwise convection to matter in the real ocean, but studying its effect on lateral buoyancy fluxes around a convective patch would require a non-hydrostatic model.

5.6 Baroclinic instability

5.6.1 Background

Long-wave, geostrophic baroclinic instability

Charney (1947) and Eady (1949) studied the instability of a baroclinic current, with different approximations. This is a mechanism of primary importance for the generation of cyclones and anticyclones in the atmosphere, hence for weather forecasting. Eady (1949) found that the growth rate was proportional to the Coriolis parameter, the vertical shear of the horizontal velocity, and inversely proportional to the stratification. Hoskins and McIntyre (1985) described the process of baroclinic instability as two counter-propagating Rossby waves held stationary by the mean sheared flow: "The induced velocity field of each Rossby wave keeps the other in step, and makes the other grow". They noted that, to get strong baroclinic instability on a scale l, the potential vorticity anomalies have to be separated by a distance fl/N where f is the Coriolis parameter and N the vertical stratification, or less.

Geostrophic baroclinic instability was first found to be important for the re-stratification after deep convection by Gascard (1978). He identified the formation of paired vortices by baroclinic instability as a likely cause for horizontal mixing. There have then been more studies in which these pairs were modelled as hetons (Hogg and Stommel, 1985; Legg and Marshall, 1993; Legg et al., 1996; Legg and Marshall, 1998).

This then led to a parameterisation of the horizontal exchange during convection based on the Eady growth rate (Jones and Marshall, 1997; Visbeck et al., 1996), presented at the end of the previous chapter:

$$\overline{v'b'} \propto \frac{\overline{b'}^2}{N} \tag{5.14}$$

If we consider a fully mixed isolated patch surrounded by linearly stratified water, we can write $\overline{b'} \propto (h - z)$, so we expect the lateral buoyancy fluxes due to baroclinic instability to only contribute as an export of water that would decrease with depth.

Poulin et al. (2003) and Pedlosky and Thomson (2003) studied the baroclinic instability of time-dependent currents. Poulin et al. (2003) carried out a linear stability analysis for oscillatory shear flows of both discrete and continuous profiles and found that "the oscillations can stabilise (destabilise) an otherwise unstable (stable) shear flow". Pedlosky and Thomson (2003) used a two-layer model in the beta-plane for periodic shear for the basic current and found similar results. They also showed that aperiodic behaviour could appear for a critical value depending on the frequency. This might be a mechanism that increases the tendency of the patch to be baroclinically unstable.

Shortwave baroclinic instability

Blumen (1979) used a linearized two-layer Eady model to study short-wave baroclinic instability. His study showed that the short and long-wave baroclinic instabilities depend on the relative layer depth and on the jump in stratification between the two layers. The short wave instability is bounded by two discontinuities in the potential vorticity, such as can occur at the base of a mixed layer and at the interface between the mixed layer and the atmosphere.

Nakamura (1988) used a 2D linear stability analysis and confirmed that the short-wave disturbances were trapped in the layer of low static stability (e.g. in the mixed layer). He found that the scale of the instability shifts to shorter scale

(and larger growth rate) as the static stability decreases - as the Richardson number decreases, non-geostrophic effects become important.

Traditional baroclinic eddies induce an ageostrophic circulation, shown on figure 5.18. Lapeyre et al. (2006) showed that this circulation affected the mean stratification profile, leading to a surface frontogenesis that makes the restratification process more effective, even though the growth rate of the eddies themselves is not affected. Nurser and Zhang (2000) also observed that the ageostrophic circulation was leading to the tilting of the buoyancy gradient and to the shallowing of the mixed layer over the front. This ageostrophic circulation is linked to that studied by Moore and Peltier (1987), whose sketch is shown on figure 5.19. The circulation linked to the long-wave baroclinic eddies leads to a secondary baroclinic instability on a smaller scale, along a small front within the eddy. Figure 5.19 shows wiggles developing around the eddies on smaller scales, which are the surface manifestation of the instability.

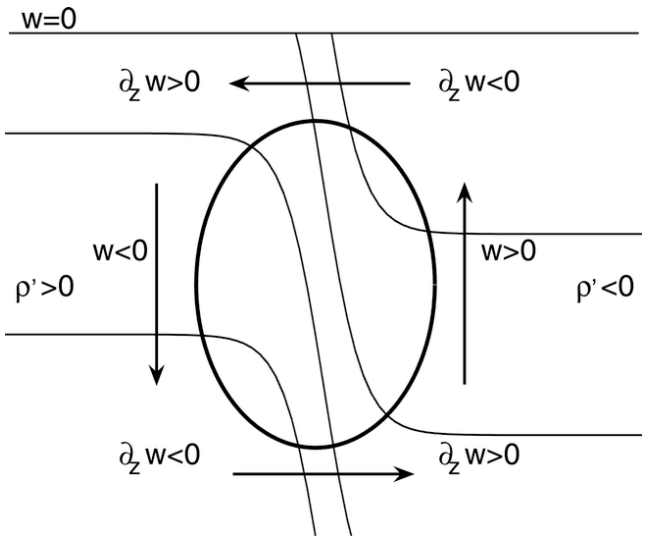

Figure 5.18: Sketch of the ageostrophic circulation that develops in response to strengthening of a horizontal density front. The figure corresponds to a vertical cross section through a submesoscale front. Thin lines are isopycnals. The arrows correspond to the ageostrophic circulation. Light fluid is on the right of the figure and dense fluid on the left. w is the vertical velocity and ρ' the density anomaly. From Lapeyre et al. (2006)

Boccaletti et al. (2007) showed the importance of baroclinic instability on the sub-mesoscale. While the deep mesoscale (long-wave)instabilities studied previously develop on a longer timescale, the mixed layer instabilities are ageostrophic and have fast growth rates of O(day) on a scale of O(1km) (Boccaletti et al., 2007; Fox-Kemper et al., 2008).

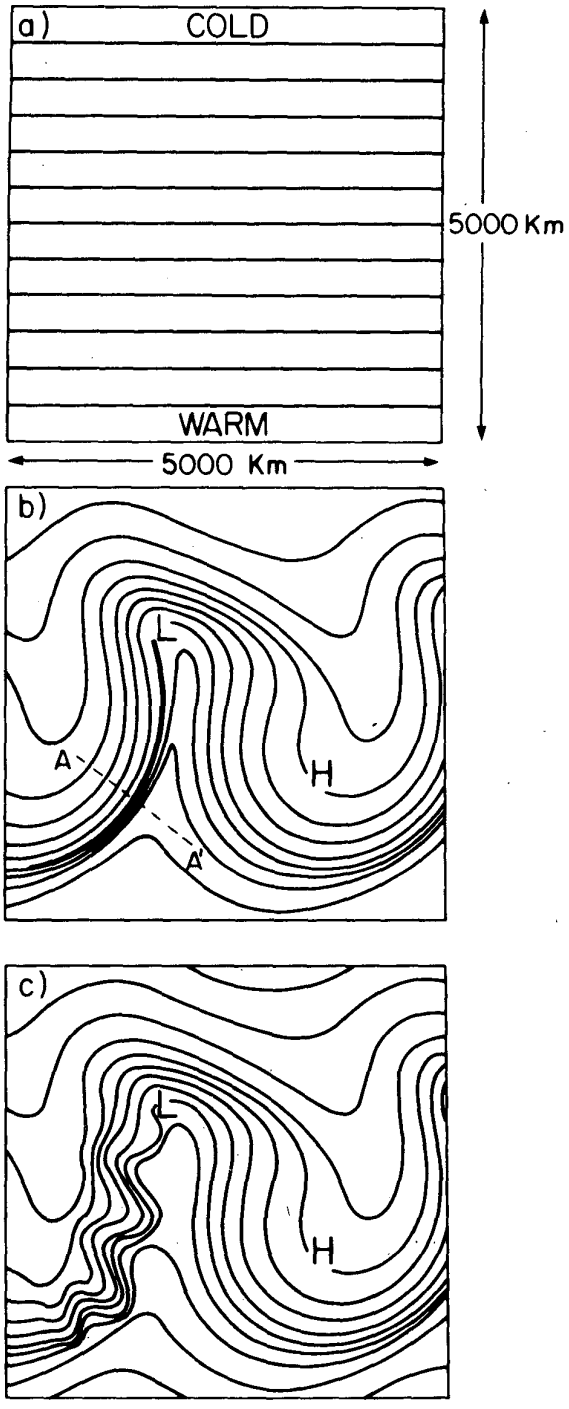

Figure 5.19: Schematic horizontal sections through an idealised atmosphere showing the first two bifurcations in the atmospheric energy cascade. The solid lines denote the potential temperature isotherms. (a) The initial state of the atmosphere with the smooth equator-pole thermal gradient. (b) The finite amplitude Charney-Eady baroclinic wave that grows on the above initial state. (c) The finite-amplitude cyclone-scale baroclinic waves that grow on the polar front. From Moore and Peltier (1987)

5.6.2 Discussion

Decomposition of the lateral buoyancy fluxes

We use temperature flux $\overline{U_{rad}T}$, proportional to the heat flux, as a proxy for the lateral buoyancy fluxes. We can decompose it: $\overline{TU_{rad}} = \overline{T} \cdot \overline{U_{rad}} + \overline{T'U'_{rad}}$. We calculate here the flux of temperature anomaly, where the temperature anomaly is the difference between the actual temperature and the zonally and vertically averaged temperature: $T - \overline{\overline{T}^z}^\theta$. Note that the temperature anomaly flux is related to the temperature flux by:

$$\overline{U_{rad}(T - \overline{\overline{T}^z}^\theta)}^\theta = \overline{U_{rad}T}^\theta - \overline{U_{rad}}^\theta \overline{\overline{T}^z}^\theta \tag{5.15}$$

Figure 5.20 displays the three terms of the decomposition of $\overline{U_{rad}(T - \overline{\overline{T}^z}^\theta)}^\theta$, which is linked to the lateral buoyancy: $\overline{U_{rad}(T - \overline{\overline{T}^z}^\theta)}^\theta$, $\overline{U_{rad}}^\theta(\overline{T}^\theta - \overline{\overline{T}^z}^\theta)$ and $\overline{U'_{rad}T'}^\theta$. The term $\overline{T}^\theta \overline{U_{rad}}^\theta$ is 2 orders of magnitude smaller, and is positive at the base of the mixed layer at the very beginning of the simulations. This behaviour is consistent with a geostrophic adjustment of the dense water that tends to slump along the isopycnals until arrested by the circulation in thermal wind balance around the patch. We notice that the term $\overline{U'_{rad}T'}^\theta$ is dominant. We associate it to eddy activity. This activity appears intensified slightly during periods of high heat loss, although this is not as pronounced as for the lateral buoyancy fluxes. This means that the term $\overline{U_{rad}}^\theta \overline{\overline{T}^z}^\theta$ is important in setting the periodicity of the signal, and it is consistent with the fact that we have a net transport of buoyancy across the edge of the patch for each layer - that term, varying with the zonal average of velocity, vanishes when vertically averaged because of mass conservation. This provides a paradoxical picture of what is happening at the edge of the patch. On the one side, the eddy term dominates the zonally averaged temperature anomaly flux across the edge of the patch, but the mean term dominates zonally averaged temperature flux.

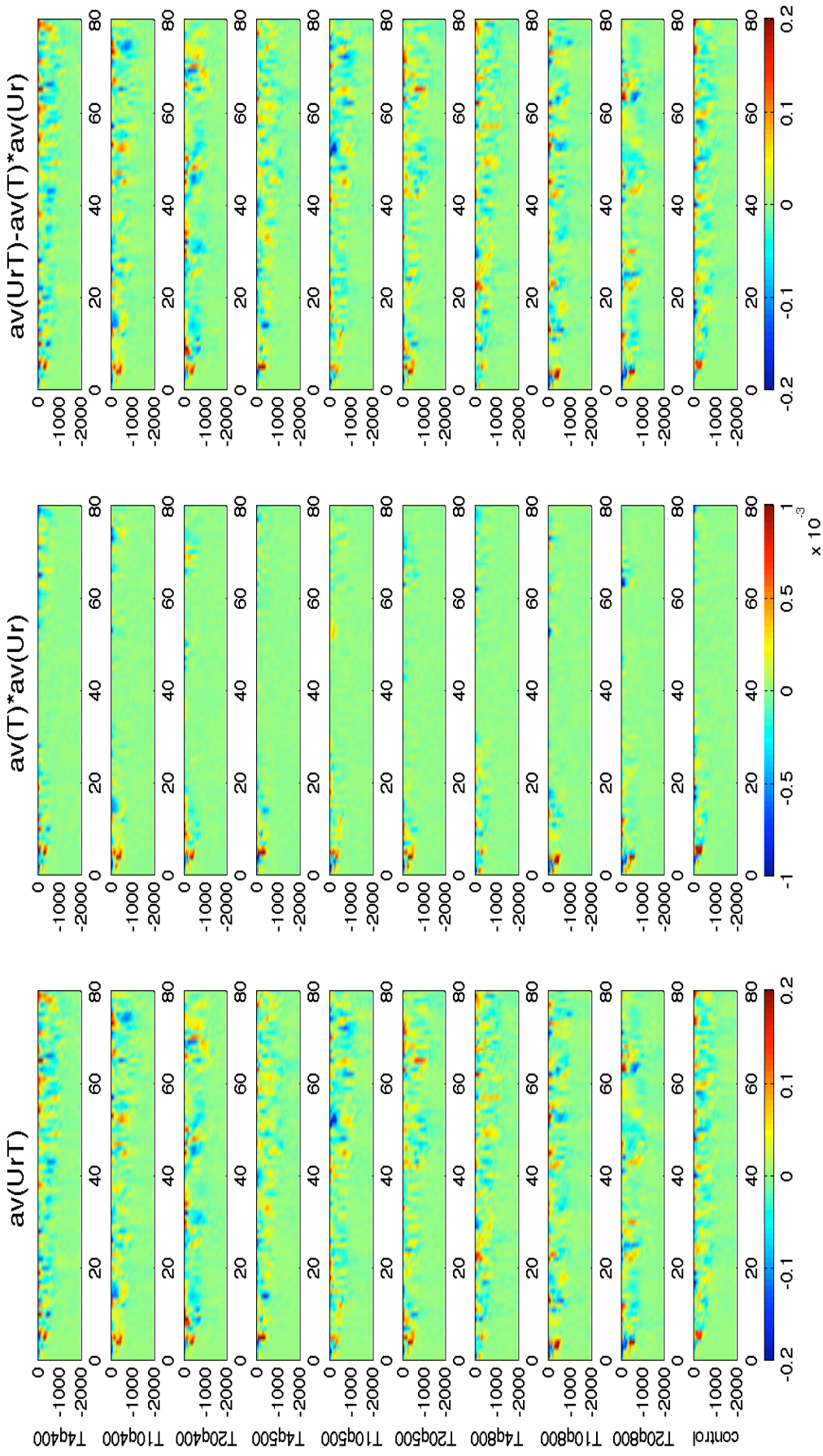

Figure 5.20: $\overline{TU_{rad}}$ (left), $\overline{T} \cdot \overline{U_{rad}}$ (middle) and $\overline{T'U'_{rad}}$ (right) for the nine experiments and the control run. Horizontal axis is time (days), and vertical is depth (m). The color scale is in Kms^{-1}.

Potential Vorticity

We now consider the potential vorticity (PV) defined as:

$$Q = -(\frac{f\vec{z} + \vec{\nabla} \wedge \vec{u}}{\rho}) \cdot \vec{\nabla}\rho \tag{5.16}$$

where $\vec{u}$ is the 3D velocity vector. Figure 5.22 shows snapshots of the potential vorticity for run T10q800 (top) and for the control run (bottom). The PV value is dominated by the term $f\frac{\partial \rho}{\partial z}$ (not shown here). Potential vorticity should be conserved for each element of volume, except in case of mixing (Haynes and McIntyre, 1990).

The initial positive potential vorticity is due to the stratification then reduced by the surface cooling. The control run again shows the difference in structure between the Turner and the post-Turner regime. We clearly see the development and pinching off of baroclinic eddies whose core is characterised by low potential vorticity. The quick recapping at the surface is particularly intense at the transition between the two regimes. This transition being sharper in run T10q800 (higher $B_{high} - Blow$), the near surface stratification linked to recapping is even higher than the initial one N_0. In the post-Turner regime, the location of the patch is much less constrained.

Figure 5.22 shows that near the surface, the stratification is stronger in the time varying case than in the control run. This is in agreement with the fact that the lateral buoyancy fluxes are much less active in the control run than in the other simulations. The difference between the time varying and the control runs is mainly due to the surface stratification, as we have seen in figures 5.21 and 5.22 that there was not much difference in the stratification below $200m$.

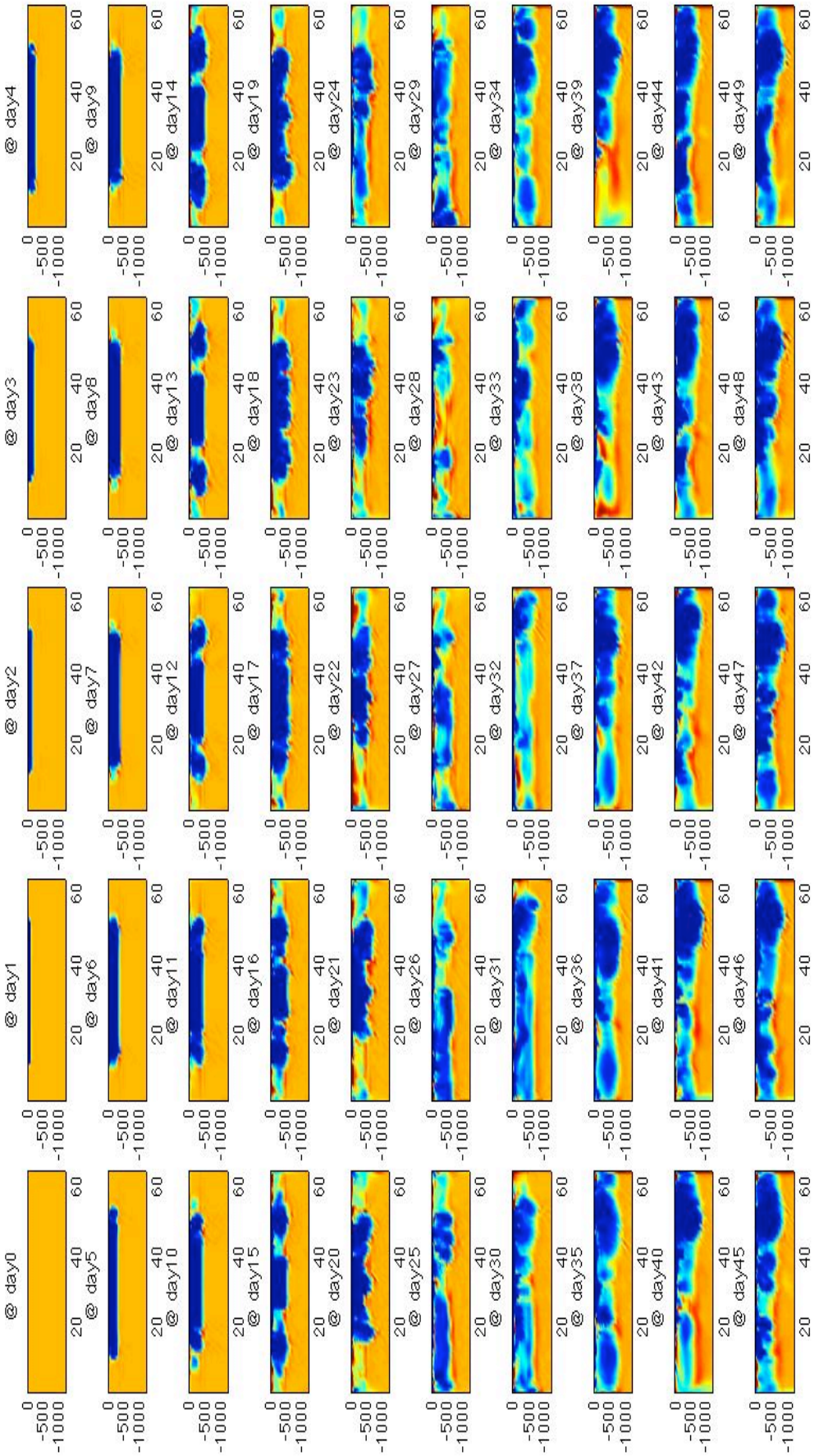

Figure 5.21: Snaphots of sections of potential vorticity (range $[0, 10^{-11}]$ from blue to red) for the 50 first days of the experiments r20q200 with open boundary conditions. Horizontal axis is distance from the centre of the patch (km), and vertical is depth (m).

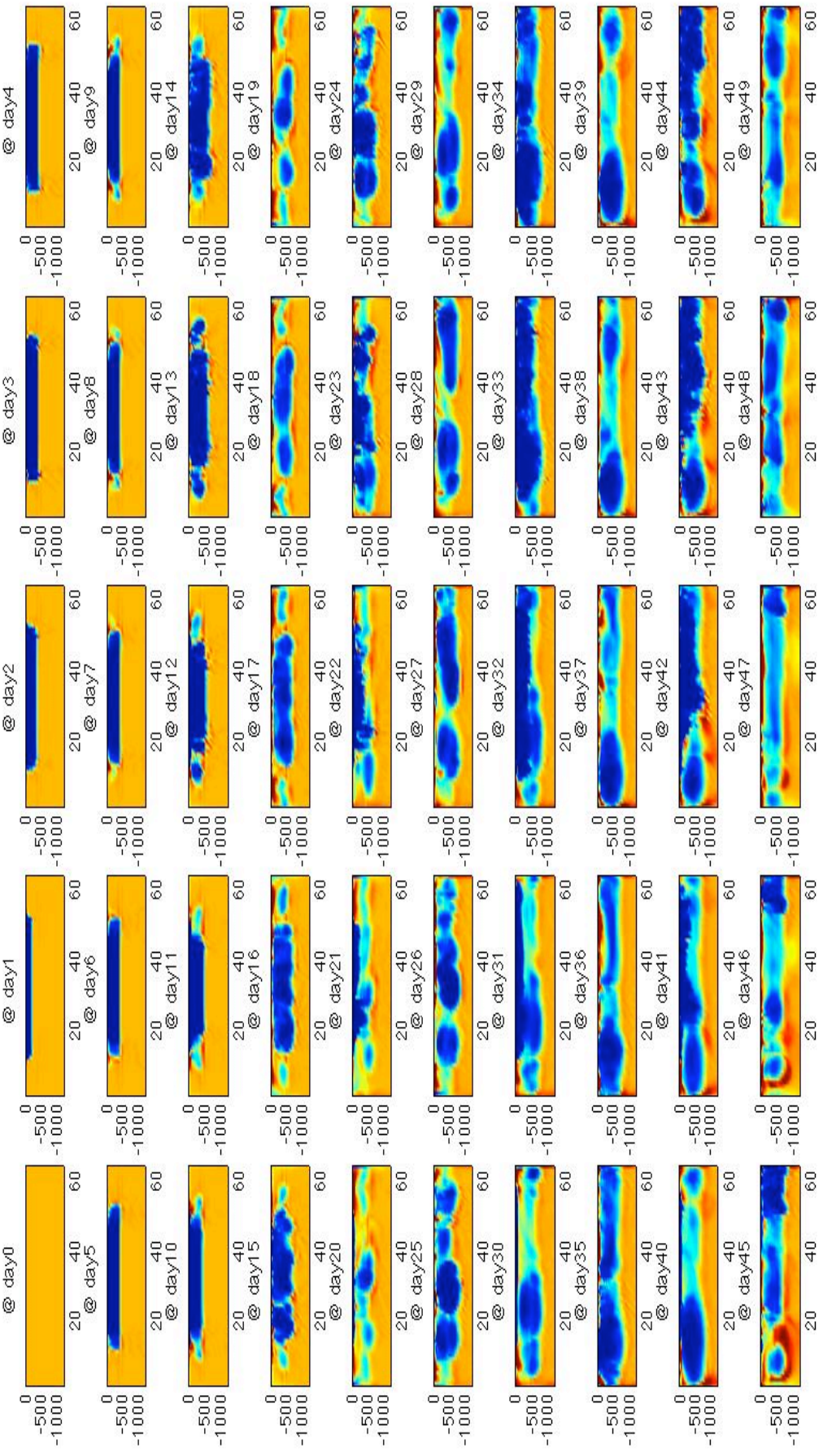

Figure 5.22: Snaphots of sections of potential vorticity (range $[0, 10^{-11}]$ from blue to red) for the 50 first days of the experiments T10q800 with open boundary conditions. Horizontal axis is distance from the centre of the patch (km), and vertical is depth (m).

Residual stratification in the mixed layer: $\mathbf{N^2_{mix}}$

Figure 5.23 displays the temperature difference between $z = -200m$ and $z = -762.5m$ at the centre of the patch ($r <= 2km$) for the different simulations. During the first 20 days or so, the temperature difference decreases, corresponding to the deepening of the mixed layer. Once the mixed layer is deeper than $-762.5m$, the stratification increases again, in a variable way depending on the simulations. There is a residual stratification in the mixed layer which is completely eroded only when the cooling lasts long enough. The run called 'short', for which the forcing is constant at $200W/m^2$ for 20 days and $0W/m^2$ thereafter, shows that the mixed layer recovers a restratification very quickly although it is not as strong as the initial stratification. It also shows that restratification is not a linear process. We saw that the integrated lateral buoyancy fluxes were smaller in the case of the control run than in the time varying simulation, explaining this by a more fully mixed layer in the case of the control run. Figure 5.23 does not show any clear evidence of this. Hence the main difference in stratification happens near the surface, above $200m$, as confirmed by figures 5.17 and 5.16.

Theory

Buoyancy conservation in the general case We write the buoyancy conservation for the cylinder of water at the surface of which the cooling is applied:

$$\frac{\partial BC}{\partial t} = LBF + SBF \tag{5.17}$$

where BC is the buoyancy content, and LBF and SBF the lateral and surface buoyancy fluxes. We have: $SBF(t) = B(t)\pi R^2$. Following the parameterisation of the lateral buoyancy fluxes used by Visbeck et al. (1996) and Jones and Marshall (1997):

$$\overline{v'b'} = c\frac{(N^2(t=0) - N^2(t))^2 h^3}{l_{bz} f} \tag{5.18}$$

if we take into account the fact that there is a residual stratification within the mixed layer. We call N_0 the stratification around the patch, which is also the initial stratification. c is a proportionality constant determined empirically from numerical and laboratory experiments. Hence:

$$LBF(t) = c2\pi R\frac{h^4(N_0^2 - N_m^2)^2}{l_{bz} f} \tag{5.19}$$

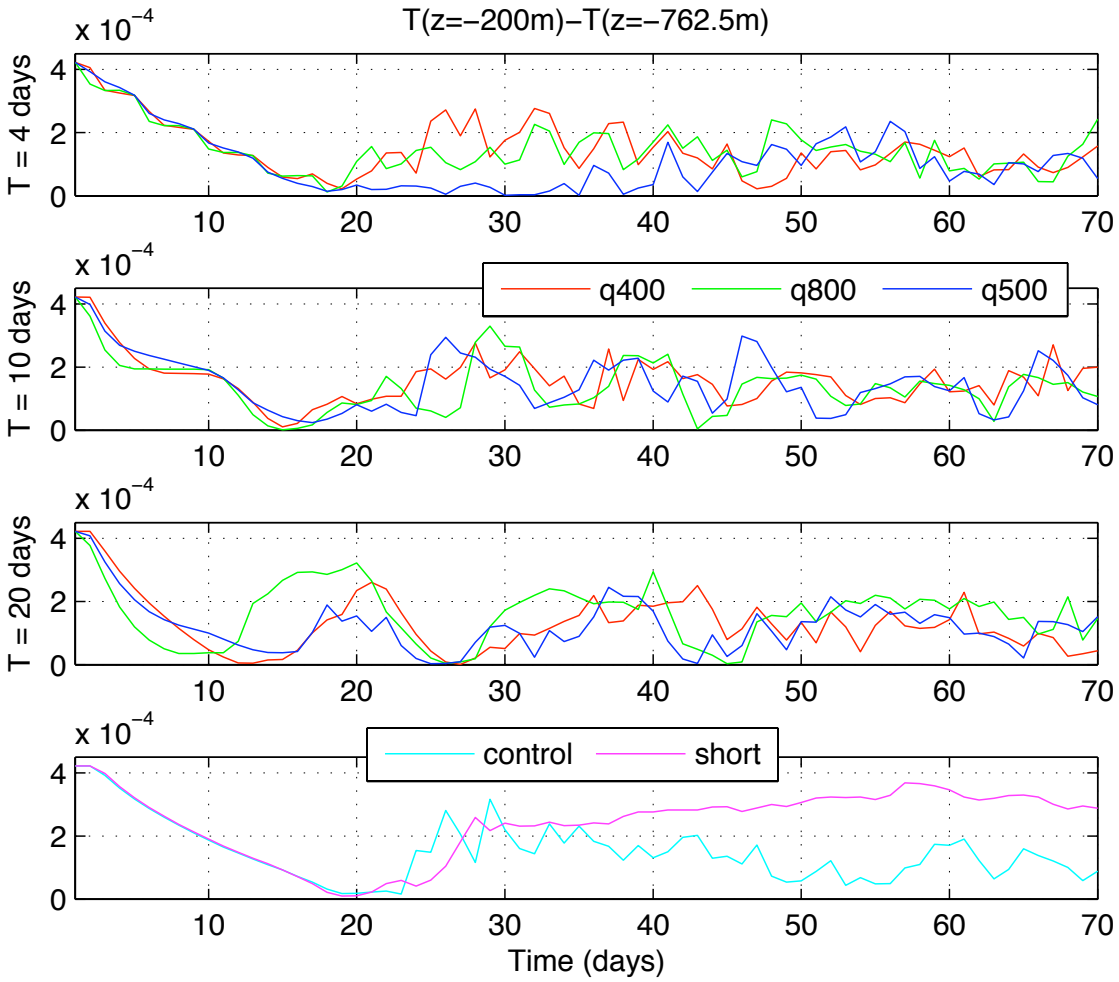

Figure 5.23: Vertical temperature difference between $z = -200m$ and $z = -762.5m$ for the nine experiments, the control run, and a run 'short' that is like the control run except that the forcing is stopped after 20 days.

in which c is a constant. If we assume that the mixed patch has a homogeneous stratification $N_m(t)$ (which, as we have seen, is not necessarily null), and that the stratification below remains unchanged we can write:

$$\frac{\partial BC}{\partial t} = \pi R^2 \frac{\partial}{\partial t} \int_{-h(t)}^{0} \bar{b} dz \tag{5.20}$$

where $\bar{b}$ is the mean buoyancy content of the mixed layer. This leads to:

$$\frac{\partial BC}{\partial t} = \pi R^2 \frac{\partial}{\partial t} (\frac{h^2 N^2}{2}) \tag{5.21}$$

$$\frac{\partial BC}{\partial t} = \pi R^2 (N(t)^2 h(t) \frac{\partial h}{\partial t} + h(t)^2 N(t) \frac{\partial N}{\partial t}) \tag{5.22}$$

The change in buoyancy content can be due to both a change of the mixed layer depth (deepening) or to a change in the mixed layer's stratification.

We can rewrite the buoyancy conservation equation:

$$N_m(t)^2 h(t) \frac{\partial h}{\partial t} + h(t)^2 N_m(t) \frac{\partial N_m}{\partial t} = c \frac{h(t)^4 (N_0^2 - N_m^2(t))^2}{l_{bz}(t) f R} + B(t) \tag{5.23}$$

Application to simple cases The one-dimensional deepening corresponds to this balance in a case of no lateral buoyancy fluxes ($LBF(t) = 0$). Visbeck et al. (1996) considers the same balance until the mixed layer has reached its final depth, after which they consider a balance with no time change ($\frac{\partial BC}{\partial t} = LBF + SBF = 0$). Jones and Marshall (1997) consider the case $B(t) = 0$ and $\frac{\partial h}{\partial t} = 0$, assuming that $N_m << N_0$ - the restratification happens through a gradual increase of the mixed layer stratification rather than through a change of the mixed layer depth.

Application to our case In most of our simulations, the mixed layer depth varies very little once the steady state is reached. We will use equation 5.23 in the case $\frac{\partial h}{\partial t} = 0$, which yields:

$$\frac{h^2}{2} \frac{\partial N_m^2}{\partial t} = c \frac{h^4 (N_0^2 - N_m^2)^2}{l_{bz} f R} + B(t) \tag{5.24}$$

There is here an important difference with the theories of Visbeck et al. (1996) and Jones and Marshall (1997) in that we do not neglect N_m^2 in the lateral buoyancy fluxes, so this introduces a relaxation term of power 2 (or 1 if l_{bz} is chosen as the Rossby radius of deformation) towards the background stratification. This equation shows that N_m^2 would follow the buoyancy forcing very closely if there were not this relaxation term, which slows down the transition. The term $(N_0^2 - N_m^2)^2$ is key to explaining the responsiveness of the lateral buoyancy fluxes to the surface forcing, which would be constant if we neglected N_m. The buoyancy forcing reduces the stratification (buoyancy loss implies $B(t) < 0$), hence increasing the $N_0 - N_m$ term and the lateral buoyancy fluxes.

Physically, the mixed layer depth is not going to change if the stratification rebuilt during the low heat loss period is equal to the stratification destroyed during the period of high heat loss. Having a constant mixed layer depth implies that the stratification within it varies in a similar way as the forcing, i.e. periodically. We now estimate the change in stratification occurring when the surface

is cooled, and the change in stratification occurring when the forcing is off. We then consider the implications of having those two changes of equal magnitude. The idea is that we can then find a threshold period above which the mixed layer depth will continue to increase over time.

We use the 1D deepening approximation to have an estimate of the stratification destroyed when the forcing is high (hence neglecting the lateral buoyancy fluxes for that time, which is realistic if the heat loss does not stay high long enough for the lateral buoyancy fluxes to adapt): $h^2N^2 = 2B_{high}T_{high}$. Considering $B_{low} = 0$ can lead to an estimate of the restratification rebuilt when a low heat loss is applied. Equation 5.24 suggests that the variation of the stratification over time in that case is proportional to $\frac{1}{t^2}$ as a leading order, hence $N_m \propto \frac{1}{T_{high}^2}$.

Equating the loss in stratification during a high heat loss period and the gain in stratification during a low heat loss period leads to $B_{high}T_{high}T_{low}^2 \propto K$, where K is a dimensional constant depending on the steady state mixed layer depth. Calculating $B_{high}T_{high}T_{low}^2$ leads to values that can be very different for all our runs, showing that this approach is too simplistic to find a threshold period above which the mixed layer keeps on deepening.

A key assumption we made was that T_{high} (i.e. the time during which high heat loss is applied) was short enough to neglect the lateral buoyancy fluxes when high heat loss is applied. This assumption stops being valid when T_{high} gets long enough, and the period for which it stops being valid is smaller than the threshold period. The non validity of this assumption is consistent with the fact that the lateral buoyancy fluxes are important when the surface heat loss is. This shows that the phenomenon of restratification cannot be considered without considering the deepening of the mixed layer.

A more sensible estimate of the threshold period is given by comparing T_{high} to $t_f(Q_{high})$ (i.e. the time at which the final mixed layer depth for a constant forcing of Q_{high} is reached). If $T_{high} > t_f(Q_{high})$, the mixed layer depth will become deeper than $h_f(\overline{Q})$ within the first cycle. Under that limit, which is not usually reached by Mistral events in the Mediterranean, for example, the time variability of the lateral buoyancy fluxes does not impact the mixed layer depth.

Richardson number

The Richardson number is defined as the ratio between the vertical stratification and the velocity shear squared: $Ri = \frac{N^2}{u_z^2+v_z^2}$. A negative Richardson number indicates gravitational instability and should lead to convective mixing. Ac-

cording to Boccaletti et al. (2007), a Richardson number close to 1 means that ageostrophic baroclinic instabilities are likely to occur while Stone (1966, 1970) finds that $Ri > 0.95$ should lead to conventional baroclinic instability. These values have been identified in limit theoretical cases, but we will use them as guidelines here.

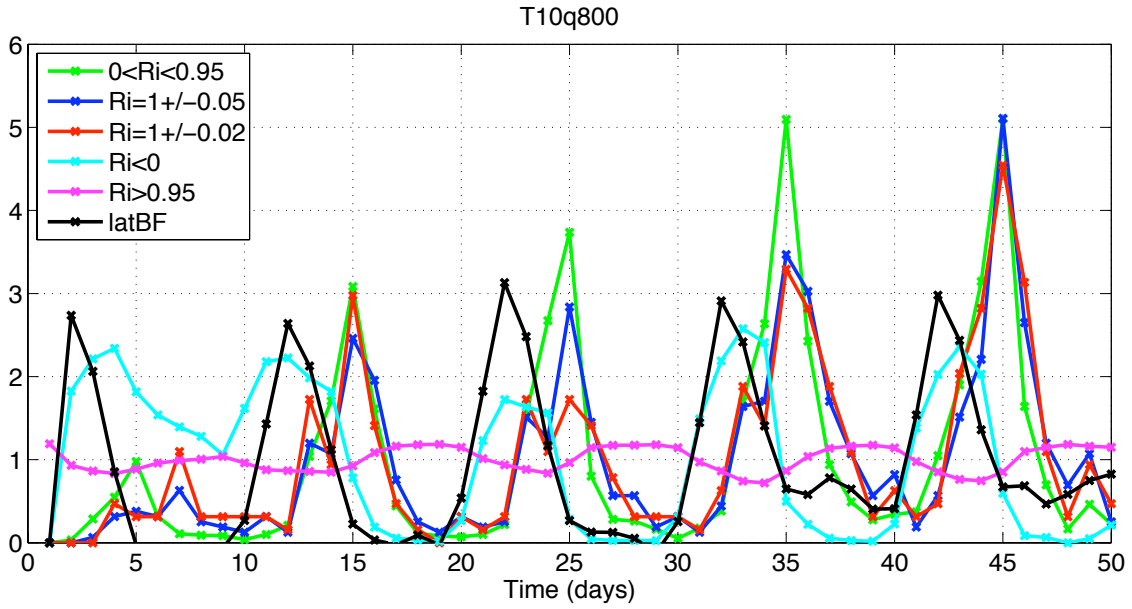

Figure 5.24: Normalised number of points in a section through the convective patch of grid points that are in the ranges of Richardson number indicated in the legend, for run T10q800. The black line represents a non-dimensional lateral buoyancy fluxes, for comparison.

For simulation T10q800, we selected a section through the patch and classified the grid cells in that section into different categories according to their value of the Richardson number. Figure 5.24 shows the normalised number of grid cells for each categories, as indicated in the legend, along with the lateral buoyancy fluxes (without any units). The aim is to compare the variations of each count with time. We see that convective instabilities and lateral buoyancy fluxes start increasing simultaneously for each cycle. However, the maximum in the number of cells that are statically unstable is reached after the maximum in lateral buoyancy fluxes. This seems to show that the lateral buoyancy fluxes are limited and cannot keep increasing even though the convective activity is still intensifying. This would be in agreement with a restratification process fed by the lateral buoyancy gradient which in turn reduces that gradient. However, the number of grid cells that have values for the Richardson number that should correspond to the other types of instabilities, including ageostrophic baroclinic instability, reach their maximum after the lateral buoyancy fluxes and the tendency for convective instability have decreased significantly. This can be explained by the fact that this

instability is fed by very local gradients within or at the edge of the mixed layer, hence require a primary process for restratification before they can start acting. Could that process be conventional baroclinic instability? Looking at the plot for $Ri > 0.95$, we see that the number of points with that value increases when there is no cooling and decreases when the cooling is on at the surface. The number of grid cells never reach zero because the cells for which the horizontal velocities are very low fall into that category, hence it might not be only representative of conventional baroclinic instability. We have seen in the previous chapter that the growth rate for baroclinic instability could be very fast, so it is possible that there are sharp variations that we do not catch with daily snapshots. As such, this does not allow us to identify clearly which process is responsible for the quick response of the lateral buoyancy fluxes to the surface forcing, although it seems to rule out ageostrophic instability.

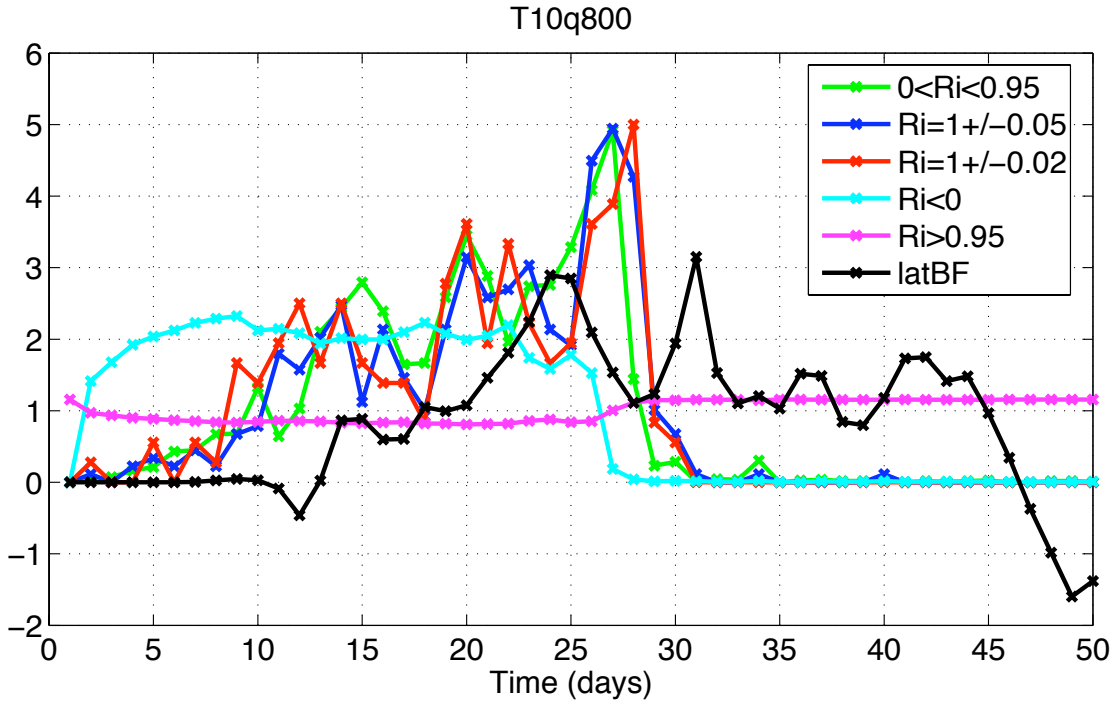

Figure 5.25: Normalised number of points in a section through the convective patch of grid points that are in the ranges of Richardson number indicated in the legend, for run short. The black line represents a non-dimensional lateral buoyancy fluxes, for comparison.

As a comparison, we show a similar plot for the simulation 'short', for which a constant forcing is applied for 20 days, and then stopped for the rest of the simulation. See figure 5.25. In that case, the lateral buoyancy fluxes are quite low for the first ten days and then increase. The number of grid cells with Richardson numbers close to one start increasing a few days before the lateral buoyancy fluxes. It also shows a further increase after 20 days, when the surface cooling

stops. The initial cooling for the 'short' run is four times less intense than for the T10q800 run, which can explain the fact that the instabilities develop later, i.e. after about 10 days instead of 3 to 5 days for the T10q800 run. In the 'short' run, the restratification seems to follow a traditional pattern, as if it were driven by a slowly (over a few days) developing baroclinic instability. This hints at a threshold effect. The mechanism that leads to a very quick response of the lateral buoyancy fluxes is put into place very quickly if the forcing is intense enough, which does not appear to be the case for a cooling of $Q = 200W/m^2$.

5.7 Properties of the water mass formed

For each simulation, we describe the properties of the mixed patch in terms of density classes. We select all profiles at $t = 80days$ from the integration box, for the simulations using periodic boundary conditions at the sides. This is, for all runs, at the end of a period of low forcing. For these profiles, we calculate the thickness of each isopycnal layer. We keep the full depth profiles as we can distinguish the water below by their higher densities and it avoids possible bias due to errors in the mixed layer depth calculation. Figure 5.26 shows the histogram for each experiment.

The histograms clearly show that the time variability of the forcing has a significant effect on the composition of the water mass formed, even though our model only takes pressure in account. They also give an indication on how well the water is mixed. A broad histogram with a not very high maximum is due to a quite stratified mixed layer. The runs $q500$ show a higher degree of vertical mixing than the other series, linked to the fact that the surface heat loss is always on ($Q_{low} = 100W/m^2$). The histograms are all getting broader as the period increases, indicating more stratification within the mixed layer. This agrees with the fact that a higher T also means a higher T_{low}, so the mixed layer has had more time to restratify in the case of long periods T.

The histogram corresponding to the experiment idealT4q800 has two local maxima. It is likely that the colder one comes from convective water while the warmer one is due to restratifying water from the surroundings. We do not see this in any other experiment, likely because for longer periods, the two waters have had time to mix/diffuse the colder maximum away and because there is less discrepancy between the convective and surrounding waters for milder forcings.

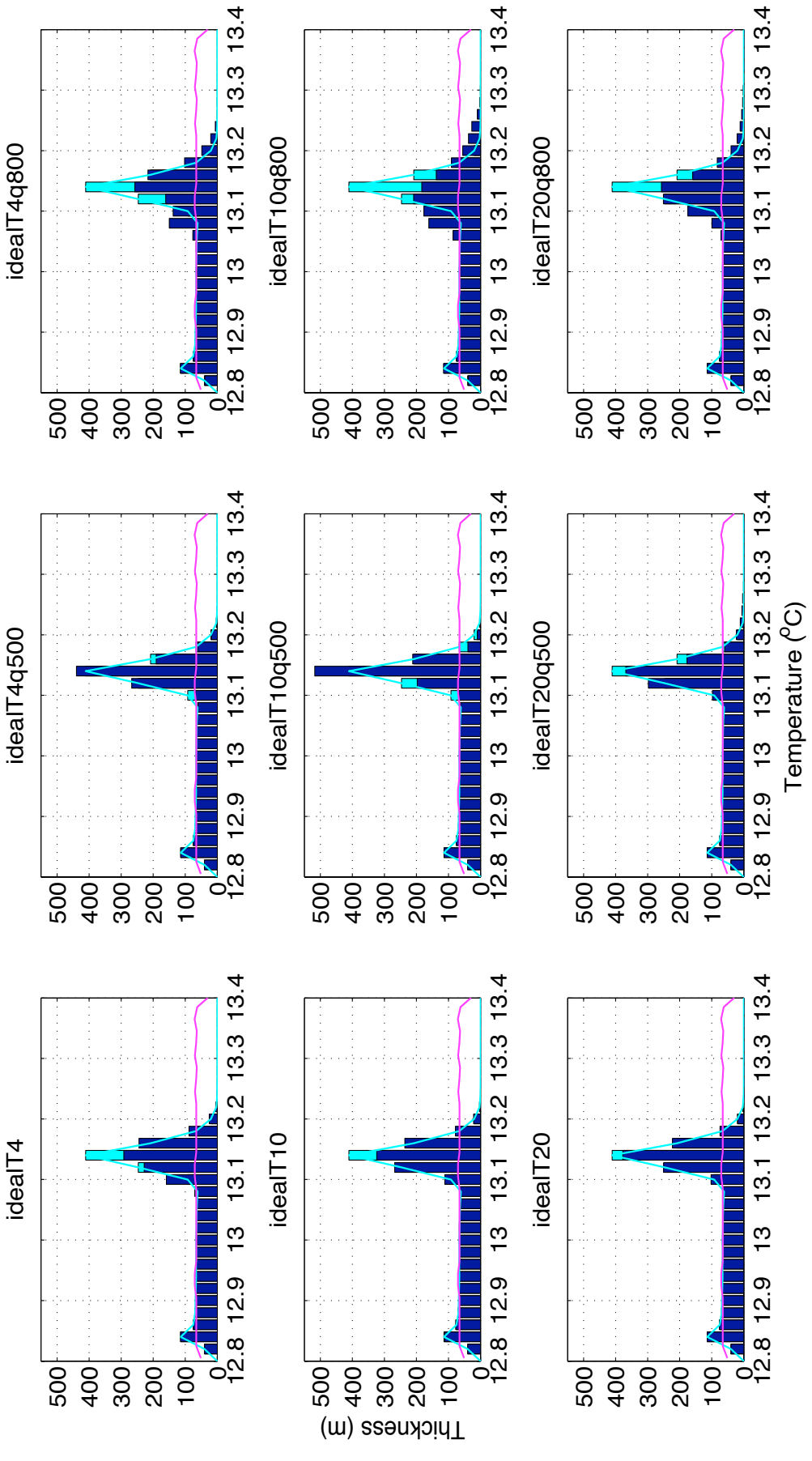

Figure 5.26: Thickness of the isopycnal layers for the nine experiments. The cyan histogram and line present the same result for the control run. The pink line shows the values of the histogram at the initial time.

We attribute the change in isopycnal layer thickness near the bottom to diffusion. This phenomenon is the same in all experiments.

5.8 Conclusion

We recap here the sequence of events at the beginning of convection. The deepening is first one-dimensional like. Then, simultaneously the patch of cold, dense water tends to slump horizontally as the horizontal buoyancy gradient develops. It gets strong enough for the rim current to develop and stop the slumping. The rim current then becomes unstable to baroclinic instability that generates eddies responsible on average for a lateral gain of buoyancy. The eddies are responsible for lateral fluxes, which offset the buoyancy loss from the surface and the deepening stops. They occasionally invert the lateral buoyancy gradient, leading to an anticyclonic rim current.

We have found that, in our model, the lateral buoyancy fluxes were reacting very quickly (faster than a day), while the traditional consensus is that baroclinic instability has growth rates slower than observed (a few days). We have investigated different physical processes that could cause either the baroclinic instability to react faster, or that could generate lateral buoyancy fluxes:

- Geostrophic adjustment: It occurs on timescales of order a day - the rim current is in thermal wind balance almost at all times - and can generate inertial waves. It also leads to frontogenesis, hence possibly increasing growth rates for baroclinic instability.

- Slantwise convection: It was ruled out because our model does not resolve plumes. However, it could have a significant effect on the restratification of a convective patch in the real ocean.

- Conventional baroclinic instability: We cannot discard it. Although the lateral buoyancy gradient does not vary as periodically as the surface forcing, we might be missing important information due to the use of daily snapshots. The Eady problem applied to high lateral buoyancy gradient leads to growth rates that can be fast, even faster that a day.

- Ageostrophic baroclinic instability: Its growth rate has been shown to reach a peak during periods of low buoyancy forcing rather that when the forcing is high.

From this, we conclude that the most likely candidate to explain the very fast response of the lateral fluxes is conventional baroclinic instability. A different configuration of the model is necessary to confirm this. A non-hydrostatic model should be used, in order to address the potential effect of slantwise convection. Indeed, modelling slantwise convection properly requires the plumes to be resolved in the model. Due to computational limitations, we suggest that the model be integrated on a small channel with periodic boundary conditions along one direction. For the other direction, a vertical wall should be used on the side of the domain that will be cooled, with open boundary condition at the other side. This way, the deepening should be 1D like at one side of the channel - the vertical wall will prevent any lateral buoyancy fluxes - and the restratification processes can be observed at the other end of the channel. Then, part of the domain can be cooled at different periods. An important point is to output results at least every hour, and maybe with an even better time resolution, even if this means that the results can only be output for one particular period.

The time variability of the buoyancy forcing has an impact on the final structure (residual stratification) of the mixed patch, hence on the characteristics of the water mass formed. This is already visible in a model with homogeneous salinity, i.e. in terms of density only, but would be even more relevant in the real ocean where, for a given density, the convected water can have a very different signature in terms of salinity and temperature than the ambient water even for water masses of same density. This could be addressed in more detail by including both temperature and salinity in the model.

Chapter 6

Convection in the Labrador Sea

6.1 Introduction

In this chapter, we will present results from a study of glider data obtained in the Labrador Sea in 2004 and 2005 by Charlie Eriksen and Peter Rhines from the School of Oceanography of the University of Washington. This study was, with the laboratory experiments described in appendix D, the object of a three-month visit to Seattle in the framework of the Research Mobility Program (RMP) of the Worldwide University Network (WUN). It aimed at finding out if the results obtained in the numerical model could be reproduced in the laboratory and if they were observed in the ocean.

The chapter is divided as follows. We will first give some background about convection in the Labrador Sea. Then, results from the gliders' data study are presented. The last section concludes.

6.2 Background

6.2.1 Water Masses and Large-Scale Circulation

Water Masses

Figure 6.1 shows typical potential temperature (T) and salinity (S) profiles for water masses in the Labrador Sea at the Bravo site and along the AR7W section (see figure 6.2 for location). We notice, at the Bravo site, a subsurface T maximum at about 200m depth.

The AR7W section shows the superposition of different water masses. In 2005, the intermediate layer is formed by two 'vintages' of Labrador Sea Water (LSW)

with the relatively warm and saline Irminger Water (IW) at the eastern side of the section. The left plot of figure 6.1 shows a more classical situation for a pre-winter period, where the IW is responsible for the subsurface temperature maximum. It is eroded during the production of LSW, in winter, so it does not appear in summer, just after convection.

Below 2000m, we find the North-East Atlantic Deep Water (NEADW), overlying the Denmark Strait Overflow Water (DSOW).

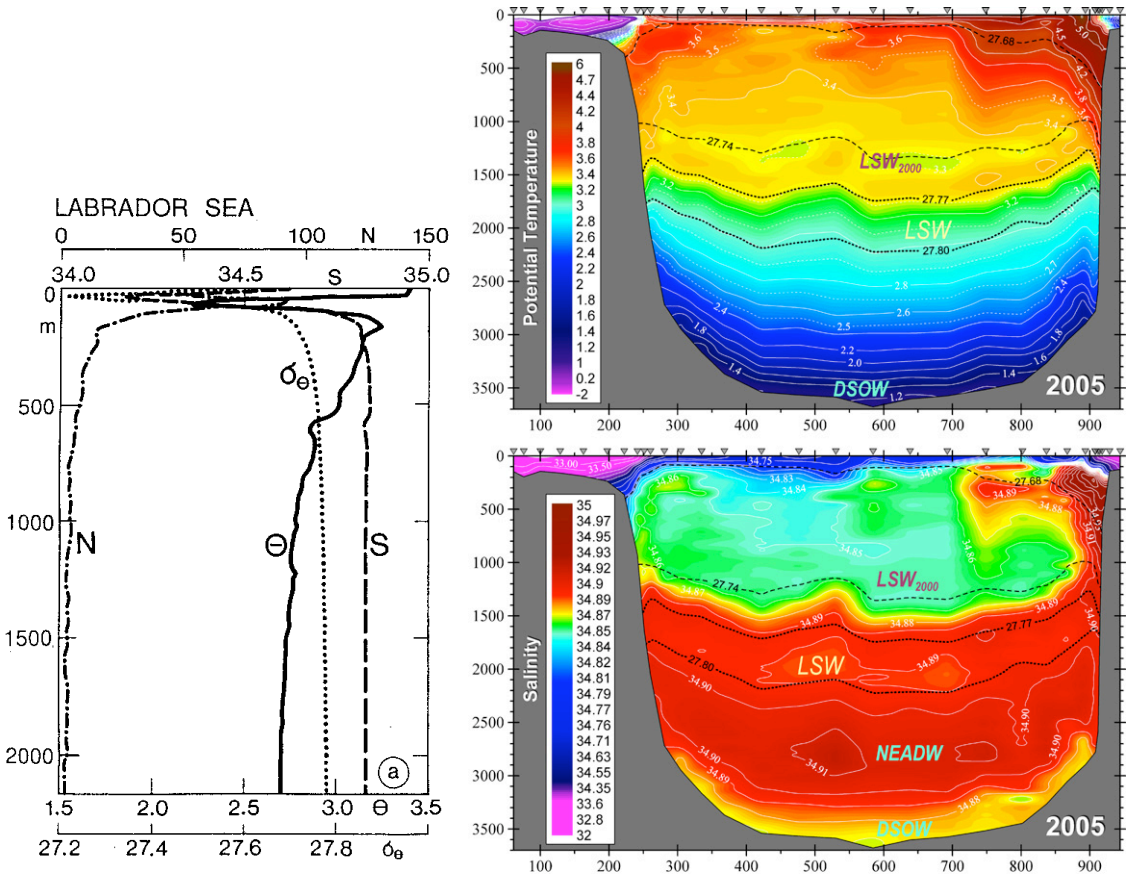

Figure 6.1: Characteristics of water masses found in the Labrador Sea. Left: Typical vertical profiles observed at station Bravo, from Marshall and Schott (1999a). Right: Vertical section plots of potential temperature (top, °C) and salinity (bottom) for the 2005 occupation of AR7W, from Yashayaev (2007). The section runs from the Labrador coast (left side) to the west coast of Greenland (right side). Depth on the vertical axis is in m and distance on the horizontal one is in km.

Large-Scale Circulation

Fresh and cold water enters the Labrador Sea along the west coast of Greenland in the Greenland Current (GC) and forms, with the Labrador Current (LC) along the Labrador coast, a cyclonic gyre of about $800km$ of diameter (figure 6.2). Further offshore the Greenland coast, at greater depths, the Irminger Current (IC)

brings warmer and saltier water into the Labrador Sea. The North Atlantic Current forms the southeastern arm of this cyclonic gyre.

One of the differences between convection in the Mediterranean and in the Labrador Sea is this difference, in the Labrador Sea, between the scale of the rim current ($r = O(20km)$) and the gyre scale ($r = O(400km)$). In the Mediterranean, these two scales coincide, making the location of the convective site more strongly controlled on a scale $r = O(40km)$. As a comparison, in the Labrador Sea, the Rossby radius of deformation has a value of a few kilometres, and the natural (non-dimensional) Rossby radius is 0.04. Lilly and Rhines (2002) observed convective eddies of horizontal scale $r \sim 5 - 15km$.

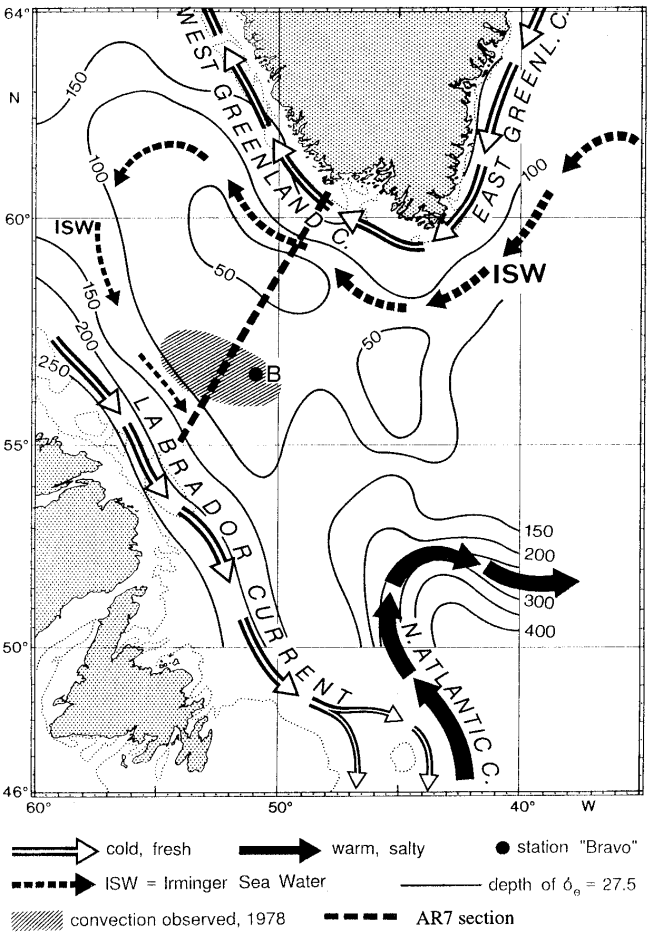

Figure 5. Circulation schematic showing the cyclonic circulation and preconditioning of the Labrador Sea convection regime. The depth of the σ_ϑ = 27.5 isopycnal in the early winter is contoured in meters. The warm circulation branches of the North Atlantic Current and Irminger Sea Water (ISW), and the near-surface, cold, and fresh East/West Greenland and Labrador Currents are also indicated. The position of *Bravo* is labeled "B." It is important to emphasize that this is a circulation schematic; in reality, the circulation is highly time dependent and comprises a vigorous eddy field on the deformation radius (~7 km).

Figure 6.2: Map of the area, main currents and position of the Bravo site. From Marshall and Schott (1999a), their figure 5.

6.2.2 History of the Observations

Early Observations

After the success of the MEDOC cruises in the Mediterranean, the CSS Hudson campaign in the Labrador Sea in 1976 brought evidence of LSW formation by convection, based on CTD and moored-current data (Gascard and Clarke, 1983; Clarke and Gascard, 1983).

The Labrador Sea Deep Convection Experiment

The Lab Sea Group in the late 1990s thoroughly observed deep convection in the Labrador Sea (Marshall et al., 1998a; Marshall and Fiadeiro, 2002; Krahmann et al., 2003).

This major effort combined data obtained from different platforms:

- Winter Cruises (Pickart et al., 2002),
- An extensive network of floats and drifters, including surface drifters (Cuny et al., 2002), Lagrangian floats (Steffen and D'Asaro, 2002), VCM floats, ALACE floats, PALACE floats (Lavender et al., 2002), RAFOS floats (Prater, 2002),
- Moorings (Lilly et al., 1999; Lilly and Rhines, 2002; Lazier et al., 2002),

complemented by modeling studies (Legg and McWilliams, 2002; Harcourt et al., 2002).

Measurements were also obtained for the atmosphere from aircraft missions, remote sensing, and in situ measurements from the RV Knorr (Bumke et al., 2002; Renfrew et al., 2002; Sathiyamoorthy and Moore, 2002).

6.2.3 Interannual Variability of Deep Convection

The variability of the T and S in the Labrador Sea has been studied by Yashayaev (2007) from the 1960s: "The basin was very warm and salty between the mid-1960s and early 1970s, and fresh and cold between the late 1980s and mid-1990s."

We will here briefly describe the very peculiar Great Salinity Anomalies (GSA) and then focus on the period 1990-2005.

Great Salinity Anomalies

Dickson et al. (1988) described the Great Salinity Anomaly as the "widespread freshening of the upper 500-800m layer of the Northern North Atlantic". It was a mainly advective event that could be traced for more than 14 years (1968-1982) around the subpolar gyre. Another GSA was identified later in the 1980s. Belkin et al. (1998) confirmed its advective character, and noticed that the second anomaly seemed to have a greater advective speed.

Belkin et al. (1998) speculated that the origin of these two anomalies was different. He argued that the GSA in the 1970s was due to a freshwater pulse from the Arctic, while the one in the 1980s formed locally in the Labrador basin, because of severe winters.

The 1990-2005 period

The 1990s started with a period of intense convection until 1993 (Lazier et al., 2002), associated with the cooling and freshening of the Labrador Sea (Yashayaev, 2007). 1994 marked the reversal from a cooling and freshening trend to a period of heat and salt accumulation (Yashayaev, 2007), which Lazier et al. (2002) called "multiyear restratification".

Avsic et al. (2006), from mooring records in the Central Labrador Sea, identified three regimes of interannual variability depending on the depth for the period 1994-2005. The top layer (0-500m) showed strong seasonal variations added to a warming trend ($+0.05°\mathrm{C}/year$ at 300m) while the salinity signal showed a pulse like decrease at the beginning of each year and a large interannual variability. The 500-1200m layer underwent two distinct warmings. The temperature increased from $3.0°\mathrm{C}$ to $3.3°\mathrm{C}$ on the 1997-1999 period, and then remained more stable until the 2003-2005 period, during which the temperature increased by $0.1°\mathrm{C}$. The warming did not appear between these two periods, likely because of the cooling of the upper 1000m in winter 1999-2000, due to intense air-sea fluxes (Yashayaev, 2007). At 1500m, the temperature increased at a rate of $+0.06°C/year$ and the salinity at $+0.005psu/year$ as part a larger scale warming.

6.2.4 Restratification and eddy field

From the mooring deployed at the Bravo site, (Lilly and Rhines, 2002) observed a number of eddies on the period June-November 1994, that can be classified in two types:

- Anticyclonic eddies ($r \sim 5 - 15km$), with a cold and fresh core at mid-depth. They were identified as coming from the convective area. Testor and Gascard (2006) identified similar eddies in the Mediterranean ($r \sim 5km$), both cyclonic and anti-cyclonic. However, they noticed that the anticyclones were longer-lived.

- Irminger rings are warm cyclones ($r \sim 15km$), probably originating from the Irminger current.

See Lilly et al. (2003) for a more extensive review on the Labrador Sea eddies.

Prater (2002) and Brandt et al. (2004) observed the eddy field using satellite data. The region around ($61°N$,$52°W$) shows very high eddy kinetic energy (EKE), as also seen in models (Eden and Böning, 2002): see figure 6.3.

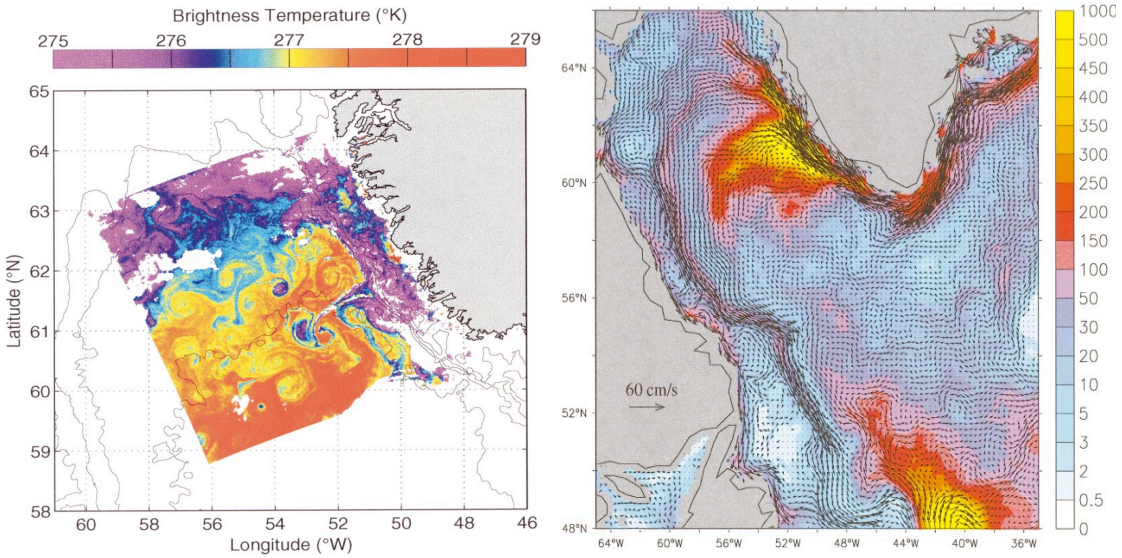

Figure 6.3: Left: Sea Surface Brightness Temperature from the alongtrack scanning radiometer (ATSR) on the European Space Agencys remote sensing satellite ERS-1 on 10 July 1992. From Prater (2002). Right: Near surface EKE and mean circulation in an eddy resolving model. From Eden and Böning (2002)

The buoyant Irminger rings are thought to be a major component of the post-convective restratification as shown by an idealized model by Katsman et al. (2004). Straneo (2006) showed that restratification was "characterized by a drift of properties toward boundary current values". Hatun et al. (2007) using gliders and altimetry, sampled Irminger rings and showed that these could account for the rapid restratification. However, Chanut et al. (2008), using a numerical model, showed that these eddies decayed before entering the convective region.

6.3 Presentation of the data set

6.3.1 Seagliders

The idea of a buoyancy driven oceanographic instrument was first envisioned by Douglas C. Webb in 1986 (Griffiths et al., 2007). The great potential of such instruments for ocean observations was seen by Stommel (1989). Gliders have since been developed (Davis et al., 2003; Rudnick et al., 2004; Eriksen et al., 2001) and are now being used by more and more research groups (Griffiths et al., 2007). Figure 6.4 describes how a glider works, and shows images of the Seaglider, which has been developed at the Applied Physics Laboratory (APL). These gliders have been shown to have the longuest endurance, with a world record of 7 months in the ocean as of December 2008. The APL and the School of Oceanography of the University of Washington (UW) are now designing gliders that should be able to go as deep as 6000m, so they would be able to sample virtually anywhere in the ocean (C. Eriksen, personal communication). All the data (uncalibrated) collected during UW's glider missions are available in real-time at http://iop.apl.washington.edu/seaglider/.

6.3.2 Data set

We use the data from three gliders, sg014, sg015 and sg016, deployed in the Labrador Sea in 2004-05. They are all deep gliders that can go down to 1000m. Figure 6.5 shows where and when the gliders sampled the water column. In most cases, we choose to treat the data set as a whole and divide it depending on location and time rather than treating each glider separately. Temperature data have been processed, calibrated and made available by Eleanor Williams at UW.

6.4 Analysis: Winter 2004-05

6.4.1 General

We here focus on the heat content of the top 1000m and on the surface heat fluxes. Figure 6.6 shows the heat content per unit surface area calculated from the temperature profiles $T(z)$ as sampled by the gliders: $HC = c\rho_0 \int_H^0 (T(z) + 273.15)dz$ where $c = 3900J/kg/K$ is the specific heat, $\rho_0 = 1000kg/m^3$ a reference density (we choose the same value as used later in the surface heat flux calculations for

Seagliders fly through the water with extremely modest energy requirements using changes in buoyancy for thrust coupled with a stable, low-drag, hydrodynamic shape. Designed to operate at depths up to 1000 meters, the hull compresses as it sinks, matching the compressibility of seawater.

The autonomous underwater vehicle (AUV) Seaglider is the result of a collaborative effort between APL-UW and the UW School of Oceanography. These small, free-swimming vehicles can gather conductivity-temperature-depth (CTD) data from the ocean for months at a time and transmit it to shore in near-real time via satellite data telemetry.

Seagliders make oceanographic measurements traditionally collected by research vessels or moored instruments, but at a fraction of the cost. They can survey along a transect, profile at a fixed location, and can be commanded to alter their sampling strategies throughout a mission.

Seaglider's cylindrical hull is a series of arched anodized aluminum panels separated by ring frames. The hull is surrounded by a fiberglass fairing to give it a low drag shape.

After each dive Seaglider dips its nose to raise its antenna out of the water. It determines its position via GPS, calls in via Iridium data telemetry satellite, uploads the oceanographic data it just collected, then downloads a file complete with any new instructions.

Seaglider is 1.8 m long and weighs 52 kg—a size and weight that allow easy launching and recovery by two people from a small boat.

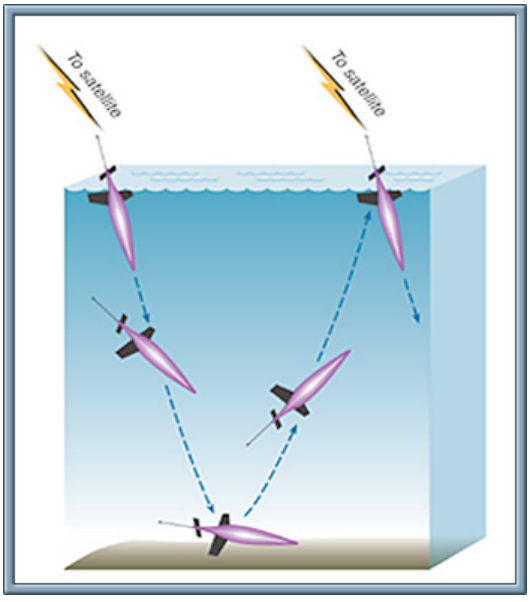

Seaglider can travel at slopes as gentle as 1:5 or as steep as 3:1. At gentle glide slopes the vehicle transits most efficiently, while steeper slopes are used to maintain position and act as a "virtual mooring."

Figure 6.4: Description of the Seaglider by the Applied Physics Laboratory (APL). From www.apl.washington.edu/projects/seaglider/summary.html

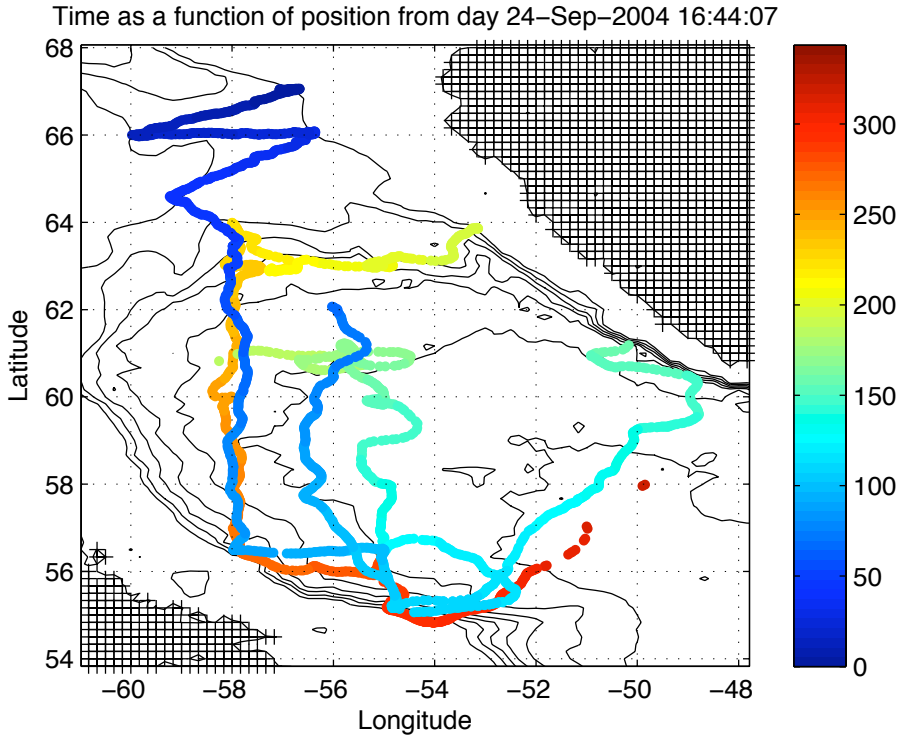

Figure 6.5: Time at which the water column has been sampled by gliders as a function of position. The time is indicated in number of days after the 24/09/2004.

consistency), and $H = 1000m$ the depth of the profile. We only consider profiles that are $1000m$ deep. It also shows the surface heat fluxes taken from the NCEP reanalysis at the time and position of the gliders. The heat flux was calculated using the same method as for the Mediterranean Sea heat fluxes, with coefficients typical of the Labrador Sea, taken from Marshall and Schott (1999a): $(\alpha, \beta) = (0.9 \cdot 10^{-4} K^{-1}, 7.8 \cdot 10^{-4} psu^{-1})$. These plots are over time, while figure 6.7 displays the same information as a function of the position.

Convection is visible on figure 6.6 (bottom plot) starting in December. The heat content of the layer 0-250m decreases until it follows the one of the 750-1000m layer in January. Then the heat content of the four layers keep on decreasing, indicating that the deepening carries on below 1000m. This observed convection coincides with high surface heat loss. During this convective event, two gliders were in the area, and both were near the Labrador current. They show similar records of heat content due to their proximity. The convection observed by the gliders is consistent with previously observed convection across the Labrador slope (Cuny et al., 2005).

Figure 6.7 shows that the heat content is lowest on the shelf ($HC \sim 1.070 \cdot 10^{12} J/m^2$), as expected. It is also expected to be fresher there. The heat content is higher in the boundary current than anywhere else ($HC > 1.082 \cdot 10^{12} J/m^2$).

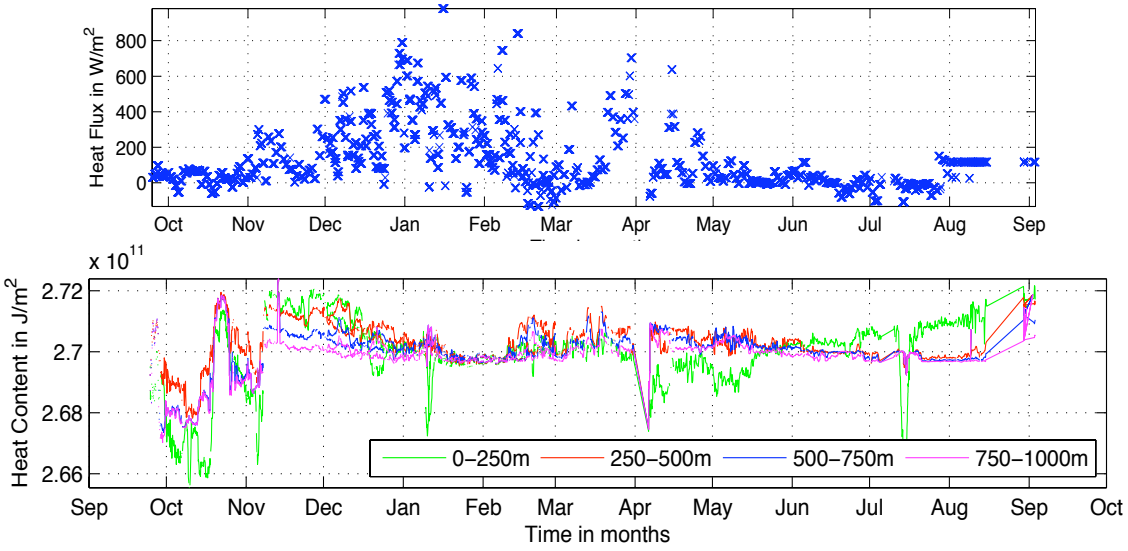

Figure 6.6: Top: Heat flux at the gliders' location as a function of time. The convention is such that a positive flux is a flux from the ocean to the atmosphere. Bottom: Heat content, for four layers, of the water column sampled by gliders as a function of time.

The inner Labrador Sea has a heat content which is significantly lower than in the boundary current ($HC \sim 1.077 \cdot 10^{12} J/m^2$). The high variability of the heat fluxes in some places is associated to a variability in time rather than in space, considering the low resolution of the NCEP data.

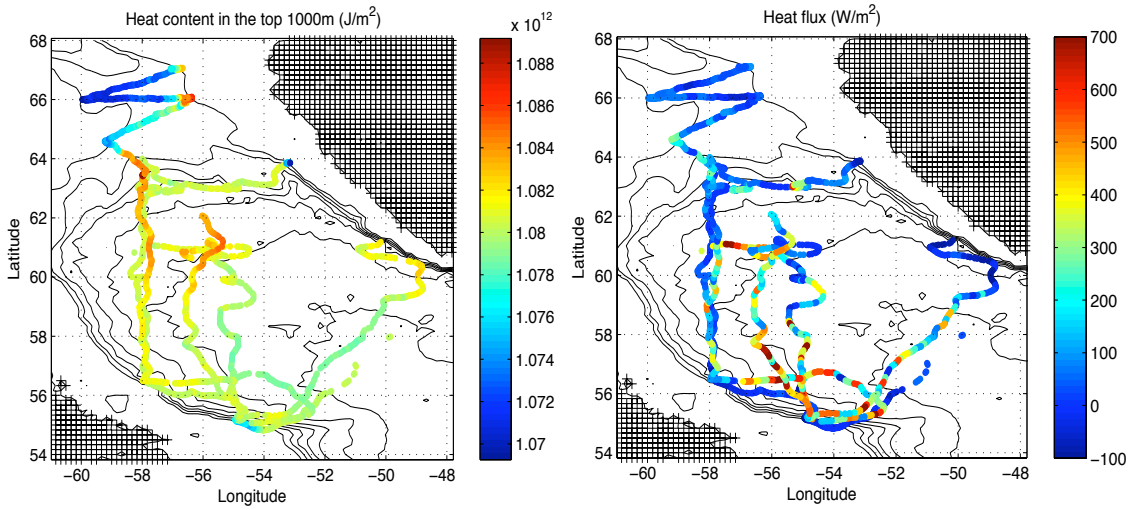

Figure 6.7: Left: Heat content for the top 1000m as a function of the glider's position. Right: NCEP surface heat flux along the gliders' track. The convention is such that a positive flux is a flux from the ocean to the atmosphere.

6.4.2 Focus on the winter period

Two gliders from our data set were in the Labrador Sea in the winter time. We focus on data from these two gliders. Figure 6.8 shows the heat content, its discrete time derivative calculated using a timestep being the time between each dive, i.e. a few hours, the NCEP heat fluxes for the time and location of the gliders and the distance between the two gliders.

We first notice the similarity between the temperature records of the two gliders as they get closer, particularly in January. This validates the measurements and confirms that inter-calibration between two gliders is possible.

Secondly, the time derivative of the heat content is generally of an order of magnitude larger than the heat fluxes, except in the interior, where deep convection is expected to be the most important. This indicates that the cause for the variability must be of advective origin, and hints at the importance of the boundary current in setting that variability.

Both records show an abrupt cooling around the 10^{th} of January. This is related to the position of the gliders. Being closer to the shelf, the surface water is a mix between cold shelf water and warmer boundary current water. There is a similar, longer lived phenomenon on the record obtained by sg015 around the 20^{th} of December, with the same cause - an incursion of the glider closer to the shelf.

We observe restratification in both records, in March. It starts earlier for glider sg014 than for sg015. This coincides with both gliders getting gloser to the boundary current again. Sg014 joins the Greenland current while sg015 gets closer to the Northwestern (NW) part of the boundary current. The restratification is more marked for sg014 which arrives in a part of the boundary current more strongly controlled by the bathymetry than the NW part of the boundary current, and where the current is stronger (see figure 6.3, right). The changes observed can be due to the time variability, but also to the fact that the gliders can move in and out the boundary current, hence observing water masses of different characteristics. The next section focuses on the winter period, and studies different areas separately to show that it is mainly due to the time variability.

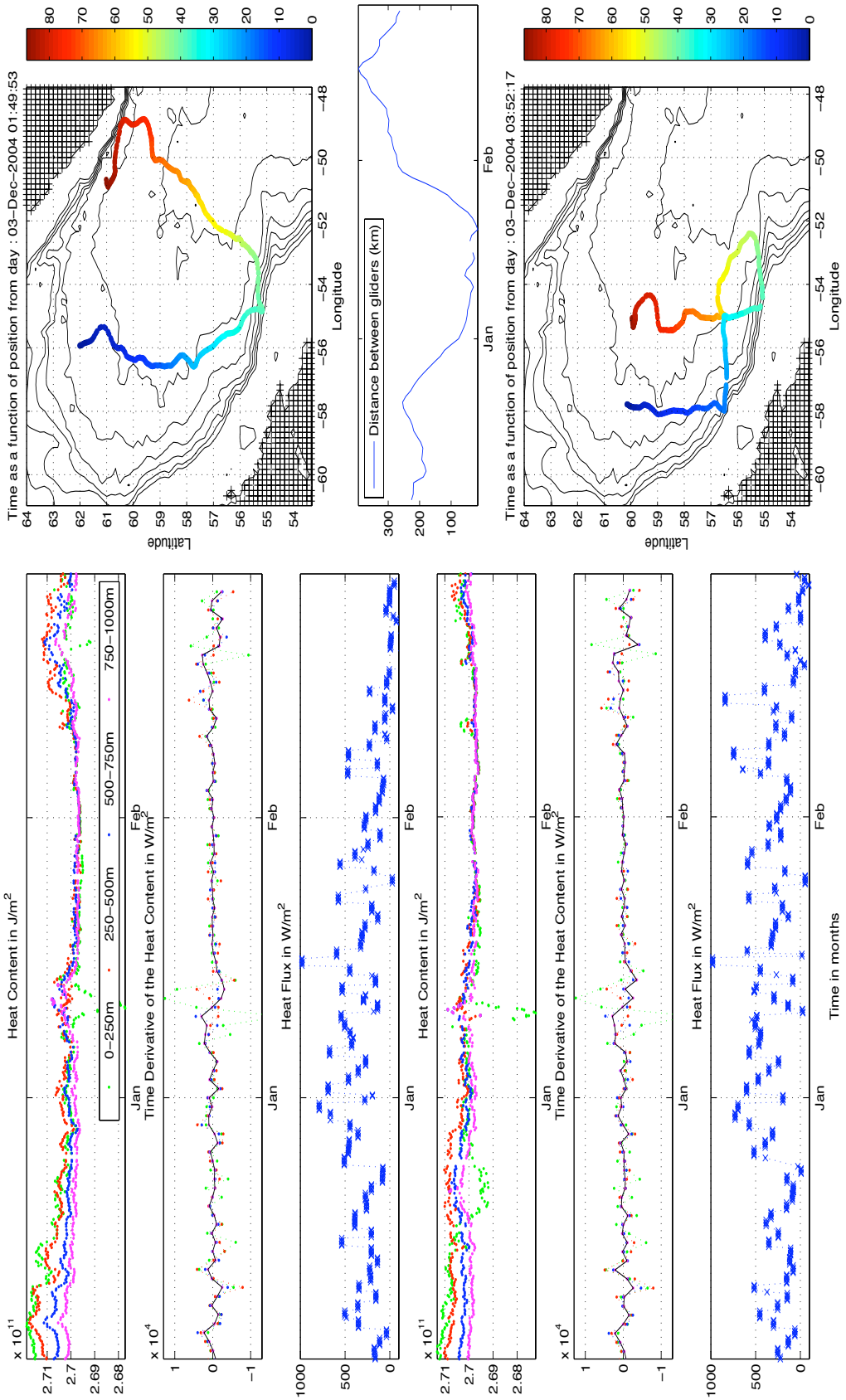

Figure 6.8: Left: Heat content and its time derivative for the four layers and the total heat content (black); surface heat fluxes at the gliders' position and time for two different gliders sg014 (top) and sg015 (bottom). Right: time and position for the corresponding glider, and the distance between the two gliders.

6.4.3 Time variability for a few areas

We define here a few areas ('boxes'; see table 6.1) along the gliders' tracks where we have data at different times to study the evolution of the heat content with time. For each of these boxes, we look at the heat content for each layer over time and compare the total heat content of the top 1000m with the time integrated NCEP surface heat flux ($intHF = \int HFdt$) - see figure 6.9. The gliders' data have been complemented here with ARGO floats. These have been quality checked and made available by Eleanor Williams. The boxes have been designed so that there are enough data in each box to observe the evolution of the convective process during the winter. We also defined a convection box representative of the inner Labrador Sea (figure 6.10).

Box number	Latitude	Longitude
1	62 ° N to 64 ° N	59 ° W to 57 ° W
2	60 ° N to 62 ° N	59 ° W to 57 ° W
3	58 ° N to 60 ° N	59 ° W to 57 ° W
4	56 ° N to 58 ° N	59 ° W to 57 ° W
5	54 ° N to 57 ° N	57 ° W to 52 ° W
6	55 ° N to 59 ° N	52 ° W to 49 ° W
7	57 ° N to 59 ° N	57 ° W to 54 ° W
8	59 ° N to 62 ° N	57 ° W to 54 ° W
9 - convective area	56 ° N to 59 ° N	53 ° W to 51 ° W

Table 6.1: Position of boxes used in figure 6.9.

All the boxes show signs of convection. We will first look at them separately. For box 1, we have data points before (November) and after (May) the winter. The difference in heat content between these two times is slightly less than the corresponding intHF. We also see in the vertical structure that while, in May, it still seems mixed between 250m and 1000m, the top layer is colder than the rest of the water column sampled. This can be linked to the proximity to the shelf and could be caused by a drift of the boundary current further south that would allow more fresh shelf water to be sampled at that location. This is a sign of exchanges with cold and fresh water from the shelf. Note that for some locations, there seems to be an incursion of the glider on the shelf. This does not happen - all the profiles considered here are 1000m. Rather, these are due to errors in the bathymetry and in the calculation of the position of the glider.

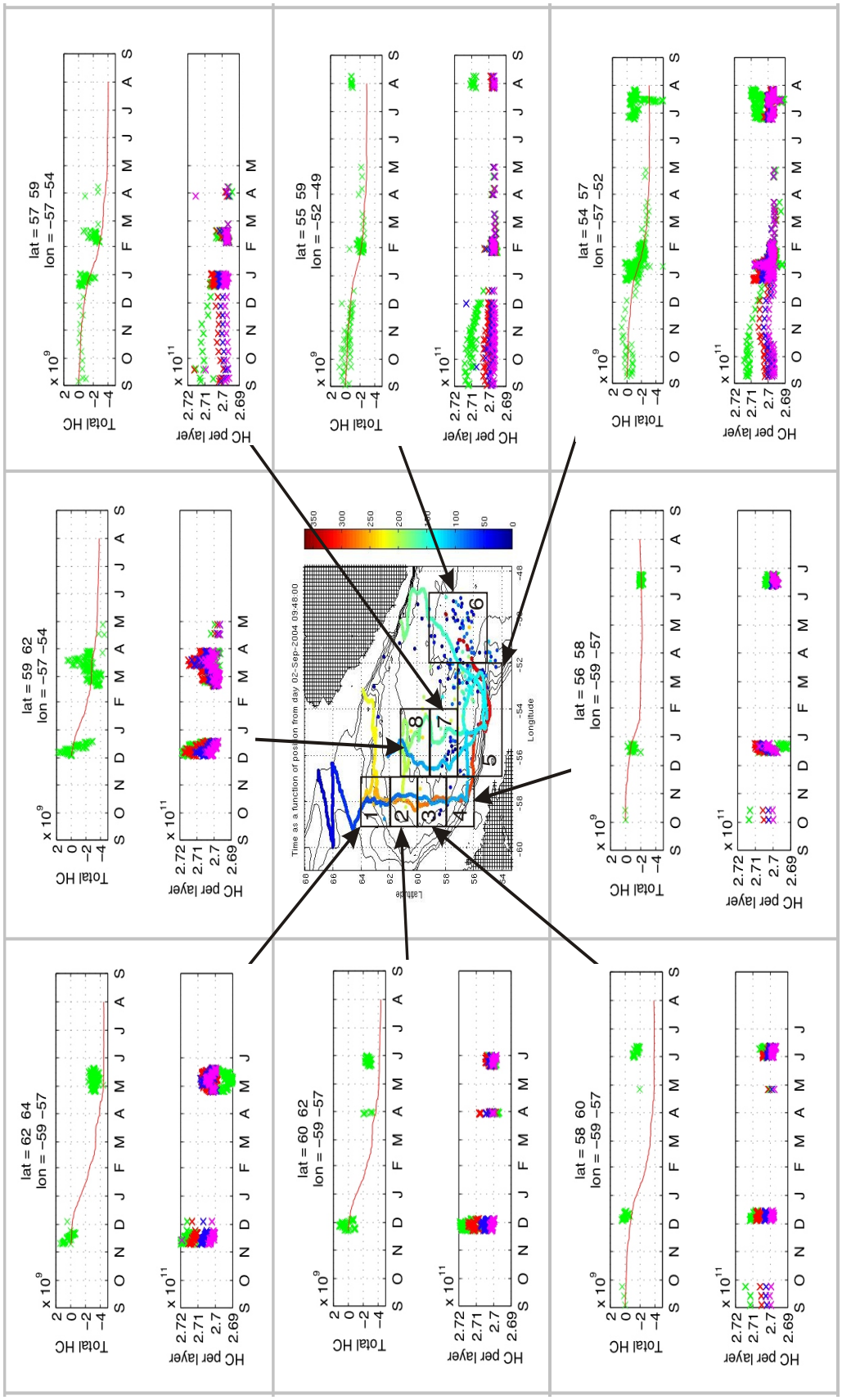

Figure 6.9: Heat content per layer and total heat content in the top 1000m compared to the NCEP surface fluxes integrated from the first data point (red) for eight of the boxes defined in table 6.1. The top 1000m is divided in four layers: 0-250m (green), 250-500m (red), 500-750m (blue) and 750-1000m (magenta).

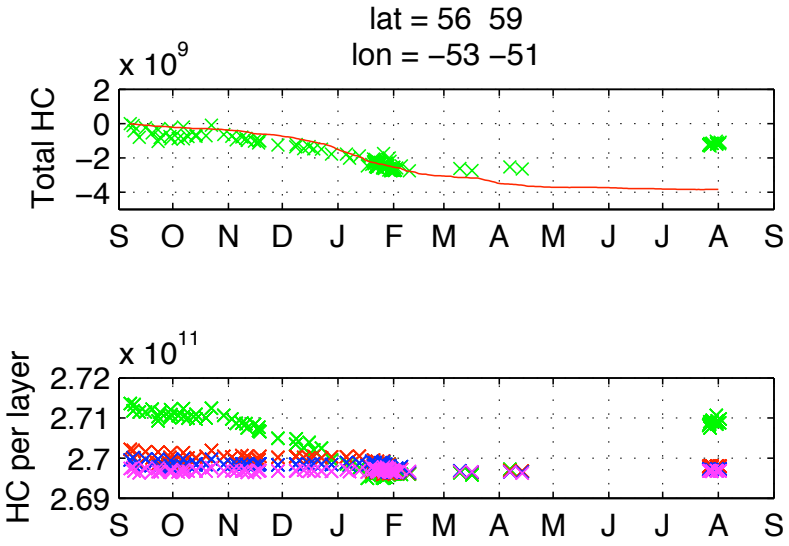

Figure 6.10: Same as figure 6.9 for the convection box (box 9).

Box 2 shows a similar behaviour as box 1, including the cooling of the top layer due to exchanges with the shelf. Having no salinity data, it is difficult to say if these exchanges helps or acts against convection. Considering only the surface layer is affected by the cooling, we can hypothesise that the shelf water is more buoyant, hence would act towards restratification.

Box 3 does not show that reversal in the vertical structure anymore, because the glider is further from the NW shelf and the Labrador current isolates the area from the Labrador shelf. The water column is better mixed in June than in December, a sign of convection. The comparison between a data point at the end of April with data of the June month shows that the heat content increased slightly.

The change in heat content fits surprisingly well with intHF for box 4. In December, we again have a top layer colder than the ones below, due to shelf water. In June 2005, the water column is more mixed than in October 2004, indicating that most of the restratification should happen between June and October if we do not consider any interannual variability.

We have a much more continuous record for box 5. There is good agreement between the change in heat content and intHF until April. The July records show that the water column started to restratify there. Briefly in January and March, there are signs of shelf water with a very cold top layer. In November, we see a period during which the temperature increases between 250 and 750m depth. It is not clear what this is due to.

Box 6 is in the inner part of the Labrador Sea, mainly sampled by ARGO floats.

Results are qualitatively similar to box 5, except that the box is too far from any coast so we do not observe any shelf influence. Also, the November record does not show any warming. On the contrary, it is as we would expect it to be if it were a purely convective area. The top layer is restratified in August, but it is still well mixed underneath at that time.

Box 7 is similar to box 5, including the indications of shelf water and the November warming. The record stops in April, so we do not observe the restratification.

Box 8 shows signs of limited convection although the difference between the well mixed column at the end of April and the stratified one in March indicates this might be a transition zone between the stratified boundary current and the more convective interior. This can be related to the not so constrained boundary current in this part of the Labrador Sea.

Box 9 is representative of the convective area and indeed shows convection starting in November during which the change in heat content follows closely intHF. The August data shows a restratified top layer on top of a still well mixed water column.

We observed convection along the Labrador slope, and in the inner Labrador Sea. Convection is inhibited in box 8, likely because of Irminger rings. With only temperature data from the top 1000m, it is difficult to say how deep the mixed layer is once it has reached 1000m, so we cannot comment much more on the localisation of deep convection.

There are evidences of exchanges with the shelf, likely to act against convection. In a few of the boxes, we observed a re-capping of the water column in Summer rather than a complete restratification of the water column, which takes longer to complete, and might not even be completed before the next winter if the convection of the previous winter is very intense.

The good agreement we have between the values of the integrated heat fluxes and the change in heat content is also due to the fact that, in the Labrador Sea, there are hardly any heating in Summer, and little effect from lateral advection. This is another main difference with the Mediterranean where restratification (and preconditioning for the next winter) is partly due to surface heat gain.

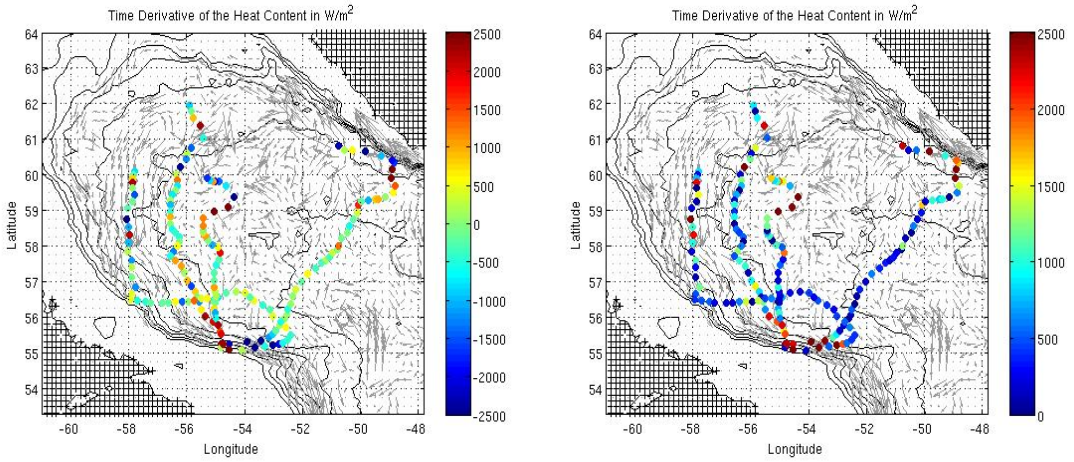

Figure 6.11: Time derivative of the heat content (left) and its magnitude (right).

6.4.4 Boundary current

Figure 6.11 displays the time derivative of the heat content and its magnitude. We use the latter as a proxy for the variability of the heat content. We see that the variability is higher in the boundary current than in the inner Labrador Sea, and is much bigger than the surface heat fluxes in the area. Only in the inner Labrador Sea is the change in heat content of the same order of magnitude than the heat fluxes. Looking at the time derivative rather than its magnitude, we see that the temperature increases when travelling across the Labrador slope towards the coast and decreases when travelling the opposite way, indicating that the glider travels through the relatively warm Labrador current. There is a similar pattern when travelling across the Greenland current. The Northern part of the boundary current, between the Greenland and Labrador slopes, is less spatially constrained and broader, as apparent in the data (also see figure 6.7, left).

An Irminger ring was sampled near (59 ° N, 55 ° W), as indicated by the warm signature of boundary current water that far from the Greenland current (Hatun et al., 2007).

6.5 Conclusion and discussion

The gliders recorded convection in the Labrador current and in the inner Labrador Sea in Winter 2004-05. Convection is inhibited in the stronger Greenland current which generates buoyant Irminger rings. These, in turn, inhibit convection in the NW part of the boundary current. The Labrador and Greenland currents are setting the change in heat content in the slope they follow. The very distinctive cold

shelf water was also sampled, indicating exchanges between the shelf and the boundary current particularly along the NW slope. The known location for convection is in the Labrador Sea interior, but it is generally closer to the Labrador current than to the Greenland current. This may be due to the modification of the boundary current as it travels around the Labrador Sea. It becomes weaker and colder, both because of cross-shelf exchanges and because it has exchanged with the atmosphere at higher, colder latitudes. The contribution of each of these processes - cross-shelf exchanges and air-sea interactions - is not clear yet, although figure 6.9 shows that the change in heat content of the boundary current as it travels around the basin could be explained by the heat fluxes alone.

Chapter 7

Conclusion

We will here recap and discuss the main results of this thesis. This thesis aimed to answer the questions about deep convection set in the introduction:

- What are the relative effects of buoyancy loss compared to preconditioning?
- What are the relative effects of the integrated buoyancy loss compared to the short-term time variability of the buoyancy loss?

We will here summarize how far we have answered these questions and discuss further work.

7.1 What are the relative effects of buoyancy loss compared to preconditioning?

Mixed Layer Depth

To answer this question, we used the NCEP, Medar/Medatlas and Dyfamed data sets, focusing our study on the Gulf of Lion, western Mediterranean Sea. We showed that, under our assumption, the variability in preconditioning was as important as the variability in the buoyancy forcing in setting the final convective depth. In particular, very intense convection occurred in winter 2004-05 not only because the heat loss to the atmosphere was very strong, but also because the water advected towards the Medoc area was relatively weakly stratified compared to the previous years. We also estimated, based on the Dyfamed and NCEP data sets, that, at the Dyfamed site, only 1/3 of winters were expected to lead to deep water formation in the Mediterranean.

A further question that this work did not address concerns the formation of that preconditioning. Here, again, we still consider hydrographic (structure and content in heat and salt of the water column) rather than dynamic preconditioning (doming of the isopycnals before the onset of convection due to the gyre circulation). This preconditioning can either be due to the advection of water through the Corsica strait, which we considered in the present work, or heating due to the summer. What is the importance of summer heating in setting the preconditioning?

Our analysis also led to the discovery of a winter maximum in the stratification in the intermediate layer. It goes against the traditional idea of the stratification being slowly eroded until violent mixing starts. This maximum was been found both in the Dyfamed and Medar data sets, and seems to be correlated with the transport through the Corsica strait. Further work is needed to explain what causes that maximum and to assess more precisely its potentially critical effect in setting the maximum depth of convection.

Composition of the deep water formed

Concerning the characteristics of the deep water formed, the picture is more complicated. We found a correlation between the interannual variability of the T/S characteristics of the WMDW and the heat loss at the surface. We also found similarities between the variability of the T/S of the WMDW with the surface T/S at the Dyfamed site. The picture emerging is that of a convection transferring surface and intermediate properties to the depths with a rate of transfer set by the mixed layer depth. The salinity of the WMDW depends mainly on the salt content of the water column before the onset of convection while the temperature depends both on the preconditioning and on the surface heat loss.

7.2 What are the relative effects of the integrated buoyancy loss compared to the short-term time variability of the buoyancy loss?

7.2.1 Numerical results

Mixed Layer Depth

We integrated a numerical model over an idealised, linearly stratified (by temperature, the salinity being kept homogeneous) domain to answer this question. We forced it periodically at periods of 4, 10 and 20 days and found that the resulting mixed layer depth was not much affected by this time variability. We looked in more detail into the lateral buoyancy fluxes. We showed that they were responding very quickly to the surface forcing, so that the mixed layer is very little affected by the period of the forcing, and the integrated buoyancy forcing is what seems to matter. The physical process responsible for these lateral fluxes could not be clearly identified, although the most likely process is conventional baroclinic instability. At first, it contradicts the idea that baroclinic instability takes some time to develop. However, we saw that if the horizontal density gradient was sharp enough, the Eady growth rate predicted that the eddies could develop on timescales faster than a day. The time it takes for the horizontal density gradient to sharpen around a convective patch under cooling is very short, hence the instability can respond very quickly to the surface forcing.

One major limitation of our configuration is that the model was hydrostatic, due to computational costs. Slantwise convection is potentially important in restratifying the convective patch, but it can only be included if the model is non-hydrostatic.

However, for longer periods of time, the mixed layer is affected by the time variability, for example if there is a period of high heat loss ($800 W/m^2$) for more than 10 days. As the analysis of the heat fluxes in chapter 2 showed, this hardly ever happens in the Mediterranean.

Characteristics of the deep water formed

We also studied the effect of this time variability on the water mass formed by convection. We showed that the time variability had an effect on the residual stratification within the mixed layer, hence on the temperature of the water mass

formed. We observed this even though the salinity was kept homogeneous in our domain, and expect the variability in the forcing to have an even more significant effect when both salinity and temperature are considered.

Consequences for climate models

The fact that the element that matters in setting the final depth of the convective mixed layer is the integrated buoyancy forcing is of importance in climate models. Indeed, it means that the time resolution at which the forcing is applied does not matter so much and that a precise knowledge of the day-to-day variability of the forcing might not be necessary for a good prediction of the mixed layer. However, we also discovered that the residual stratification of the mixed layer was of importance when parameterising restratification processes. The parameterisation mostly used relies on the horizontal density gradient, hence it needs to be accurate in the model, and is over-estimated by assuming a fully mixed layer. The last point of importance for climate models relates to the characteristics of the water mass formed by convection. This is related to the previous point in that the residual stratification present in the water mass formed affects its properties. We found that the density of the water mass formed was affected by the time variability of the forcing through this residual stratification.

Further work

Two points at least need further investigation. First, the mechanism that causes the lateral buoyancy fluxes to be so responsive needs to be identified with more certitude. We suggest that a periodic channel should be modeled non-hydrostatically, and forced periodically, with hourly outputs. Due to the size of the output, this would mean outputting data over only a few periods. Looking at the Richardson number should provide useful information to identify the processes in action. Second, this setup of the model should have both temperature and salinity to further study the effect of the periodic forcing on the characteristic of the water mass formed.

7.2.2 In the real Ocean

We then investigated the convection processes using gliders' data from the Labrador Sea. We showed that, in that area, the variability in heat content in the top $1000m$ was very much affected by the boundary current. This variability appeared to be

mainly due to advection rather than to surface fluxes. This advection is thought to be due to interactions with the boundary current independent of the convection process.

The Labrador Sea and the Gulf of Lion seem to be in different dynamical regimes. In the Gulf of Lion, the boundary current is of a comparable scale as that of the rim current, and is intensified, rather than generated, by winter convection. In the Labrador Sea, there is a clear separation as the boundary current forms a gyre much bigger than the convective area. Hence, we expect our numerical results to be more relevant to the case of Gulf of Lion than to the Labrador Sea.

It would be interesting to compare our results with estimates of lateral buoyancy fluxes from the Gulf of Lion. Measurements of the residual stratification within the mixed layer in comparison with the surface forcing would be a simple way to give insights on how the lateral buoyancy fluxes vary. This might be achieved by using the data acquired during winter 2006-07 and 2007-08 by a collaborative European network of gliders deployed in the Mediterranean Sea. The data acquired by the gliders deployed by Lucas Merckelbach from NOCS would be particularly useful - they would provide repeated sections through the convective patch over the winter.

Appendix A

Winter Heat and Buoyancy Fluxes in the Gulf of Lion

A.1 Winter Heat Fluxes in the Gulf of Lion

Figure A.1 displays the heat fluxes for winters of year 1949-50 to 2004-05, from the NCEP reanalysis data set. Details on how these data have been processed are given in chapter 2.

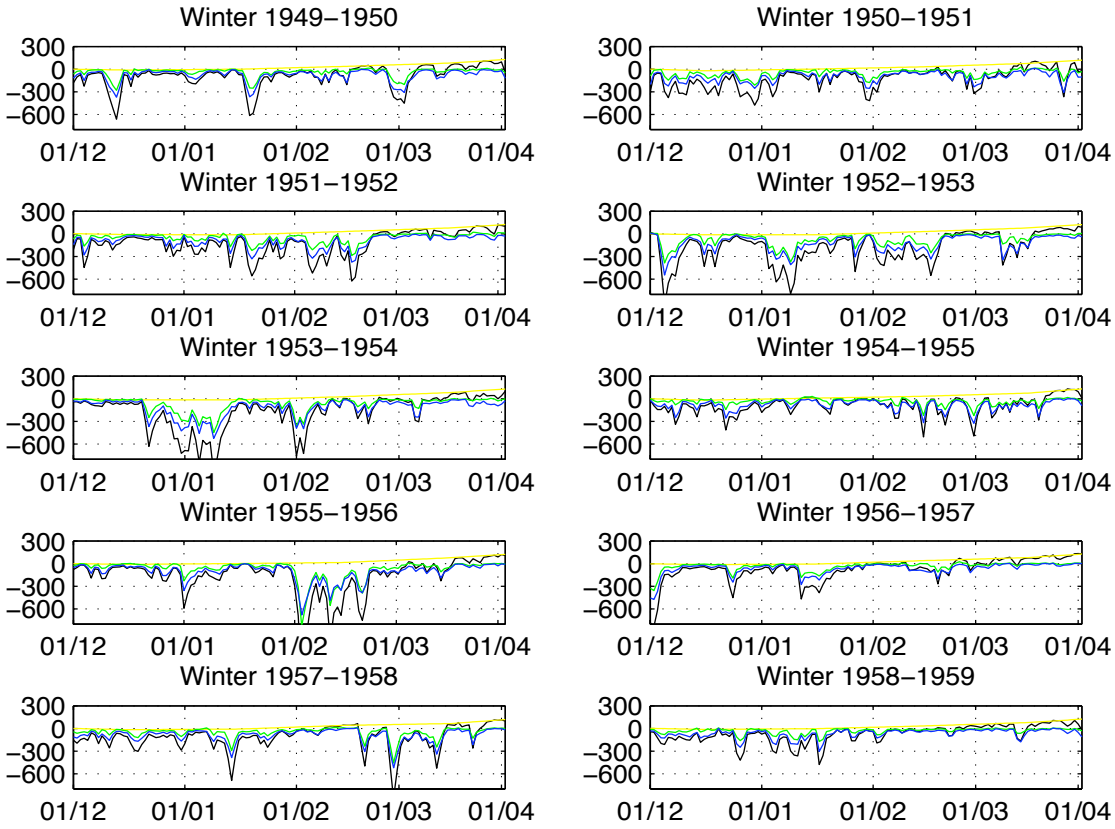

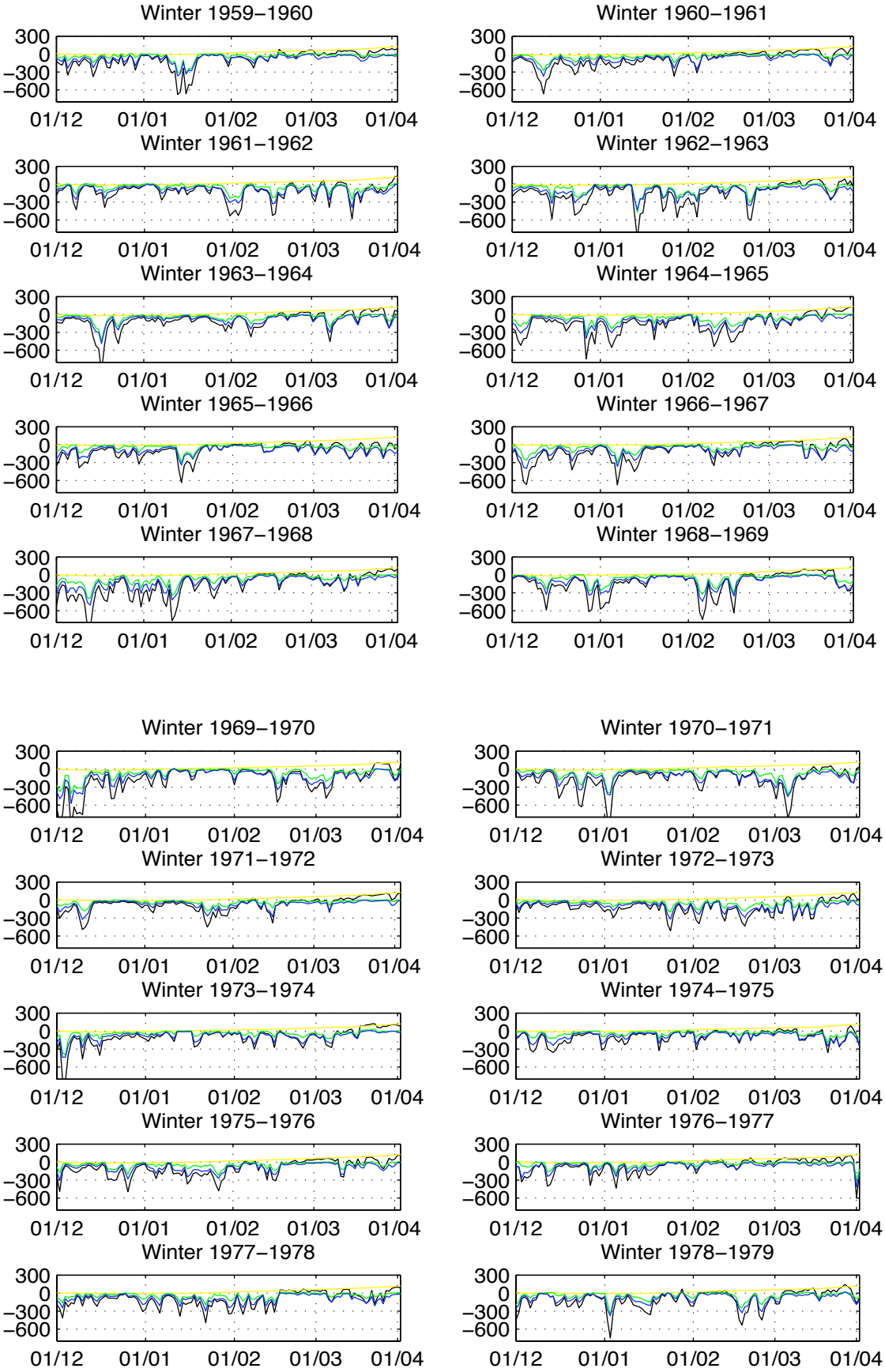
Winter 1959–1960
Winter 1960–1961
Winter 1961–1962
Winter 1962–1963
Winter 1963–1964
Winter 1964–1965
Winter 1965–1966
Winter 1966–1967
Winter 1967–1968
Winter 1968–1969
Winter 1969–1970
Winter 1970–1971
Winter 1971–1972
Winter 1972–1973
Winter 1973–1974
Winter 1974–1975
Winter 1975–1976
Winter 1976–1977
Winter 1977–1978
Winter 1978–1979
300
0
−300
−600
01/12
01/01
01/02
01/03
01/04

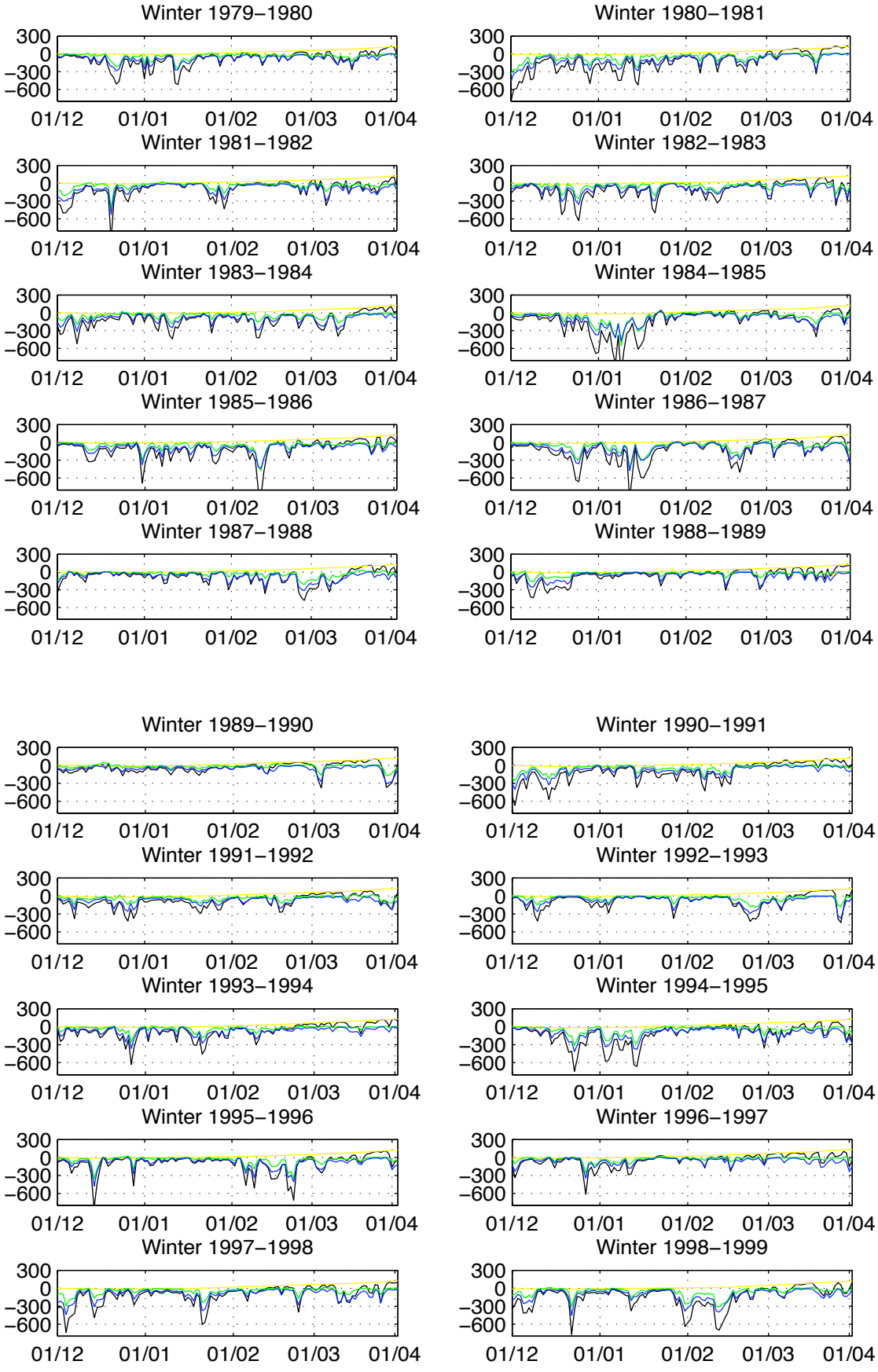
Winter 1979–1980
Winter 1980–1981
Winter 1981–1982
Winter 1982–1983
Winter 1983–1984
Winter 1984–1985
Winter 1985–1986
Winter 1986–1987
Winter 1987–1988
Winter 1988–1989
Winter 1989–1990
Winter 1990–1991
Winter 1991–1992
Winter 1992–1993
Winter 1993–1994
Winter 1994–1995
Winter 1995–1996
Winter 1996–1997
Winter 1997–1998
Winter 1998–1999
300
0
−300
−600
01/12
01/01
01/02
01/03
01/04

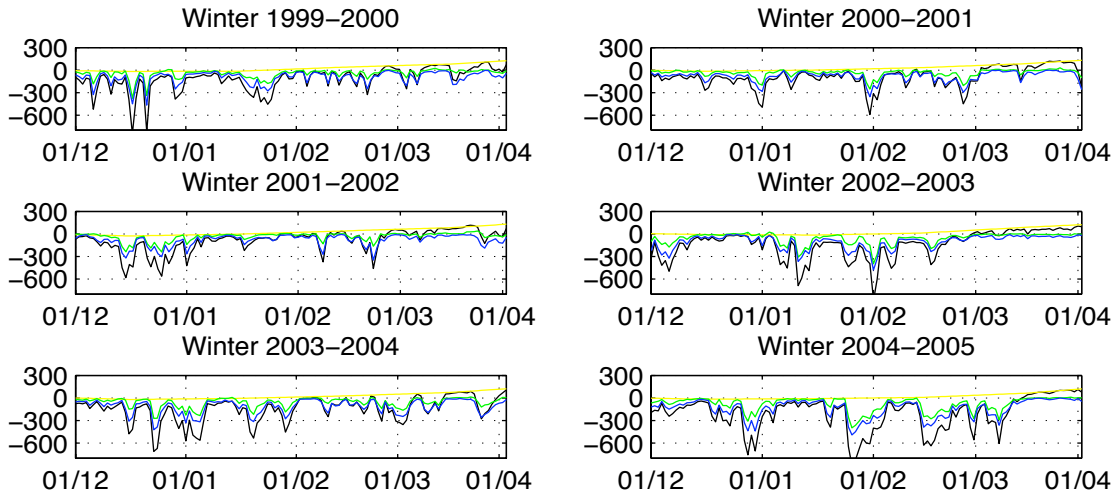

Figure A.1: Latent (blue), sensible(green), radiative (yellow) and total (black) heat fluxes. The abscissa shows the number of days since the 1st of December, until the 31 of March. Heat fluxes are in W/m^2.

A.2 Composition of the Winter Heat Fluxes

Figure A.2 displays the monthly mean contribution of each component of the heat fluxes for winters (1^{st} of December until 31 of March) of year 1949-50 to 2004-05, from the NCEP reanalysis data set.

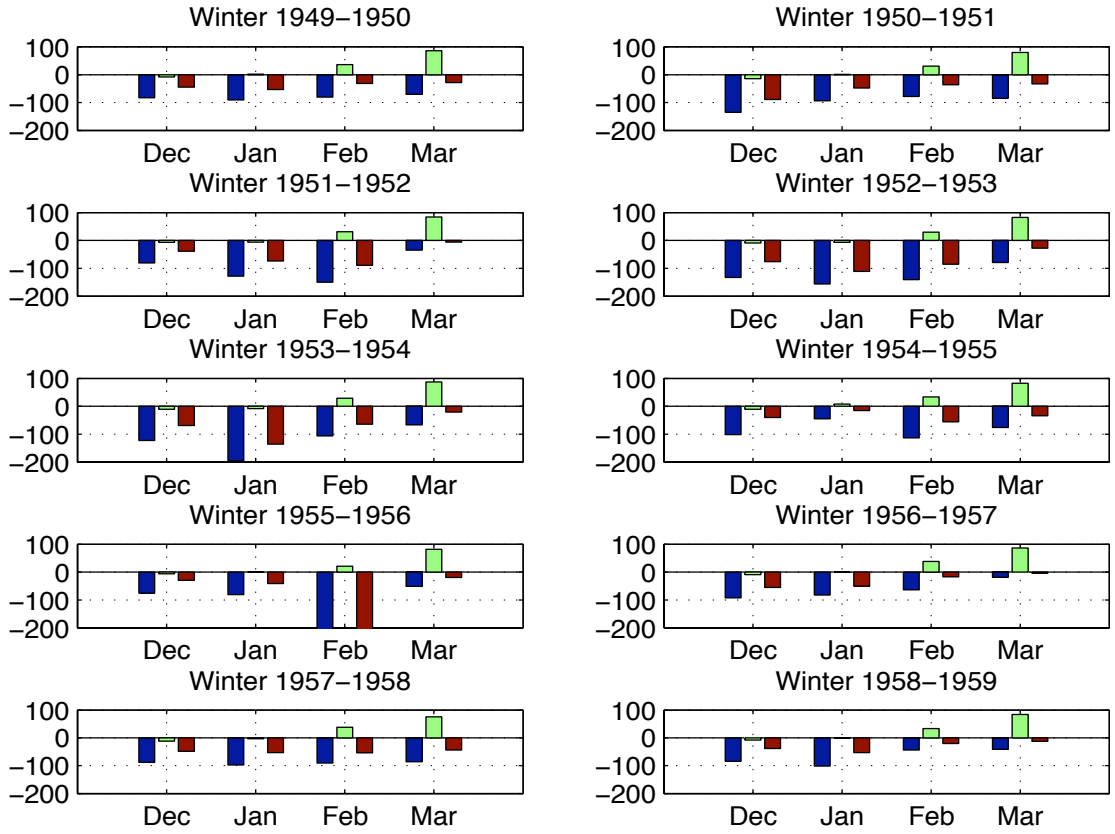

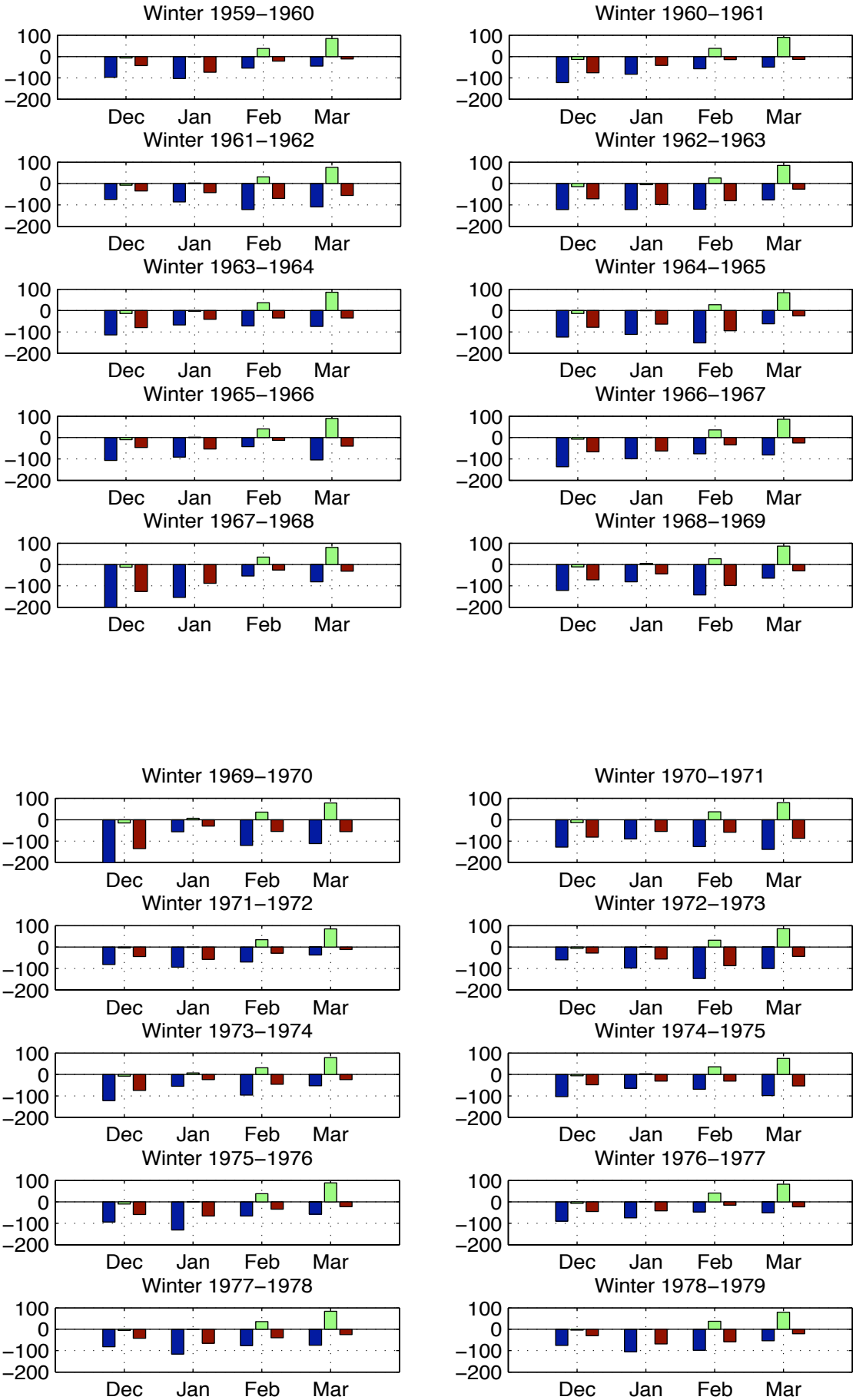
Winter 1959–1960
Winter 1960–1961
Winter 1961–1962
Winter 1962–1963
Winter 1963–1964
Winter 1964–1965
Winter 1965–1966
Winter 1966–1967
Winter 1967–1968
Winter 1968–1969
Winter 1969–1970
Winter 1970–1971
Winter 1971–1972
Winter 1972–1973
Winter 1973–1974
Winter 1974–1975
Winter 1975–1976
Winter 1976–1977
Winter 1977–1978
Winter 1978–1979
100
0
−100
−200
Dec
Jan
Feb
Mar

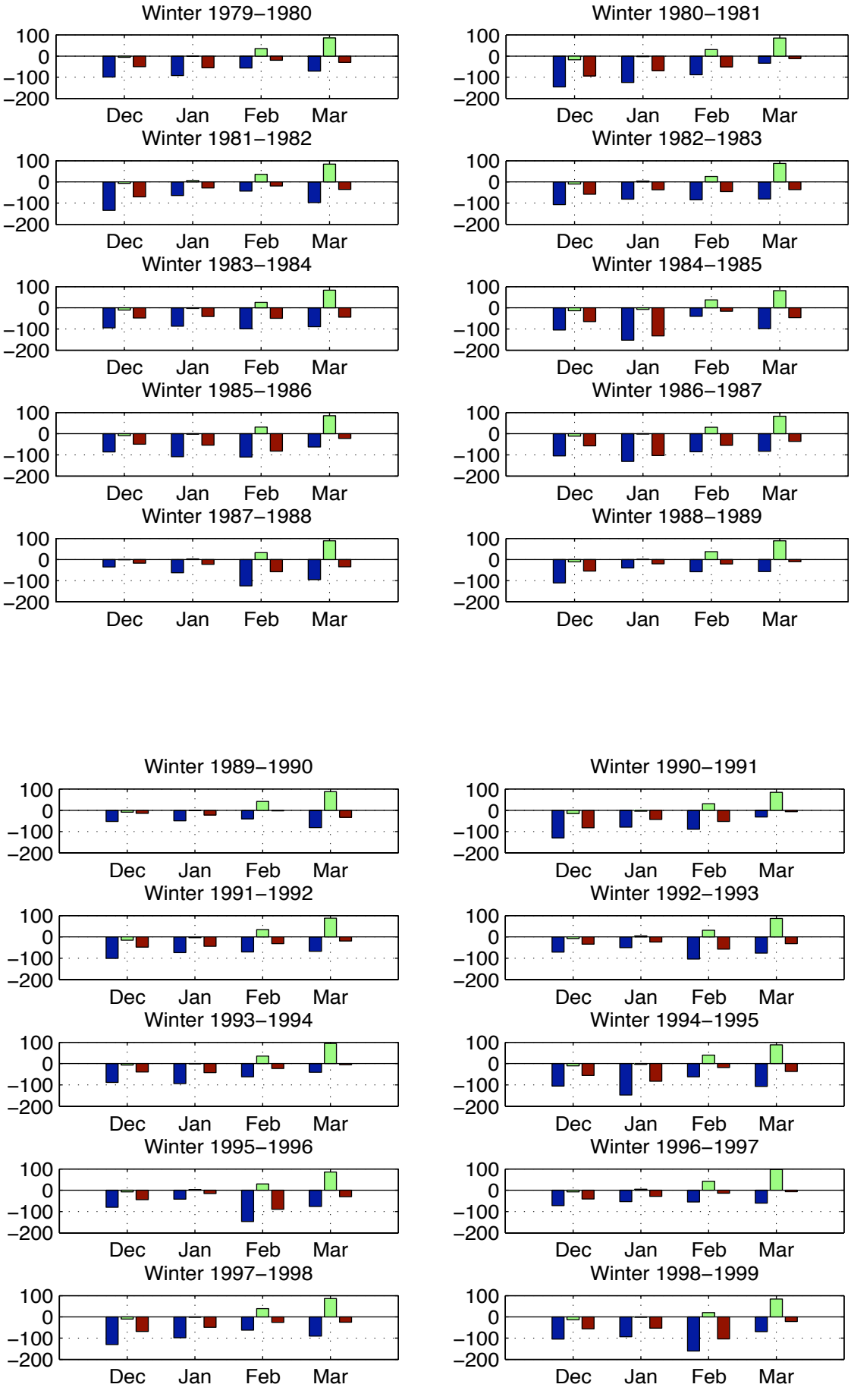
Winter 1979–1980
Winter 1980–1981
Winter 1981–1982
Winter 1982–1983
Winter 1983–1984
Winter 1984–1985
Winter 1985–1986
Winter 1986–1987
Winter 1987–1988
Winter 1988–1989
Winter 1989–1990
Winter 1990–1991
Winter 1991–1992
Winter 1992–1993
Winter 1993–1994
Winter 1994–1995
Winter 1995–1996
Winter 1996–1997
Winter 1997–1998
Winter 1998–1999
100
0
−100
−200
Dec
Jan
Feb
Mar

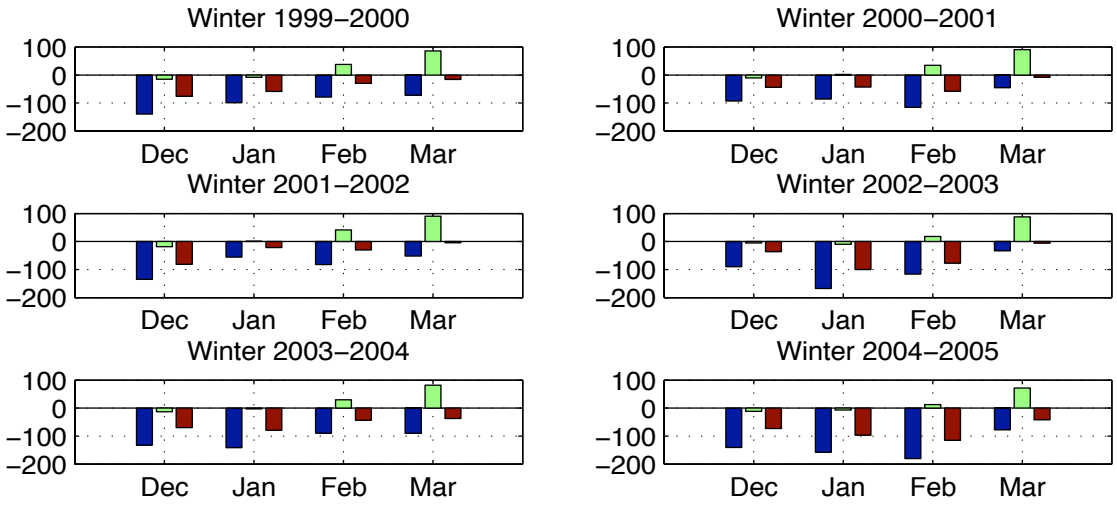

Figure A.2: Composition of the heat fluxes (latent in blue, sensible in red and radiative in green) from the winter 1949-1950 to the winter 2004- 2005. The abscissa shows the number of months since the beginning of 1949. Heat fluxes are in W/m^2. Monthly values are used here. There are four histograms for each winter, for December, January, February and March).

A.3 Buoyancy Fluxes

Figure A.3 displays the buoyancy fluxes for winters (1^{st} of December until 31 of March) of year 1949-50 to 2004-05, from the NCEP reanalysis data set. Details on how these data have been processed are given in chapter 2.

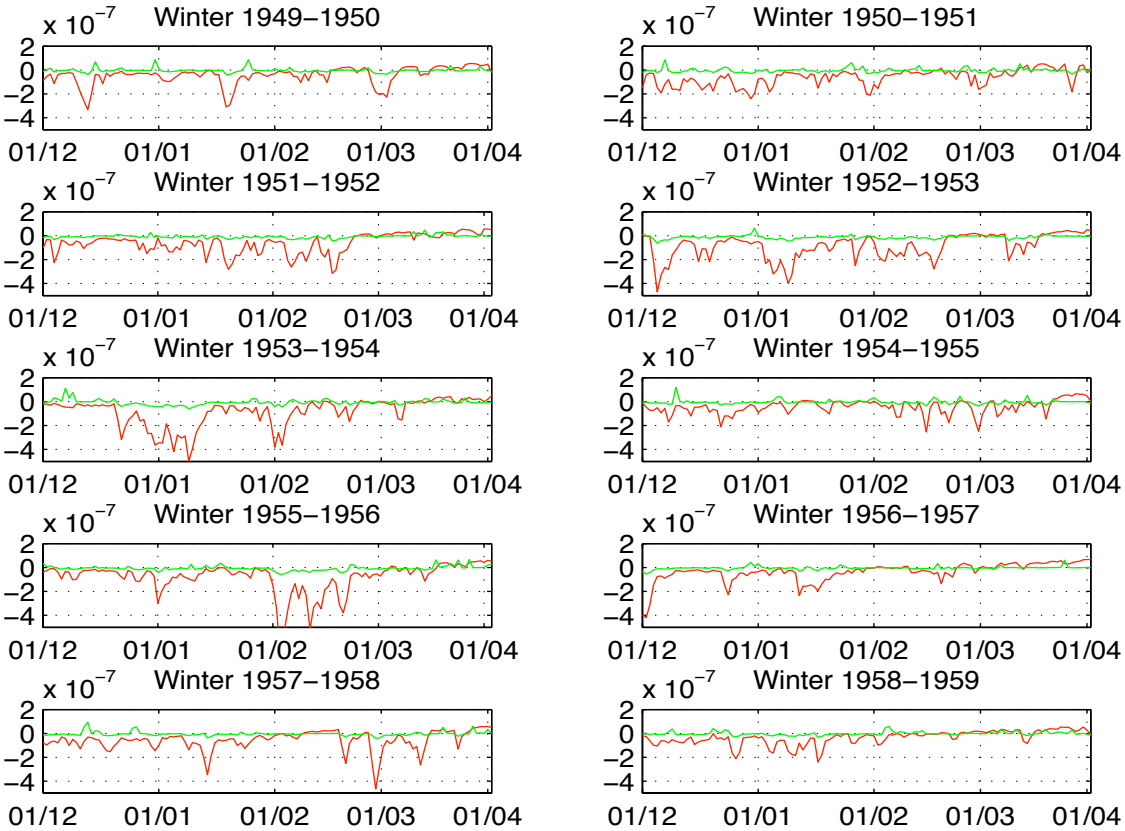

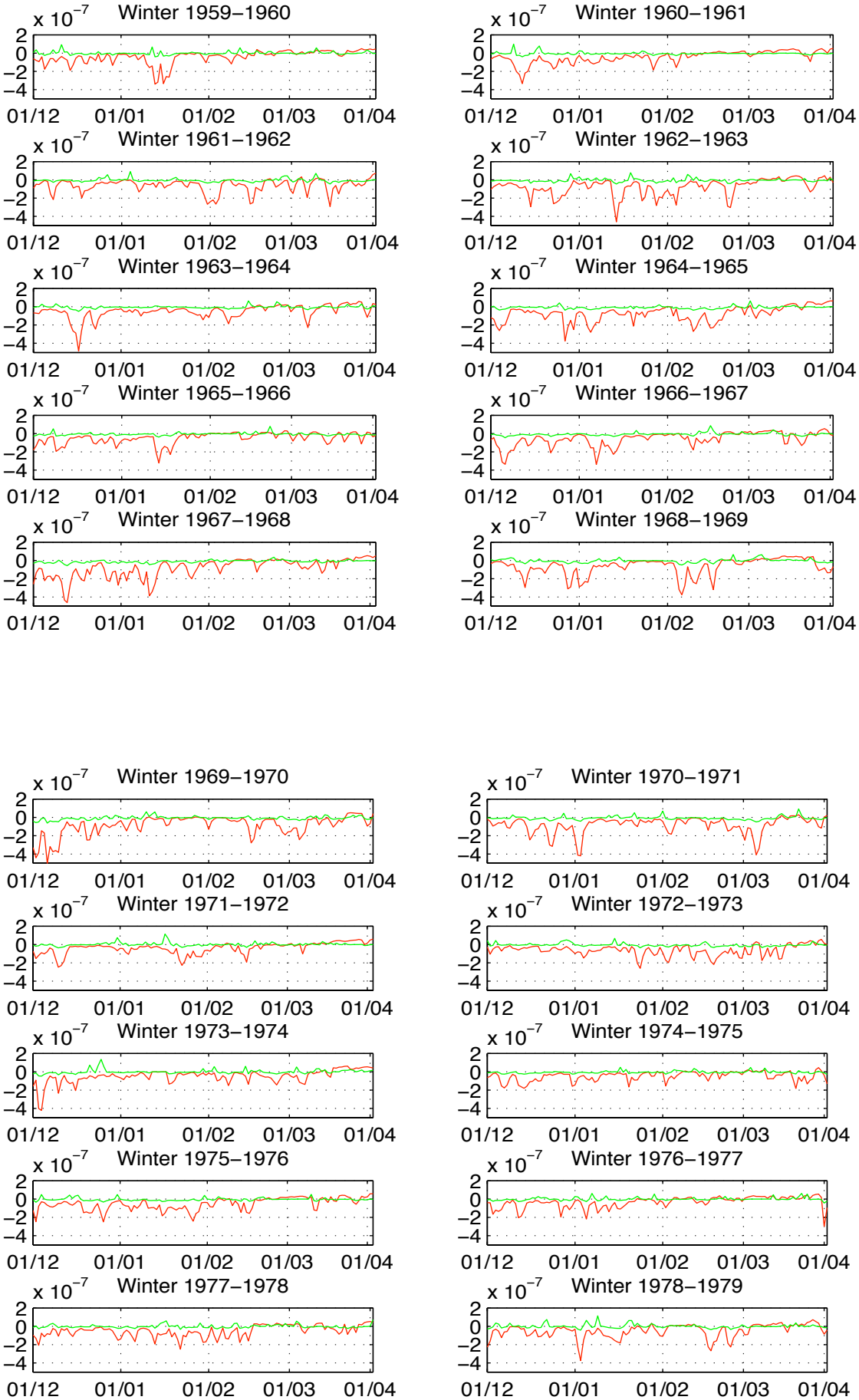
x 10^-7
Winter 1959–1960
Winter 1960–1961
Winter 1961–1962
Winter 1962–1963
Winter 1963–1964
Winter 1964–1965
Winter 1965–1966
Winter 1966–1967
Winter 1967–1968
Winter 1968–1969
Winter 1969–1970
Winter 1970–1971
Winter 1971–1972
Winter 1972–1973
Winter 1973–1974
Winter 1974–1975
Winter 1975–1976
Winter 1976–1977
Winter 1977–1978
Winter 1978–1979
2
0
−2
−4
01/12
01/01
01/02
01/03
01/04

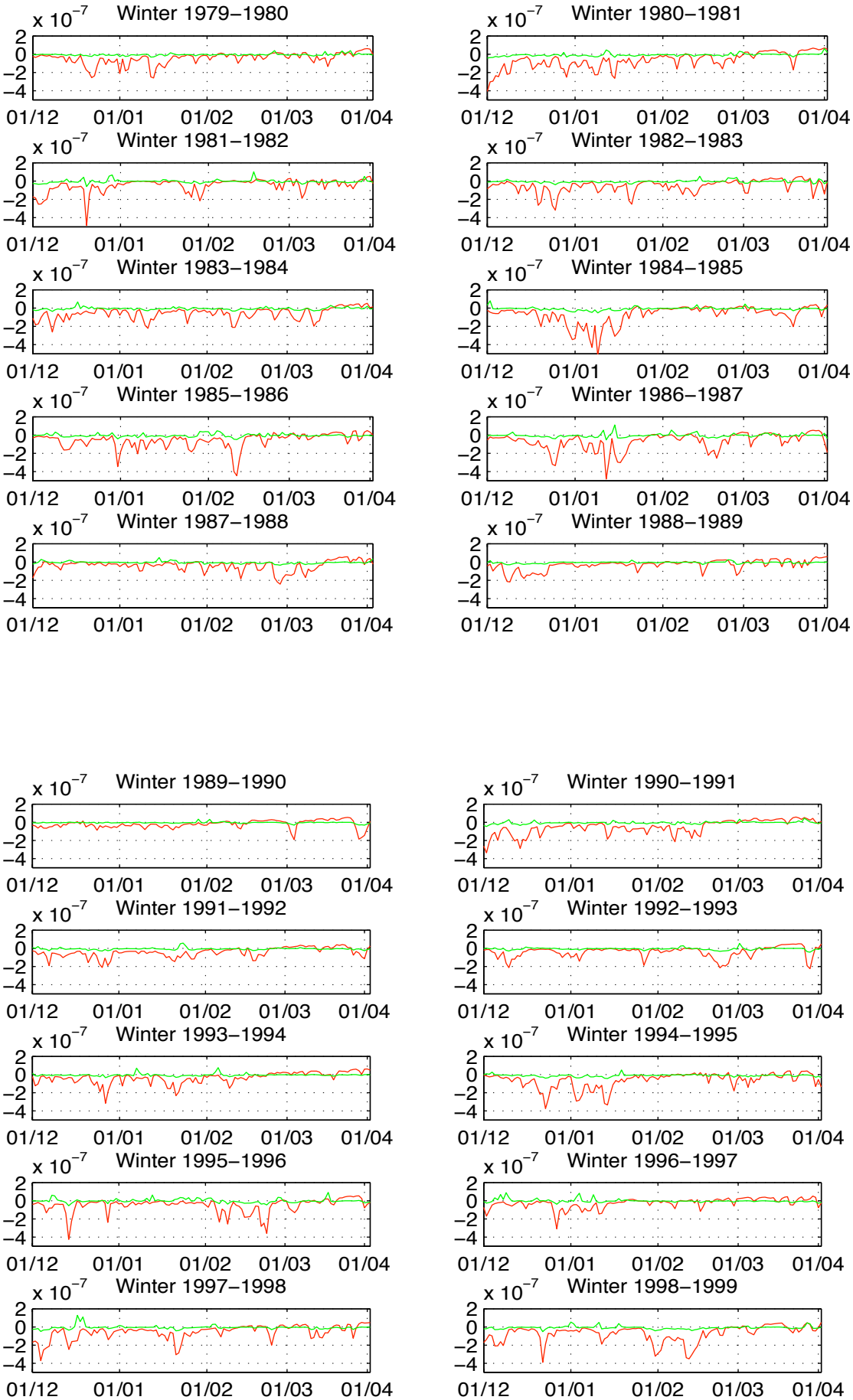
x 10^-7
Winter 1979–1980
Winter 1980–1981
Winter 1981–1982
Winter 1982–1983
Winter 1983–1984
Winter 1984–1985
Winter 1985–1986
Winter 1986–1987
Winter 1987–1988
Winter 1988–1989
Winter 1989–1990
Winter 1990–1991
Winter 1991–1992
Winter 1992–1993
Winter 1993–1994
Winter 1994–1995
Winter 1995–1996
Winter 1996–1997
Winter 1997–1998
Winter 1998–1999
2
0
−2
−4
01/12
01/01
01/02
01/03
01/04

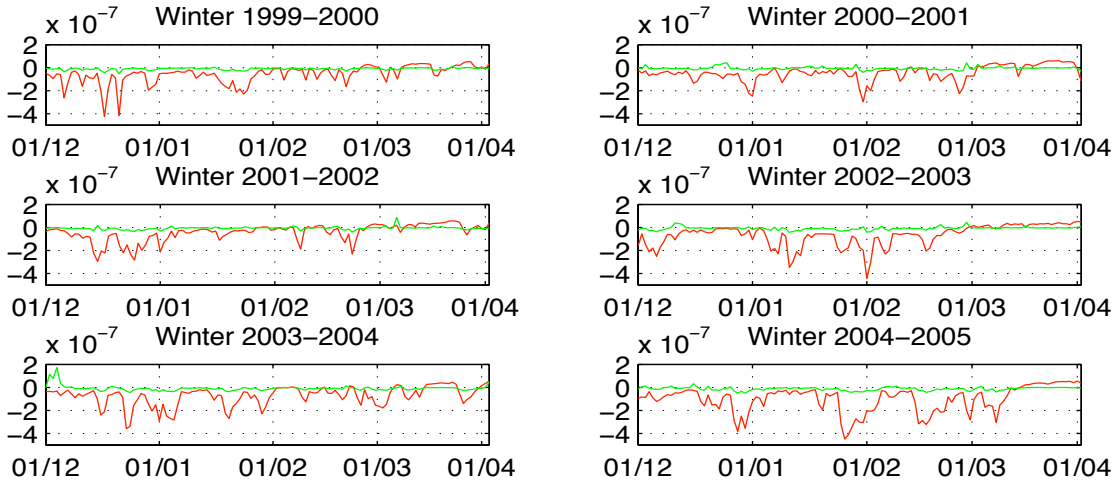

Figure A.3: Buoyancy fluxes for the winters from 1949-1950 to 2004-2005. The green plot shows the haline component of the buoyancy flux and the red one the thermal component. The black one shows the total buoyancy flux, and follows very closely its thermal component. Units are m^2/s^3.

Appendix B

Statistics

The techniques are briefly described here. For more details, see Stuart et al. (1999) or Green and Margerison (1978).

B.1 Poisson process and Exponential Distribution

In the Poisson process, events occur randomly in time (in our case) or space.The numbers of event in any given time have a Poisson distribution while the intervals between consecutive event have an exponential distribution (Green and Margerison, 1978).

In the case of the heat fluxes, we are interested in the time interval between events.

The exponential distribution has one parameter m and is defined by:

$$exppdf(x, m) = \frac{1}{m} \times exp(-\frac{x}{m}), x \geq 0 \tag{B.1}$$

Calculating the mean of the distribution, we find that it takes the value m.

B.2 Maximum Likelihood Method

The likelihood function is defined by:

$$L(x|m) = \prod f(x_i|m) \tag{B.2}$$

A method to find an estimate of the parameter is to solve:

$$\frac{\partial L(x|m)}{\partial m} = 0 \tag{B.3}$$

For an exponential distribution, we have, for a sample of size n:

$$L(m) = (\frac{1}{m})^n exp(-n \cdot mean(x)/m) \tag{B.4}$$

This always yields $m = mean(x)$ as a best fit to an exponential distribution

B.3 χ^2 Goodness of Fit Test

B.3.1 Hypothesis testing: Principles

We define H_0 as the hypothesis being tested, called null hypothesis. In our case, it will be: "The data are a random sample from an exponential distribution". We cannot say if this hypothesis is true, but the hypothesis will be rejected if it fails the test hereby described.

The level of confidence α is the maximum probability of rejecting H_0 if H_0 is true. It usually takes the values of 5, 1, or 0.1%.

We then define a test statistic T. c is the critical value such that $\alpha = P(T \geq c|H_0)$, i.e. the level of confidence is the probability that the test statistic is bigger than the critical value supposing the null hypothesis is true.

H_0 is rejected at the α level of significance if there is a realisation t of T that exceeds the critical value.

We have the data $X = (x_1, x_2, ..., x_N)$ where N is the number of data points. There are different ways of distributing the x_i in bins. The value of T will depends on that repartition. Each repartition leads to a value t called realisation of T.

To sum up, the hypothesis will not be rejected if there are no repartition of the x_i in bins that leads to $t > c$.

B.3.2 Test

Here, we use the test statistic

$$T = \sum_{i \in I} \frac{(O_i - E_i)^2}{E_i} \tag{B.5}$$

where O_i and E_i are the observed and expected frequencies or counts for each bin.

If N is large and none of the E_i is too small (usually, $E_i > 5$ is considered safe), T is approximatively distributed as χ^2_ν where ν is the number of degree of

freedom. $\nu = k - 1 - h$ where k is the number of categories (bins) used and h the number of parameters in the distribution function that have to be estimated ($h = 1$ for a normal distribution). Then, the hypothesis is rejected if we find a realisation where $t > \chi^2_\nu$. A table with the value of this function can be found in Stuart et al. (1999).

Appendix C

Details and Validation of the 1D model

C.1 Description

The model used here is very basic, and does not include wind effect, and 2D/3D phenomena such as baroclinic instability. Therefore, no restratification processes are taken into account in this model. Moreover, the mixed-layer is assumed fully homogeneous.

C.1.1 Rate of deepening

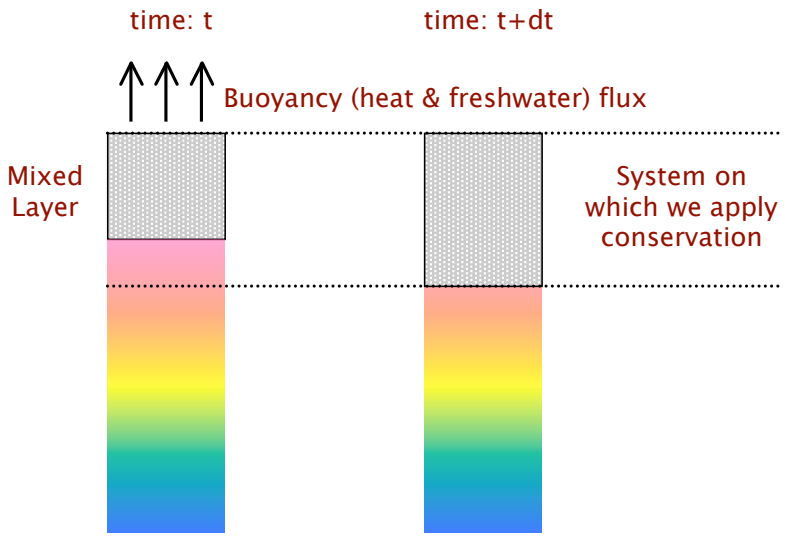

Figure C.1: Sketch defining the system considered here.

From Turner (1973), the depth of the mixed layer h during a buoyancy loss B_0

for a fluid with constant buoyancy frequency N^2 can be approximated by:

$$h = \sqrt{\frac{2 \cdot \int B_0 dt}{N^2}} \tag{C.1}$$

This formula is derived considering buoyancy conservation in a non-rotating fluid.

We would like to use a similar formula for the real ocean, but we want to consider the effect of the initial preconditioning, so the constant buoyancy frequency is an assumption that is not adapted to our study. We are going to re-derived Turner's formula, going as far as possible in the general case.

The buoyancy content is defined by:

$$BC(t) = \frac{g}{\rho_0} \int \rho(z,t) dz \tag{C.2}$$

although here, we will lighten the equations by using the definition:

We write the conservation of buoyancy content BC for the system defined in figure C.1, undergoing a buoyancy flux BF between times t and $t + dt$:

$$BC(t + dt) - BC(t) = \int BF dt \tag{C.3}$$

The density of the mixed layer is the same one than the one observed at the mixed layer depth before the deepening (non-penetrative convection). That is, if $h(t)$ is the depth of the mixed layer at time t, the density $\rho(z,t)$ at depth z is

$$\rho(z \leq h(t), t) = \rho(h(t), t = 0) \tag{C.4}$$

The buoyancy content then becomes:

$$BC(t) = \frac{g}{\rho_0} \cdot [\rho(h(t), 0) \cdot h(t) + \int_{h(t)}^{h(t+dt)} \rho(z, 0) dz] \tag{C.5}$$

$$BC(t + dt) = \frac{g}{\rho_0} \int_0^{h(t+dt)} \rho(z, t + dt) dz = \frac{g}{\rho_0} \cdot \rho(h(t + dt), 0) \cdot h(t + dt) \tag{C.6}$$

Therefore, in the general case, we obtain:

$$\begin{aligned}\rho(h(t+dt),0)\cdot h(t+dt)-[\rho(h(t),0)\cdot h(t)+\int_{h(t)}^{h(t+dt)}\rho(z,0)dz]\\ =\frac{\rho_0}{g}\int_t^{t+dt}BF(t)dt\end{aligned} \tag{C.7}$$

If we consider a linear density profile, like Turner (1973), we can introduce

$$K=\frac{d\rho}{dz}(z,0)=\frac{\rho_0}{g}N^2 \tag{C.8}$$

This leads to:

$$\begin{aligned}\rho(h(t+dt),0)\cdot h(t+dt)-[\rho(h(t),0)\cdot h(t)+\int_{h(t)}^{h(t+dt)}\rho(z,0)dz]=\\ K\cdot h^2(t+dt)+\rho_{surf}\cdot h(t+dt)-K\cdot h^2(t)-\rho_{surf}\cdot h(t)\\ -\int_{h(t)}^{h(t+dt)}[Kz+\rho_{surf}]dz=\\ K[h^2(t+dt)-h^2(t)]+\rho_{surf}[h(t+dt)-h(t)]-K\frac{h^2(t+dt)-h^2(t)}{2}\\ +\rho_{surf}[h(t+dt)-h(t)]=\\ \frac{K}{2}[h^2(t+dt)-h^2(t)]\end{aligned} \tag{C.9}$$

Therefore:

$$\frac{\rho_0}{g}\int_t^{t+dt}BF(t)dt=\frac{\frac{\rho_0}{g}N^2}{2}[h^2(t+dt)-h^2(t)] \tag{C.10}$$

,and

$$h^2(t+dt)-h^2(t)=\frac{2\int_t^{t+dt}BF(t)dt}{N^2} \tag{C.11}$$

If we use this formula between an initial time $t_i=0$ and a final time $t_f=t$ with initial condition $h(t=0)=0m$, and a constant buoyancy forcing we find Turners formula.

In the 1D model presented here, we are going to use this formula for a piece-

wise constant initial buoyancy frequency:

$$2\int_t^{t+dt} BF(t)dt = N_{j+1}^2(h(t_f)^2 - h_j^2) + \sum_{k=i}^{j-1} N_{k+1}^2(h_{k+1}^2 - h_k^2) + N_i^2(h_i^2 - h(t_i)^2) \tag{C.12}$$

where the subscripts k, i and j correspond to the different layers of definition of N^2, that is, N^2 is constant between h_k and h_{k+1}. Decreasing the thickness of the layers can allow us to reach an almost continuous N^2 profile. At time t_i, we start in layer i between depths h_{i-1} and h_i. At time $t_f > t_i$, we are in layer j between depths h_j and h_{j+1}. The Brunt-Vaisala frequency is N_k between depths h_{k-1} and h_k.

In the algorithm, we first define a limit value BF_{lim} the integrated buoyancy flux necessary that would necessary to reach the next layer. If it is bigger than the actual buoyancy flux BF, the new depth of the mixed layer is in the same layer, so we apply the formula directly. Otherwise, we set $BF = BF - BF_{lim}$ for the next time we go through the loop, and so on until we are in the good layer.

C.1.2 Salinity and Temperature profiles

At each integration step (typically, every day), the new depth $h(t+1)$ of the mixed layer is first calculated. We then calculate the heat and salt content $HC(t)$ and $SC(t)$ between the surface and $h(t+1)$ at time t. We have: $HC(t+dt) = HC(t) - HL(t+dt)$ and $SC(t+dt) = SC(t) - SG(t+dt)$, where HL is the heat loss, calculated using the thermal component of the buoyancy flux, and SG is the salt gain calculated using the haline component. Finally, we calculate the homogeneous temperature and salinity of the mixed layer using the heat and salt contents.

C.1.3 Matlab function

These steps are implemented in the Matlab function deepening3:
function [time,depth,MLdepth,temp,sal] =
deepening3(depthin,Ti,Si,time,Bs,Bt,timestep,pot).

T_i and S_i are the initial temperature and salinity depth profiles, along a grid given in depth. pot is a character string indicating if the temperature given is potential (pot=pot) or in situ (pot=insitu) temperature. B_S and B_T are the time

series of the haline and thermal components of the buoyancy flux, along a time grid given in time. $timestep$ gives the duration on which each element given in the buoyancy fluxes arrays is averaged, in seconds (i.e., $24 \times 3600s$ for daily average).

$MLdepth$ is a vector giving the time variation of the mixed layer depth, the time being given in the vector time (same that the input time vector). $temp$ and sal are matrices, the row representing the variation over depth, and the columns the variations over time, where time is defined by the input vector, and depth is a vector interpolated from depth, with a more regular resolution.

C.2 Validation

We check the model by running it for a simple case, which can be solved analytically. We force the model with a constant buoyancy flux. In the first test, this flux only has a thermal component; in the second one, only a haline component. In both cases, the potential temperature T_i and salinity S_i profiles are varying linearly with depth ($T_i = [13.7 : -0.02 : 12.7]$ and $S_i = [37.8 : 0.014 : 38.5]$), so the buoyancy frequency is constant: the solution for the mixed layer depth can be calculated analytically, using Turners formula. The model is run for 150 days, corresponding to 5 months. Then, to check the heat and salt fluxes are calculated properly, we compare the difference between the heat/salt/buoyancy contents at the beginning of the run, and the ones at the end with the integrated heat flux over the period considered. Results are shown in figures C.2 and C.3, and tables 1 and 2, for each run.

	$\mathbf{F}$	$\mathbf{C_i - C_f}$	$\mathbf{C_i - C_f - F}$
Heat ($T \cdot m$)	-659.8778	659.8778	$7.26 \cdot 10^{-10}$
Salt ($psu \cdot m$)	0	$-1.57 \cdot 10^{-8}$	$-1.57 \cdot 10^{-8}$
Buoyancy (s^2)	131.9756	-131.9756	$-1.56 \cdot 10^{-8}$

Table C.1: Comparison between integrated flux and difference in content for the heat, salt and buoyancy for the first run (heat flux only). C_i is the initial content, C_f the final one. F is the integrated flux over the run period.

The results for heat, salt and buoyancy contents show negligible errors for a run of 5 months. The mixed layer depth is predicted analytically to be the same than numerically.

We now do a second test, to validate the mixed layer depth calculation: we check the stability of the water at the interface between the mixed layer and the

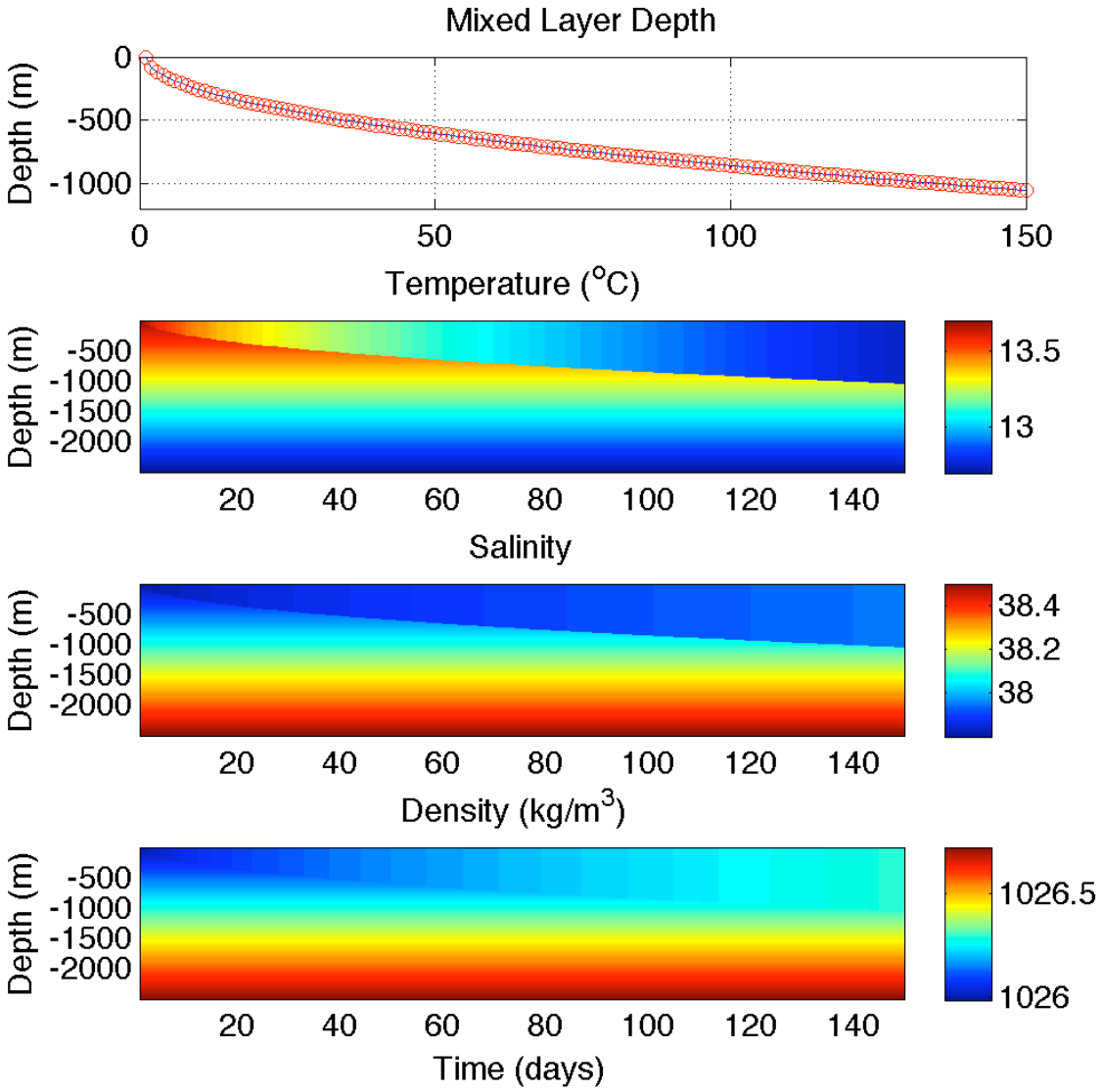

Figure C.2: Mixed layer depth, potential temperature, salinity and density evolution during the run for the first test (heat flux only). The top figure shows the mixed layer depth evolution calculated by the model (blue) and analytically (red).

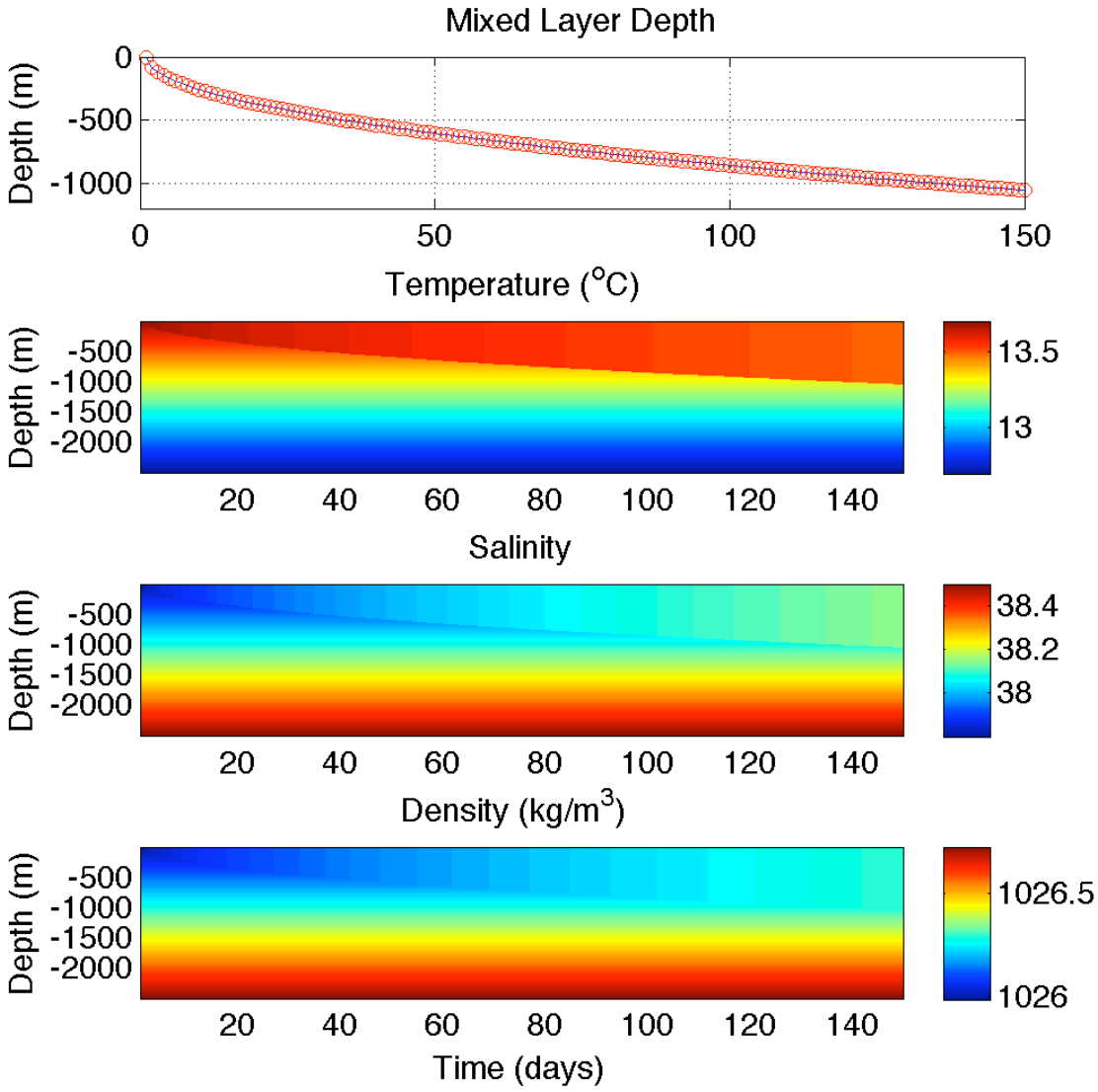

Figure C.3: Mixed layer depth, potential temperature, salinity and density evolution during the run for the second test (salt flux only). The top figure shows the mixed layer depth evolution calculated by the model (blue) and analytically (red).

	F	$\mathbf{C_i - C_f}$	$\mathbf{C_i - C_f - F}$
Heat ($T \cdot m$)	0	$-7.35 \cdot 10^{-10}$	$-7.35 \cdot 10^{-10}$
Salt ($psu \cdot m$)	173.6521	-173.6521	$4.06 \cdot 10^{-9}$
Buoyancy (s^2)	131.9756	-131.9756	$1.47 \cdot 10^{-8}$

Table C.2: Comparison between integrated flux and difference in content for the heat, salt and buoyancy for the first run (salt flux only). C_i is the initial content, C_f the final one. F is the integrated flux over the run period.

stratified underlying water: we compare the potential density, calculated again with a linear equation of state, above the mixed layer with the one just below. We find that the underlying water is always denser than the water in the mixed layer, with a difference of about 10^{-3}, which is in agreement with the values of the initial gradient of both temperature and salinity.

Appendix D

Effect of time varying forcing on convection: Laboratory experiments

D.1 Introduction

Our modeling study showed that the final convective depth was not sensitive to the time variability of the forcing if this time variability was on a timescale of a few days. In this appendix, we want to see if laboratory experiments give similar results. Indeed, there are elements, like plumes, not resolved by our model that will be present in the laboratory experiments. This study was done at the Geophysical Fluid Dynamics Laboratory (GFDL) of the University of Washington, in Seattle, with Eric Lindahl, Bob Koon and Peter Rhines. Funds came from the Worldwide University Network (WUN) through the Research Mobility Program (RMP).

This work is innovative in two aspects. First, we want to be in a rotating environment, with a localised forcing over a stratified tank. To our knowledge, there are only two studies meeting these three conditions (Ivey et al., 1995; Whitehead et al., 1996). Most of the previous works were focusing on the study of plumes (Boubnov and Golitsyn, 1990; Fernando et al., 1991). Jacobs and Ivey (1999), for a homogeneous fluid, identify three regimes: a rotationally controlled regime, a baroclinically unstable regime and a stable one, depending on the initial parameters. The second innovative feature of our experiments is the application of a time-varying forcing at the surface.

We will first give details about the setup used, and then show results from an experiment. The last section concludes the appendix.

D.2 Setup

Figure D.1 presents a picture summarising one of the experiments (called CV2) performed at the GFD laboratory of the University of Washington in Seattle. We will here describe the instrumentation used.

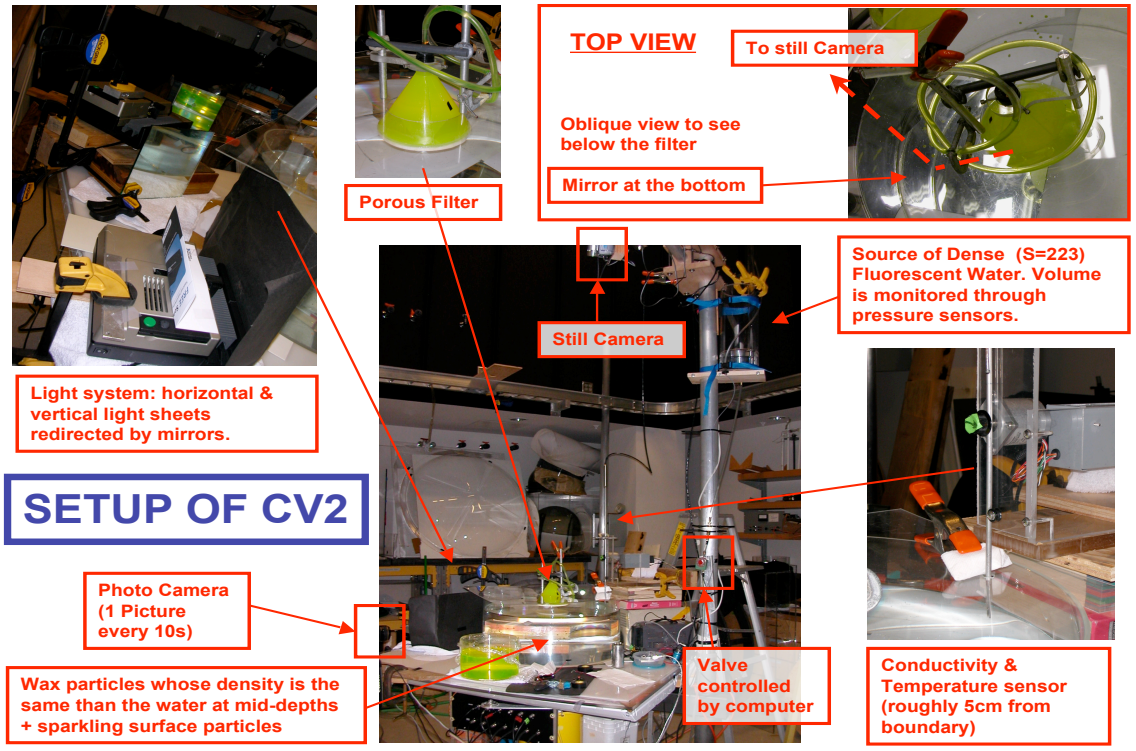

Figure D.1: Setup of the laboratory experiment.

D.2.1 Convection in the laboratory

We want to reproduce convection caused by a surface forcing applied on a linearly stratified fluid. Ivey et al. (1995) simulated convection by heating from below a thermally stratified fluid. This present two major difficulties. First, it is makes the visualisation of surface eddies more difficult, and we want to be able to observe baroclinic eddies. Second, a thermal stratification can be quickly eroded by diffusion, and so the experiment will have to be started rapidly after building the stratification, unless there is a way to maintain it through the experiment. Whitehead et al. (1996) sprayed salt over a localised area on a salt-stratified fluid. The issue in that case is that the salt does not only result in a buoyancy loss, but also in a gain of momentum. Moreover, this method does not guarantee a homogeneous cooling over the convective area, and we want to be able to mirror our numerical experiments as closely as possible.

There is also an additional complication in our case. We want to be able to switch the forcing on and off quite quickly. We choose a salt stratification, realised using the two-tank method (Hill, 2002). We force the fluid locally using a very dense (salty) solution going through a porous filter (see figure D.1). Darcy's law of flow through porous surfaces then tells us that the flow rate is proportional to the pressure above the interface. The source of dense water is situated a few meters above the surface of the tank. It allows us to neglect the variations of the source water's surface compared to that height, so we can assume that the flow rate through the filter is constant, set by the height of the surface of the dense water. A pressure sensor at the bottom of the dense water source tank allows us to monitor the volume of water that went through the filter, whose time derivative is the flow rate. On the hose connecting the filter with the dense water tank, there is a remotely controlled valve to allow a time varying forcing.

D.2.2 Observing and measuring convection

The dense water released at the surface is mixed with a fluorescent dye. We use two light sheets, one horizontal near the surface to have a top view, and the other vertical through the centre of the tank to observe a section across the convective patch. The side view is obtained with a photo camera on the side, taking a picture every 10s, and the top view by a still camera situated above the tank. There is a mirror below the tank to visualise what happens below the filter.

Wax particles designed to be neutrally buoyant in the mixed layer and sparkling particles lighter than the fluid, hence staying at the surface, have been added to ease the visualisation.

On the side of the tank, roughly $5cm$ from the boundary, a conductivity and temperature sensor will take CTD profiles during the experiment.

D.2.3 Parameters and non-dimensional numbers

The tank is filled with water stratified at $N = 1.4s^{-1}$, and we choose a rotation rate $f = 1.6s^{-1}$, hence $\frac{N}{f} = 0.87$. The tank is $25cm$ deep, leading to a Rossby radius of deformation $R_0 = \frac{NH}{f}$ smaller than $21.75cm$ (full depth mixed layer). However, the mixed layer does not deepen below $16cm$, corresponding to a $R_0 = 14cm$. Towards the end of the experiment, R_0 gets bigger than the radius of the cooling patch R.

Baroclinic eddies starts forming on the Rossby radius scale $R_0 \sim 3cm$. The filter has a radius of $R = 7.5cm$, hence $\frac{R}{R_0} = 2.5$. In a previous experiment (called cv1), we had a lower rotation rate $f = 0.8s^{-1}$, and $\frac{R}{R_0}$ closer to 1, and we could clearly see that the regime was different than observed in the numerical experiment. Figure D.2 shows the side view during a portion of the experiment cv1. We notice eddies almost as big as the convective patch. The advection of these eddies away from the mixed patch can drag most of the dense water away. Experiment cv2 also has a patch's radius close to the Rossby radius of deformation, but the patch is not as much affected as in experiment cv1.

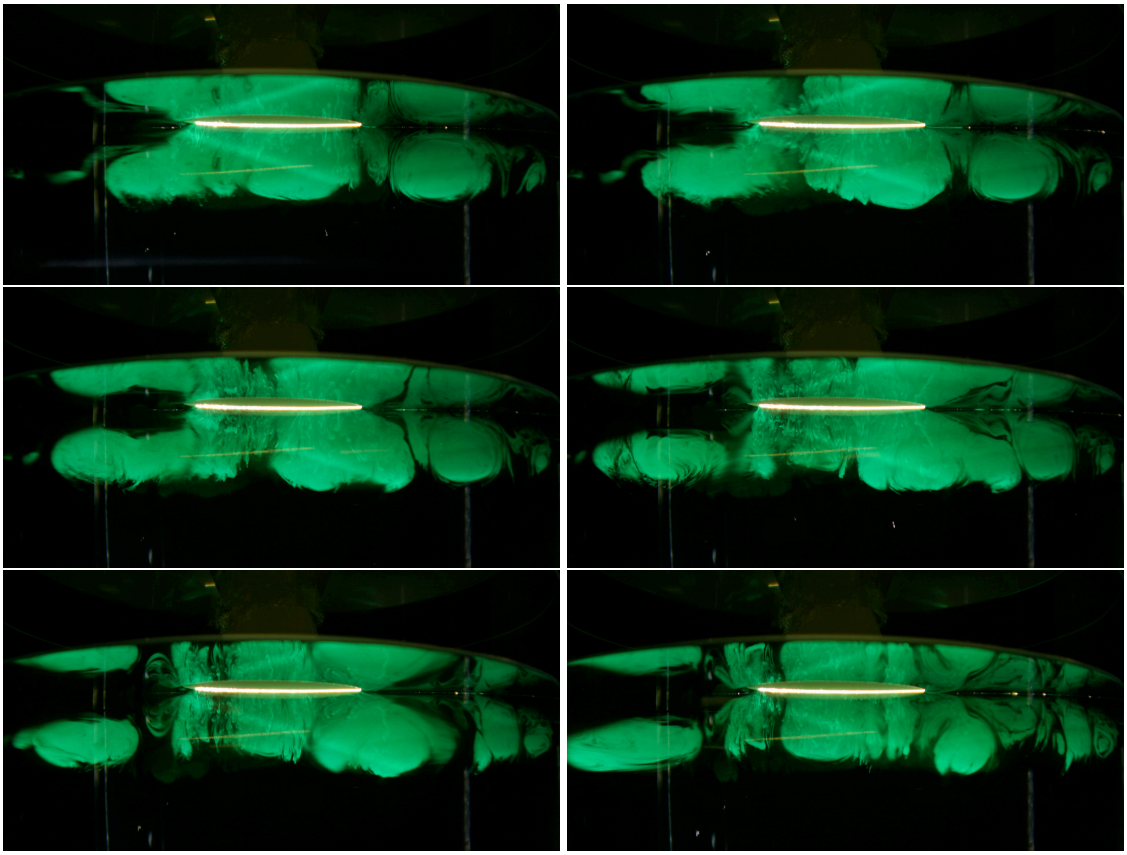

Figure D.2: Side view for experiment cv1. Pictures were taken every 12s, corresponding roughly to a rotation period. The white disc is the filter through which the dense fluorescent solution is released. We are interested in what happens below (above is only the reflection on the surface of the water).

At the end of convection, we have $h_f = 17cm$, hence the Taylor and Rayleigh numbers are $Ta \sim 10^7$ and $Ra_f \sim 10^{16}$. From Boubnov and Golitsyn (1990), we can conclude than the convection regime at the end of the experiment is the one called "thermal turbulence", although the system briefly experiences the other regimes first (thermoconductivity, regular vortex grid and then irregular geostrophic turbulence). What is thermal in their case relates to the salinity in our case. The thermoconductivity regime corresponds to the very beginning of

the experiment, during which the heat loss is absorbed by conduction. It is very brief. The regular vortex grid corresponds to plumes regularly spaced. In the irregular geostrophic turbulence, the plumes are not regularly spaced anymore. The thermal turbulence regime corresponds to a turbulent mixed layer.

Jacobs and Ivey (1999) define two non dimensional numbers marking the transition between regimes in the case of non stratified convection. The Rossby number $R_{0_R} = (\frac{B_0}{f^3 R^2})^{1/4} \sim 1.7$ is related to the transition between baroclinically stable and unstable regimes while the natural Rossby number $R_0^* = (\frac{B_0}{f^3 h})^{1/2} \sim 0.54$ indicates if the small-scale turbulence is controlled by rotation or by buoyancy forces. We are in the baroclinically unstable regime, so we will be able to observe baroclinic eddies, and the value of R_0^* is adapted to the parallel between the laboratory and the oceans ((Marshall and Schott, 1999b).

We apply a time varying forcing with periods of a few rotation periods, hence we are exploring a different range of parameter than the numerical experiments, with a much shorter time-scale.

D.3 Results

D.3.1 Top View

Some images of the top view of the experiment are on figure D.3. We observe the development of baroclinic eddies around the patch. One of them is visible in the lower part of the photo. We see it slowly pinching off. The last pictures show that similar eddies have formed all around the patch. These eddies are cyclonic. The cyclonic rim current developping around the patch is visible on the movie of the top view (not shown here). Away from the patch, we also observed anticyclones with the buoyant particles at the surface.

D.3.2 Side View

A sequence of photos from the side view of the experiment is on figure D.4. When the forcing is on, we see plumes reaching the depth of the mixed layer. The deepening is characterised by a mixed layer deeper at the centre than around the cooling disc. During the restratification period, we see that the patch is less well mixed. We can even distinguish some eddies within patch. The side view present similarities with the potential vorticity plot from the numerical experiments.

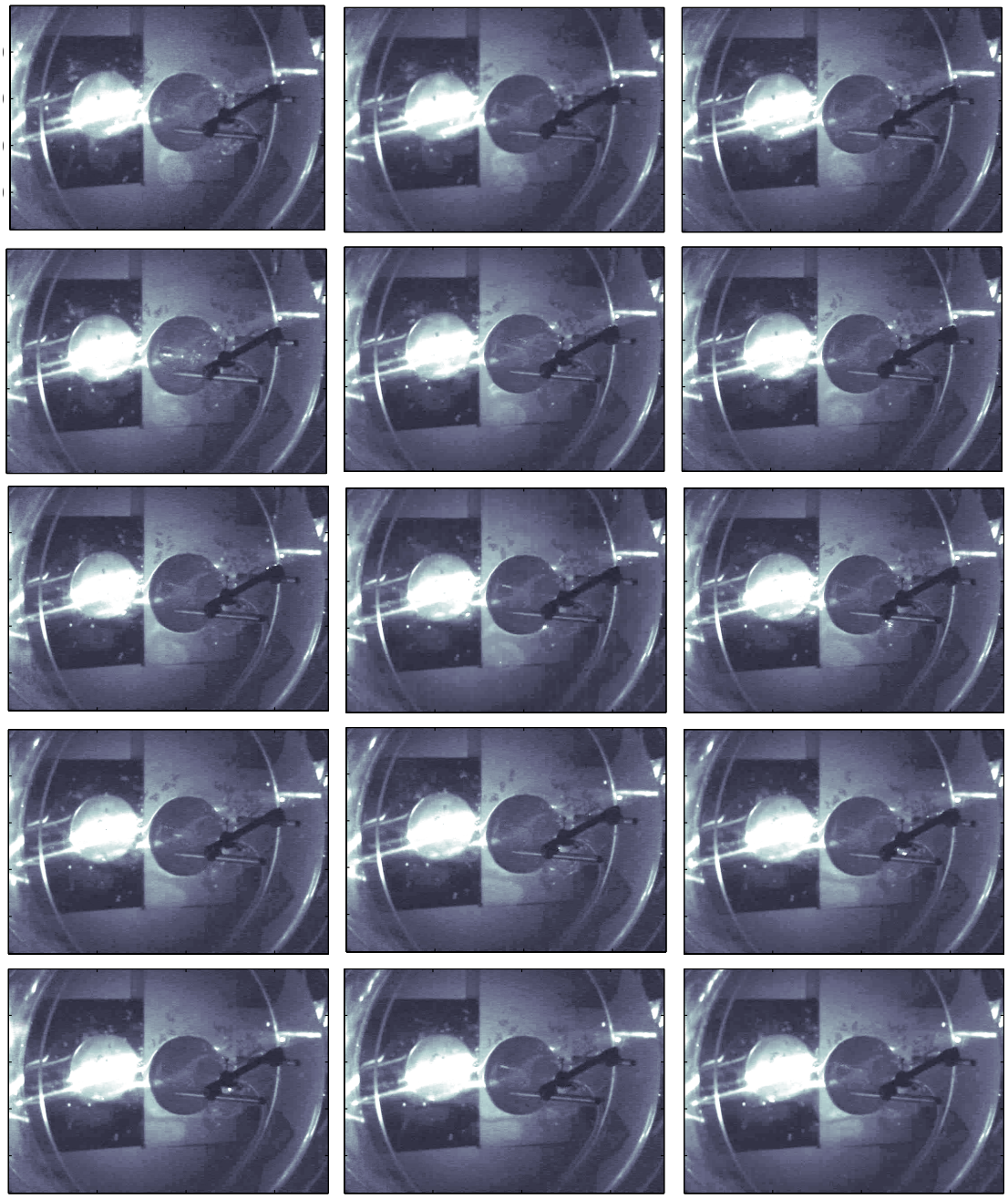

Figure D.3: Top view for experiment cv2.

D.3.3 Mixed layer depth, forcing and CTD casts

Figure D.5 shows the mixed layer depths and the salinity profiles obtained by the CTD. The flow rate was calculated as the time derivative of the pressure record obtained at the bottom of the source tank. The acquisition period and the accuracy of the pressure sensor only allow an approximate estimate of the flow rate, as we need the time derivative rather than the volume of liquid released. There are problems with the flow record, partly because of the acquisition period, so it is not displayed here. This makes the analysis of this experiment much more

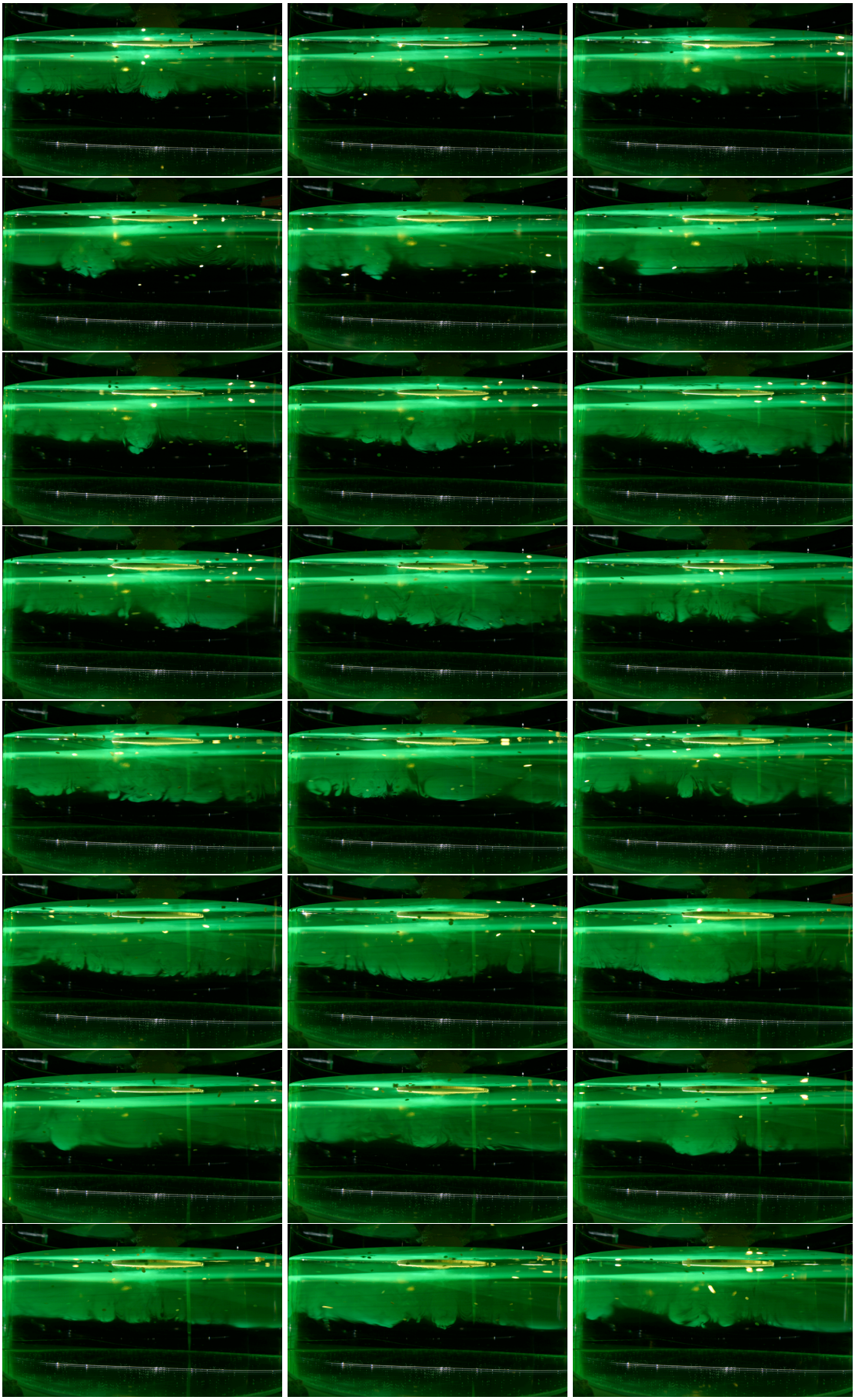

Figure D.4: Side view for experiment cv2.

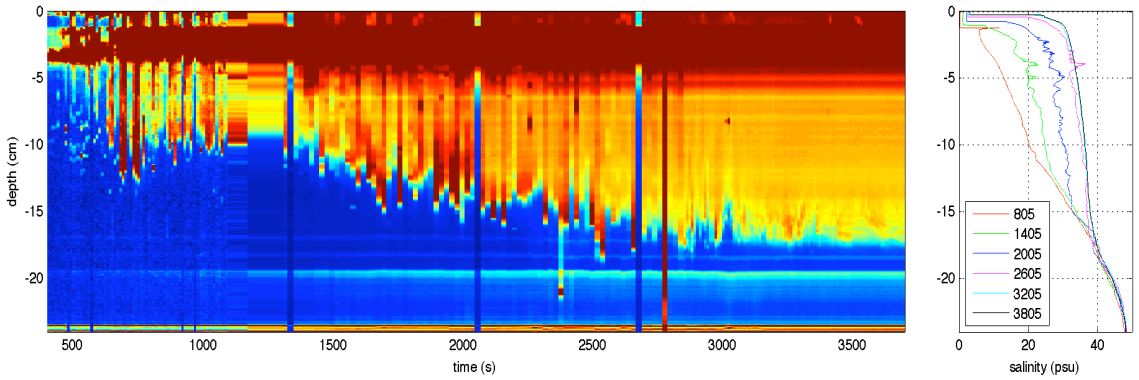

Figure D.5: Flow rate (top), mixed layer depth (bottom) and salinity profiles (right).

difficult, hence we will only make qualitative comments.

The mixed layer depth plot was obtained using the side view images. We selected a rectangular zone at the centre of the disc, from the surface of the disc down to the horizontal ray of light marking the bottom of the tank, and then scaled it using the known depth of the tank. A problem in the settings of the camera made the first images very dark, so their contrast has been enhanced in the processing of the images. Hence, what we see is simply the amount of light for a profile at the centre of the tank.

The CTD was calibrated before calculating the salinity. The record shows the deepening of the mixed layer, which is felt even further from the patch. The profiles at time $1405s$, $2005s$ and 2605 are not very smooth. We can probably associate this to the eddies passing nearby. Once the deepening has stopped, for profiles at $3205s$ and 3805, we do not see this signal anymore. We suspect this is because the last release of dense water was far enough in time to have been mixed.

D.4 Conclusion

During the experiments presented here, there were a few technical problems that prevent us from being able to conclude quantitatively. However, we can conclude qualitatively. The main point is that we confirmed that the convective patch is not fully mixed at all time. The second point is that there is more activity at the rim of the patch when the forcing is on than when it is off. We have observed both elements in the numerical simulations.

Bibliography

Adcroft, A., Campin, J.-M., Hill, C., and Marshall, J. (2004). Implementation of an atmosphere-ocean general circulation model on the expanded spherical cube. *Monthly Weather Review*, 132(12):2845–2863.

Adcroft, A., Hill, C., and Marshall, J. (1997). Representation of topography by shaved cells in a height coordinate ocean model. *Monthly Weather Review*, 125:2293–2315.

Afanasyev, Y. D., Rhines, P. B., and Lindahl, E. G. (2008). Emission of inertial waves by baroclinically unstable flows: Laboratory experiments with altimetric imaging velocimetry. *Journal of the Atmospheric Sciences*, 65(1):250–262.

Alverson, K. (1997). Mechanisms for lateral exchange with oceanic convection sites. *Journal of Physical Oceanography*, 27:1436–1446.

Arakawa, A. and Lamb, V. (1977). *Methods in Computational Physics*, volume 17, chapter Computational design of the basic dynamical processes of the UCLA general circulation model, pages 174–267. Academic Press.

Avsic, T., Karstensen, J., Send, U., and Fischer, J. (2006). Interannual variability of newly formed Labrador Sea Water from 1994 to 2005. *Geophysical Research Letters*, 33(L21S02).

Belkin, I., Levitus, S., Antonov, J., and Malmberg, S. (1998). "Great Salinity Anomalies" in the North Atlantic. *Progress In Oceanography*, 41:1–68.

Béthoux, J. and Gentili, B. (1996). The Mediterranean sea, coastal and deep-sea signatures of climatic and environmental changes. *Journal of Marine Systems*, 7:383–394.

Béthoux, J. P., Gentili, B., Raunet, J., and Tailliez, D. (1990). Warming trend in the western Mediterranean deep water. *Nature*, 347:660–662.

Béthoux, J. P., Gentili, B., and Tailliez, D. (1998). Warming and freshwater budget change in the Mediterranean since the 1940s, their possible relation to the greenhouse effect. *Geophysical Research Letters*, 25(7):1023–1026.

Blumen, W. (1979). On short-wave baroclinic instability. *Journal of the Atmospheric Sciences*, 36(10):1925–1933.

Blumen, W. and Wu, R. (1995). Geostrophic adjustment - frontogenesis and energy-conversion. *Journal of Physical Oceanography*, 25(3):428–438.

Boccaletti, G., Ferrari, R., and Fox-Kemper, B. (2007). Mixed layer instabilities and restratification. *Journal of Physical Oceanography*, 37:2228–2250.

Boscolo, R. and Bryden, H. (2001). Causes of long-term changes in Aegean Sea deep water. *Oceanologica Acta*, 24:519–527.

Boubnov, B. and Golitsyn, G. (1990). Temperature and velocity field regimes of convective motions in a rotating plane fluid layer. *Journal of Fluid Mechanics*, 219:215–239.

Brandt, P., Schott, F., Funk, A., and Martins, C. (2004). Seasonal to interannual variability of the eddy field in the Labrador Sea from satellite altimetry. *Journal of Geophysical Research-Oceans*, 109(C02028).

Broecker, W. (1991). The Great Ocean Conveyor. *Oceanography*, 4(2):79–89.

Bumke, K., Karger, U., and Uhlig, K. (2002). Measurements of turbulent fluxes of momentum and sensible heat over the Labrador Sea. *Journal of Physical Oceanography*, 32:401–410.

Canals, M., Puig, P., de Madron, X. D., Heussner, S., Palanques, A., and Fabres, J. (2006). Flushing submarine canyons. *Nature*, 444(7117):354–357.

Chanut, J., Barnier, B., Large, W., Debreu, L., Penduff, T., Molines, J. M., and Mathiot, P. (2008). Mesoscale eddies in the labrador sea and their contribution to convection and restratification. *Journal of Physical Oceanography*, 38(8):1617–1643.

Chapman, D. (1998). Setting the scales of the ocean response to isolated convection. *Journal of Physical Oceanography*, 28:606–620.

Chapman, D. and Gawarkiewicz, G. (1997). Shallow convection and buoyancy equilibration in an idealized coastal polynya. *Journal of Physical Oceanography*, 27(4):555–566.

Charney, J. G. (1947). The dynamics of long waves in a baroclinic westerly current. *Journal of Meteorology*, 4:165–163.

Clarke, R. and Gascard, J. (1983). The formation of Labrador Sea Water. 2: Large-scale processes. *Journal of Physical Oceanography*, 13:1764–1778.

Cuny, J., Rhines, P., Niiler, P., and Bacon, S. (2002). Labrador sea boundary currents and the fate of the Irminger Sea Water. *Journal of Physical Oceanography*, 32:627–647.

Cuny, J., Rhines, P., Schott, F., and Lazier, J. (2005). Convection above the Labrador continental slope. *Journal of Physical Oceanography*, 35:489–511.

Davis, R. E., Eriksen, C. C., and Jones, C. (2003). *Technology and applications of autonomous underwater vehicles*, chapter Autonomous buoyancy-driven underwater vehicles. Taylor and Francis, London.

Dickson, R., Meincke, J., Malmberg, S., and Lee, A. (1988). The Great Salinity Anomaly in the Northern North-Atlantic 1968-1982. *Progress In Oceanography*, 20:103–151.

Eady, E. (1949). Long waves and cyclone waves. *Tellus*, 1(3):33–52.

Eden, C. and Böning, C. (2002). Sources of eddy kinetic energy in the Labrador Sea. *Journal of Physical Oceanography*, 32:3346–3363.

Emanuel, K. (1994). *Atmospheric convection*. Oxford University Press.

Emelianov, M., Font, J., Turiel, A., Millot, C., Sole, J., Poulain, P.-M., Julia, A., and Vitria, M.-R. (2006). Transformation of Levantine Intermediate Water tracked by MEDARGO floats in the Western Mediterranean. *Ocean Science*, 2:281–290.

Eriksen, C. C., Osse, T. J., Light, R. D., Wen, T., Lehman, T. W., Sabin, P. L., Ballard, J. W., and Chiodi, A. M. (2001). Seaglider: A long-range autonomous underwater vehicle for oceanographic research. *Journal of Oceanic Engineering*, 26(4):424–436.

Fernando, H. J., Chen, R.-R., and Boyer, D. L. (1991). Effect of rotation on convective turbulence. *Journal of Fluid Mechanics*, 228(513-547).

Font, J., Salat, J., Emelianov, M., Puig, P., Palanques, A., Julia, A., Lopez-Jurado, J. L., Gonzalez-Pola, C., and Flos, J. (2006). A new deep water formed in the NW Mediterranean in 2005. *Geophysical Research Abstracts - European Geophysical Union General Assembly 2006*.

Fox-Kemper, B., Ferrari, R., and Hallberg, R. (2008). Parameterization of mixed layer eddies. Part I: Theory and diagnosis. *Journal of Physical Oceanography*, 38:1145–1165.

Garwood, R. W. J. (1991). *Deep convection and deep water formation in the ocean*, chapter Enhancements to deep turbulent entrainment. Elsevier.

Gascard, J. and Clarke, RA, R. (1983). The formation of Labrador Sea Water. 2: Mesoscale and smaller-scale processes. *Journal of Physical Oceanography*, 13:1779–1797.

Gascard, J. C. (1978). Mediterranean deep water formation, baroclinic instability and oceanic eddies. *Oceanologica Acta*, 1(3):315–330.

Gent, P. and McWilliams, J. C. (1990). Isopycnal mixing in ocean circulation models. *Journal of Physical Oceanography*, 20:150–155.

Green, J. and Margerison, D. (1978). *Statistical treatment of experimental data*, volume 141. Elsevier Scientific Publishing Company.

Griffiths, G., Jones, C., Ferguson, J., and Bose, N. (2007). Undersea gliders. *Journal of Ocean Technology*, 2(2).

Haine, T. and Marshall, J. (1998). Gravitational, symmetric, and baroclinic instability of the ocean mixed layer. *Journal of Physical Oceanography*, 28:634–658.

Harcourt, R., Steffen, E., Garwood, R., and D'Asaro, E. (2002). Fully Lagrangian floats in Labrador Sea deep convection: Comparison of numerical and experimental results. *Journal of Physical Oceanography*, 32:493–510.

Hatun, H., Eriksen, C. C., Rhines, P. B., and Lilly, J. M. (2007). Buoyant eddies entering the Labrador Sea observed with gliders and altimetry. *Journal of Physical Oceanography*, 37:2838–2854.

Haynes, P. and McIntyre, M. (1990). On the conservation and impermeability theorems for potential vorticity. *Journal of the Atmospheric Sciences*, 47:2021–2031.

Hill, D. (2002). General density gradients in general domains: the "two-tank" method revisited. *Experiments In Fluids*, 32:434–440.

Hogg, N. G. (1973). The preconditioning phase of MEDOC 1969 - II. Topographic effects. *Deep-Sea Research*, 20:449–459.

Hogg, N. G. and Stommel, H. M. (1985). Hetonic explosions: The breakup and spread of warm pools as explained by baroclinic point vortices. *Jounal of the Atmospheric Sciences*, 42(14):1465–1476.

Hong, X., Hodur, R. M., and Martin, P. J. (2007). Numerical simulation of deep-water convection in the Gulf of Lion. *Pure and Applied Geophysics*, 164:2101–2116.

Hoskins, B. and McIntyre, M.E.and Robertson, A. (1985). On the use and significance of isentropic potential vorticity maps. *Quarterly Journal of the Royal Meteorological Society*, 111(470):877–946.

Hurrell, J. (1995). Decadal trends in the North Atlantic Oscillation and relationships to regional temperature and precipitation. *Science*, 269(676-679).

Ivey, G. N., Taylor, J. R., and Coates, M. J. (1995). Convectively driven mixed-layer growth in a rotating, stratified fluid. *Deep-Sea Research Part I-Oceanographic Research Papers*, 42(3):331–349.

Jacobs, P. and Ivey, G. (1999). Rossby number regimes for isolated convection in a homogeneous, rotating fluid. *Dynamics of Atmospheres and Oceans*, 30:149–171.

Jones, H. and Marshall, J. (1993). Convection with rotation in a neutral ocean - a study of open-ocean deep convection. *Journal of Physical Oceanography*, 23(6):1009–1039.

Jones, H. and Marshall, J. (1997). Restratification after deep convection. *Journal of Physical Oceanography*, 27:2276–2287.

Katsman, C., Spall, M., and Pickart, R. (2004). Boundary current eddies and their role in the restratification of the Labrador Sea. *Journal of Physical Oceanography*, 34:1967–1983.

Killworth, P. (1983). Deep convection in the world ocean. *Reviews of Geophysics*, 21:1–26.

Killworth, P. (1985). A 2-level wind and buoyancy driven thermocline model. *Journal of Physical Oceanography*, 15:1414–1432.

Killworth, P. (1989). On the parameterisation of deep convection in ocean models. In *Parameterizing small scale processes in the ocean, Proceedings of the Hawaiian Winter Workshop.*

Killworth, P. (1996). Time interpolation of forcing fields in ocean models. *Journal of Physical Oceanography*, 26(1):136–143.

Klinger, B. A., Marshall, J., and Send, U. (1996). Representation of convective plumes by vertical adjustment. *Journal of Geophysical Research-Oceans*, 101(C8):18175–18182.

Krahmann, G. and Schott, F. (1998). Longterm increases in Western Mediterranean salinities and temperatures: anthropogenic and climatic sources. *Geophysical Research Letters*, 25(22):4209–4212.

Krahmann, G., Visbeck, M., Smethie, W., D'Asaro, E., Rhines, P., Clarke, R., Lazier, J., Davis, R., Niiler, P., Guest, P., Meincke, J., Moore, G., Pickart, R., and Owens, W. (2003). The Labrador Sea deep convection experiment data collection. *Geochemistry Geophysics Geosystems*, 4(1091).

Kraus, E. and Turner, J. (1967). A one-dimensional model of the seasonal thermocline. *Tellus*, 19:88–97.

Lapeyre, G., Klein, P., and Hua, B. L. (2006). Oceanic restratification forced by surface frontogenesis. *Journal of Physical Oceanography*, 36(8):1577–1590.

Large, W., McWilliams, J. C., and Doney, S. (1994). Oceanic vertical mixing: A review and a model with a nonlocal boundary layer parameterization. *Reviews of Geophysics*, 32(4):363–404.

Lascaratos, A., Roether, W., Nittis, K., and Klein, B. (1999). Recent changes in deep water formation and spreading in the eastern Mediterranean Sea: a review. *Progress In Oceanography*, 44:5–36.

Lavender, K., Davis, R., and Owens, W. (2002). Observations of open ocean deep convection in the Labrador Sea from subsurface floats. *Journal of Physical Oceanography*, 32:511–526.

Lazier, J., Hendry, R., Clarke, A., Yashayaev, I., and Rhines, P. (2002). Convection and restratification in the Labrador Sea, 1990-2000. *Deep-Sea Research Part I-Oceanographic Research Papers*, 49:1819–1835.

Legg, S. and Marshall, J. (1993). A heton model of the spreading phase of open-ocean deep convection. *Journal of Physical Oceanography*, 23(6):1040–1056.

Legg, S. and Marshall, J. (1998). The influence of the ambient flow on the spreading of convected water masses. *Journal of Marine Research*, 56(1):107–139.

Legg, S. and McWilliams, J. (2002). Sampling characteristics from isobaric floats in a convective eddy field. *Journal of Physical Oceanography*, 32:527–544.

Legg, S., McWilliams, J., and Gao, J. B. (1998). Localization of deep ocean convection by a mesoscale eddy. *Journal of Physical Oceanography*, 28(5):944–970.

Legg, S. Y., Jones, H., and Visbeck, M. (1996). A heton perspective of baroclinic eddy transfer in localized open ocean convection. *Journal of Physical Oceanography*, 26(10):2251–2266.

Lilly, J. and Rhines, P. (2002). Coherent eddies in the Labrador Sea observed from a mooring. *Journal of Physical Oceanography*, 32:585–598.

Lilly, J., Rhines, P., Schott, F., Lavender, K., Lazier, J., Send, U., and D'Asaro, E. (2003). Observations of the Labrador Sea eddy field. *Progress In Oceanography*, 59:75–176.

Lilly, J., Rhines, P., Visbeck, M., Davis, R., Lazier, J., Schott, F., and Farmer, D. (1999). Observing deep convection in the Labrador Sea during winter 1994/95. *Journal of Physical Oceanography*, 29:2065–2098.

Lopez-Jurado, J. L., Gonzalez-Pola, C., and Velez-Belchi, P. (2005). Observation of an abrupt disruption of the long-term warming trend at the Balearic Sea, Western Mediterranean Sea, in summer 2005. *Geophysical Research Letters*, 32(L24606).

Madec, G., Chartier, M., and Crépon, M. (1991). The effect of thermohaline forcing variability on deep-water formation in the Western Mediterranean sea - a high-resolution 3-dimensional numerical study. *Dynamics of Atmospheres and Oceans*, 15(3-5):301–332.

Madec, G., Lott, F., Delecluse, P., and Crépon, M. (1996). Large-scale preconditioning of deep-water formation in the northwestern Mediterranean Sea. *Journal of Physical Oceanography*, 26(8):1393–1408.

Manalotte-Rizzoli, P. (1991). The northern Adriatic Sea as a prototype of convection and water mass formation on the continental shelf. In Elsevier, editor, *International Monterey Colloquium on deep convection and deep water formation in the oceans*.

Marotzke, J. (1991). Influence of convective adjustment on the stability of the thermohaline circulation. *Journal of Physical Oceanography*, 21:903–907.

Marshall, J., Adcroft, A., Campin, J.-M., and Hill, C. (2004). Atmosphere-ocean modeling exploiting fluid isomorphisms. *Monthly Weather Review*, 132(12):2882–1894.

Marshall, J., Adcroft, A., Hill, C., Perelman, L., and Heisey, C. (1997a). A finite-volume, incompressible Navier Stokes model for studies of the ocean on parallel computers. *Journal of Geophysical Research*, 102(C3):5753–5766.

Marshall, J., Dobson, F., Moore, K., Rhines, P., Visbeck, M., d'Asaro, E., Bumke, K., Chang, S., Davis, R., Fischer, K., Garwood, R., Guest, P., Harcourt, R., Herbaut, C., Holt, T., Lazier, J., Legg, S., McWilliams, J., Pickart, R., Prater, M., Renfrew, I., Schott, F., Send, U., and Smethie, W. (1998a). The Labrador Sea deep convection experiment. *Bulletin of the American Meteorological Society*, 79:2033–2058.

Marshall, J. and Fiadeiro, M. (2002). The Labrador Sea deep convection experiment. *Journal of Physical Oceanography*, 32:381–381.

Marshall, J., Hill, C., Perelman, L., and Adcroft, A. (1997b). Hydrostatic, quasi-hydrostatic, and nonhydrostatic ocean modeling. *Journal of Geophysical Research*, 102(C3):5733–5752.

Marshall, J., Jones, H., and Hill, C. (1998b). Efficient ocean modeling using non-hydrostatic algorithms. *Journal of Marine Systems*, 18:115–134.

Marshall, J., Jones, H., Karsten, R., and Wardle, R. (2002). Can eddies set ocean stratification? *Journal of Physical Oceanography*, 32(1):26–38.

Marshall, J. and Schott, F. (1999a). Open-ocean convection: Observations, theory, and models. *Reviews of Geophysics*, 37(1):1–64.

Marshall, J. and Schott, F. (1999b). Open-ocean convection: Observations, theory, and models. *Reviews of Geophysics*, 37(1):1–64.

MEDOC-Group (1970). Observation of formation of deep water in the Mediterranean Sea, 1969. *Nature*, 227(5262):1037–1040.

Mertens, C. and Schott, F. (1998). Interannual variability of deep-water formation in the northwestern Mediterranean. *Journal of Physical Oceanography*, 28(7):1410–1424.

Millot, C. and Taupier-Letage, I. (2004). Circulation in the Mediterranean Sea. In Editor, S.-V., editor, *The Handbook of Environmental Chemistry, Vol. 1 (The Natural Environment and the Biological Cycles)*.

Moore, G. and Peltier, W. (1987). Cyclogenesis in frontal zones. *Journal of the Atmospheric Sciences*, 44(2):384–409.

Nakamura, N. (1988). Scale selection of baroclinic instbaility - effect of stratification and nongeostrophy. *Journal of the Atmospheric Sciences*, 45(21):3253–3267.

Nurser, A. (1996). A review of models and observations of the oceanic mixed layer. Southampton Oceanography Centre Internal Document 14.

Nurser, A. and Zhang, J. (2000). Eddy-induced mixed layer shallowing and mixed layer/thermocline exchange. *Journal of Geophysical Research-Oceans*, 105(C9):21851–21868.

Ou, H. (1986). On the energy-conversion during geostrophic adjustment. *Journal of Physical Oceanography*, 16(12):2203–2204.

Ou, HW, H. (1984). Geostrophic adjustment - a mechanism for frontogenesis. *Journal of Physical Oceanography*, 14(6):994–1000.

Paluszkiewicz, T. and Romea, R. (1997). A one-dimensional model for the parameterization of deep convection in the ocean. *Dynamics of Atmospheres and Oceans*, 26:95–130.

Pedlosky, J. and Thomson, J. (2003). Baroclinic instability of time-dependent currents. *Journal of Fluid Mechanics*, 490:189–215.

Pickart, R., Spall, M., Ribergaard, M., Moore, G., and Milliff, R. (2003). Deep convection in the Irminger Sea forced by the Greenland tip jet. *Nature*, 424:152–156.

Pickart, R., Torres, D., and Clarke, R. (2002). Hydrography of the Labrador Sea during active convection. *Journal of Physical Oceanography*, 32:428–457.

Pickart, R. S. and Spall, M. A. (2007). Impact of Labrador Sea convection on the North Atlantic meridional overturning circulation. *Journal of Physical Oceanography*, 37:2207–2227.

Plougonven, R. and Zeitlin, V. (2005). Lagrangian approach to geostrophic adjustment of frontal anomalies in a stratified fluid. *Geophysical and Astrophysical Fluid Dynamics*, 99(2):101–135.

Poulin, F., Flierl, G., and Pedlosky, J. (2003). Parametric instability in oscillatory shear flows. *Journal of Fluid Mechanics*, 481:329–353.

Prater, M. (2002). Eddies in the Labrador Sea as observed by profiling RAFOS floats and remote sensing. *Journal of Physical Oceanography*, 32:411–427.

Rahmstorf, S, S. (1995). Bifurcations of the Atlantic thermohaline circulation in response to changes in the hydrological cycle. *Nature*, 378:145–149.

Renfrew, I., Moore, G., Guest, P., and Bumke, K. (2002). A comparison of surface layer and surface turbulent flux observations over the Labrador Sea with ECMWF analyses and NCEP reanalysis. *Journal of Physical Oceanography*, 32:383–400.

Reznik, G., Zeitlin, V., and Ben Jelloul, M. (2001). Nonlinear theory of geostrophic adjustment. part 1. rotating shallow-water model. *Journal of Fluid Mechanics*, 445:93–120.

Rixen, M., Beckers, J. M., Levitus, S., Antonov, J., Boyer, T., Maillard, C., Fichaut, M., Balopoulos, E., Iona, S., Dooley, H., Garcia, M. J., Manca, B., Giorgetti, A., Manzella, G., Mikhailov, N., Pinardi, N., and Zavatarelli, M. (2005). The Western Mediterranean Deep Water: A proxy for climate change. *Geophysical Research Letters*, 32(L12608).

Roether, W., Manca, B., Klein, B., Bregant, D., Georgopoulos, D., Beitzel, V., Kovacevic, V., and Luchetta, A. (1996). Recent changes in eastern Mediterranean deep waters. *Science*, 271:333–335.

Rohling, E. and Bryden, H. (1992). Man-induced salinity and temperature increases in western Mediterranean deep-water. *Journal of Geophysical Research-Oceans*, 97(C7):11191–11198.

Rossby, G. (1938). On the mutual adjustment of pressure and velocity distributions in certain simple current systems. *Journal of Marine Research*, 1:239–263.

Rudnick, D. L., Davis, R. E., Eriksen, C. C., Fratantoni, D. M., and Perry, M. J. (2004). Underwater gliders for ocean research. *Marine Technology Society Journal*, 38(2):73–84.

Sander, J., Wolfgladrow, D., and Olbers, D. (1995). Numerical-studies of open-ocean deep convection. *Journal of Geophysical Research-Oceans*, 100(C10):20579–20600.

Sathiyamoorthy, S. and Moore, G. (2002). Buoyancy flux at ocean weather station Bravo. *Journal of Physical Oceanography*, 32:458–474.

Schott, F. and Leaman, K. D. (1991). Observations with moored Acoustic Doppler Current Profilers in the convection regime in the Golfe du Lion. *Journal of Physical Oceanography*, 21(4):558–574.

Schott, F., Visbeck, M., Send, U., Fischer, J., Stramma, L., and Desaubies, Y. (1996). Observations of deep convection in the Gulf of Lions, northern Mediterranean, during the winter of 1991/92. *Journal of Physical Oceanography*, 26(4):505–524.

Schott, F, F., Visbeck, M, M., and Fischer, J. (1993). Observations of vertical currents and convection in the central Greenland Sea during the winter of 1988-1989. *Journal of Geophysical Research-Oceans*, 98:14401–14421.

Schroeder, K., Gasparini, G., Tangherlini, M., and Astraldi, M. (2006). Deep and intermediate water in the Western Mediterranean under the influence of the Eastern Mediterranean Transient. *Geophysical Research Letters*, 33(L21607).

Send, U. and Marshall, J. (1995). Integral effects of deep convection. *Journal of Physical Oceanography*, 25(5):855–872.

Smith, R., Bryden, H. L., and Stansfield, K. (2008). Observations of new western Mediterranean deep water formation using Argo floats 2004-2006. *Ocean Science*, 4:133–149.

Somot, S., Sevault, F., and Deque, M. (2006). Transient climate change scenario simulation of the Mediterranean Sea for the twenty-first century using a high-resolution ocean circulation model. *Climate Dynamics*, 27(7-8):851–879.

Steffen, E. and D'Asaro, E. (2002). Deep convection in the Labrador Sea as observed by Lagrangian floats. *Journal of Physical Oceanography*, 32:475–492.

Stommel, H. M. (1989). The Slocum mission. *Oceanus*, 32(4):93–96.

Stone, P. (1966). On non-geostrophic baroclinic instability. *Journal of the Atmospheric Sciences*, 23:390–400.

Stone, P. (1970). On non-geostrophic baroclinic instability: Part ii. *Journal of the Atmospheric Sciences*, 27:721–726.

Straneo, F. (2006). Heat and freshwater transport through the central Labrador Sea. *Journal of Physical Oceanography*, 36:606–628.

Straneo, F., Kawase, M., and Riser, S. (2002). Idealized models of slantwise convection in a baroclinic flow. *Journal of Physical Oceanography*, 32:558–572.

Stratford, K. and Haines, K. (2002). Modelling changes in Mediterranean thermohaline circulation 1987-1995. *Journal of Marine Systems*, 33:51–62.

Stuart, A., Ord, K., and Arnold, S. (1999). *Kendall's advanced theory of statistics. Volume 2A: Classical inference and the linear model*. Arnold, London.

Testor, P. and Gascard, J. C. (2006). Post-convection spreading phase in the northwestern mediterranean sea. *Deep-Sea Research Part I-Oceanographic Research Papers*, 53(5):869–893.

Theocharis, A., Klein, B., Nittis, K., and Roether, W. (2002). Evolution and status of the Eastern Mediterranean Transient (1997-1999). *Journal of Marine Systems*, 33:91–116.

Turner, J. (1973). *Buoyancy effects in fluids*. Cambridge University Press.

Vignudelli, S., Gasparini, G., Astraldi, M., and Schiano, M. (1999). A possible influence of the north atlantic oscillation on the circulation of the western mediterranean sea. *Geophysical Research Letters*, 26(5):623–626.

Visbeck, M., Marshall, J., and Jones, H. (1996). Dynamics of isolated convective regions in the ocean. *Journal of Physical Oceanography*, 26(9):1721–1734.

Viudez, A. and Dritschel, D. (2006). Spontaneous generation of inertia-gravity wave packets by balanced geophysical flows. *Journal of Fluid Mechanics*, 553:107–117.

Voorhis, A. D. and Webb, D. C. (1970). Vertical currents in a winter sinking region. *Transactions-American Geophysical Union*, 51(4):315.

Whitehead, J. A., Marshall, J., and Hufford, G. E. (1996). Localized convection in rotating stratified fluid. *Journal of Geophysical Research-Oceans*, 101(C11):25705–25721.

Wu, P., Haines, K., and Pinardi, N. (2000). Toward an understanding of deep-water renewal in the eastern Mediterranean. *Journal of Physical Oceanography*, 30:443–458.

Yashayaev, I. (2007). Hydrographic changes in the Labrador Sea, 1960-2005. *Progress In Oceanography*, 73:242–276.

Yin, F. and Sarachik, E. (1994). An efficient convective adjustment scheme for ocean general circulation models. *Journal of Physical Oceanography*, 24(6):1425–1430.

Young, W. and Chen, L. (1995). Baroclinic instability and thermohaline gradient alignment in the mixed layer. *Journal of Physical Oceanography*, 25(12):3172–3185.

Zeitlin, V., Reznik, G., and Ben Jelloul, M. (2003). Nonlinear theory of geostrophic adjustment. part 2. two-layer and continuously stratified primitive equations. *Journal of Fluid Mechanics*, 491:207–228.